

VIBRATIONS

IN PHYSICAL SYSTEMS

VOLUME 30, No. 2

POZNAŃ 2019



VIBRATIONS IN PHYSICAL SYSTEMS

EDITORS

Czesław CEMPEL (honorary editor)

Tomasz STRĘK (editor in-chief)

Maciej TABASZEWSKI (editor)

TECHNICAL EDITORS

Paweł FRITZKOWSKI

Tomasz HERMANN

Hubert JOPEK

PUBLISHER

Institute of Applied Mechanics,
Poznan University of Technology

EDITORIAL OFFICE

Poznan University of Technology

Institute of Applied Mechanics

ul. Jana Pawła II 24, 61-139 Poznań, Poland

tel. +48 61 665 23 01

vibsys@put.poznan.pl

vibsys.put.poznan.pl

ISSN 0860-6897

Poznan, Poland 2019



VIBRATIONS IN PHYSICAL SYSTEMS

EDITORIAL BOARD

Vladimir I. ALSHITS
Jan AWREJCEWICZ
Wojciech BATKO
Romuald BĘDZIŃSKI
Tadeusz BURCZYŃSKI
Czesław CEMPEL
Enzo CIANCIO
Evgen CZAPLA
Zbigniew DĄBROWSKI
Marian W. DOBRY
Antoni GAJEWSKI
Joseph GRIMA
Jan HOLNICKI-SZULC
Erik V. JANSSON
Jarosław JĘDRYSIAK
Stefan JONIAK
David JOU
Jerzy KALETA
Jan KOŁODZIEJ
Tomasz ŁODYGOWSKI

Krzysztof MAGNUCKI
Krzysztof MARCHELEK
Stanisław MATYSIAK
Wolfgang MUSCHIK
Józef NIZIOŁ
Andrzej RADOWICZ
Stanisław RADKOWSKI
Liliana RESTUCCIA
Hamid M. SEDIGHI
Roman STAROSTA
Tomasz STREK
Tomasz SZOLC
Maciej TABASZEWSKI
Franciszek TOMASZEWSKI
Andrzej TYLIKOWSKI
Tadeusz UHL
Jerzy WARMIŃSKI
Józef WOJNAROWSKI
Alexandr YAVLENSKY

COPYRIGHT / OPEN ACCESS

Articles published in *Vibrations in Physical Systems* will be Open-Access articles distributed under the terms and conditions of the Creative Commons Attribution License (CC BY).

CONTENTS

1. Stefan WEYNA	2019201
Effective Diagnostic of Local Noise Sources with Acoustic Imaging	
2. Zbigniew KOZANECKI, Eliza TKACZ, Jakub ŁAGODZIŃSKI, Malgorzata GIZELSKA	2019202
Dynamic Stability of Rotating Systems in Turbomachinery Under API Standards	
3. Mateusz KOZIOŁ, Piotr CUPIAŁ	2019203
Experimental Investigation of Rotor Vibration by Using Full Spectra from Shaft Mounted Piezoelectric Patches	
4. Maciej TABASZEWSKI	2019204
Identification of Rolling Bearing Condition by Means of a Classification Tree	
5. Michał ŚMIEJA, Sławomir WIERZBICKI, Magdalena KURIATA, Tomasz CIEPLIŃSKI, Łukasz SZUMILAS	2019205
Visualization of Vibrations in Structural Diagnoses of Technical Objects	
6. Grzegorz M. SZYMAŃSKI, Maciej TABASZEWSKI	2019206
Identification of Technical Condition of Valve Clearance Compensators Using Vibration Measurement and Machine Learning	
7. Andrzej PUCHALSKI, Iwona KOMORSKA	2019207
Application of the Wavelet Multifractal Analysis of Vibration Signal for Rotating Machinery Diagnosis	
8. Zbyszko KLOCKIEWICZ, Grzegorz ŚLASKI, Mikołaj SPADŁO	2019208
Simulation Study of the Method of Random Kinematic Road Excitation's Reconstruction Based on Suspension Dynamic Responses with Signal Disruptions	
9. Bogdan ŻÓLTOWSKI	2019209
Elements of the Statistical System for Vibration Tests of Machine	
10. Sebastian GARUS, Wojciech SOCHACKI	2019210
Designing of Quasi One-Dimensional Acoustic Filters Using Genetic Algorithm	
11. Sebastian UZNY, Łukasz KUTROWSKI, Tomasz SKRZYPCZAK	2019211
Free Vibrations of the Column Taking Into Account Compressive and Thermal Load	
12. Wiesław Jerzy STASZEWSKI	2019212
Fatigue Crack Detection Using Diffused Lamb Wave Field – Damage Index vs. Crack Length Estimation	

- 13. Paweł LÓJ, Wojciech CHOLEWA2019213**
Diagnostics of Rotary Vane Vacuum Pumps Using Signal Analysis
and Processing Methods
- 14. Zbyszko KLOCKIEWICZ, Grzegorz ŚLASKI.....2019214**
The Method of Estimating Kinematic Road Excitation with Use of Real
Suspension Responses and Model
- 15. Dorota GÓRNICKA, Grzegorz KLEKOT, Michał MICHALIK.....2019215**
Acoustic Signal as a Carrier of Information on Breathing Sleep Disorders
- 16. Dorota GÓRNICKA, Katarzyna SZWEDZKA2019216**
Vibration Signal as a Support for the Processes Production Management
in Enterprises of the Furniture Industry
- 17. Sebastian UZNY, Michał OSADNIK2019217**
Nonlinear Vibrations of the Partially Tensioned System Taking into Account
the Asymmetry of the Stiffness of Supports
- 18. Jan WARCZEK2019218**
The Opinion of Impact of Energy Dissipation in a Vehicle Suspension
on Mechanical Energy Transfer
- 19. Jacek DZIURDŹ2019219**
The Use of Computer Simulations in the Analysis of Physical Phenomena
Models
- 20. Mateusz KOZIOL2019220**
Modelling of a Rotor with Gyroscopic Coupling in a Rotating Reference
Frame Using Ansys and Matlab
- 21. Michał MAKOWSKI, Wiesław GRZESIKIEWICZ2019221**
Numerical Investigation of the Influence of Aerodynamic Forces and Wheel
Dynamic Loads of a Vehicle Subjected to Kinematic Excitations
- 22. Marek IWANIEC, Jerzy STOJEK.....2019222**
Application of Machine Learning to Classify Wear Level of Multi-Piston
Displacement Pump
- 23. Bartosz JAKUBEK, Roman BARCZEWSKI,
Maciej TABASZEWSKI2019223**
Localization of Noise Sources in Electric Cookers Based on Sound Pressure
and Intensity Measurements
- 24. Krzysztof LALIK, Szymon PODLASEK, Wojciech GORYL,
Grzegorz GÓRA.....2019224**
The Steam Pressure Impacts Reducing System for a Biomass Cogenerator
Based on Monitoring of the Frequency Characteristics of the Steam Actuator

Effective Diagnostic of Local Noise Sources with Acoustic Imaging

Stefan WEYNA

*West Pomeranian University of Technology,
Marine Technology and Transport Dep., Szczecin, Poland*

Abstract

In this article, the author described methods of visualizing the acoustic flow and showed how these methods can help scientists understand the complex flow of acoustic energy in a real field. A graphical method for determining the distribution of acoustic waves in a real 3D flow field will be presented. Vector imaging of acoustic events is not possible with the use of traditional metrology applied in pressure acoustics. Based on research using measurements of sound intensity and distribution of vector acoustic field by acoustic orthogonal decomposition method (SI-AOD), the article will present examples of practical applications of these analyses. The described measurement technique, including the method of graphical presentation of results, enriches the knowledge about the mechanism of the flow of acoustic energy stream in real working conditions of the source. The SI-AOD analysis system sets a milestone in the monitoring of sound landscapes and the precise finds noise sources.

Keywords: sound intensity, acoustic imaging, vibroacoustic, noise abatement

1. Introduction

The aim of this work is to present results of experimental investigation a vector fields, shaped in natural conditions by industrial sources of noise; mechanisms and vibrating structures, pipes and HVAC installations systems, transport vehicles, etc. Acoustic intensity measurement technique has been used for the visualization of the energetic sound flow field. When the acoustic field is described by sound intensity, we may understand the mechanisms of propagation, diffraction and scattering of acoustic waves, as energy form of flow wave. Energy distribution images in acoustic fields, connected with the graphical presentation of the flow wave (derived from direct measurements) are a new element in acoustic metrology.

The result of investigation shows the three-dimensional distribution of vector acoustic fields created as an acoustic *intensity streamlines*, propagating *wave shapes* and 3D *intensity isosurface*, all enable a full interpretation of vector phenomena in generated flow field. The visualization of real-live sound fields is useful for understanding the directional radiation of noise sources into three-dimensional space. For that, the vector distribution field will be done of phenomena unknown to us so far. Using own post-processing software (*SIWin*) which are developed for analyses and acoustic image investigated, including method of animation the flow wave (*AnimView*).

Application of the sound intensity method, including the presentation of space vector distribution of acoustic power of noise, may bring new insight into the nature of acoustic field formation in real conditions of working sources. Acoustic conditions in these areas are much different from the theoretical assumptions ascribed to free or diffuse field. It is

a frequent occurrence that the sound intensity measurements in real conditions may show great disparity between the theoretical assumptions of the acoustic fields and the actual measurements [1]. The disparity results mainly from simplifications accompanying the analytical methods due to lack of complete data concerning physical properties of an investigated object.

The approach taken here is to use direct measurement sound intensity describing the flow field around two or three-dimensional solid obstacles and illustrate the flow around them as an intensity streamline. The study was conducted to analyze and to improve the comprehension of the mechanism of energy transfer between a turbulent flow and acoustic fields. Aerodynamic results are needed to formulate equivalent source terms while the acoustic results are needed when a coupling procedure based on acoustic boundary conditions is used. It can be expected that through the development of the proper connectivity boundary conditions between the different zones a feedback of acoustic waves from the source region to the propagation region can be incorporated.

2. Visualization of acoustic flow waves

This work presents results of investigation the real-live sound or noise field as a form of acoustic energy radiated by vibrating structures and a noise generated around obstacles as a vortex effect in disturbed acoustic wave flow. In traditional acoustic metrology, the analysis of acoustic fields concerns only the distribution of pressure levels but in a real acoustic field acoustic flow energy pressure and acoustic particle velocity (vector value) effects are closely related. Only when the acoustic field is described by sound intensity, we may truly understand the mechanisms of propagation, diffraction and scattering of acoustic waves, as an energy form of flow wave. We can now see what flow wave was hitherto invisible. Energy distribution images in acoustic fields, connected with the graphical presentation of the flow wave (derived from direct measurements) are a new element in noise diagnostic in industrial and living areas. Introduction of these possibilities have greatly changed the approach to examining many unknown acoustic phenomena [2, 5]. This sort of visualization of sound fields is also very useful for understanding of the sound formation mechanism and the transport of acoustic energy in real terms.

The visualization methods to the graphic description of the effects of fluid flow have been developed over the past several years and are widely described in literature [1]. Many of the techniques used in computer graphics flow visualization have been adapted from the traditional methods practiced in wind and water tunnels. Scientific visualization is the use of computer graphics to create visual images, which aid the understanding of this often-immense data set. Visualization system, by serving a dual role as a provider of exploration and exposition capabilities, have become indispensable to the analysis of *Computational Fluid Dynamics* (CFD) modelling results. Generally, a fluid is a rather complex three-dimensional time-dependent phenomenon, however, in many situations, it is possible to make simplifications that allow a much easier understanding of the problem without sacrificing needed accuracy. One of these simplifications involves approximating a real flow as a simple one- or two-dimensional flow, but in many situations the three-dimensional flow characteristics are particularly very important

terms of the physical effects they produce [3]. For these situations it is necessary to analyse the flow in its complete three-dimensional character using the velocity components of the flow (acoustic particle velocity components as value of v_x , v_y , v_z to the sound flow, for example).

Acoustic flow imaging is not often enough used in the analysis of noise sources, although, the acoustic energy stream represented by the sound intensity - the vector parameter of the acoustic wave - can directly and relatively easily be measured today using a suitable measuring transducer; the intensity probe. Measured experimentally acoustic wave flow parameters can be used to collect the sound intensity vectors data to visualisation all the wave phenomena occurring in real physical space [2].

The visualization of the distribution of the active and reactive parts of the acoustic field gives the possibility of a full analysis of an acoustic wave. A properly used sound intensity method ensures a chance of measurement of the vector distribution in any place and time of the restricted space, even within a near field.

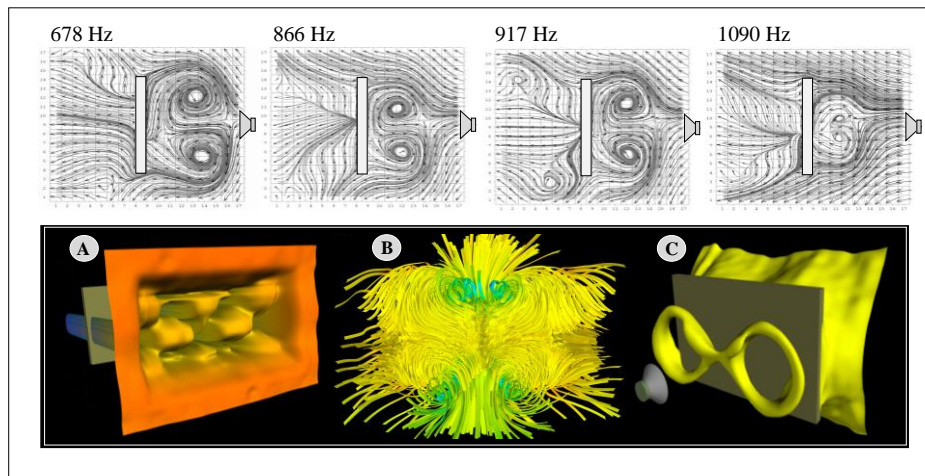


Figure 1. Sound intensity wave distribution around hard rectangular plate (for some selected frequencies): 2D intensity map with vectors (arrows) and SI, 3D shape of wave (A) and SI streamlines in the rear side of plate (B), SI isosurface in the front and rear side (C)

The applied research technique using sound intensity measurements is the vector distribution analysis of acoustic fields generated by sources in the real-live conditions and the creation of spatial visualization of the acoustic wave response to the obstacles in the way of its propagation. Experiments are carried out laboratory research and in industrial conditions using a new method for analysis of the acoustics wave flow as the acoustic energy or noise flux in the real sound field. To the study of the wave acoustics flow, own post-processing program called *SIwin* is used. The distribution acoustic field is presented graphically on the 2D plane or in 3D space as a sound intensity maps, acoustic energy flux lines, shapes of the travelling acoustic wave or as

a spatial distribution of intensity iso-surfaces (Fig.1). Based on the measurement data, we also can create animations of the actual forms and wave motions using *AnimWiew* programme [2].

The presented method visualizes the results of acoustics flow and interprets the shapes of the travelling wave, the effects of vortex rotation and the collapse of the wave on obstacles. Even for acousticians, it is so far unknown form of experimental investigations of vector visualization of the flow of events in the acoustic wave like hydrodynamic flows in fluid mechanics. The new testing methods in the acoustic research improve and develop modern diagnostic techniques used to the machinery and mechanical appliances conducted with acoustic methods. They become a very useful tool in optimizing the choice of technical methods for the noise abatements on the workplace.

3. Acoustical imaging and orthogonal decomposition of flow field

The possibility of direct measurement of sound intensity appeared only in the 80s of the last century, when Frank Fahy (1977 [4]) presented intensity probe as a practical measurement tool meets the applicable principles of metrology. Vector analyses give the opportunity to visualize real acoustic wave flows and “watch” the structural effects caused by the wave reaction on obstacles. They are a suitable material for the validation of theoretical analytical and numerical methods built for the study of acoustic sources and acoustic wave-flows. Today we can to *see the flow of an acoustic wave* in the air, similarly to aerodynamic or hydrodynamic flows. Thanks to sound intensity measurement technique and a vector studies on wave motion effects, we may now visualize dynamic phenomena in an acoustic field, just as in other areas of physics and experimental techniques. We can perceive the flow of acoustic stream energy or the shape of an acoustic wave as a disturbance effects on obstacles placed in a field.

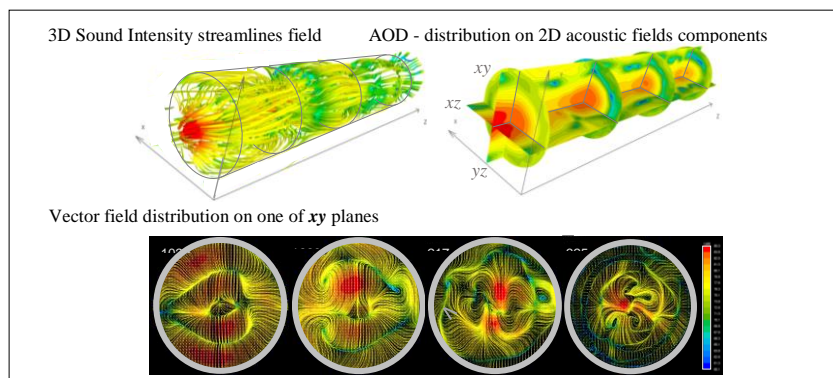


Figure 2. SI-AOD - distribution of vectors acoustic flow field inside circular duct as a function of space, frequency and amplitude

A useful form of analysis for visualization of disturbed acoustic fields is the use of three-dimensional decomposition of vector values represented by the sound intensity. This is a very handy form of analysis. In our research we use a novel tool called orthogonal acoustic decomposition AOD. Spatial SI vectors are divided into three orthogonal component planes in the Cartesian system: xy , xz and yz . After decomposition of the field into 2D images, it turns out that orthogonal components of chaotic wave motion depict deterministic features of chaos. By combining the commonly used frequency decomposition of acoustic field in the range of standard octave frequencies (13, 1/12 octave band) with the SI-AOD decomposition methods, we obtain images containing regular deterministic forms of chaotic wave motion (images of vortices, sources and sinks, rotations, saddles, bifurcating lines - see Fig. 2). It turns out that the SI-AOD method used in experimental studies brings to acoustic analyses the previously unknown possibilities of describing wave motion *in-situ*.

4. Technical acoustic decontamination of noise sources

Acoustic energy distribution images in real-live fields, connected with the graphical presentation of the dynamic flow waves as a vector effect are a rather new element in acoustic metrology. Introduction of these useful possibilities have greatly changed the approach to examining many acoustic phenomena and allows you to effectively use acoustic visualizations to diagnose local noise sources. The sound intensity measurement technique has been used in various studies on theoretical and applied acoustics, greatly simplifying the methods of research. This is because it does not require criteria as strict as in traditional measurements, and the precision of direct measurements in real-life situations does not vary from laboratory experiments. The measurements can be carried out in a near field and in the fields with presence of parasite noise, which is a significant advantage in research. In the paper, experimental studies carried out on real models and structures are documented with graphical records of acoustic fields created by surface sources (radiation of vibrating structures) and the effects of wave interference on obstacles and barriers placed in the flow field.

Direct measurements of sound intensity representing the flow of energy in sound fields has revolutionized acoustical diagnostic methodology. It is now possible to measure the sound power output of individual noise sources of all forms and sizes in their operational environments. In-situ measurements can be achieved even when sources operate in the presence of other comparable physical powers, a process impossible with conventional acoustic measurement instrumentation. Investigations carried out with sound intensity techniques may be compared against those made by classical methods. This enables us to obtain significantly new information related to energetic acoustic fields in near and far fields, which in turn facilitates the diagnostics of noise sources.

5. Examples of applications for SI-AOD testing of noise sources

Having the technical possibilities of measuring a sound intensity vector in three-dimensional space, it was necessary to work out a proper form for the graphical presentation of the acoustic vector field distribution. The problem involved a way of

demonstrating, on a two-dimensional or three-dimensional form of a vector field. In opposite to the classically described acoustical fields with acoustical pressure distributions, the graphical presentation of the acoustic energy flow in real-life acoustic fields as a vectors mapping, can explain many particulars concerning the areas in which it is difficult to make theoretical analysis (direct and near field, vortex flow, effects of scattering on obstacles, reflection on partitions, efficiency of acoustics barrier, etc.).

The paper presents three cases of SI-AOD applications, the results of which are presented in a very brief form. These are only signal possibilities of graphical presentation of research results. More information can be found in other publications from our team.

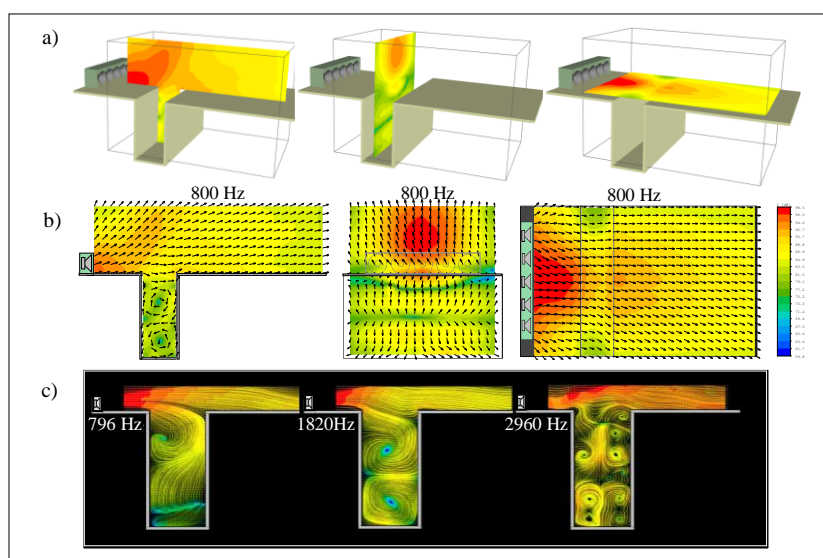


Figure 3. SI flow field for the loudspeaker line array system radiated over a flat plate with rectangular deep cavity: a) - intensity orthogonal maps; yz , xy , xz plane, b) – vectors distributions, c) – characteristic Rossiter modes in the cavity influence on the main flow

5.1. The influence of a niche on the changes in the flow of acoustic wave

As the first example of investigation, on the Figure 2 a graphic presentation of spatial distribution the acoustic power flow is show. The analysis of the field includes the vector distributions and the map of the sound intensity flux. It is a certain form of qualitative analysis for stationary fields which consists in a complex evaluation of paths along which the acoustic energy flow. The results of research represent a two-dimensional flow map of time-averaged active intensity space SI vector as a projection on the orthogonal plane and intensity field in the plane is show. The tests concern the vector distribution of the field in an axis of symmetry of the broad-band 5 loudspeakers (*line source*) installed in four discriminate environment conditions. Measurements are curry

out in third-octave bands and vectors map have been built in the frequency range between 25 Hz and 6300 Hz. On this figure some example maps of one-third octave band result is show. This kind of visualization may involve depicting various acoustic phenomena, depending on the area of interest. The verifying tests using the SI-AOD technique have shown how much cavity influence on the shape of the flow field. Please put your attention on the vortex *feedback reactions* in the niche for some frequency (*Rossiter mode*).

5.2. Noise radiation to the inside of the ship's cabin

Reducing noise in ship rooms to the level required by standards is not an easy structural and technological task. Noise in the cabin is a complex process of interaction of structure-borne and airborne noise [5] and in case of exceeding the permissible level the process of its reduction is often very expensive. In the case of technical noise reduction on the finished vessel, it is therefore necessary to clearly indicate the local element of cabin equipment, from which changes the optimisation works should be started. From the research presented fragmentarily in Figure 4 this is clear that the wall with windows is this element, so the correction works should be started from changing the window construction for liquidation of local sources of noise radiation. Only SI-AOD can effectively diagnose noise from so small local sources.

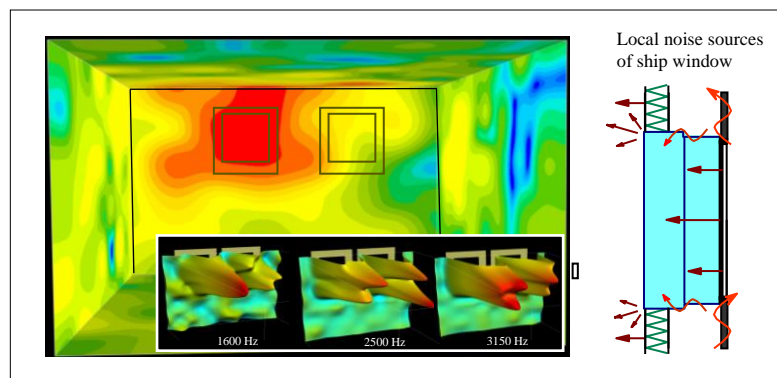


Figure 4. Searching for local noise sources in the ship's cabin using the acoustic imaging

5.3. Noise optimisation of the electric motor prototype

The acoustic visualization of the noise generated by an electric motor is another example of effective applications of the SI-AOD research results. The motor prototype was to be subjected to acoustic optimization. It was to be particularly quiet. Figure 5 shows - very fragmentarily - the results, which clearly indicate the mechanism of noise radiation and the local structural elements of the engine, which are its sources.

On this small fragment of the research results one can also appreciate the advantages of the SI-AOD technique.

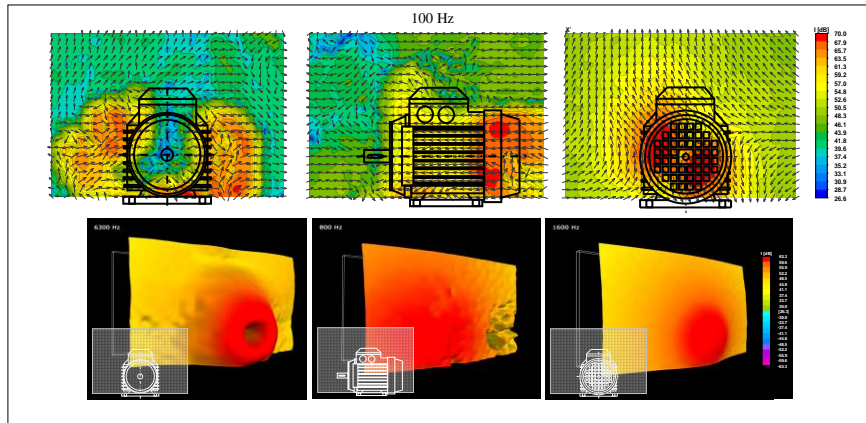


Figure 5. Diagnosis of local sources of noise generated (for $f = 100$ Hz) by elements of an operating electric motor

6. Conclusions

Main advantages of the research carried out with the application of a SI-APOD technique consist in the fact that the noise measurements taken refer to energy dependencies of the field. As it has been pointed out, this technique is much more effectively than classical methods e.g. to verify the theoretical methods of field modelling with check-up measurements taken in real conditions.

The tests of the acoustic energy flow and presentation of the results in a graphic form shows, that the wave distributions in real acoustic fields can explain many, concerning in the areas for which it is difficult to make theoretical analysis (direct and near field, effects of scattering, shielding area, etc.). Described investigation can enrich the knowledge of the scattering effects and influence of environment conditions on formation of noise sources. Direct energy analysis of acoustic fields was not possible earlier because the classical pressure acoustic used a scalar element of acoustic waves. Only when direct measurements of sound intensity became possible, could the wave distribution be analysed in the form of wave acoustic energy transport.

References

1. E. G. Williams, *Fourier Acoustics - Sound radiation and nearfield holography*, Academic Press, San Diego, London, New York 1999.
2. S. Weyna, *Acoustic intensity imaging methods for in-situ wave propagation*, Archives of Acoustics, **35**(2) (2010) 265 – 273.
3. S. Weyna, *Experimental study of sound propagation in open duct with variable geometry*, 16-th Int. Congress on Sound and Vibration, ICSV16 S-18, Kraków 2009.
4. F. Fahy, *Sound Intensity*, Elsevier Applied Science, London 1989.
5. S. Weyna, *The use of Acoustics Vector Decomposition of Sound Fields to Vibroacoustic Protection on Ships*, Archives of Acoustics, **42**(2) 2017.

Dynamic Stability of Rotating Systems in Turbomachinery Under API Standards

Zbigniew KOZANECKI

*Lodz University of Technology, 90 - 924 Łódź, 219/223 Wólczańska Street,
zbigniew.kozanecki@p.lodz.pl*

Eliza TKACZ

*Lodz University of Technology, 90 - 924 Łódź, 219/223 Wólczańska Street,
eliza.tkacz@p.lodz.pl*

Jakub ŁAGODZIŃSKI

*Lodz University of Technology, 90 - 924 Łódź, 219/223 Wólczańska Street,
jakub.lagodzinski@p.lodz.pl*

Małgorzata GIZELSKA

*Lodz University of Technology, 90 - 924 Łódź, 219/223 Wólczańska Street,
malgorzata.gizelska@p.lodz.pl*

Abstract

The stability of rotating systems in turbomachinery has to account for the structure design, the actual geometry of bearings and all of the remaining forces, including operational data as well as temperature of the bearing lubricating oil. Thus, a study of the dynamic stability of rotating machines is complex and time consuming in terms of modelling and calculations. Even though it is recognized that other methods of analysis and acceptance criteria have been used to evaluate stability, API standardization procedures ensure appropriate notification and participation in the development process. According to these procedures, firstly we prepare a rotor technical documentation based on geometry measurements, frequently with optical scanning. Secondly, a theoretical analysis consisting of calculations with the finite element method based on the program that allows us to build a numerical model of rotor dynamics, is carried out. Then, the so-called “bump test” is performed to measure natural frequencies of a freely suspended rotor, which makes it possible to “tune” the theoretical model, making it compatible with the real object not only in terms of geometric dimensions and mass, but also from the point of view of the form and frequency of free vibrations. Thus, we obtain an experimentally verified numerical model which can be used for future machine diagnostics and other needs.

Keywords: turbomachinery, rotating system stability, model tuning, API standards

1. Introduction

In all types of rotating machines, a rotating force is periodically applied to the rotor of the machine during its operation. Its presence follows from the way the machine works and the unbalance. A periodically variable force acting on the rotor results usually in a periodic shaft movement in different directions, i.e., vibrations. Under certain conditions, phenomena such as resonance or instability of vibrations can lead to much larger displacements of the shaft and acting forces than during the normal operation. Excessive forces can lead to faster fatigue wear of some parts. Too large displacements

can cause rotating parts to come into contact with fixed parts, which, consequently, can be followed by damage of the machine. Other effects of excessive vibrations may yield a reduced operational precision, e.g., in machine tools and medical devices, or an increased clearance in seals and a deterioration of the efficiency in turbomachines (turbines, pumps or compressors and fans).

Therefore, it is necessary to design machines in a way that guarantees operation at a sufficiently low level of vibrations. A meticulous and reliable theoretical dynamic analysis of the structure is required for newly built or modernized machines to confirm their compliance with the requirements of standards. In relation to industrial turbomachines, these are usually API 617, API 612 and API 610 standards describing in detail the methodology and methods for such an analysis as well as specifying the requirements the designed structure has to meet in terms of dynamics during its operation.

The present article describes an example of a theoretical model and its tuning for large industrial compressors and shows the usefulness of this procedure and its impact on the reliability of the dynamic analysis results. The ultimate purpose was to develop a numerical model of the free-hanging rotor of the compressor and tune it on the basis of the experiment to allow the users to conduct stability calculations according to their needs.

In modern calculations of machine dynamics, the finite element method (FEM) is most commonly used. It requires a theoretical model of the structure to be developed by dividing it into a number of elements (finite elements) in order to generate a computational grid. Then, the equations of displacement and motion are determined in every possible direction (depending on the number of degrees of freedom), for each of mesh nodes, depending on node forces. The acting forces and the number of degrees of freedom are known due to the given boundary conditions and the relationships existing between individual nodes.

According to API 617, it is necessary to perform vibration analysis of the compressor rotating system, which should include, among others, values of all critical speeds, from 0 to as high as 2.2 times the maximal rotational speed during continuous operation, determined at the rotational speeds from 25% to 125% of this speed. If the bearing foundation is not rigid enough and it is necessary to model it, the machine body can be modelled as a beam system placed on the foundation with certain stiffness and damping. The described stages of works are connected to preparation and tuning of the rotor model and to selected stability issues of the machine dynamical analysis.

2. Stability analysis of the machine rotating system

The majority of failures of overcritical rotors are caused by a local increase in the synchronous or asynchronous vibration amplitude and by exceeding the clearances when the critical frequency or the stability threshold of the rotating system is exceeded. It is evident that dynamic characteristics of the machine rotating system depends on rotor-support dynamic properties. It means that the external forces generated during machine operation can alter the dynamic properties of the whole rotating system. However, this

effect depends strongly on flexibility of the shaft and dynamic properties of the rotating system components (bearings, seals and centrifugal or axial flow stages).

Let us consider a generalized two-degree-of-freedom linear rotor system presented in Fig. 1.

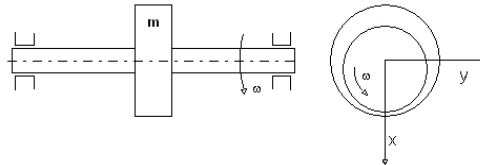


Figure 1. Two-degree-of-freedom linear rotor system

A simplified equation of the lateral movement of the rotating shaft mass m at a constant speed Ω can be written in the following way:

$$\begin{bmatrix} m & 0 \\ 0 & m \end{bmatrix} \begin{Bmatrix} \ddot{x} \\ \ddot{y} \end{Bmatrix} + \begin{bmatrix} c_{xx} & c_{xy} \\ c_{yx} & c_{yy} \end{bmatrix} \begin{Bmatrix} \dot{x} \\ \dot{y} \end{Bmatrix} + \begin{bmatrix} k_{xx} & k_{xy} \\ k_{yx} & k_{yy} \end{bmatrix} \begin{Bmatrix} x \\ y \end{Bmatrix} = \begin{Bmatrix} m e \Omega^2 \cos(\Omega t) \\ m e \Omega^2 \sin(\Omega t) \end{Bmatrix} \quad (1)$$

The generalized damping and stiffness matrix of equation (1) contains all forces acting on the flexible shaft, i.e., bending stiffness, internal and external damping, bearing stiffness and damping, fluid cross-coupling forces, auxiliary active support damping and stiffness, as well as other forces acting on the mass m . The generalized stiffness $[k_{ij}]$ and damping $[c_{ij}]$ matrices can be decomposed as follows:

$$\begin{bmatrix} k_{xx} & k_{xy} \\ k_{yx} & k_{yy} \end{bmatrix} = K_{el} + K_{rot} \quad \begin{bmatrix} c_{xx} & c_{xy} \\ c_{yx} & c_{yy} \end{bmatrix} = C_{diss} + C_{gir} \quad (2)$$

where:

$$K_{el} = \begin{bmatrix} k_{xx} & \frac{1}{2}(k_{xy} + k_{yx}) \\ \frac{1}{2}(k_{xy} + k_{yx}) & k_{yy} \end{bmatrix} \quad K_{rot} = \begin{bmatrix} 0 & \frac{1}{2}(k_{xy} - k_{yx}) \\ -\frac{1}{2}(k_{xy} - k_{yx}) & 0 \end{bmatrix} \quad (3)$$

$$C_{diss} = \begin{bmatrix} c_{xx} & \frac{1}{2}(c_{xy} + c_{yx}) \\ \frac{1}{2}(c_{xy} + c_{yx}) & c_{yy} \end{bmatrix} \quad C_{gir} = \begin{bmatrix} 0 & \frac{1}{2}(c_{xy} - c_{yx}) \\ -\frac{1}{2}(c_{xy} - c_{yx}) & 0 \end{bmatrix} \quad (4)$$

From the point of view of the rotating shaft vibration control, this decomposition into conservative (K_{el} and C_{gir}) and non-conservative (C_{diss} and K_{rot}) parts allows us to analyze an influence of the additional cross-coupled forces furnished by the bearing/seals system as well as an effect of the flow stages on the shaft energy level in each cycle of motion. The total work of conservative forces per one cycle of motion is still equal to zero but the total work of non-conservative forces can disturb the energy balance of the rotating system even under steady-state conditions. These energy considerations show the following requirements for an external additional active support

of the flexible rotating shaft in order to improve the reliability of the machine rotating system without risk of its destabilization:

1. During one cycle, the work generated by non-conservative damping forces expressed by the matrix C_{diss} has always a negative value and decreases the energy balance of the rotating system regardless of the precession direction. Therefore, an influence of external support damping forces is absolutely beneficial and always stabilizes the rotating system, lowering the energy of the total precession.
2. During one cycle, the sign of the work performed by non-conservative forces of coupled stiffness depends on the direction of the total precession. This indicates that the sign of the term $(k_{xy}-k_{yx})$ becomes decisive for stabilization of the forward and backward modes of the shaft elliptical movement. For $(k_{xy}-k_{yx}) > 0$, energy increases for the forward precession and decreases for the backward precession and, consequently, for $(k_{xy}-k_{yx}) < 0$, energy decreases for the forward precession and increases for the backward one.

From the point of view of the stability margin of the flexible rotating shaft, let us consider an influence of the residual unbalance on the energy balance in the elliptical motion. The above-mentioned considerations related to the energy balance in the elliptical motion of the flexible shaft allow us to formulate general recommendations for the forces of the rotating shaft that should act without a risk of destabilization of the machine rotating system. These recommendations are as follows:

- possibly high values of external damping forces that absolutely stabilize the rotating system,
- in the case of permissible alternations in the dynamic characteristics of the system from the viewpoint of its operation conditions, the forces that increase direct stiffness (k_{xx} , k_{yy}) are acceptable,
- the forces that are related to the forces altering the cross-coupled stiffness terms (k_{xy} , k_{yx}) should be seriously analyzed and avoided as far as possible.

The latest editions of the API standards draw special attention to a theoretical stability analysis taking into consideration anticipated cross-coupling terms of the rotating system. A simple and very useful technical indicator of the machine rotating system stability estimations used in the API standards methodology is a logarithmic decrement of damped natural frequencies of the whole rotating system. A negative logarithmic decrement or a damping factor indicates system instability. A stability analysis shall be performed for those machines, where the maximal speed is greater than the first undamped critical speed on rigid supports, especially when all interactions that are related to the forces altering the cross-coupled stiffness terms (k_{xy} , k_{yx}) are considered. These forces are connected to dynamic properties of the rotating system support components (bearings, seals) as well as to interactions related to the flow in machine centrifugal or axial stages.

3. Model of the rotor dynamics

The dynamic model built to determine, among others, the eigenfrequencies of the considered object have to be composed of an appropriate number of elements with specific material properties. These can be elements of the shaft-type, which affect the

inertia and rigidity of the model, or of the disc-type, which influence the rigidity of the model only. Disc-type elements represent components of the shaft (half-couplings, rotors, balance disks, bushes, etc.). In specific sections (corresponding to the centres of gravity of these elements), their mass and moments of inertia (necessary to take into account the gyroscopic effect) are introduced. An influence of bearings and seals is taken into account by determining the centre position of this type of elements and specifying the matrix of the values of stiffness and damping coefficients as boundary conditions.

In fact, shield-type components also add extra rigidity to the shaft, especially if they fit tightly in the shaft. In this case, their absence in the model may lead to an underestimation or overestimation of the rigidity. In engineering practice, an impact of this additional stiffness is difficult to determine and, therefore, usually not considered at the design stage. However, if the experimental results differ from the model predictions by more than 5%, the model tuning is required in accordance with the standard.

Figure 2 shows a scheme of the rotor structure with its corresponding dynamic model developed on the basis of optical scan measurements. The calculated parameters of the rotor are given in Table 1.

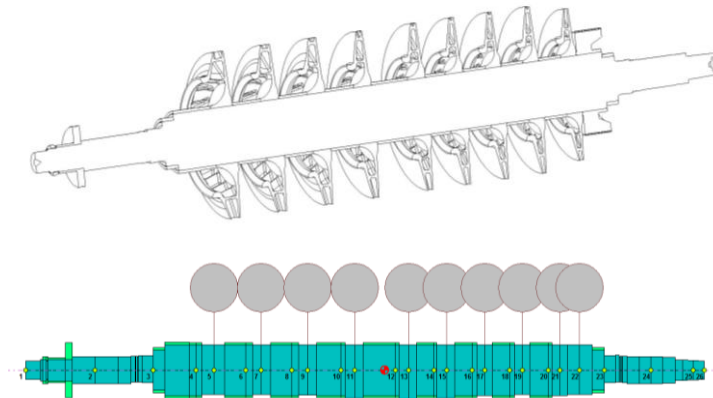


Figure 2. Scheme and visualization of the numerical model of the rotor structure

Table 1. Calculated parameters of the rotor

total length [mm]	total mass [kg]	position of the centre of mass (from suction side) [mm]	moment of inertia (diametral) [kg m ²]	moment of inertia (polar), [kg m ²]
2570	831.8	1362	249.9	14.658

Rotor wheels and a relieving piston were modelled on the basis of the developed technical documentation and in the dynamic model they were symbolically represented as disks with a concentrated mass in nodes (stations) of the rotor numerical model. Physical parameters of these elements were calculated and listed in Table 2.

Table 2. Physical parameters of model elements

element	node	element mass [kg]	moment of inertia (diametral) [kg m ²]	moment of inertia (polar) [kg m ²]
disc 1	5	40.660	0.80078	1.5309
disc 2	7	37.750	0.74076	1.4356
disc 3	9	39.460	0.75184	1.4597
disc 4	11	36.700	0.67967	1.3302
disc 5	13	34.760	0.65008	1.2752
disc 6	15	34.290	0.63731	1.2527
disc 7	17	33.050	0.60466	1.1892
disc 8	19	35.680	0.66280	1.3057
disc 9	21	28.280	0.44547	0.87582
piston	22	40.000	0.44938	0.83794

4. Bump test and model adjustment

In order to verify and adjust the model, a bump test needs to be carried out to identify eigenfrequencies of the analysed rotor. Figure 3 shows the free-hanging compressor rotor used to record the spectrum of frequencies. The aim of the bump test is to verify and tune the numerical model developed. Below, we can see how vibration sensors were positioned. In addition, optical markers, which were used for measurements of the rotor geometry with a scanner – a 3D measuring system operating on the principle of streak projection, ensuring a high precision and a detailed resolution at high speeds, are visible.



Figure 3. Free-hanging rotor of the compressor during natural vibration measurements for numerical model tuning

Figure 4 shows test results. During the tuning of the theoretical model, the first three eigenfrequencies of the object under analysis, pointed with arrows, were taken into

account. Table 3 summarizes their values and shapes of free vibrations from the rotor measurements along with those calculated theoretically after model tuning.

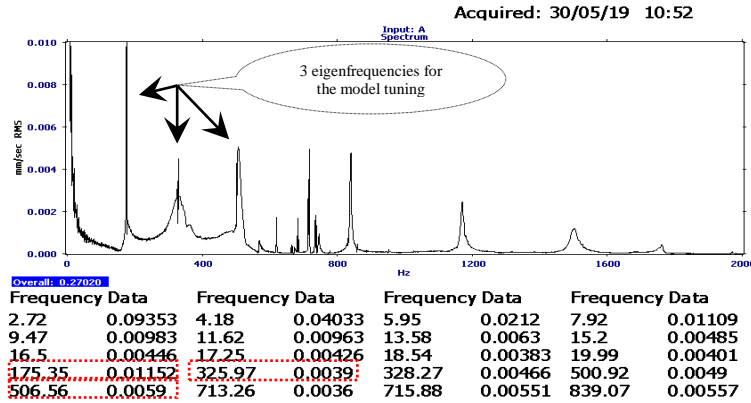


Figure 4. Example of the recorded vibration spectrum of the excited free-hanging rotor with the 3 first eigenfrequencies pointed

Table 3. Eigenmodes and eigenfrequencies from the calculations and from the measurements

Rotor eigenmode shape and frequency from the calculations and the measurements			
1 st eigenmode	175.18 Hz	175.13 Hz	Spin/Whirl Ratio = 1, Stiffness: (Kxx+Kyy)/2 Critical Speed = 10511 rpm = 175.18 Hz
2 nd eigenmode	325.12 Hz	325.97 Hz	Spin/Whirl Ratio = 1, Stiffness: (Kxx+Kyy)/2 Critical Speed = 19507 rpm = 325.12 Hz
3 rd eigenmode	508.85 Hz	506.56 Hz	Spin/Whirl Ratio = 1, Stiffness: (Kxx+Kyy)/2 Critical Speed = 30531 rpm = 508.85 Hz
Rotor mass	831 kg	830 ± 2 kg	

As follows from these results, the model after tuning shows a very good conformity with the real rotor dynamic behaviour and, thus, it can be used in further investigations for designing or diagnostic purposes.

5. Conclusions

API standards related to technical conditions of turbomachines, increasingly used in industry, require a reliable theoretical analysis of the dynamic state of the machine rotating system. The latest editions of these standards draw special interest to ensuring a high stability margin and an elimination of sources of self-excited vibrations in the rotating system of modern (modernized) machines.

Currently available calculation methods allow for reliable modelling and a theoretical dynamic analysis of turbomachinery, both for designing or modernization purposes. However, such an analysis should be conducted on the basis of detailed data as regards the machine design and operating requirements. An experimentally verified (tuned) model of the real rotor shaft allows us to determine an impact of structural changes on machine dynamics as well as to simulate some symptoms of incorrect operation long after the model was built.

References

1. D. W. Childs, *Dynamic Analysis of Turbulent Annular Seals Based on Hirs Lubrication Equation*, J. of Lubr. Techn., **105** (1983) 429 – 436.
2. W. J. Chen, E. J. Gunter, *Introduction to Dynamics of Rotor-Bearing Systems*, Trafford Publishing, Eigen Technologies Inc., 2005.
3. D. Kozanecka, *Dynamics of the Flexible Rotor with an Additional Active Magnetic Bearing*, Machine Dyn. Probl., **25**(2) (2001) 21 – 38.
4. Z. Kozanecki, *Rotating Systems of the Low and Medium Power Turbomachinery* (in Polish), ITE Publishing House, 2008, ISBN 978-83-7204-693-2.
5. Z. Kozanecki et al., *Application of Active Magnetic Bearings for Identification of the Force Generated in the Labyrinth Seal*, Journal of Theoretical and Applied Mech., **45**(1) (2007) 53 – 60K.
6. API Standard 617, *Axial and Centrifugal Compressors and Expander-compressors* – eighth edition, September 2014, errata 1, August 2016.
7. API Standard 684, *Tutorial on the API Standard Paragraphs Covering Rotor Dynamics and Balancing: An Introduction to Lateral Critical and Train Torsional Analysis and Rotor Balancing*.

Experimental Investigation of Rotor Vibration by Using Full Spectra from Shaft Mounted Piezoelectric Patches

Mateusz KOZIOŁ

*AGH University of Science and Technology, Faculty of Mechanical Engineering
and Robotics, al. Mickiewicza 30, 30-059 Kraków, makoziol@agh.edu.pl*

Piotr CUPIAŁ

*AGH University of Science and Technology, Faculty of Mechanical Engineering
and Robotics, al. Mickiewicza 30, 30-059 Kraków, pcupial@agh.edu.pl*

Abstract

The work considers the applicability of signals coming from rotor-mounted sensors in machine diagnostics. In the experiments, such sensors were implemented by piezoelectric patches bonded to the surface of a shaft. The laboratory stand also included more common sensors: laser sensors that measured the displacement of the central disc, as well as accelerometers mounted on the supports. The signals measured are analysed using the so-called full FFT method and the spectra are compared. The results show that the signals from piezoelectric sensors can be processed so that their spectral content is similar to typical spectra obtained using stator-mounted sensors.

Keywords: rotor dynamics, piezoelectric patches, frequency spectrum, signal processing, diagnostics

1. Introduction

Many types of rotating machinery are required to work continuously for a long time. Since the functioning of these devices is very often crucial for society, condition monitoring becomes important, even if it results in additional costs. As one of the symptoms, a vibrational signal carries information about the health condition of a machine. However, proper diagnostics depends on many factors, among others on the type of sensors and their placement, appropriate signal processing techniques, as well as expert knowledge.

The condition monitoring systems of rotating machinery currently used incorporate mainly displacement and acceleration sensors that measure the vibrations of the shaft and bearing supports [1, 2]. There have been many studies that search for vibrational indicators of most common rotor problems, such as misalignment [3, 4], cracks [5], rubs [6], etc. In general, in these studies the stator-mounted sensors are utilized, mainly because mounting such sensors on non-rotating parts is easy and reliable. The signals obtained from such sensors will be considered as referenced to an inertial or stationary reference frame (SRF). Studies where the sensors are mounted directly on the shaft are less common, as an example, papers [7, 8] can be mentioned. In this paper the signals obtained from rotor-mounted sensors will be used and throughout the paper they will be referred to as referenced to a rotating reference frame (RRF). Generally, in such

configurations a slip ring assembly has to be used, which is an important element of such a solution.

With technological advances in MEMS, it becomes reasonable to use rotor-mounted sensors more widely. By applying the currently available communications technology and telemetry systems, wireless measurements can meet high requirements, and some rotor-related problems can be better observed using sensors fixed directly to the shaft. Therefore, such an approach is recently getting more attention from scientists. As an example, in reference [9] the authors use a MEMS-type accelerometer mounted on to the surface of a circular shaft. This work concentrates on the torsional vibrations arising from misalignment, so that only the tangential to shaft surface component of the acceleration is being analysed. The radial component is taken into account in reference [10], where a MEMS sensor is mounted as before, and additional stationary referenced accelerometers are used. The study includes the run-up conditions as well as the passage through the first critical speed. In publication [11] it is showed that axially mounted MEMS accelerometers can be used to measure the unbalance response. The authors also propose a method of estimating the rotational speed, which is based on a gravity component of accelerometer signals.

In general, rotor-mounted sensors generate signals referenced to a rotating frame, and in most cases these signals are qualitatively different from those measured in a stationary (inertial) frame. By analysing a standard spectrum plot for signals from RRF, it may be difficult to assess the full meaning and significance of different vibration spectrum components. The current work shows that the use of the so-called full FFT [1] (or complex FFT [12]) for signals from RRF can be beneficial. This approach requires two sensors, which measure the motion in two perpendicular directions. The paper will compare the use of full spectra for experimental signals referenced to stationary (SRF) and rotating reference frame (RRF), and the similarities and differences will be emphasized. The experimental tests were performed on a laboratory stand, equipped with piezoelectric patch sensors mounted on a rotating shaft, that is also used to test active control of flexible rotors.

2. Test facility

The experiment has been conducted on a laboratory stand presented in Fig. 1. The elastic rotor made of aluminium is horizontally mounted in two supports. The supports consist of lathe chucks and ball bearings. There is a steel disc in the middle of the length of the rotor. Eight piezoelectric patches (PZT26) are glued to the surface of the shaft near the rotor ends. The polarisation of all elements is away from the shaft surface. Two piezoelectric patches placed on the same surface are connected in parallel, so that all patches are connected into four pairs (marked by the same hatching in Fig. 1). The piezoelectric signals from the rotational reference frame are transferred by a classic slip ring assembly (not shown). To achieve higher gains and lower phase shifts for low frequency components of the PZT signals, two charge amplifiers have been used. The displacement of the disk is measured by two perpendicular laser triangular sensors. Additionally, acceleration in two perpendicular directions is measured on each support, and the encoder of the motor is used as the absolute phase marker (the so-called

key-phasor). The rotor speed is constant and it is equal to 540 rpm. All signals are sampled and acquired simultaneously, using one master clock, FPGA chip and the LabView software.

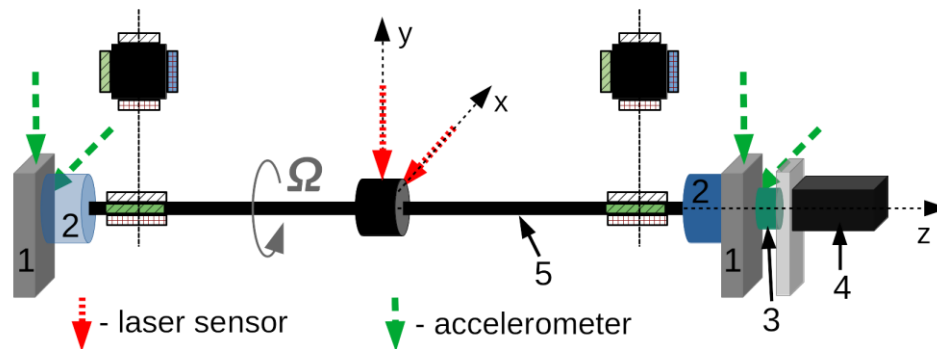


Figure 1. The scheme of the laboratory stand: 1 – support, 2 – lathe chuck, 3 – flexible coupling, 4 – motor with encoder, 5 – shaft with bonded piezoelectric patches and a disc

3. Data processing

The main advantage of applying full FFT is that it provides information about the phase correlation between the two measured channels. In the experimental set-up, sensors were mounted perpendicular to each other. The phase correlation between the channels is not lost thanks to the use of a complex signal, the real part of which is the signal measured in one direction and the imaginary part is that measured perpendicularly to it [12]. When the Fourier transformation is performed on such a complex signal, it is possible to distinguish the direction of rotation of individual frequency components, which is not true with the standard Fourier spectrum calculated using a single real signal. A very intuitive explanation of this feature can be found in reference [13]. The full frequency spectra were calculated using the FFT function of the MATLAB software. In order to minimize spectral leakages, time series of duration corresponding to an integer multiple of the number of turns are being used.

To allow for a comparison of the results obtained using different signals, the latter will be scaled to the same engineering units (e.g. to mm or m/s^2), before the Fourier transformation. The signals from piezoelectric sensors are scaled by using the laser sensors. When the structure does not rotate, the first mode of vibration is excited and the responses of the sensors are measured. Then, using a laser sensor as reference, the scaling factor is determined. This procedure was performed separately for each direction of rotor motion, to account for mounting imperfections.

4. Results and discussion

Before the analysis of the results, the directional information of the frequency components should be systematised. Let us assume that there are two sensors (x , y)

referenced to SRF, and two additional sensors (ξ , η) referenced to RRF. All sensors measure signals in the directions shown in Fig. 2a, and the shaft rotates counter clock-wise (CCW).

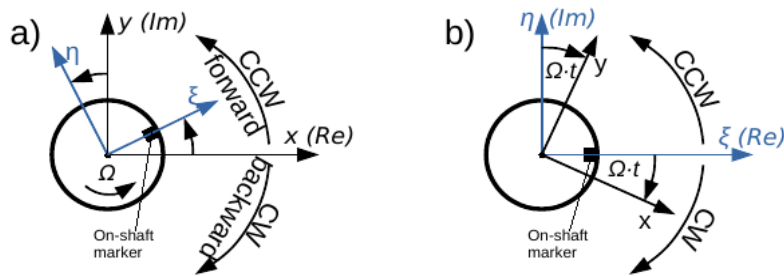


Figure 2. Interpretation of full spectrum directivity information: a) in SRF, b) in RRF

The double-sided spectrum of a complex signal ($x + iy$) has the following interpretation: the components with a positive frequency have CCW direction of rotation (in reference to SRF), and since they are consistent with the direction of the rotation of the shaft, they are called the forward components (Fig. 2a). The components with negative frequencies are called backward, because they rotate opposite to the shaft, that is in the clock-wise (CW) direction. Similarly, using the full spectrum approach for the RRF-referenced complex signal ($\xi + i\eta$), the components with a positive frequency will have CCW direction (in reference to RRF), and those with negative – CW (Fig. 2b). It implies, that a static force acting in SRF, e.g. the gravity force, will have a CW component in RRF. Usually, in the literature, the full spectra of SRF referenced signals are presented in such a way that the forward frequency components are always positive, regardless of the direction of the rotation of the rotor or positions of the sensors. Thus, the full spectrum obtained for RRF referenced signals will always have a gravity related component with negative frequency ($-1X$, i.e. -1 times the frequency of rotation), for any direction of rotation.

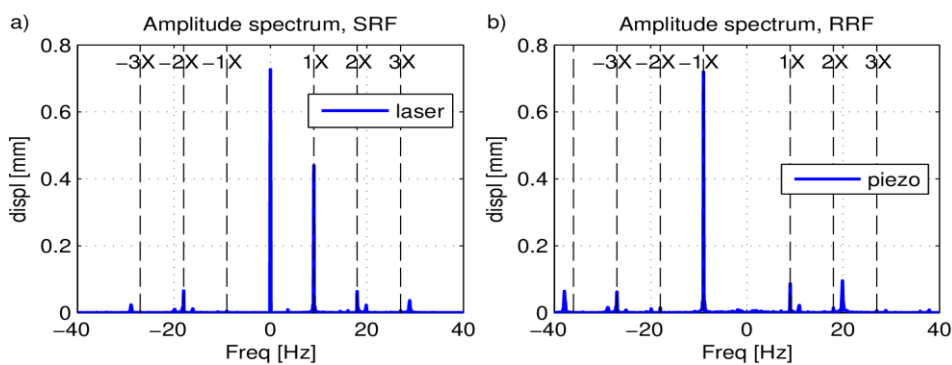


Figure 3. The obtained full spectra for: a) the laser sensors, SRF spectrum, b) the piezoelectric patches, RRF spectrum

The two main components of the SRF spectrum (Fig. 3a) are 0X and +1X, which are due, respectively, to the gravity force and to the combination of the unbalance and a possible shaft bow. The RRF spectrum has only one significant peak (Fig. 3b), due to gravity, as discussed above. The unbalance and bow related deflections are absent from the RRF spectrum, because the piezoelectric patches are unable to measure constant static strains (the static charges are slowly discharged by measurement instrumentation). It may be difficult to measure the shaft deflection due to the gravitational force using a laser sensor, since the undeformed shaft position is usually not known. On the other hand, the -1X component of the RRF spectrum can be conveniently used to estimate the deflection of the shaft caused by gravity. To this end, the amplitude of this component was measured by the piezoelectric sensors for several rotational speeds of the shaft, and the obtained values were averaged. Using this value the reference undeformed shaft position was established, which allowed the measurement of the static component in Fig. 3a.

By taking a closer look at the other components, further similarities can be observed. There is a simple relationship between the spectra, the RRF components are shifted by 1X to the left relative to SRF, and vice versa. Using this principle, a plot in Fig. 4 has been obtained, showing a comparison of the spectra obtained with different sensors. It can be seen that the signals obtained from different types of sensors contain nearly the same components, except that the unbalance information cannot be obtained using piezoelectric sensors that rotate together with the shaft. Two important conclusions follow from this observation: firstly, the typical symptoms, which are well established and described for sensors working in SRF can also be used for signals that come from the shaft-mounted sensors. Secondly, the use of a one-side full spectrum for signals from RRF would cause averaging of components that do not correspond to each other. For example, when a one-sided view were used to signals presented in Fig. 3b, the amplitudes of components -1X and 1X would be averaged. When one looks at these components from the SRF perspective, it turns out that 0X and +2X components are averaged, which clearly disrupts diagnostic information carried by the signals.

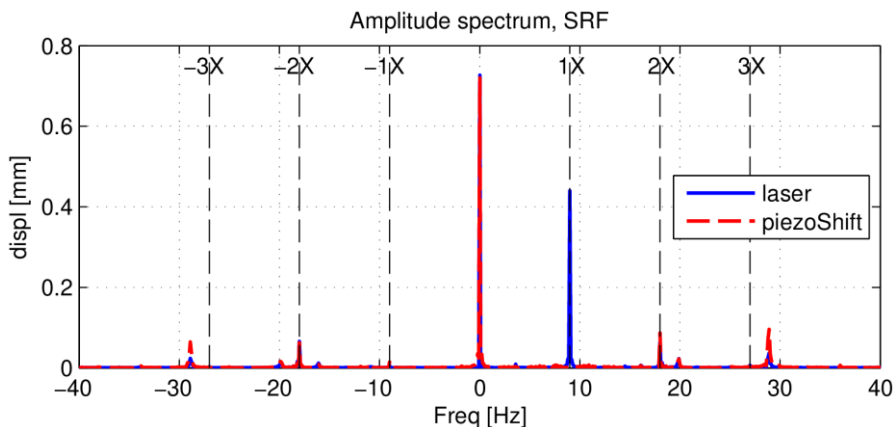


Figure 4. The comparison of the spectra, when RRF spectrum is shifted by +1X

The full spectra for signals obtained from the accelerometers are presented in Fig. 5b. The previously dominating components are less pronounced, because acceleration is measured, so that the higher-frequency components become better visible. The two main components in Fig. 5b are non-integer multiples of the frequency of rotation, what is typical of vibrations generated by ball bearings [12]. Two 3204 2RS bearings were used in the laboratory stand, for which one can calculate the outer race order, which is about 3.2X. The experimental results are in good agreement with the calculated value. The same components can be found in the shifted spectrum (Fig. 5a) obtained using piezoelectric patches. Even though the sensors rotate with the shaft, the components related to bearings can be clearly observed after proper data processing.

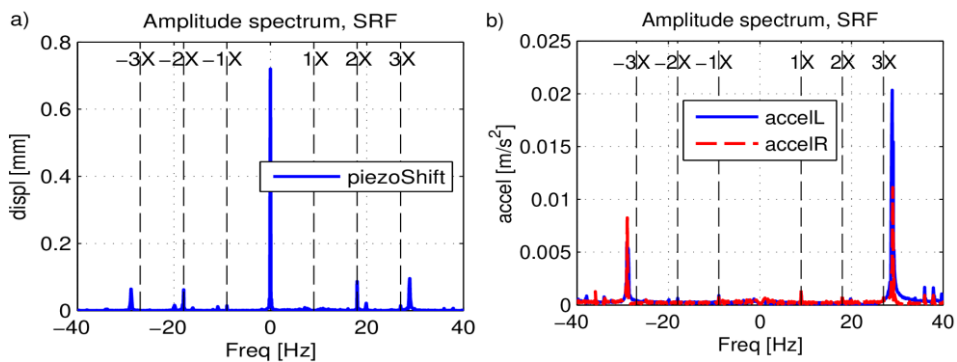


Figure 5. The full spectrum of signals from: a) piezoelectric patches, shifted by +1X, b) accelerometer on bearings supports

Piezoelectric patches also preserve the phase information that exists in the vibrational signals. As an example, the orbit plots [1] for SRF and RRF sensors are compared in Fig. 6. The displacements from the laser sensors have been filtered using band-pass filter with centre frequency that corresponds to 3.2X (Fig. 6a) and zero phase shift. The signals generated by piezoelectric patches must be first transformed to SRF and then filtered using the same filter as earlier. The plots (Fig. 6) show 4 revolutions of the shaft, and the red dots mark that 0° absolute angular position of the shaft is crossed (as measured by the motor encoder). The orientation of semi-major and semi-minor axes in both ellipses, as well as the phase relations with respect to the absolute phase marks are in good agreement.

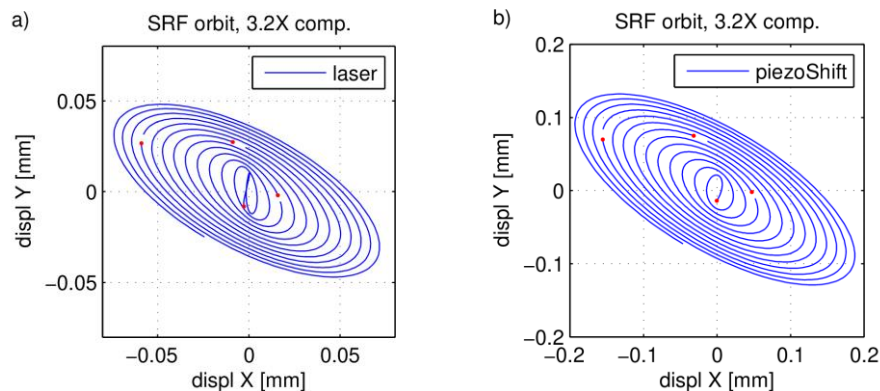


Figure 6. 3.2X-filtered orbits based on displacements from: a) the laser sensors, b) transformed (shifted) piezoelectric patches

5. Conclusions

The paper has discussed experimental results, obtained for an elastic rotor that has a constant rotational speed. Piezoelectric patches bonded to the shaft have been used as one of the sensors measuring vibrations. As expected, the static strains that are generated in rotating shafts are lost by piezoelectric sensors. The work shows that PZT patches are capable of measuring the other significant information, however it requires proper data processing to compare it with other sensors that do not rotate with the shaft.

As the results show, the use of the full spectrum is especially advisable to process signals that come from RRF. With a RRF spectrum, the one-side view (which has been used in the literature to analyse signals from sensors referred to a rotating frame) can be inadequate, since it averages unrelated components. Using the approach discussed in this paper, the fact that the sensors rotate with the shaft ceases to be relevant, and the full SRF referenced spectrum can be easily reconstructed. It has the advantage that the well-studied SRF spectra signatures of rotor problems (like misalignment, rub, rotor crack) can be adapted to signals that come from rotor-mounted sensors.

Acknowledgments

The first author would like to acknowledge the support of the Dean of the Faculty of Mechanical Engineering and Robotics of AGH UST under grant number: 16.16.130.942/Kozioł.

References

1. A. Muszyńska, *Rotordynamics*, CRC Press, Boca Raton, 2005.
2. J. Kiciński, *Dynamics of Rotors and Sliding Bearings* (in Polish), IMP PAN, Gdańsk, 2005.

3. M. Monte, F. Verbelen, B. Vervisch, *The Use of Orbitals and Full Spectra to Identify Misalignment*, in: A. Wicks (Ed.), *Structural Health Monitoring*, Springer International Publishing, Cham, **5** (2014) 215 – 222.
4. R. R. Da Silva, E. S. Costa, R. Oliveira, A. Mesquita, *Fault diagnosis in rotating machine using full spectrum of vibration and fuzzy logic*, *Journal of Engineering Science and Technology*, **12** (2017) 2952 – 2964.
5. A. A. Cavalini Jr, L. Sanches, N. Bachschmid, V. Steffen Jr, *Crack identification for rotating machines based on a nonlinear approach*, *Mechanical Systems and Signal Processing*, **79** (2016) 72 – 85, doi:10.1016/j.ymssp.2016.02.041.
6. M. A. Abuzaid, M. E. Eleshaky, M. G. Zedan, *Effect of partial rotor-to-stator rub on shaft vibration*, *Journal of Mechanical Science and Technology*, **23** (2009) 170 – 182, doi:10.1007/s12206-008-0717-x.
7. H. Kunze, M. Riedel, K. Schmidt, E. Bianchini, *Vibration reduction on automotive shafts using piezoceramics*, in: E. H. Anderson (Ed.), San Diego, CA, 2003: p. 382, doi:10.1117/12.483891.
8. P. J. Sloetjes, A. De Boer, *Vibration Reduction and Power Generation with Piezoceramic Sheets Mounted to a Flexible Shaft*, *Journal of Intelligent Material Systems and Structures*, **19** (2008) 25 – 34, doi:10.1177/1045389X06072753.
9. L. Arebi, F. Gu, A. Ball, *A comparative study of misalignment detection using a novel Wireless Sensor with conventional Wired Sensors*, *Journal of Physics: Conference Series*, **364** (2012) 012049, doi:10.1088/1742-6596/364/1/012049.
10. M. E. Elnady, A. Abdelbary, J. K. Sinha, S. O. Oyadiji, *FE and Experimental Modeling of On-shaft Vibration Measurement*, *Proceedings of the 15th International Conference on Aerospace Sciences & Aviation Technology*, (2013) 1 – 18.
11. S. Jiménez, M. O. T. Cole, P. S. Keogh, *Vibration sensing in smart machine rotors using internal mems accelerometers*, *Journal of Sound and Vibration*, **377** (2016) 58 – 75, doi:10.1016/j.jsv.2016.05.014.
12. Y. Ishida, T. Yamamoto, *Linear and Nonlinear Rotordynamics: A Modern Treatment with Applications*, Wiley-VCH, Weinheim, 2012.
13. M. Owen, *Practical Signal Processing*, Cambridge University Press, 2012.

Identification of Rolling Bearing Condition by Means of a Classification Tree

Maciej TABASZEWSKI

*Faculty of Mechanical Engineering and Management,
Institute of Applied Mechanics, Poznan University of Technology,
maciej.tabaszewski@put.poznan.pl*

Abstract

The paper deals with the problem of evaluation of technical condition of rolling bearings on the basis of synchronously measured vibroacoustic symptoms and temperature. Rolling bearings were subjected to accelerated wear under controlled conditions. The values recorded in the study were sound pressure in a broad band including ultrasound (band up to 40 kHz), vibration acceleration in a radial direction, ultrasound in a band up to 100 kHz (processed into audible band), and bearing housing temperature. The identification of the condition was carried out with the help of a supervised learning system. Two conditions were distinguished: fit - examples were obtained in the initial phase of bearing operation in temperature stability conditions, and pre-failure - examples were obtained from fragments of recording just before the occurrence of bearing failure. The CART (Classification and Regression Tree) binary tree method was used to determine the technical condition and significance of particular diagnostic symptoms.

Keywords: vibroacoustic diagnostics, rolling bearings, classification tree

1. Introduction

It can be assumed that up to 80% of machines have rolling bearings in their design and therefore they are very important elements in the context of machine maintenance. Rolling bearings are the cause of a significant number of failures in industry. They occur before the nominal life of the bearings is reached and result from incorrect installation or operating conditions (poor lubrication conditions, grease contamination, excessive loads [1]). Of course, there are many methods of diagnosing bearings based on such symptoms as: increase in temperature, increase in resistance to motion, grease or oil pollution, increase in emitted noise (in audible and ultrasound bands) and/or vibrations, phenomena of acoustic emission. In the case of vibrations, the SMP (Shock Pulse Method) method is commonly used in industry [2]. Bearing damage can also be detected by measurement of kurtosis, observation of crest factor changes in a broad frequency band, envelope analysis, wavelet analysis, synchronous averaging and many others [3-7]. In order to clearly determine the technical condition of a rolling bearing, especially in automatic systems, synchronous observation of many diagnostic symptoms and the use of classification methods give good results [8]. In order to build the classifier it is necessary to have a rich collection of training examples. However, in the case of a large number of data concerning the same or similar objects, the construction of such a system is feasible.

Classifiers are used in a wide range of fields, for example in the processing of large data resources [9-15]. There are many publications on the use of machine learning,

including deep learning, in diagnostics, for example: [16-22]. The classification process can be carried out using many methods with specific properties and capabilities [22-26]: neural networks, distance classifiers, statistical classifiers, approximation classifiers, fuzzy classifiers, etc. One of the widely used methods are CART classification and regression trees developed by Breiman in 1984 [23, 25, 26]. The advantage of the tree structure is the way the knowledge can be represented after the learning process. It is easy to generate a set of human-readable rules on the basis of such a structure, which is very important at the stage of preparing diagnostic procedures to be used by maintenance services. This is one of the main reasons why the classification tree method has been proposed here. In addition, the tree enables to identify those diagnostic symptoms that are relevant to the process of classification of state. This is another important reason for proposing this method for classification in this work. The CART method does not require the user to discretize the values of input variables, which undoubtedly facilitates its use. Details of the operation of the tree structure algorithm can be found, for example, in [23].

2. Description of tests

Diagnostic data on rolling bearing vibrations in various phases of their life were obtained during accelerated bearing wear tests carried out on a test stand specially designed for this purpose. Figure 1 shows a photograph of the stand, including the measuring head, in which the bearing was mounted. The effect of accelerated wear was achieved by improper lubrication conditions and excessive axial loads on the bearing.

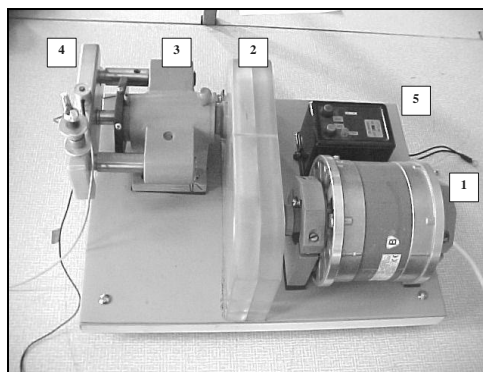


Figure 1. General view of the test stand (1 – motor, 2 – belt transmission, 3 – support, 4 – measuring head, 5 – motor control and protection system) – photo by R. Barczewski

The bearings were monitored during continuous operation. The temperature of the casing, acceleration of absolute vibrations in the band up to 1000 Hz and up to 12800 Hz, sound pressure levels in the band up to 40 kHz, and ultrasound signal in the band up to 100 kHz processed into the audible band (in the range from 50 Hz to 3 kHz) were recorded. Based on the signals, a number of measures were determined (34 different components of the observation vector). Teaching examples were obtained by selecting a few initial observations after stabilization of thermal conditions and a few

observations immediately preceding the failure. A total of 16 bearings were tested. The vectors of observation were described with the label – “fit” and “pre-failure”. As a result of the experiment, 160 examples were collected, with almost half (77 examples) referring to a fit condition and the second part to a pre-failure condition. The uneven distribution was due to the omission of a few unusual observations (outliers) probably resulting from the fact of getting into the bearing contamination in the form of solid substance. To measure vibration acceleration in both bands and the ultrasonic signal in the band from 20 kHz to 100 kHz recorded with the Ultraprobe 2000 instrument, the following measures were used: rms value, peak (upper and lower peak), mean, absolute peak, interpeak, kurtosis, crest factor, clearance and shape. The maximum, minimum and average sound pressure levels were used to measure the sound pressure in the band from 16 Hz to 40 kHz. All measurements were obtained from 30 second recording buffers acquired every 10 minutes.

Figure 2 shows a block diagram of the measuring chain.

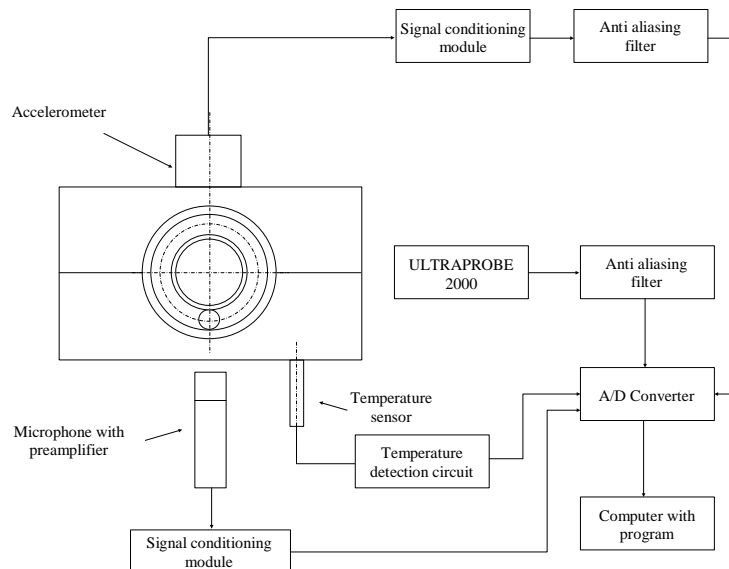


Figure 2. Block diagram of the measuring chain

Figure 3 shows examples of symptom life curves for one of the bearings. In order to present them in a clear way on one drawing and simultaneously show the dynamics of changes during the experiment, the measured values were normalized to the mean of several initial values.

As the figure shows, an unambiguous assessment of the technical condition of the bearing is not simple in the case at hand. There are rapid increases in the values of some symptoms and then decreases in their values before failure. In addition, there is a problem of determining limit values for individual symptoms. Taking into account the whole set of bearings it seems that the application of diagnostics based on many symptoms and the application of machine learning should facilitate such diagnosis,

especially because the proposed method can provide clear rules to determine the technical condition of the bearing.

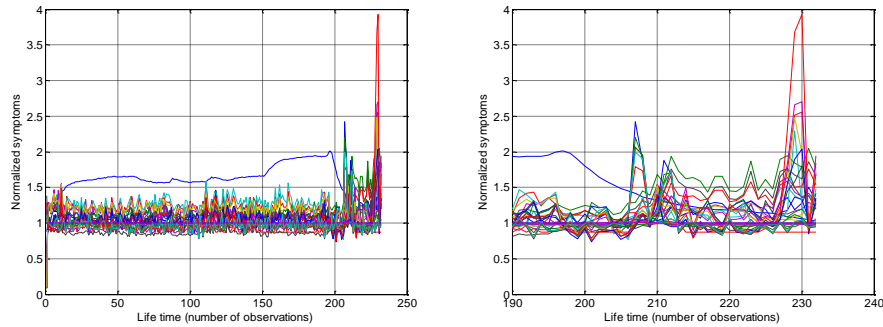


Figure 3. Normalized values for vibroacoustic symptoms and temperatures obtained during the experiment. Drawing on the left - all life curves, drawing on the right - the final fragment just before the failure

Figure 4 presents the data obtained in the space of features created by selected features.

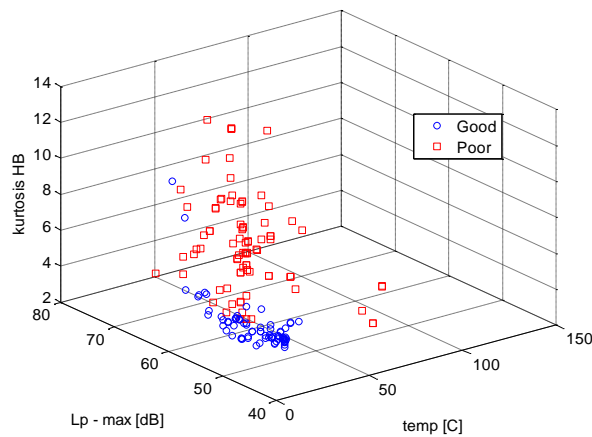


Figure 4. Measurements obtained in the sample space of features formed by temperature, maximum sound pressure level and vibration acceleration kurtosis in the HB band (up to 12.8 kHz)

3. Application of the CART method to data

In order to develop the methodology of two-state classification of rolling bearing condition, a CART type tree was used. The Gini index [26] was used as a measure of node contamination. The main advantage of classification trees here is generation of clear rules, which will allow to develop a simple algorithm for detecting the pre-failure condition of a bearing. Such understandable diagnostic rules may be used by maintenance services to identify the technical condition of an object. Another important

advantage is that there is no need to select diagnostic features. This selection is performed by the algorithm during the tree construction.

The first step in building a tree was to optimize it. For this purpose, a leave-one-out cross validation test was used for different values of the minimum leaf size. The choice of this test was based on a small number of available data. The analysis shows that the optimal tree is a tree in which the hyperparameter associated with the minimum number of observations in a leaf is 1 or 2. In the next step the most important input features of the classifier were selected. This is done by examining the change in the mean square error (MSE) at each breakdown for each predictor. Table 1 shows the three best rated measures of recorded signals.

Table 1. The best symptoms obtained on the basis of the classification tree

Pos.	Symptom
1	Rms value of vibration acceleration in the HB band (up to 12.8 kHz)
2	Bearing temperature
3	Peak value of vibration accelerations in the LB band (up to 1 kHz)

As can be seen from the table above, the most important parameter in determining the condition of the bearing in the conducted experimental studies was the rms value of vibration accelerations in a wide frequency band, which confirms the validity of the measurement of this value. The second parameter turned out to be the temperature. This is due to the fact that the bearing was brought to failure and thus also reached the thermal phase of wear. The last parameter affecting the determination of the technical condition of the tested bearings was the peak value of vibration accelerations. However, it appears that it should be determined in a narrower frequency range than the rms value. Of course it is not possible to generalize this conclusion for all bearings, but it may turn out that measures such as the crest factor may not be effective in diagnosis, because both values on which it depends should be determined in different bands.

After determining the most important predictors, the tree was re-constructed on their base. On the basis of the leave-one-out test, results were obtained, which are presented in Table 2.

Table 2. Results obtained for the optimally selected classifier's hyper-parameter and a limited number of the best predictors

Total classification error	True Positive Rate TPP	True Negative Rate TNR	Positive Predictive Value PPV	Negative Predictive Value NPV
0.019	0.998	1.000	1.000	0.987

A small classification error of 1.9% shows the possibilities of the method in the case of an optimally selected hyperparameter as well as input quantities. The probability of detecting an impending bearing failure when it is actually in this state is close to 1.0

(0.998 to be precise). The TNR indicator indicates the probability that a fit condition will be detected if the bearing is in that condition. On the other hand, PPV determines to what extent it is possible to be sure that the result is true if a pre-failure condition is detected. Similarly, the NPV indicator for the fit condition can be defined. All values indicate very good properties of the classifier.

An important reason for using the classification tree was to generate knowledge that could be useful for maintenance services. For example, the following rules can be generated from the finally built classifier:

R1: IF RMS (in the HB band) $\geq 4,8 \text{ m/s}^2$ AND TEMP $\geq 34,7 \text{ C}$ THEN PRE-FAILURE CONDITION

R2: IF RMS (in the HB band) $\geq 4,8 \text{ m/s}^2$ AND TEMP $< 34,7 \text{ C}$ THEN FIT CONDITION

R3: IF RMS (in the HB band) $< 4,8 \text{ m/s}^2$ AND PEAK (in the LB band) $\geq 16,7 \text{ m/s}^2$ THEN PRE-FAILURE CONDITION

R4: IF RMS (in the HB band) $< 4,8 \text{ m/s}^2$ AND PEAK (in the LB band) $< 16,7 \text{ m/s}^2$ THEN FIT CONDITION

where: RMS – rms value of absolute vibration accelerations, PEAK – peak value of absolute vibration accelerations, TEMP – bearing housing temperature, HB – measurement in the band up to 12.8 kHz, LB – measurement in the band up to 1 kHz.

The simple rules generated can enable you to make the right diagnostic decisions. Of course, in the case of bearings and operating conditions other than the tested ones, it may turn out that the given rules do not work. The presented methodology, however, can be easily applied in other cases (e.g. by bearing manufacturers), as soon as a suitable database is available.

4. Conclusions

Vibroacoustic diagnostics of rolling bearings is a very important element of the machine maintenance strategy depending on the technical condition. By using classification methods it is possible to assess the technical condition of bearings on the basis of many symptoms measured synchronously. Such an approach may be necessary in many cases, as it may turn out that the measurements of one measure of the diagnostic signal are insufficient to determine the technical condition of the bearing. This creates the problem of defining limit values for various measures that can be used in the diagnosis process. In addition, it may turn out that one combination of measures will work in a given case and not in another one. The use of machine learning methods makes it easy to develop a statistical approach to the problem and to eliminate these disadvantages. The only serious problem is the need to teach the system using examples that also include bearing damage. It may turn out, however, that with proper separation of vibroacoustic phenomena, it is sufficient to test the bearings themselves under more sterile conditions and extrapolate the results to complex objects. Furthermore, with a sufficiently large set of the same machines (pumps, fans, electric motors), obtaining a minimum number of training examples may be realistic. It is also important that thanks to the tree method, a clear knowledge base can be obtained in the form of a set of simple rules allowing its

easy direct application in machine monitoring. In addition, information on the significance of the measured parameters is obtained, which may allow to reduce the redundancy of the diagnostic system over time.

The proposed methodology was applied to small-size bearings 608, but it can also be applied in other cases. In the example described above, a total classification error of 1.9% was achieved, which is a very good result. The entire diagnostic inference was reduced to just four simple rules.

It is also important to note that useful signal measures can be determined in different frequency bands, which means that the use of relative measures (e.g. crest factor, etc.) for bearing diagnostics may not be appropriate.

Acknowledgements

The presented research results were financed from a science grant awarded by the Ministry of Science and Higher Education 02/21/DSPB/3546.

References

1. S. Szymaniec, *Diagnostics of motor rolling bearings in conditions their industrial operating* (in Polish), *Maszyny Elektryczne*, **74** (2006).
2. N. Tandon, G. S. Yadava, K. M. Ramakrishna, *A comparison of some condition monitoring techniques for the detection of defect in induction motor ball bearings*, *Mechanical Systems and Signal Processing*, **21**(1) (2007) 244 – 256.
3. N. Tandon, A. Choudhury, *A review of vibration and acoustic measurement methods for detection of defects in rolling elements bearings*, *Tribology International*, **32**(8) (1999) 469 – 480.
4. Y. Yang, D. Yu, J. Cheng, *A fault diagnosis approach for roller bearings based on IMF envelope spectrum and SVM*, *Measurement*, **40**(9) (2007) 943 – 950.
5. Q. Sun, Y. Tang, *Singularity analysis using continues wavelet transform for bearing fault diagnosis*, *Mechanical Systems and Signal Processing*, **16**(6) (2002) 1025 – 1041.
6. P. McFadden, M. Toozhy, *Application of synchronous averaging to vibration monitoring of rolling element bearings*, *Systems and Signal Processing*, **14**(6) (2000) 891 – 906.
7. J. Wodecki, R. Zdunek, A. Wyłomańska, R. Zimroz, *Local fault detection of rolling element bearing components by spectrogram clustering with Semi-Binary NMF*, *Diagnostyka*, **18**(1) (2017) 3 – 8.
8. M. Tabaszewski, *Forecasting in multi-symptom condition monitoring of machines* (in Polish), *Wydawnictwo Politechniki Poznańskiej*, 2010, pp. 153.
9. Y. Lei, Z. He, Y. Zi, *Application of an intelligent classification method to mechanical fault diagnosis*, *Expert Systems with Applications*, **36**(6) (August 2009) 9941 – 9948.
10. F. Sunar Erbek, C. Özkan, M. Taberner, *Comparison of maximum likelihood classification method with supervised artificial neural network algorithms for land use activities*, *International Journal of Remote Sensing*, **25**(9) (2004) 1733 – 1748.

11. H. Zhang, J. Li, Y. Huang, L. Zhang, *A Nonlocal Weighted Joint Sparse Representation Classification Method for Hyperspectral Imagery*, IEEE Journal of Selected Topics in Applied Earth Observations and Remote Sensing, **7**(6) (2014) 2056 – 2065.
12. Abeer Badr El Din Ahmed, Ibrahim Sayed Elaraby, *Data Mining: A prediction for Student's Performance Using Classification Method*, World Journal of Computer Application and Technology, **2** (2014) 43 – 47.
13. C. Gorges, K. Oztruk, R. Liebich, *Impact detection using a machine learning approach and experimental road roughness classification*, Mechanical Systems and Signal Processing, **117** (2019) 738 – 756.
14. V. Leemans, H. Magein, M.-F. Destain, *Defect segmentation on 'Jonagold' apples using colour vision and a Bayesian classification method*, Computers and Electronics in Agriculture, **23**(1) (1999) 43 – 53.
15. T. Nguyen, G. Armitage, *A survey of techniques for internet traffic classification using machine learning*, IEEE Communications Surveys & Tutorials, **10**(4) (2008) 56 – 76.
16. C. Sobie, C. Freitas, M. Nicolai, *Simulation – driven machine learning: Bearing fault classification*, Mechanical Systems and Signal Processing, **99** (2018) 403 – 419.
17. A. Lahrache, M. Cocconcelli, R. Rubini, *Anomaly detection in a cutting tool by K-Means clustering and Support Vector Machines*, Diagnostyka, **18**(3) (2017) 21 – 29.
18. P. Potocnik, E. Govecar, *Semi-supervised vibration - based classification and condition monitoring of compressors*, Mechanical Systems and Signal Processing, **93** (2017) 51 – 65.
19. M. Ruiz, L. E. Mujica, S. Alférez, L. Acho, Ch. Tutivén, Y. Vidal, J. Rodellar, F. Pozo, *Wind turbine fault detection and classification by means of image texture analysis*, Mechanical Systems and Signal Processing, **107** (2018) 149 – 167.
20. F. Jia, Y. Lei, N. Lu, S. Xing, *Deep normalized convolutional neural network for imbalanced fault classification of machinery and its understanding via visualization*, Mechanical Systems and Signal Processing, **110** (2018) 349 – 367.
21. C. Mechefske, J. Mathew, *Fault detection and diagnosis in low speed rolling element bearings Part II: The use of nearest neighbour classification*, Mech. Syst. Sign. Process., **6**(4) (1992) 309 – 316.
22. J. Korbicz, J. M. Kościelny, Z. Kowalczyk, W. Cholewa (ed.), *Fault Diagnosis: Models, Artificial Intelligence, Applications*, Springer Science & Business Media, (2012) pp. 922.
23. D. T. Larose, *Discovering Knowledge in Data. An Introduction to DATA MINING*, John Wiley & Sons, Inc., (2005) pp. 227.
24. D. T. Larose, *Data Mining Methods and Models*, John Wiley & Sons, Inc., 2006.
25. O. Maimon, L. Rokach (ed.), *Data Mining and Knowledge Discovery Handbook*, Springer New York Dordrecht Heidelberg London, (2010) pp. 1285.
26. A. Géron, *Hands-On Machine Learning with Scikit-Learn and Tensor Flow*, O'Reilly Media, (2017) pp. 574.

Visualization of Vibrations in Structural Diagnoses of Technical Objects

Michał ŚMIEJA, Sławomir WIERZBICKI, Magdalena KURIATA
*University of Warmia and Mazury in Olsztyn, Faculty of Technical Sciences,
Oczapowskiego str. 11, 10-957 Olsztyn, Poland,
smieja@uwm.edu.pl, slawekw@uwm.edu.pl, magdalena.kuriata1@gmail.com*

Tomasz CIEPLIŃSKI, Łukasz SZUMILAS
*I-Care Polska Sp. z o.o., ul. Puskarska 9, 30-644 Kraków, Poland,
tomasz.cieplinski@icareweb.com, lukasz.szumilas@icareweb.com*

Abstract

One of the key methods for diagnosing the structural degradation of technical objects relies on observations of mechanical vibrations that accompany equipment operation and damage. Hardware and software advancements and the development mathematical methods for modelling and inference have increased the popularity of vibroacoustic diagnostics in mechanical systems. Displacement in the time domain of physical points in a vibrating object is the primary diagnostic symptom that undergoes further processing in the measurement system. At present, vibrations are usually registered with the use of accelerometers or optical sensors. Advanced tools for image recording, processing and analysis are deployed in quasi-realistic observations of motion that cannot be perceived by the human senses. This article discusses a method for visualizing vibrations based on deliberate deformation of the registered image through motion magnification. The presented approach is illustrated with selected examples.

Keywords: motion magnification, vibration, image processing, diagnostics

1. Introduction

Mechanical vibration is a phenomenon that accompanies the operation of machines. In most cases, vibration is regarded as residual process that accompanies the normal operation of machines. Vibration compromises a machine's durability and process parameters, and it exerts a negative influence on the operating environment [1].

In both cases, a thorough knowledge of the parameters describing vibrations and their source is required to guarantee optimal machine operation. Vibrations are monitored to control process parameters, determine the extent of structural wear, and identify assembly defects.

In the traditional approach, a mechanical assembly is inspected during a visual evaluation. This approach has significant limitations because humans are unable to perceive motion that exceeds a certain velocity threshold or the magnitude of the resulting displacement. The subjective character of the human perception and the inability to estimate the observed phenomena in numerical quantities also play an important role in many cases.

Processes that cannot be perceived by the human sense of sight can be observed with the use of indirect methods and physical phenomena that depict motion parameters on

a scale that can be interpreted by the observer. This is the basic operating principle of acceleration, speed and location sensors such as accelerometers, optical sensors and eddy current sensors [2].

The primal parameter that describes the state of a vibrating object is the location of a selected point that is related to that object in space and time. In analyses of vibrations resulting from the deformation of physical structures, the mutual location of selected points in the analyzed object is evaluated. Vibration is analyzed by observing changes in the location of points and by determining motion parameters such as trajectory, velocity and acceleration. In practice, one or more parameters are used, subject to the analyzed case.

The manner in which data are acquired based on signals that render motion parameters is dependent on the applied tool. Accelerometers, devices that measure proper acceleration, are most widely used in vibroacoustic analyses. Laser sensors are increasingly often used, and, subject to their design, they measure the location (triangulation sensors) or velocity (Doppler sensors) of a moving object. Subject to the applied sensor and the measured motion parameters, the signal generated by a sensor can be interpreted directly or converted by differentiation or integration. Advanced sensors and the development mathematical methods create new opportunities for observing vibration in research and in industrial applications. However, real-world applications have numerous limitations [2].

Conventional signal transducers generally measure a signal associated with single point in an object. In many applications, the resulting data are sufficient to describe or evaluate the state of a given object or phenomenon. However, the number of measured points has to be increased during observations of complex objects, sets of elements with many degrees of freedom, and structural deformations. These requirements significantly increase the complexity and cost of measuring systems, and not all requirements can be met in practice. The applied solutions often rely on simulation methods and theoretical models.

However, in many situations, a problem cannot be rapidly identified based on a researcher's or diagnostician's experience or routine proceedings. The selection and location of a measuring point can pose a challenge in complex objects.

Selected types of sensors are not suitable for vibroacoustic analyses because a sensor's mass can affect the dynamic parameters of a vibrating object, which detracts from the accuracy of measurements in a real-world setting. Sensors that come into direct contact with the analyzed object can also be difficult to deploy due to limited assembly space or high operating temperature. Such difficulties can be overcome by using contactless sensors, such as laser sensors, provided that their assembly point does not exert a disrupting influence on the conducted measurements [2].

The advancements in image analysis and processing have extended the scope of measuring methods in vibroacoustic analyses of technical objects. The methods discussed in this article present a novel approach to observing vibration processes, and they facilitate rapid evaluation of the phenomena that occur in complex objects. The above approach involves the visualization of the displacement of measuring points that cannot be perceived by the human senses. In the literature, such methods are referred to motion microscopy techniques [3]. The displacement of the points measured

on a technical object is recorded with a video camera, and the resulting data are transformed. The result is a set of deformed images, and subtle motions in a video sequence are amplified to visualize deformations that would otherwise be invisible for the analyst. In the literature, this method is known as motion magnification.

2. Review of motion magnification methods

Image processing methods for depicting and describing motion are widely used in many areas, such as traffic monitoring. In vibroacoustic analyses, the direct application of motion magnification techniques can be challenging due to relatively small values of the changes captured in video material and due to human sensory limitations. This chapter reviews the applicability of image processing techniques for observation of mechanical vibration processes.

In methods for the visualization of vibration data, the location of points related to the analyzed object is monitored in regular time intervals in a selected area of a 2D plane (matrix of the registering device). The instantaneous location of these points in a system of coordinates in a 2D plane is described by geometric coordinates x, y . The images in a video sequence are described by variables t_0, t_1, \dots, t_n in successive moments of time.

In visualizations of vibration data, images are processed in the spatial domain x, y , in the temporal dimension t , and in the spatio-temporal domain, as shown in figure 1a. The formal description of changes in plane x, y , illustrating the displacement / deformation of the represented points is based on the principles of fluid mechanics.

In the Lagrangian approach, geometrical changes are observed by monitoring a point on the studied object. The point's geometric coordinates in the evaluated system (individual frames in a video sequence) are determined based on its location in successive time intervals. In other words, the trajectory of the point's motion is monitored.

The Eulerian approach describes changes in the parameters of a point in a specific location in a given pair of coordinates. In image analyses, these parameters are mostly represented by the brightness B or intensity I of a pixel. Lagrangian and Eulerian approaches to monitoring dynamic changes in an object are presented in figure 1b, 1c.

Lagrangian and Eulerian approaches can be used interchangeably to elicit information about motion dynamics. The concept of optical flow has been inspired by methods used to model gas and fluid flow. Optical flow is determined based on the sequence of successive images. Pattern preparing methods have been proposed by Lucas-Kanade, Horn-Schunck and Black-Jepson. Their effectiveness and applicability was compared by [4].

The general principle for computing optical flow in the Lucas-Kanade approach is presented in Figure 2. In this method, the information from several nearby pixels is compared in successive frames of the video sequence based on the assumption that the analyzed parameter is characterized by small and approximately constant differences. The motion magnification technique for visualizing small differences in a video sequence in the Lagrangian approach was presented by [5]. The instantaneous velocities of the measured points determined with the use of the Lucas-Kanade method were used to group the trajectories of objects with correlated motions. A set K of trajectories was

created. Optical flows were interpolated over all pixels, and pixels were assigned to clusters of trajectory layers. The representation of images in layers was demonstrated by [6]. Motion was magnified by multiplying the displacement of each pixel in the corresponding layers and rendering the pixels in each layer from back to front. The applied algorithm is highly complex and requires sophisticated calculations; therefore, it is difficult to use in real-time. The image holes that are revealed after point displacement (motion magnification) are filled with the texture synthesis method [7].

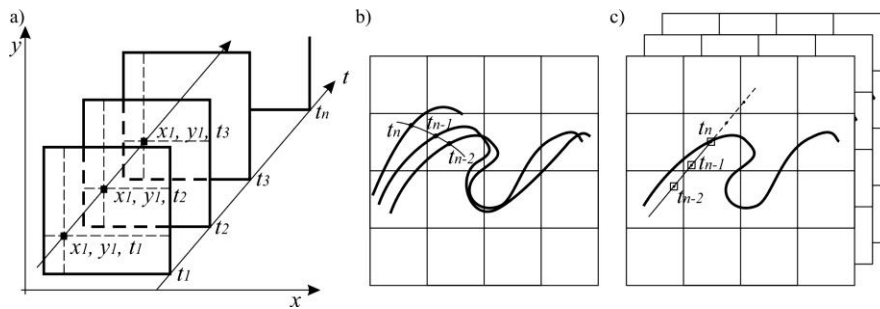


Figure 1. Spatiotemporal representation: pixel in space and time domain (a), Lagrangian (b) and Eulerian (c) approaches to temporal image presentation

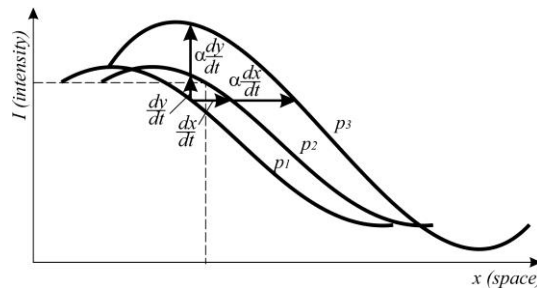


Figure 2. Intensity changes in linear Eulerian motion magnification

In the Lagrangian approach, an image’s content and its characteristic points and fragments in the frame are analyzed.

In contrast, the Eulerian approach [8] focuses on changes in the close neighbourhood of pixels in coordinates x , y , and the trajectory of image components is not explicitly determined. Changes in pixel intensity result from the displacement of the image relative to the frame in successive time intervals, as shown in figure 4. Pixel intensity can also be defined as brightness.

Similarly to the Lucas-Kanade approach, it is assumed that changes in intensity are linear. Lines p_1 and p_2 represent the intensity profile at time t_1 and t_2 , respectively. The relation can be represented by equation (1):

$$\frac{dI}{dt} = \frac{dI}{dx} \frac{dx}{dt} \tag{1}$$

Motion is magnified by introducing coefficient α (equation (2)).

$$\alpha \frac{dI}{dt} = \frac{dI}{dx} \alpha \frac{dx}{dt} \quad (2)$$

Line p_3 corresponds to the intensity profile resulting from motion magnification. However, this translation also augments noise in the image. The overbumping of line p_3 in figure 4 can produce artefacts in the final image. The stages of data processing in the discussed method are presented in the diagram in figure 3.

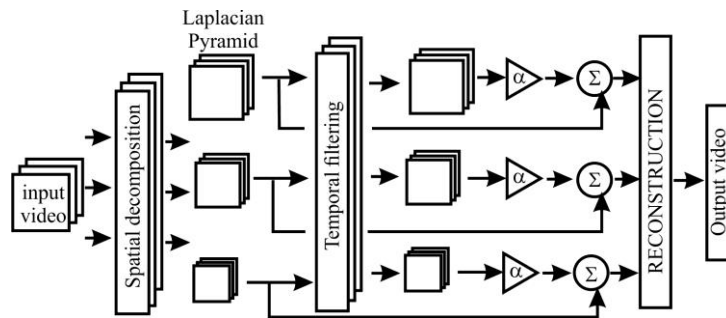


Figure 3. Scheme of linear Eulerian motion magnification

In the Laplacian pyramid approach [9], every frame of the input video sequence is spatially decomposed by temporal filtering of every image layer; the signal is reinforced and added to the original signal to obtain a reconstructed output video. According to some authors, the Laplacian of Gaussian (LoG) operation should be performed to eliminate noise. Due to the linear character of the described processes, this method is referred to as the linear Eulerian motion magnification technique.

The applicability of the Eulerian approach to motion magnification can be improved by abandoning the linearity assumption and rendering intensity with the use of local sine waves. The effectiveness of this method has been validated in contactless monitoring of life functions as well as in technical applications, such as the modal identification of simple structures [10]. In this case, motion is magnified by shifting the local phase. For this purpose, the input video was decomposed with a complex steerable pyramid rather than the Laplacian pyramid [11]. This approach supported amplitude and phase decomposition of local wavelets. Phases were filtered in every location, orientation and scale. The temporary – band passed phases were amplified, and the video was reconstructed. This method is known as phase-based video motion processing [12]. The complex steerable pyramid technique requires numerous calculations, and its applicability for spatial decomposition in real time is limited.

A new compact image pyramid representation for real-time phase-based motion magnification was proposed by [13]. In this approach, the complex steerable pyramid was replaced by the Riesz pyramid what speeds up the processing of video data four-fold.

The Eulerian methods presented in [14, 15] are effective in observations of small motions, but their applicability is limited when both small and large motions appear in a single image. Large motions create significant artefacts. Artefacts and large motions significantly decrease the visibility of small displacements. In the layer-based video magnification approach proposed by [16], the selected region is temporally aligned before subtle variations are magnified. This technique, referred as dynamic video motion magnification (DVMAG), has two main components: warping to discount large motion based on KLT tracking or optical flow, and layer-based Eulerian magnification. The input image is decomposed through an alpha-matte. Images are decomposed into three layers: opacity matte, foreground, and background. Images in opacity and foreground layers are magnified and overlaid onto the background layer. The image holes revealed by the magnified motion are filled in by texture synthesis. In the last stage, the magnified sequence is de-warped back to the original space-time coordinates. In a study by [17], user interactions were reduced through a modified alpha-matte. The distinguishing responses from the background and the foreground based on depth map were presented in a [18].

The motion magnification method continues to be developed. Attempts have been made by [19] to simplify the time-consuming process of filter tuning with the use of convolutional neural networks in the Eulerian approach.

3. Practical application of the motion magnification technique in diagnoses of technical objects

The progress in motion magnification techniques has led to the development of commercial applications for diagnosing industrial objects based on observations of vibration processes. The applicability of the analyzed tools for diagnostic purposes in a real-world industrial setting was evaluated based on an analysis of the problems reported by automation maintenance services:

- Case 1: Supply pump in a heat plant,
- Case 2: Dry feed extruder,
- Case 3: Machine hall ventilation fan.

In each case, the environment of the operating machine was recorded with a video camera. The obtained video footage was enhanced during post-processing in the Motion Amplification program. The condition of each machine was diagnosed based on the enhanced video sequence.

Supply pump in a heat plant. Considerable vibrations on pump casing as well as seal failure were noted during pump operation. An analysis based on the motion magnification method revealed axial motion of the pump's mechanical seal clamps and bearing housing on the side of the delivery casing. Video presenting the movement of pump seals is shown in

http://www.uwm.edu.pl/wnt/mechatronika/images/vibsys/CHV_blisko_fi_ltered_stabilization.mp4.

Dry feed extruder. Vibrations were observed on the extruder casing and the accompanying installations (pipelines, platforms, mezzanine). An observation of the

registered vibrations revealed visible motion of the elements mounting the extruder to the ground/foundations. The vibrations were caused by excess clearance of assembly bolts. In the

http://www.uwm.edu.pl/wnt/mechatronika/images/vibsys/12_02_2019_02%20extruder%20%20x5115-12_03_filtered.mp4

and

http://www.uwm.edu.pl/wnt/mechatronika/images/vibsys/NO.1%2012_02_2019_02%20extruder%20%20x5115-12_08.mp4

there is shown video presenting the displacements of elements of object. The frequency of vibrations in the accompanying systems corresponded to the operating frequency of the extruder shaft.

Machine hall ventilation fan. A visible increase in vibration of the fan's drive system was observed during operation. Video data were processed with the motion amplification technique to reveal displacement of the fan's motor and shaft on the side of the gearbox.

In the

http://www.uwm.edu.pl/wnt/mechatronika/images/vibsys/se%20went%20rekuperacja_filtered.mp4

there is shown video presenting the displacements of elements of object.

The motor casing was axially displaced relative to the shaft and the bearing housing, indicating that the clutch had been incorrectly assembled.

4. Conclusions

The diagnostic processes in the described cases confirmed the source of vibroacoustic signals, thus validating the applicability of the motion magnification techniques in an industrial setting. The described method supports observations of numerous machine elements whose motion cannot be captured with the involvement of conventional tools. One of the most important advantages of the discussed technique is that it does not interfere with technological processes. None of the diagnosed objects had to be shut down to enable the analysts to enter the safety zone or install sensors. In all cases, the test stand was prepared and the measurements were conducted in a matter of minutes. These findings indicate that the motion magnification method can be applied in preliminary inspections, including in cases where more sensitive equipment is required for further measurements.

References

1. B. Zoltowski, M. Zoltowski, *Selection measure of energy propagation in vibration diagnostic and modal analysis methods*, *Diagnostyka*, **19**(4) (2018) 19 – 26.
2. M. Azzouz, R. Diarra, D. Popescu. *Fault diagnosis of sensors, actuators and wind turbine system*, *Diagnostyka*, **19**(4) (2018) 3 – 10.
3. N. Wadhwa, J. G. Chen, J. B. Sellon, D. Wei, M. Rubinstein, Roozbeh Ghaffari, Dennis M. Freeman, Oral Büyüköztürk, Pai Wang, Sijie Sun, S. H. Kang,

- K. Bertoldi, F. Durand, W. T. Freeman, *Motion microscopy for visualizing and quantifying small motions*, PNAS, **114**(44) (2017) 11639 – 11644.
4. J. L. Barron, D. J. Fleet, S. S. Beauchemin, *Performance of optical flow techniques*, International Journal of Computer Vision, **12**(1) (1994) 43 – 77.
 5. Ce Liu, Antonio Torralba William T. Freeman Frédo Durand Edward H. Adelson, *Motion magnification*, ACM Transactions on Graphics, **24**(3) (2005) 519 – 526.
 6. J. Y. A. Wang, E. H. Adelson, *Representing moving images with layers*. IEEE Transactions on Image Processing, **3**(5) 1994.
 7. A. A. Efros, T. K. Leung, *Texture synthesis by non-parametric sampling*, Proceedings of the Seventh IEEE International Conference on Computer Vision. IEEE. 1999.
 8. W. Hao-Yu, M. Rubinstein, E. Shih, J. Guttag, F. Durand, W. Freeman, *Eulerian video magnification for revealing subtle changes in the world*, ACM Transactions on Graphics, **31**(4) (2012) 1 – 8.
 9. E. H. Adelson, C. H. Anderson, J. R. Bergen, P. J. Burt, J. M. Ogden, *Pyramid methods in image processing*. RCA Engineer, **29**(6) (1984) 33 – 41.
 10. J. G. Chen Neal, W. Young-Jin Cha, F. Durand, WT. F. O. Buyukozturk, *Modal identification of simple structures with high-speed video using motion magnification*, Journal of Sound and Vibration, **345**(9) (2015) 58 – 71.
 11. A. Karasaridis, E. P. Simoncelli, *A filter design technique for steerable pyramid image transforms*, IEEE International Conference on Acoustics. 1996.
 12. N. Wadhwa, M. Rubinstein, F. Durand, W. Freeman, *Phase-based Video Motion Processing*, ACM Trans. Graph, **32**(4) (2013).
 13. N. Wadhwa, M. Rubinstein, F. Durand, W. T. Freeman, *Riesz pyramids for fast phase-based video magnification*, IEEE International Conference on Computational Photography (ICCP) (2014).
 14. L. Sarode, N. N. Mandaogade, *Review on Video Motion Magnification*, International Journal of Advance Research in Computer Science and Management Studies, **2**(1) (2014) 480 – 484.
 15. K. Kamble, N. Jagtap, R. A. Patil, A. Bhurane, *A review: Eulerian video motion magnification*, International Journal of Innovative Research in Computer and Communication Engineering, **3**(3) (2015) 2384 – 2390.
 16. M. Elgharib, M. Hefeeda, F. Durand, W. T. Freeman, *Video magnification in presence of large motions*, The IEEE Conference on Computer Vision and Pattern Recognition (CVPR), (2015) 4119 – 4127.
 17. M. Verma, S. Raman, *Interest region based motion magnification*, Lecture Notes in Computer Science, **10484** (2017) 27 – 39.
 18. J. Kooij, J. C. van Gemert, *Depth-aware motion magnification*, European Conference on Computer Vision, (2016) 467 – 482.
 19. S. Takeda, Y. Akagi, K. Okami, M. Isogai, H. Kimata, *Video magnification in the wild using fractional anisotropy in temporal distribution*, The IEEE Conference on Computer Vision and Pattern Recognition (CVPR), (2019) 1614 – 1622.

Identification of Technical Condition of Valve Clearance Compensators Using Vibration Measurement and Machine Learning

Grzegorz M. SZYMAŃSKI
*Institute of Combustion Engines and Transport,
Poznan University of Technology,
grzegorz.m.szymanski@put.poznan.pl*

Maciej TABASZEWSKI
*Faculty of Mechanical Engineering and Management,
Institute of Applied Mechanics, Poznan University of Technology,
maciej.tabaszewski@put.poznan.pl*

Abstract

The dynamic development of internal combustion engine design and requirements for high reliability generates the need to apply a strategy of their operation based on the current technical condition. The paper concerns vibration diagnostics of automatic compensators of valve lash of a combustion engine. It presents the course of an active experiment conducted in order to develop a methodology for identifying the state of compensators based on measures of vibration signals measured at the engine head. Based on the results of the experiment, a classifier was developed in the form of a decision tree, which with high accuracy identified the technical condition of the compensators. The set of simple rules obtained thanks to the built up trees allows for easy implementation of the diagnostic system in practice.

Keywords: vibroacoustic diagnostics, combustion engine, machine learning

1. Introduction

One of the key problems affecting the correct operation of an internal combustion engine is the correct setting of control parameters. Incorrectly set control parameters may cause: deterioration of the effectiveness of the internal combustion engine, decrease in its mechanical efficiency, thermal efficiency and filling ratio, increase in toxic compounds emission in exhaust gases, increase in the probability of failure of internal combustion engine components. One of the most important control parameters is valve clearance (between valve stem and lever or other valve actuating element). The data presented in [1] show that increasing the valve lash may cause an increase in fuel consumption of the tested internal combustion engine by up to approx. 9%.

Automatic valve backlash compensation eliminates the need for periodic adjustment. This solution, however, has its drawbacks, because the introduction of additional masses into the engine timing system increases the inertia forces, and the additional device increases the probability of failure, because it is often connected in series in the kinematic chain of the camshaft system. The consequence of damage to the automatic valve lash compensator is an uncontrolled increase in valve lash resulting in the phenomena described above and which may lead to damage to other components of the internal combustion engine timing system, e.g. burning of valve faces or valve seats,

knocking out valve faces. Therefore, it is also necessary to evaluate the clearance (state of adjustment) of engines equipped with automatic valve clearance compensators.

One of the possible approaches to state classification in technical diagnostics is the use of machine learning methods. In order to apply such methods, it is necessary to have a large set of teaching examples covering all recognized state classes. This requirement is difficult to meet in the case of individual objects, but it should not be a problem in the case of internal combustion engines of a given type produced in large numbers. It is also important that taking into account the relatively repetitive cycle of engine operation, we are able to obtain a large number of examples in a relatively short time from one object. Usually in diagnostics it is particularly difficult to obtain examples related to a faulty condition, because in many cases it may be associated with the occurrence of an unacceptable failure. However, in case of identification of incorrect operation of a valve lash compensator it is possible to perform an active experiment, obtaining a large set of examples in a short time.

Classification methods are used in many different fields. One could mention here, for example, the analysis of texts, power engineering, medicine, image identification, transport, hydrology, agriculture, computer science, mechanical engineering, economics and many others [2-11].

The use of classifiers in the diagnosis of machines, equipment, processes or tools has been described in many publications - for example [12-25, 37]. Classification methods were also used in the diagnostics and modelling of processes in internal combustion engines [9, 26-28]. The classification process can be carried out using many methods [29-32]. One can mention here: neural networks, deep neural networks, classifiers based on different distance measures (dissimilarity), regression (e.g. logistic regression), set of induced rules, set of fuzzy rules, etc. One of the widely used methods are CART classification and regression trees developed by Breiman in 1984 [29, 31, 32].

Unquestionable advantages of trees are their simplicity of construction, easy interpretation of the acquired knowledge, which can be easily transformed into a set of classification rules, versatility, performance and the selection of important input features built into the tree construction algorithm that affect the correct prediction of the class [29, 32]. Thus, the tree allows you to identify those diagnostic symptoms that are relevant to the process of state classification. Of course, the trees also have their drawbacks, such as a large number of necessary teaching examples, sometimes unnecessarily complicated decision limits, which can lead to overtraining the classifier or high sensitivity to a small variance in the set of training data [32].

The effectiveness of the classification can be increased by using families of classifiers. It turns out that a large set of independent classifiers, each of which gives slightly better results than random classification, can work out correct decisions by majority voting [32]. Averaging the forecasts developed by many trees improves the stability of the classifier. Such methods as bagging and boosting apply here. The idea of creating a family of classifiers and voting can be applied to different methods, but they are particularly important for classification trees, giving, according to the literature, a significant improvement in results compared to a single tree. Boosting algorithms are among the best classification algorithms, which do not require any preliminary preparation of data [32]. An important method based on the family of classification trees

is the random forest method. Random forests combine poorly interdependent trees into a family. In this method, classifiers are built based on input vectors drawn with a replacement from the set of available examples (as in the bagging method). The size of the pseudo-sample drawn is the same as the size of the whole training set. Additionally, in each node a sampling of only some of the attributes of the input vector is made without replacement, and based on the drawn attributes, the quality measure of data division in the node is evaluated. In this way, a greater variety of trees is obtained, which leads to a lower variance of the model. The classification of data is based on the principle of majority voting on the basis of many independent trees constructed in this way [32].

2. Methodology of testing

The object of research concerning the assessment of the technical condition of automatic valve lash compensators was the a8C22 engine, which is used, among others, for propulsion of diesel locomotives, generator sets and as an auxiliary engine of vessels. The engine uses the classic timing system, the diagram of which is shown in Figure 1a. The test engine heads have four valves. The lever timing system of the test engine head is shown in Figure 1b. The adjustment of valve clearance in this engine is carried out in two stages: the first stage is the initial mechanical adjustment, the second stage is carried out by automatic (hydraulic) valve clearance compensators.

The research was carried out in two stages. In the first stage, impulse tests were conducted to determine the vibration acquisition points on the internal combustion engine head. In the second stage the vibrations of engine heads for various configurations of failures of automatic valve lash compensators were tested. The methodology was developed based on the assumptions of an active experiment [33, 34]. The input parameters were the changes in the states of automatic valve lash compensators of the internal combustion engine timing system. The controlled parameters were the internal combustion engine load and crankshaft speed. The output parameters were the accelerations of vibrations of the engine head.

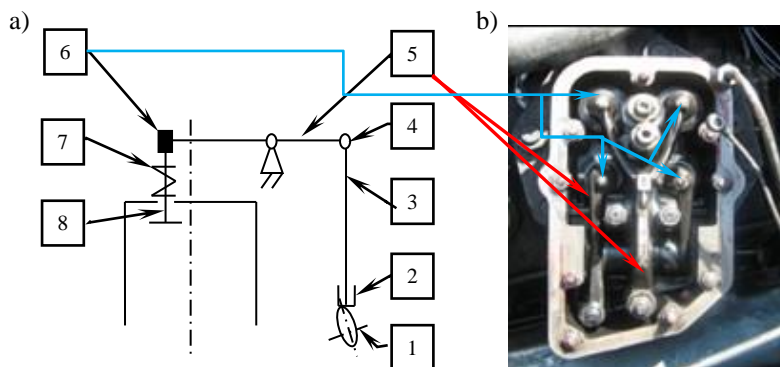


Figure 1. a) diagram of the timing system used in the engine; 1 – camshaft, 2 – tappet, 3 – push rod, 4 – screw valve lash adjustment mechanism, 5 – rocker arm, 6 – automatic valve backlash compensator, 7 – valve spring, 8 – valve; b) engine head timing system

Measurements were made in accordance with the principle of three starts, i.e. each series of measurements was made three times and between each series of measurements the engine was shut down. The method described above was used in order to avoid random values of parameters of vibration signal characteristics.

The general scheme of the measurement system used to record vibration signals during impulse tests is shown in Figure 2.

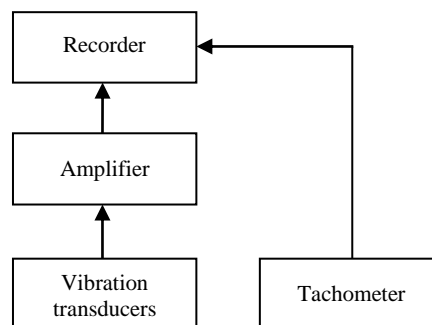


Figure 2. Diagram of the measuring system used for measuring engine head vibrations during operation [1]

Brüel&Kjær type 4504 vibration acceleration transducers have been selected based on the guidelines contained in [35], and the linear frequency response of the selected transducers was up to 18 kHz. During the tests, signals in the 0.1 Hz-25 kHz band were recorded. The vibration measurement directions were as follows: X direction parallel to the cylinder diameter and set at 45° to the crankshaft axis, Z direction parallel to the cylinder axis, and Y direction perpendicular to the other two. The sampling rate was set to 65536 Hz. To record vibration signals, a Brüel & Kjær PULSE multi-analyzer was used, which enables recording of fast alternating signals in parallel on 17 channels with dynamics up to 160 dB.

The vibration transducers were mounted on the combustion engine head with glue. When choosing the measurement locations, the principle was adopted that the transducer should be as close as possible to the place of vibration signal generation associated with the operation of the valves and in an accessible place [36]. The selection of the vibration measurement point was preceded by an analysis of the head design, research on the influence of diesel engine valve clearance on selected vibration parameters and impulse tests consisting in hitting valves on valve seats. The impacts were carried out by removing the gauge block placed between the valve stem and the lever. This was repeated several times for each valve to eliminate random errors and perform the averaging process. It was important to establish a vibration signal measurement point that would allow the impact of each valve to be assessed. Considering the dynamics of the signals recorded during the impulse tests, it was decided that the signals registered in the X, Y and Z directions will be taken into account for the testing of the correctness of the operation of the automatic valve clearance compensators.

Tests of the working engine were carried out at: crankshaft speed of 500 rpm, no external load (drive unit's own resistance), and coolant temperature maintained at 75°C.

Figures 3 and 4 show exemplary cut-out fragments of the time signal relating to the closing moments of the inlet and exhaust valves for the working and faulty condition of the compensator. The cut out fragments were obtained based on information about the position of the shaft identified by a marker.

The waveforms in Figures 3 and 4 show clear responses of the system to the stimulation by hitting the valve on the valve seat. In the case of the exhaust valve, another fading signal can also be seen, but in a slightly lower frequency range (see the time-frequency analysis in Figure 5). Since the origin of the individual fragments of the structure response associated with the exhaust valve closure was not identified, it was decided to consider the whole section together. At this stage it is also difficult to determine why the signals associated with each valve are significantly different when the compensator is operating correctly. Minor signal shifts in time for the sample waveforms in working and faulty conditions of the compensators result from unevenness in the motor speed. In the case of an inlet valve, the identification of a compensator malfunction is very simple based on the simplest estimates, while in the case of an exhaust valve it is not so obvious.

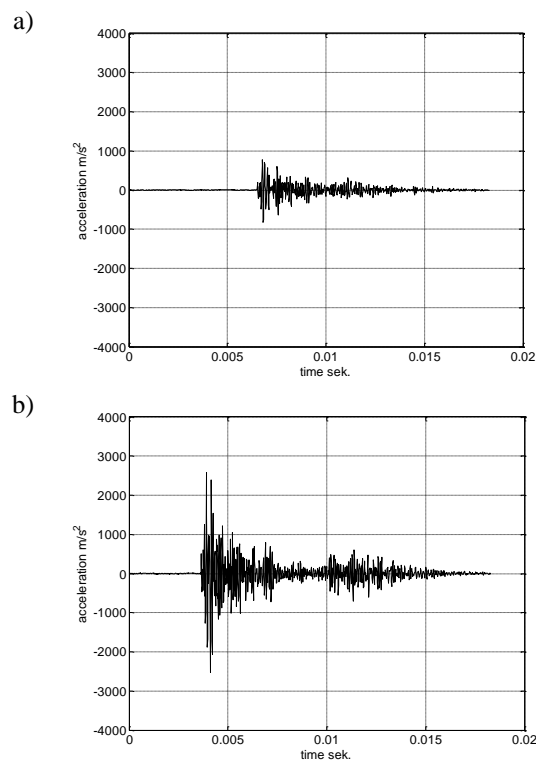


Figure 3. Cut-out sequences associated with inlet valve closing - measuring direction X;
a) correctly functioning compensator; b) incorrectly operating compensator

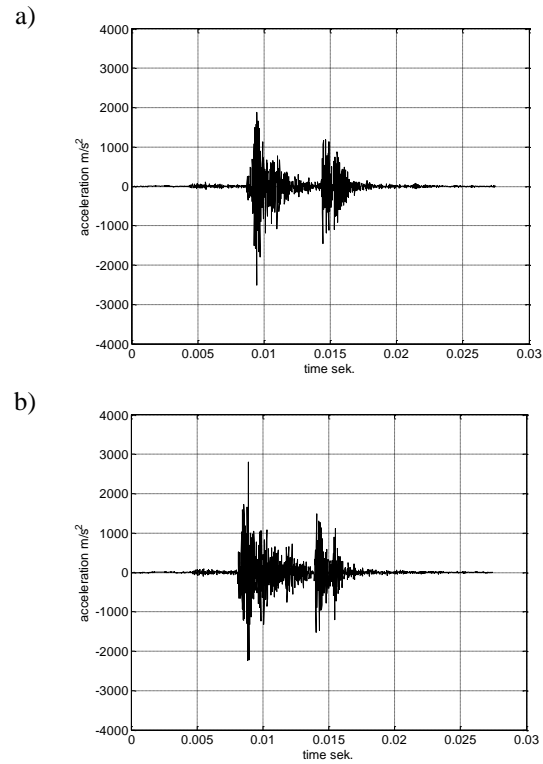


Figure 4. Cut-out sequences associated with exhaust valve closing - measuring direction X; a) correctly functioning compensator; b) incorrectly operating compensator

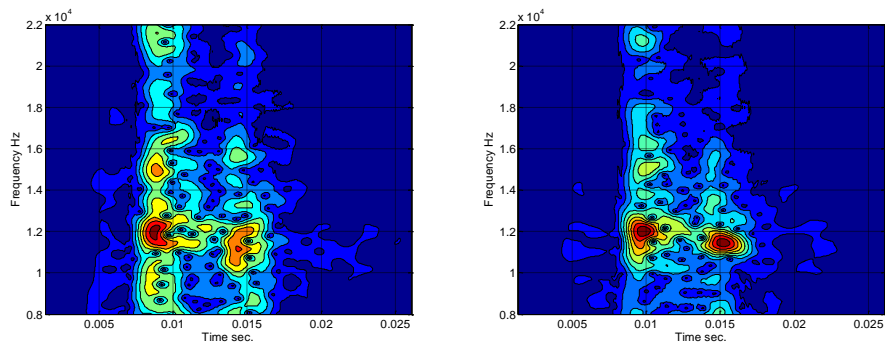


Figure 5. Short-Time Fourier Transform for the signals shown in Figure 4

Table 1 shows the rms values of vibration accelerations determined on the cut-out fragments of the signal for individual cases. As one can see, in the case of the inlet valve,

distinguishing the state of the compensator is very simple on the basis of even the rms value calculated in the whole band, and any possible mistake in determining the class is very unlikely. In the case of signals concerning the exhaust valve, the consideration of the rms value alone may not be sufficient to delimit the classes. An attempt can be made to laboriously obtain other measures that would give better distinguishability here. Another solution is to determine multiple measures and use a learning system based on examples, which itself will choose the right measures from the set of proposed ones.

Table 1. Rms values of vibration accelerations determined on the cut-out sections of the signal for individual cases

Data set	RMS [m/s ²]	Three times the standard deviation RMS [m/s ²]
Inlet valve – compensator in working order	98.8	18.6
Inlet valve – compensator out of order	266.1	80.4
Exhaust valve – compensator in working order	252.3	117.3
Exhaust valve – compensator out of order	355.2	75.9

3. Data analysis

Due to the lack of precise identification of phenomena and the difficulty in constructing an explicit model combining vibration signal estimates and the compensator state class, as well as due to the need to use several measures simultaneously to determine this state, an approach based on machine learning, specifically using classification trees, was applied. From the obtained recordings of acceleration waveforms, appropriate sections were cut out, obtaining examples of correct operation and compensator malfunction determining the inlet and exhaust valve operation. Table 2 summarizes the number of cases obtained.

Table 2. Summary of the number of cases obtained

Data set	Number of examples
Inlet valve – compensator in working order	489
Inlet valve – compensator out of order	374
Exhaust valve – compensator in working order	371
Exhaust valve – compensator out of order	492

In the first stage of construction of the classifier, the obtained waveforms were parameterized. On the basis of the analyzed signals the following parameters were determined in the band up to 32 kHz: coordinates of the center of gravity of the waveform, abscissa of the center of gravity of the signal square, rms value in the whole band, ordinary, central and central normalized moments of the first and second order, upper peak, lower peak, and interpeak value. In addition, the rms values of the signal were determined in 10 separate frequency bands (the width of each band was about

3.2 kHz). The division of the measurement band into 10 intervals was arbitrary. All the measures were determined for the three measuring directions X, Y, Z obtaining a total of 72 features. As an output two possible states were assumed: the compensator is in working order and technically inoperative. Further steps have been taken separately for signal fragments related to the inlet and exhaust valves. The CART (classification and regression tree) binary tree based in the assessment of the quality of the division on Gini index was used as the classifier. The next step was to optimize the parameter defining the minimum number of examples in a leaf. For this purpose, a cross validation test for $k = 10$ (10 fold cross validation on the training data) was used. The minimum number of observations in a leaf was being changed from 1 to 10. The classification error was averaged. Figure 6 shows the obtained dependence of the classification error on the minimum number of observations in the leaf for data related to the more difficult case - the classification of the condition of the exhaust valve.

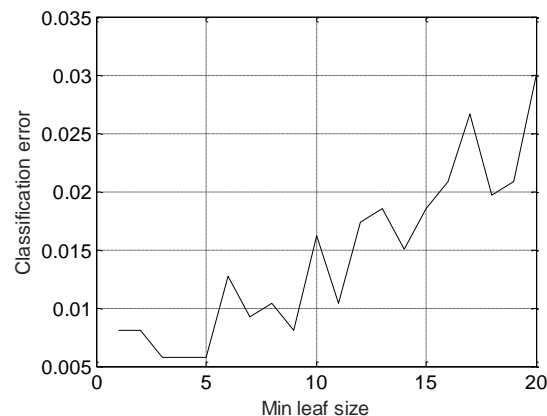


Figure 6. The dependence of the classification error on the minimum number of observations in the leaf for the data related to the classification of the exhaust valve

The optimal values of the hyperparameter in question turned out to be 1 (for signals concerning inlet valve closing, and 4 (or 5) for exhaust valve closing). The features of the input vectors present in trees were also identified. It turned out that in the case of the inlet valve, one feature was sufficient to unambiguously determine the state class - the abscissa of the center of gravity of the signal square calculated over the entire band and the X direction. The state distinction for inlet valve related signals is obvious and does not actually require a multi-feature approach. For signal sections related to the closing of the exhaust valve, two rms values calculated in the appropriate bands proved to be the dominant features. The rms value of the vibration acceleration signal measured in the X direction for the band from 6.4 to 9.6 kHz (i.e. in the band not coinciding with that with maximum amplitudes - see Figure 5) and the rms value of the vibration acceleration signal measured in the Z direction for the band from 3.2 to 6.4 kHz proved to be important.

Table 3 presents the average values of the classification error obtained by means of the aforementioned cross-validation test for individual signal sections, as well as for classifiers based on all features and on features limited to the best ones. It should be noted that during the construction process the algorithm selects the most important features due to the quality of data division in a given node. However, it may turn out that for some of the pseudo-samples drawn during the cross-validation test, these may be different features. Therefore, both cases of tree construction, based on all available features and limited to the most relevant ones, may give a different assessment of the classification error.

Table 3. Average values of the classification error for individual cases

Identification of the state	Average classification error [%] for all features	Average classification error [%] for the most important features
Compensator – inlet valve	0.0	0.0
Compensator – exhaust valve	0.9	0.8

As shown in Table 3, the identification of the compensator malfunction for the inlet valve is error-free and, as mentioned above, requires only one signal feature. For the exhaust valve, the error is less than 1% regardless of whether the best features or all available ones will be used to build the classifier. It turns out that the smaller testing error, i.e. related to the pseudo-sample not used at the moment for construction of the classifier, can be obtained taking into account only two features, from which the tree must be built.

4. Conclusions

The proposed methodology may be used to build a system for identification of valve lash compensators malfunctions. It should be noted that the classification of the state of the compensators based on the vibration acceleration signal and simple signal measures can be determined with negligible error and, in addition, based on a small number of measures. The built trees enable to generate simple diagnostic rules (one rule to determine the state of the inlet valve backlash compensator and a set of two rules for the second case), which in a very simple way allows the implementation of the solution in a simple system in terms of hardware construction. Even more accurate results with an exhaust valve compensator can be obtained by classifying several successive engine work cycles and, in case of contradictions, selecting the class that has been identified the most frequently. During motor operation, a very large number of repetitions of this state recognition can be achieved. The only difficulty in the construction of the system is the need to mount a marker determining the position of the shaft, but in modern engines such information is available in the engine ignition control systems.

Acknowledgments

The presented research has been subsidized by the Ministry of Science and Higher Education 02/21/SBAD/3558 and 05/52/SBAD/0295.

References

1. G. M. Szymański, F. Tomaszewski, *Diagnostics of automatic compensators of valve clearance in combustion engine with the use of vibration signal*, Mech. Syst. Signal Process., **68–69** (2016) 479 – 490, doi:10.1016/j.ymsp.2015.07.015.
2. L. Arras, F. Horn, G. Montavon, K.-R. Müller, W. Samek, *What is Relevant in a Text Document?*, PLoS One., **12** (2016) 1 – 19.
3. D. Dey, B. Chatterjee, S. Dalai, S. Munshi, S. Chakravorti, *A deep learning framework using convolution neural network for classification of impulse fault patterns in transformers with increased accuracy*, IEEE Trans. Dielectr. Electr. Insul., **24** (2017) 3894 – 3897, doi:10.1109/TDEI.2017.006793.
4. F. Fraggetta, G. Salvatore, G. F. Zannoni, L. Pantanowitz, E. D. Rossi, *Review of “Digital Pathology” Workflow: The catan*, J. Pathol. Inform., **8** (2017) 1 – 12, doi:10.4103/jpi.jpi.
5. F. Gao, T. Huang, J. Wang, J. Sun, A. Hussain, E. Yang, *Dual-Branch Deep Convolution Neural Network for Polarimetric SAR Image Classification*, Appl. Sci. **7** (2017) 447, doi:10.3390/app7050447.
6. C. Gorges, K. Öztürk, R. Liebich, *Impact detection using a machine learning approach and experimental road roughness classification*, Mech. Syst. Signal Process., **117** (2019) 738 – 756, doi:https://doi.org/10.1016/j.ymsp.2018.07.043.
7. Y. A. Pachepsky, W. J. Rawls, H. S. Lin, *Hydropedology and pedotransfer functions*, Geoderma, **131** (2006) 308 – 316, doi:10.1016/j.geoderma.2005.03.012.
8. J. H. Min, Y. C. Lee, *Bankruptcy prediction using support vector machine with optimal choice of kernel function parameters*, Expert Syst. Appl., **28** (2005) 603 – 614, doi:10.1016/j.eswa.2004.12.008.
9. P. K. Wong, J. Zhong, Z. Yang, C. M. Vong, *Sparse Bayesian extreme learning committee machine for engine simultaneous fault diagnosis*, Neurocomputing, **174** (2016) 331 – 343, doi:https://doi.org/10.1016/j.neucom.2015.02.097.
10. T. T. Nguyen, G. Armitage, *A survey of techniques for internet traffic classification using machine learning*, IEEE Commun. Surv. Tutorials, **10** (2008) 56 – 76, doi:10.1109/SURV.2008.080406.
11. J. Korbicz, J. M. Kościelny, Z. Kowalczyk, W. Cholewa, eds., *Models, Artificial Intelligence, Applications*, Springer-Verlag Berlin Heidelberg, 2004, doi:10.1007/978-3-642-18615-8.
12. D. Kateris, D. Moshou, X. E. Pantazi, I. Gravalos, N. Sawalhi, S. Loutridis, *A machine learning approach for the condition monitoring of rotating machinery*, J. Mech. Sci. Technol., **28** (2014) 61 – 71, doi:10.1007/s12206-013-1102-y.
13. A. Kothuru, S. P. Nooka, R. Liu, *Application of audible sound signals for tool wear monitoring using machine learning techniques in end milling*, Int. J. Adv. Manuf. Technol., **95** (2018) 3797 – 3808, doi:10.1007/s00170-017-1460-1.
14. M. R. R. Lahrache, A. Cocconcelli, *Anomaly detection in a cutting tool by k-means clustering and support vector machines*, **18** (2017) 21 – 29.

15. P. Potočník, E. Govekar, *Semi-supervised vibration-based classification and condition monitoring of compressors*, Mech. Syst. Signal Process, **93** (2017) 51 – 65, doi:<https://doi.org/10.1016/j.ymssp.2017.01.048>.
16. M. Ruiz, L. E. Mujica, S. Alférez, L. Acho, C. Tutivén, Y. Vidal, J. Rodellar, F. Pozo, *Wind turbine fault detection and classification by means of image texture analysis*, Mech. Syst. Signal Process., **107** (2018) 149 – 167, doi:<https://doi.org/10.1016/j.ymssp.2017.12.035>.
17. F. Jia, Y. Lei, N. Lu, S. Xing, *Deep normalized convolutional neural network for imbalanced fault classification of machinery and its understanding via visualization*, Mech. Syst. Signal Process., **110** (2018) 349 – 367, doi:<https://doi.org/10.1016/j.ymssp.2018.03.025>.
18. L. Ren, Y. Sun, H. Wang, L. Zhang, *Prediction of bearing remaining useful life with deep convolution neural network*, IEEE Access., **6** (2018) 13041 – 13049, doi: 10.1109/ACCESS.2018.2804930.
19. G. Robles, E. Parrado-Hernández, J. Ardila-Rey, J. M. Martínez-Tarifa, *Multiple partial discharge source discrimination with multiclass support vector machines*, Expert Syst. Appl., **55** (2016) 417 – 428, doi:10.1016/j.eswa.2016.02.014.
20. M. Tabaszewski, *Optimization of a nearest neighbors classifier for diagnosis of condition of rolling bearings*, Diagnostyka, **15** (2014).
21. V. T. Tran, H. Thom Pham, B. S. Yang, T. Tien Nguyen, *Machine performance degradation assessment and remaining useful life prediction using proportional hazard model and support vector machine*, Mech. Syst. Signal Process., **32** (2012) 320 – 330, doi:10.1016/j.ymssp.2012.02.015.
22. T. Van Tran, B. S. Yang, *Machine fault diagnosis and condition prognosis using classification and regression trees and neuro-fuzzy inference systems*, Control Cybern., **39** (2010) 25 – 54.
23. F. Q. Yuan, *Critical issues of applying machine learning to condition monitoring for failure diagnosis*, IEEE Int. Conf. Ind. Eng. Eng. Manag., 2016-Decem, (2016) 1903 – 1907, doi:10.1109/IEEM.2016.7798209.
24. J. Zhi-qiang, F. Hang-guang, L. Ling-jun, *Support Vector Machine for mechanical faults classification*, J. Zhejiang Univ. A., **6** (2005) 433 – 439, doi: 10.1631/jzus.2005.a0433.
25. C. Sobie, C. Freitas, M. Nicolai, *Simulation-driven machine learning: Bearing fault classification*, Mech. Syst. Signal Process., **99** (2018) 403 – 419, doi:<https://doi.org/10.1016/j.ymssp.2017.06.025>.
26. F. Feng, A. Si, H. Zhang, *Research on fault diagnosis of diesel engine based on bispectrum analysis and genetic neural network*, Procedia Eng., **15** (2011) 2454 – 2458, doi:10.1016/j.proeng.2011.08.461.
27. J. Liu, X. Li, X. Zhang, S. Xu, L. Dong, *Misfire diagnosis of diesel engine based on rough set and Neural Network*, Procedia Eng., **16** (2011) 224 – 229, doi:10.1016/j.proeng.2011.08.1076.

28. J. Porteiro, J. Collazo, D. Patiño, J. L. Míguez, *Diesel engine condition monitoring using a multi-net neural network system with nonintrusive sensors*, *Appl. Therm. Eng.*, **31** (2011) 4097 – 4105, doi:10.1016/j.applthermaleng.2011.08.020.
29. D. T. Larose, *Discovering Knowledge in Data*, An Introduction to DATA MINING, 2005.
30. D. T. Larose, *Data Mining Methods and Models*, John Wiley & Sons, Inc., New York, NY, USA, 2007.
31. O. Maimon, L. Rokach, eds., *Mining and Knowledge Discovery Handbook*, Springer New York Dordrecht Heidelberg London, 2010.
32. A. Géron, *Hands-On Machine Learning with Scikit-Learn and TensorFlow*, O'Reilly Media, 2017.
33. C. Cempel, *Modern issues of methodology and research philosophy*, Instytut Technologii Eksploatacji, Radom, 2003.
34. W. Matzke, *Four-stroke engine timing*, WKiŁ, Warszawa, 1967.
35. T. R. Serridge, M. Licht, *Piezoelectric accelerometers and vibration preamplifiers*, Brüel & Kjær, 1987.
36. S. Nizinski, R. Michalski, *Diagnostics of technical objects*, Library for Problems of Operation Polish Society for Technical Diagnostics, Department of Vehicle and Machine Operation, Faculty of Technical Sciences, University of Warmia and Mazury in Olsztyn, Institute for Sustainable Technologies in Radom, 2002.
37. A. Lahrache, M. Cocconcelli, R. Rubini. *Anomaly detection in a cutting tool by K-Means clustering and Support Vector Machines*, *Diagnostyka*, **18**(3) (2017) 21 – 29.

Application of the Wavelet Multifractal Analysis of Vibration Signal for Rotating Machinery Diagnosis

Andrzej PUCHALSKI

*University of Technology and Humanities in Radom,
ul. Malczewskiego 29, 26-600 Radom, andrzej.puchalski@uthrad.pl*

Iwona KOMORSKA

*University of Technology and Humanities in Radom,
ul. Malczewskiego 29, 26-600 Radom, iwona.komorska@uthrad.pl*

Abstract

The paper proposes the WLMF (Wavelet Leaders Multifractal Formalism) method enabling the adoption of multifractal parameters mapped by vibration signal log-cumulants as diagnostic features, in the procedure of automatic classification of assembly errors and wear of demonstration gearbox. In the analysis of vibration time signals, initially, a multifractal formalism was used based on the study of time series local regularity, which is measured by Holder exponents. The presented test results relate to time-frequency multifractal analysis, the starting point of which was a continuous wavelet transform. Discrete wavelet transform allowed for much better grounded multifractal formalism and more accurate estimation of multifractal parameters using wavelet leaders, which are determined based on wavelet coefficients and are representatives of Holder exponents.

Keywords: rotating machines, multifractal analysis of vibration signal

1. Introduction

In the era of industry digitization and its transformation to Industry 4.0 standards, making diagnostic decisions involves the analysis of large databases from earlier registers as well as data downloaded from machines in real time via the industrial internet of things. More and more often a better option than searching for specific models is a direct analysis and diagnostics based on experimental data. The process requires advanced methods of stochastic analysis and solutions from the field of machine learning. Models and diagnostic features stop being physically interpreted, giving way to the statistical indicators.

This way of modeling and quantitative analysis of the dynamics of complex systems, consisting of many non-linear interacting systems operating at variable loads, is a big challenge for modern diagnostics of rotating machines. The solution to the task becomes closer due to the study of monitored real vibration signals using advanced numerical algorithms and the increasing computing power of computers.

Multifractal analysis, which is mainly based on estimates of the scaling exponents of the recorded signal, has become a popular tool for statistical analysis of empirical data. The observed properties of time series scaling measures can be used to characterize various states of a complex system [1].

In the analysis of vibration time signals, initially, a multifractal formalism was used based on the study of their local regularity, which is measured by Holder exponents [2]. Trend elimination from the studied time series in the multifractal detrended fluctuation analysis (MF-DFA) leads to the determination of diagnostic features in the form of multifractal spectrum parameters. Detrended fluctuation analysis is an important tool in the study of variable-scale and long-term properties as well as the selection and classification of diagnostic features of vibration signals generated by complex rotating machinery [3-6]. The large computational complexity of the algorithm for the approximation of the time series of N samples, with a polynomial of the order m , is estimated at $2(m + 2)^2N$.

Time-frequency analysis of signals based on discrete wavelet transform allowed for much better grounded multifractal formalism and more accurate estimation of multifractal parameters using wavelet leaders, which are determined based on wavelet coefficients and are representatives of Holder's exponents [7]. The algorithm implemented by Mallat pyramid scheme shows a much lower computational complexity than the fluctuation analysis and is estimated to be $M\log N$.

Chapter 2 highlights the theoretical basis and algorithms diagram of time-frequency multifractal formalism. Chapter 3 discusses and verifies the WLMF (Wavelet Leaders Multifractal Formalism) method enabling the adoption of multifractal parameters mapped by vibration signal log-cumulants as diagnostic features, in the procedure of automatic classification of assembly errors and wear of demonstration gearbox. Chapter 4 provides a summary of the studies and the results obtained.

2. Theoretical background. Time-frequency multifractal formalism

Time-frequency signal analysis methods have allowed a new look at the problem of estimating local scaling exponents as a way of testing the regularity of time series and their multifractality. From both a conceptual and practical point of view, the wavelet transform played a special role [8].

The WTMM (Wavelet Transform Modulus Maxima) method is based on the continuous wavelet transform (CWT). It consists in determining wavelet skeleton defined by the set of all maxima lines, summation executed along q -th power of maxima chains and its scaling exponents and Legendre transforms. Practical implementations of such an algorithm have shown some disadvantages that make it impossible to carry out tests for some types of real signals. For wavelet coefficients centered around zero values, it is difficult to guarantee numerical stability. This problem does not appear in the case of the WLMF method, in which the base is the wavelet coefficients obtained as a result of the discrete wavelet transform (DWT) according to the Mallat pyramid scheme. The next steps of the algorithm include the selection of coefficients called wavelet leaders, the determination of the structural function and scaling exponents as well as the multifractal spectrum $D(h)$ or the direct determination of spectrum parameters using a log-cumulants (Figure 1).

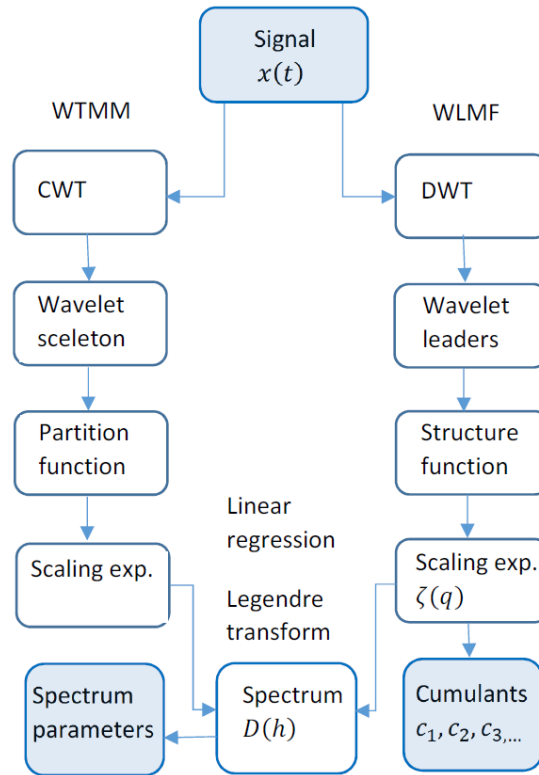


Figure 1. Block diagram of time-frequency multifractal analysis according to the WTMM and WLMF scheme

Wavelet leaders are local maxima of discrete wavelet coefficients $d_{\lambda'}$: $L_x(j, k) = \sup_{\lambda' \in 3\lambda} |d_{\lambda'}|$, where $3\lambda := 3\lambda_{j,k} = \lambda_{j,k-1} \cup \lambda_{j,k} \cup \lambda_{j,k+1}$ and $\lambda := \lambda_{j,k} = [k2^j, (k + 1)2^j]$ at any scale. Wavelet leaders are representatives of the Holder exponents h : $L_x(j, k) \sim 2^{jh}$. Structure-function $Z_L(q, j)$ is defined as a spatial average of the q -th order of the leaders. It can be shown that: $Z_L(q, j) \sim 2^{j\zeta(q)}$ in the limit $2^j \rightarrow 0$ [9]. Besides, the Legendre transform of the scaling exponent $\zeta(q)$ of the structure-function, provides an upper bound for the multifractal spectrum .

Knowledge of the scaling exponent $\zeta(q)$ also allows direct estimation of multifractal spectrum $D(h)$ parameters using a log-cumulants c_p of order $p \geq 1$, obtained as a result of Taylor series expansion.

Log-cumulant c_1 describes the location of the highest multifractal spectrum value, while c_2 and c_3 describe the level of multifractality: spectrum width and asymmetry, respectively. The scaling exponents of the structural function are not dependent on the choice of the wavelet, provided that the number of zero moments of the wavelet is two times greater than the largest exponent of the Holder exponent. The use of a discrete wavelet transform has also reduced the time costs of calculations.

3. Implementation of the diagnostic algorithm

Measurements were carried out on a demonstration stand (Figure 2). The influence of assembly errors and wear of gear teeth on vibrations was investigated. The electric motor allows speed control in the range of 100 - 3000 rpm (no load). The load is pressure regulated using an overflow valve up to 5 MPa. The acceleration of vibrations was measured utilizing an accelerometer screwed to the gear bearing housing in a vertical direction. The optimal backlash was set to 0.1 mm.

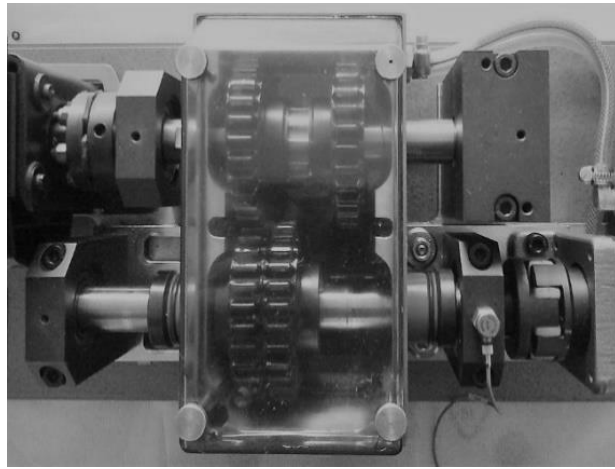


Figure 2. The test stand

Measurements were carried out for the following 5 states:

- fault-free (new gears, the optimal backlash, parallel shaft location),
- new gears and misalignment by an angle $1/3^\circ$,
- new gears and increased backlash +0.2 mm,
- worn teeth,
- worn teeth and increased backlash +0.2 mm.

Vibration acceleration signals were recorded for a rotational speed of 1365 rpm and a load of 12% - pressure 0.6 MPa (Figure 3). Each sample included a time series with a length of $N = 10.000$, recorded at a sampling frequency of 10 kHz.

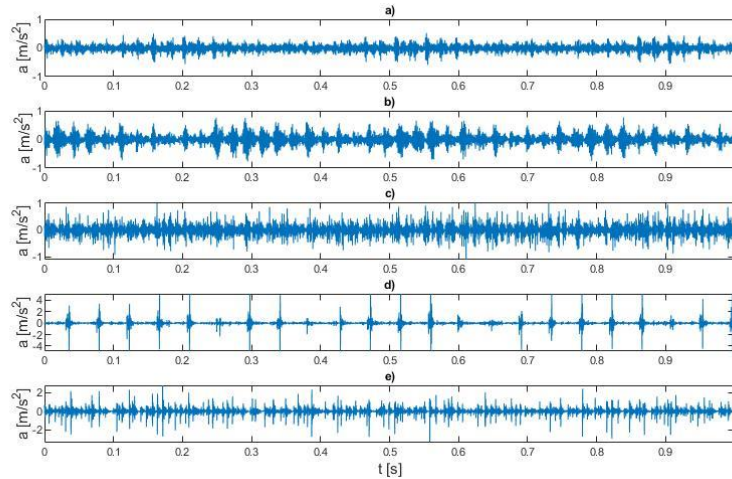


Figure 3. Waveforms of vibration signals recorded in 5 states of the gearbox:
 a) fault-free state, b) misalignment, c) increased backlash, d) worn teeth,
 e) worn teeth, and increased backlash

Figure 4 shows the maps of wavelet leaders designated for two states: fault-free and worn teeth. For the classification of the tested operating states of the propulsion system, mapped using multifractal spectra (Figure 5), log-cumulants of the 1st and 2nd order were selected, determined based on wavelet leaders of the vibration acceleration signal.

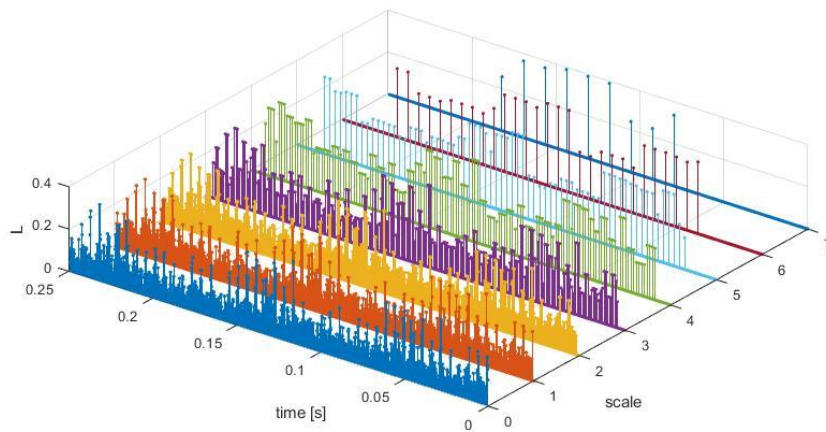


Figure 4a. Sample values of vibration signals wavelet leaders for gearbox in fault-free state

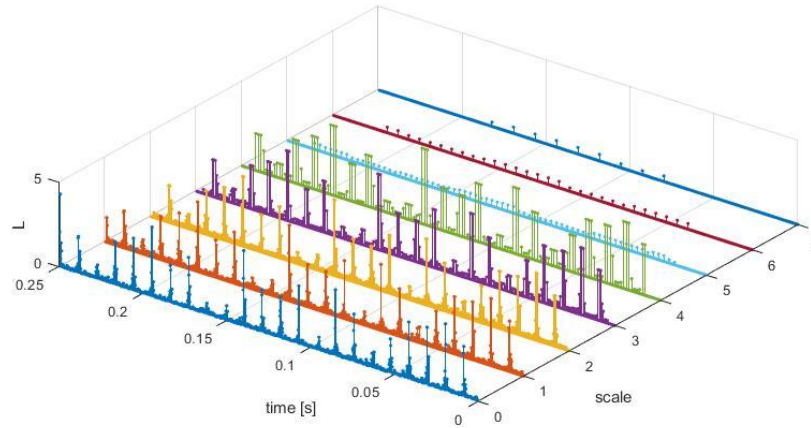


Figure 4b. Sample values of vibration signals wavelet leaders for gearbox in worn teeth

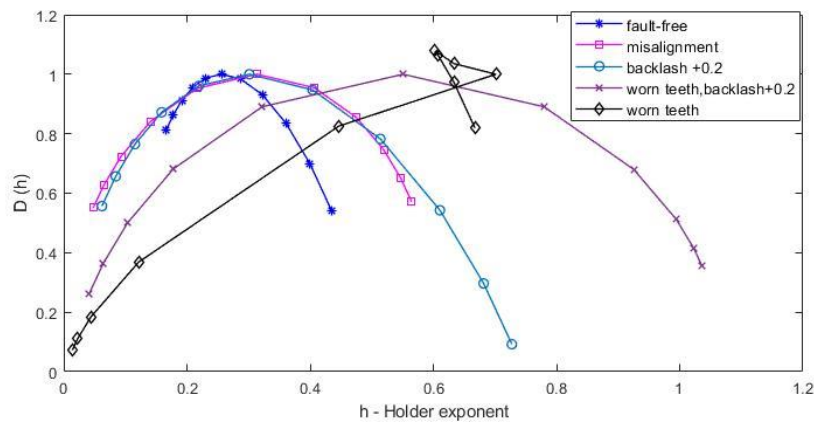


Figure 5. Multifractal spectra of vibration signals recorded in 5 states of the gearbox

A series of 30 measurements were taken in each state. Classification of the tested state of the system to the appropriate class and analysis of the quality of the classification was carried out using the method of the nearest neighbors. The cross-validation technique was used to estimate accuracy. Classification accuracy was assessed based on the ratio of the number of correctly classified results of the experiments to their total number. All tested states of the system were separated with 92% accuracy of classification. The classification errors referred to the states: fault-free, misalignment, and increased backlash.

For improving the classification efficiency, other signal measures were determined: RMS, skewness, kurtosis. The scattering analysis of the tested parameters showed that achieving 100% accuracy in the classification of the tested operating states of the transmission is enabled by a feature vector whose third coordinate, in addition to the two log-cumulants, is skewness (Figure 6).

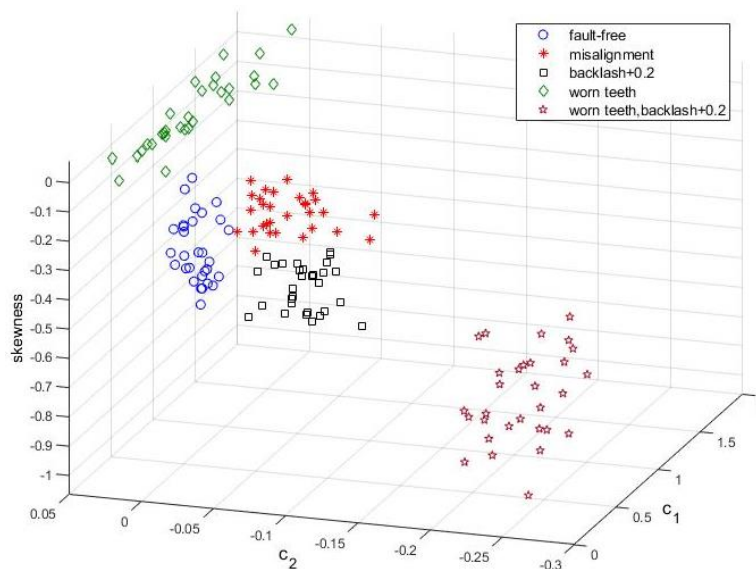


Figure 6. Scattering plot of selected diagnostic features: log-cumulants c_1 , c_2 , and skewness for 30 signal samples in each of the tested states

4. Conclusions

Most of the real vibration time series exhibit properties well described by local scaling exponents, which can act as diagnostic features. Multifractal formalism makes it possible to describe such signals that potentially contain an infinite number of singularities. There are several methods to study time series for their fractality. The possibilities of time and time-frequency algorithms were compared. Considering the greatest universality in real signal analysis and the lowest numerical complexity (time and requirements for memory resources) of the wavelet leader algorithm, its operation has been verified for use in vibration diagnostics of rotating systems. Multifractal parameters estimated using the log-cumulants were adopted as diagnostic features in the classification procedure by the method of nearest neighbors.

As part of the continuation of research, tests are carried out on multidimensional feature vectors of low-energy damage to rotating machines defined based on log-cumulants and the other values of scaling exponents of the structural function and multifractal spectra for a selected range of moments.

References

1. I. W. Kantelhardt, *Fractal and Multifractal Time Series*, Mathematics of Complexity and Dynamical Systems, Springer-Verlag, New York (2011) 463 – 487.
2. S. J. Loutridis, *An algorithm for the characterization of time-series based on local regularity*, Physica A, **381** (2007) 383 – 398.
3. S. Zhang, Y. He, J. Zhang, Y. Zhao, *Multi-fractal based fault diagnosis method of rotating machinery*, Applied Mechanics and Materials, **130**(2) (2012) 571 – 574.
4. A. Puchalski, I. Komorska, *A generalised entropy in multifractal time signals analysis of mechanical vibration*, JVE Journal of Vibroengineering, **20**(4) (2018) 1667 – 1675.
5. H. Liu, X. Wang, C. Lu, *Rolling bearing fault diagnosis based on LCD-TEO and multifractal detrended fluctuation analysis*, Mechanical Systems and Signal Processing, **60-61** (2015) 273 – 288.
6. A. Puchalski, I. Komorska, *Stable Distributions and Fractal Diagnostic Models of Vibration Signals of Rotating Systems*, Appl. Condition Monitoring (Springer Int. Pub. AG), **9** (2018) 91 – 101.
7. A. J. Chen, Z. Li, J. Pan, G. Chen, Y. Zi, J. Yuan, B. Chen, Z. He, *Wavelet transform based on inner product in fault diagnosis of rotating machinery*, Mechanical Systems and Signal Processing, **70-71** (2016) 1 – 35.
8. W. Du, J. Tao, Y. Li, C. Liu, *Wavelet leaders multifractal features based fault diagnosis of rotating mechanism*, Mechanical Systems and Signal Processing, **43** (2014) 57 – 75.
9. H. Wendt, S. G. Roux, S. Jaffard, P. Abry, *Wavelet leaders and bootstrap for multifractal analysis of images*, Signal Processing, **89**(6) (2009) 1100 – 1114.

Simulation Study of the Method of Random Kinematic Road Excitation's Reconstruction Based on Suspension Dynamic Responses with Signal Disruptions

Zbyszko KLOCKIEWICZ, Grzegorz ŚLASKI, Mikołaj SPADŁO
Poznan University of Technology,
zbyszko.j.klockiewicz@doctorate.put.poznan.pl, grzegorz.slaski@put.poznan.pl,
mikolaj.spadlo@put.poznan.pl

Abstract

The paper presents the results of simulation studies of the method of random kinematic road excitation's reconstruction based on the dynamic responses of the suspension acquired in road tests. The method uses registered unsprung mass accelerations as well as model of suspension's vertical dynamics and tracking control with PID controller to monitor unsprung mass accelerations' signal in simulation. In the simulation the quality of reconstruction of random irregularities of the road profile was tested. The road profiles were generated based on their power spectral density of road profile heights that is in line with the description given in ISO 8608 standard. Four road classes had their profiles estimations tested – A, B, C and D (corresponding to highways through city roads to the very bad quality roads). The influence of the simulated noise in the suspension's dynamic response signal – i.e. unsprung mass acceleration – was also tested. The methods of processing of the initial acceleration's signal from the road tests were proposed and achieved accuracy was defined. Lastly, the necessary requirements to use the method effectively were defined and its limitations were listed.

Keywords: suspension, kinematic excitation, dynamic responses

1. Introduction

There are two types of excitations that are encountered in vehicle's exploitation – the dynamic and kinematic ones, the latter of which is the focus of this paper. They appear due to the changing road profile irregularities' heights and their value depends on the velocity of the vehicle. Road profile and kinematic excitations are not the same tough – rather, kinematic excitations are derived from road profile, but modified through environmental factors and filtering properties of the pneumatic tyres. Acquisition or prediction of the kinematic excitation signal is hard, as it depends on variety of the mentioned factors. On one hand, researchers could measure road profile and try to calculate kinematic excitations using transfer functions, however this has limited use as the linear model assumption is necessary, and that cannot be always fulfilled. On the other hand, vehicle's responses can be measured and the kinematic excitations could be calculated from the dynamic responses of the suspension, such as the accelerations. That precisely is the approach of researchers in this paper. The problem encountered with this approach is that even the most similar to road excitations, easily measurable dynamic response, i.e. unsprung mass acceleration, cannot be used to calculate kinematic excitation by just a simple double integration. That is why the researchers proposed a method of estimating this excitation via the use of feedback-loop with PID controller,

which uses the registered unsprung mass acceleration's signal as a reference and applies a correction based on error which occurs, when the input to the simulation is the result of double integration of recorded unsprung mass acceleration. The specifics were described in author's other work [1]. The results from testing on the determined excitation signal that were meant to be replicated were promising, showing the maximum error of less than 8% of the amplitude for the 25 Hz sine wave and much less for lower frequencies (1% to 5.5% of the amplitude). Those results lead researchers to believe that the proposed method can be successfully implemented in the estimation of real road kinematic excitation of random character.

The authors' goal in the research described in this paper was to verify whether or not the proposed method is suited for replicating randomized signals that represent kinematic excitation on roads of various classes. Secondly, the authors want to analyse the influence of noise added to the signal on the accuracy of the kinematic excitation estimation.

2. Research method

The models used to test the estimation method were three-fold: the vehicle model, road model and noise model. The vehicle model was a simple linear quarter car model with 2 DOF and parameters typical for a C segment vehicle – Table 1. The input to the model are the kinematic excitations and the outputs are the dynamic responses used for later verification of the signals, i.e. suspension deflections and unsprung mass accelerations. The parameters used to describe the model were the sprung mass M , the unsprung mass m , tyre damping c_m and tyre stiffness k_m as well as suspension damping c_M and suspension stiffness k_M .

Table 1. Quarter car model parameters used in research

m [kg]	M [kg]	c_m [Ns/m]	k_m [N/m]	c_M [Ns/m]	k_M [N/m]
50	400	220	138200	2500	19300

The road model used in the research was generated so that it corresponds to the road classes described in the ISO 8608 standard [2]. The generation process was described for example in [3], [4]. The researchers chose the longest and the shortest irregularity wavelengths to be included in the profile to be 100 m and 0.1 m respectively. They generated road profiles for four different road classes, from A (new highways and airstrips), through B (standard quality asphalt roads) and C (damaged, aging pavements) to D class (unpaved and rural roads). The tire filtration was implemented by using a moving average that smoothed out the unrealistically sharp edges.

To simulate the noise present in real measurements, the researchers used the white noise generated with use of dedicated block from *Simulink* library. It generated noise signal of unsprung mass acceleration every 0.0003 s with the noise PSD equal of 10^{-5} [(m/s²)²/Hz]. That simulated noise was then added to the original acceleration signal (Figure 1) and the result was used for profile reconstruction after proper processing, which is described in chapter 4.

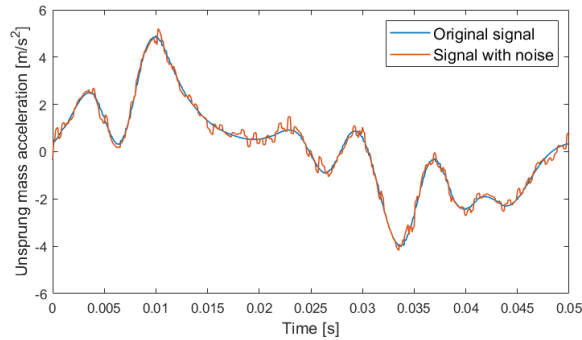


Figure 1. The effects of adding noise to the acceleration signal

Having created aforementioned models, the kinematic excitation reconstruction method was tested. The method uses (obtained in tests) unsprung mass acceleration \ddot{z}_{m_T} signal as an input for estimating kinematic excitations. That acceleration signal is integrated twice, resulting in obtaining wheel displacement signal z_m . This signal is different from kinematic excitation z_r , however it is fed to the quarter car model as an input and the output is unsprung mass acceleration from simulation \ddot{z}_{m_S} . The error is calculated as the difference between accelerations from test \ddot{z}_{m_T} and from simulation \ddot{z}_{m_S} . This error is then also double integrated and its value is added to the wheel displacement signal, creating an estimation of kinematic excitation. It must be noted, that this correction happens an iteration after the original error was calculated, this however can be dealt with by having small time steps – in the case of this research, the time step was set to 0.0001 s. This allows the correction to occur after only a miniscule change in acceleration, allowing for the reconstruction method to work [1].

The reconstruction process went as follows: firstly, road profiles of classes A to D were generated. After that, they were used as inputs to quarter car models and unsprung mass acceleration registered in these test was saved, to be used later as a reference, “test” acceleration \ddot{z}_{m_T} . Then, this acceleration signal is ran through the reconstruction algorithm described above. Finally, the original excitation signal is compared with the reconstructed one and conclusions are drawn. The modification that needed to be done when compared to reconstructing simpler, determined signals like sine waves of differing frequencies, was that in the case of randomized signals postprocessing in the form of detrending data was necessary.

3. Results

The kinematic excitation reconstruction method was first tested without added noise, on roads of classes from A to D. Acceleration signal on every road was acquired, while the simulated quarter car model was travelling at different speeds (Table 2).

Table 2. Velocities on different roads for “test” unsprung mass acceleration generation

	A class	B class	C class	D class
Speed [m/s]	40	30	20	5

All of the reconstructed signals displayed strong linear trends, that were eliminated in postprocessing by calculating that trend's equation and subtracting the resulting values from the signal. The results are presented in Figure 2 and Figure 3. The full, 30 s long series is not shown for the clarity of the image. The original and reconstructed signals can be observed to be virtually the same for all presented road classes. It should be noted though, that with worsening road class, the absolute differences between those two profiles are getting bigger and bigger. This however is mitigated by the fact, that the profile itself has much greater changes in value, so the relative error is in similar range of values for all road classes.

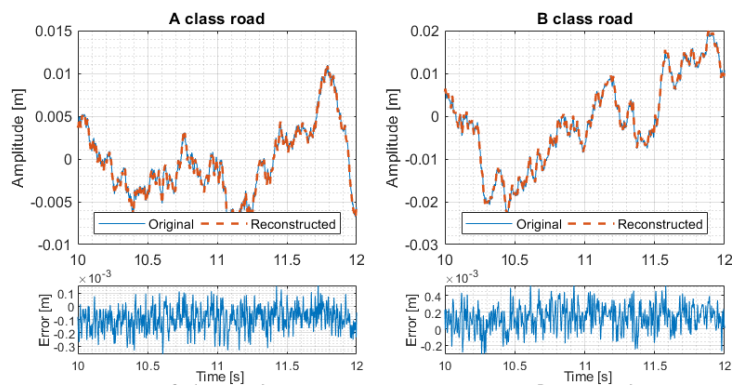


Figure 2. Comparison of reconstructed and original kinematic excitation signals – classes A and B

The other observation to be made, although it is not so clearly visible for such short plotted periods, is the occurring linear trend for all errors, causing the absolute value of error to grow with time. This growth however also does not decrease the accuracy of the reconstructed profile, as the difference caused by this linear trend is less than 1 cm at 150 m, which translates to 0.007% slope – a value which will not affect the simulation results in regard to vehicle's dynamic responses in any significant way.

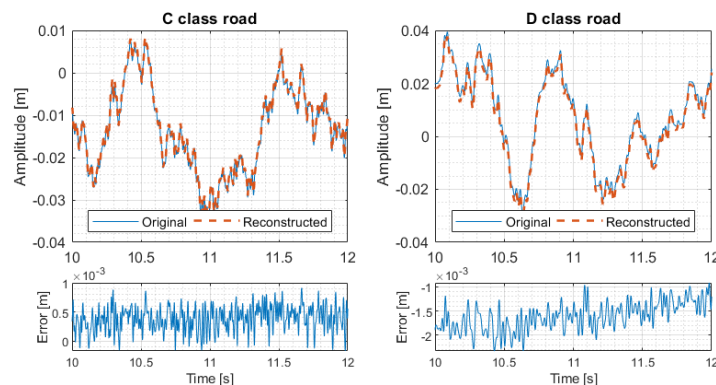


Figure 3. Comparison of reconstructed and original kinematic excitation signals – classes C and D

In order to compare the quality of results, besides comparing signals in the time domain, two indicators were calculated. First of these indicators was the goodness of fit in reference to standard deviation (fit for short from now on) and the second was International Roughness Index or IRI. Fit was chosen as it is a relative indicator, so it allows for direct comparisons between signals. Fit is calculated using the following formula

$$fit = 100 \cdot \frac{\|z_{r,R} - z_{r,O}\|}{N \cdot \sigma(z_{r,O})} \tag{1}$$

where $z_{r,O}$ is original kinematic excitation vector, $z_{r,R}$ is reconstructed kinematic excitation vector, $\sigma(z_{r,O})$ is standard deviation of the original kinematic excitation and N is the length of $z_{r,O}$ vector.

IRI was calculated, as it is an indicator often used to measure the smoothness of pavement, so the original and reconstructed signal should have its value as similar as possible. IRI is calculated by summing the total suspension deflection of a quarter car model with the parameters of a “Golden Car” [5]. The formula for calculating IRI ([6]) is

$$IRI = \frac{1}{L} \int_0^L \frac{1}{v} |\dot{z}_M - \dot{z}_m| dt \tag{2}$$

where L is the distance that vehicle travels, v is its speed, which is always 80 km/h, $\dot{z}_M - \dot{z}_m$ is the velocity of suspension deflection. The results for both fit and IRI calculations are gathered in Table 3.

Table 3 IRI and fit values for original (org.) and reconstructed (rec.) kinematic excitation signals. Values for fit are calculated with original signal as the reference

	A org.	A rec.	B org.	B rec.	C org.	C rec.	D org.	D rec.
IRI [m/km]	2.07	2.10	3.70	3.81	5.96	6.06	7.94	8.05
fit [%]	0.0059		0.0042		0.0079		0.0164	

The IRI values are very similar for all four road classes and they all belong to the same categories of roads, as described in [7]. All reconstructed profiles have slightly higher IRI values, which means that the ride on them can be expected to cause slightly bigger dynamic responses, this difference however is almost negligible when compared to the reference value. The biggest relative difference in IRI value is registered for the B class road and its value is 2.97%.

The fit is very good for all road classes, as the small value of that parameter means the reconstructed profile is closer to the original one. This time the lowest fit value, so the closest to original, is for the reconstructed profile from B class. The fact that it had the highest relative and absolute difference in IRI might be caused by greater amount of sharp changes of value, which make the reconstructed profile closer to the original, while at the same time causing greater suspension deflections, which is reflected in higher IRI value.

4. Method verification for noisy signals

Once the method has been established to be suited for reconstructing excitations from random road profiles, the researchers tested the method on signal with artificially added noise, what simulates real acceleration signal typically registered during road tests.

The goal was to simulate signals that are measured in real life and always exhibit some form of imperfections, often in the form of noise of high frequency. The way that noise was simulated is described in chapter 0. As was to be expected, reconstruction of kinematic excitation from such a signal caused large errors to occur.

That is why the researchers came to the conclusion that preliminary filtration of the noisy signal is necessary. The chosen method of filtration was using a low-pass filter with the stop frequency of 650 Hz. Such a high frequency ensured that only noise was filtered out, leaving all the important (from the dynamic responses' point of view) frequency components intact. The effects of this filtration are showcased in Figure 4.

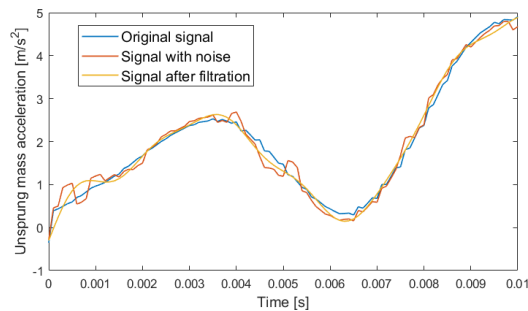


Figure 4. The effects of filtering noisy acceleration signal

After the preliminary filtration, the acceleration signal was ready to be used as an input to the reconstruction algorithm. The results needed to be further filtered, this time using the high-pass filter. The researchers found out that the most effective method of filtering those long wavelengths is by using long moving average (from 20000 closest samples) across the whole timeseries, and subtracting the moving average value from the reconstructed signal. The results of that process are shown in Figure 5.

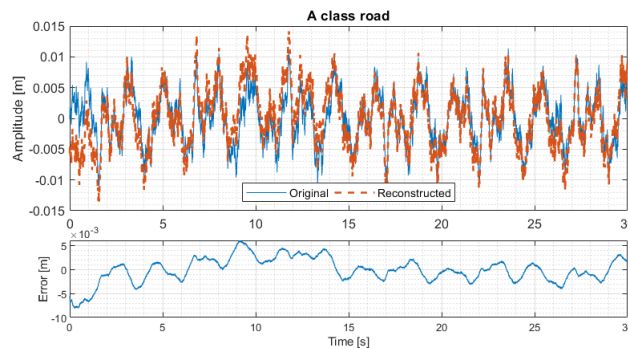


Figure 5. Reconstruction of kinematic excitation of class A from the noisy acceleration signal

The reconstructed signal differs significantly from the original one for the first second or so, this however is caused by the way the low-pass filter works and things quickly stabilize after that and the error value drop to much lower values, oscillating around 0 mm. There are points in which the estimated profiles exhibits quite a large difference in momentary value from the original one, those however mostly stem from the inability to completely filter out the long wavelengths, that still influence the reconstruction, but do not affect significantly the model's responses.

Table 4. IRI and fit values for original and reconstructed kinematic excitation signals from noisy data. Values for fit are calculated with original signal as the reference

	A org.	A rec.	B org.	B rec.	C org.	C rec.	D org.	D rec.
IRI [m/km]	2.07	2.17	3.70	3.86	5.96	6.02	7.94	8.04
fit [%]	0.1108		0.0875		0.1062		0.1368	

In terms of the indicators of similarity between signals, fit and IRI values were calculated once again. The IRI value for the original A class road's kinematic excitation was 2.07 m/km, while the value for reconstruction was 2.17 m/km. It is a much bigger difference than in the case of signal without any noise added (0.1 compared to 0.03 difference), it still however is a satisfactory result, which puts the reconstructed profile in the same category of roads as the original one. As the quality of the road decreases, the difference in IRI becomes smaller and smaller, with classes C and D having even slightly more similar IRI values than before. The fit value for the two profiles is also worse than for the reconstructed signal without noise – it is 0.111%, which is much bigger compared to 0.0059% for A class road and similar decrease in similarity is noticeable for all road classes. Considering how much worse the reconstruction from noisy signal was, it is still a satisfactory result for the researchers.

5. Conclusions

The proposed method of kinematic excitation reconstruction was tested on the random kinematic excitation signals generated according to the contents of ISO 8608 standard. The authors implemented models for the roads of different classes (A to D), as well as linear quarter car model and noise model. In the first part of the research, the authors focused on testing how well the method is able to reconstruct excitations close to those encountered in real life. The results, after postprocessing involving detrending the reconstructed signal, are very good and they closely resemble original kinematic excitations.

To check their similarity the researchers used two indicators – the fit and IRI. The IRI values for all four road classes differed by no more than 0.11 m/km and reconstructed profiles fit in the same road categories established by Sayers and Karamihas [7]. The fit values were also very small, which means the signals were similar, with bigger fit values for worse quality roads that had their kinematic excitations reconstructed.

Having established that the method was well suited for the reconstruction of random profiles, the researchers added noise to acceleration signals, that constituted an input to the reconstruction algorithm to test its influence on the results. They came to

the conclusion that in order to get satisfactory results, signal preparation and postprocessing of results was needed. Preparation involves using low-pass filter on the noisy signal, while postprocessing is done by using high-pass filter in the form of subtracting moving average of the profile. Those practices allow for satisfactory reconstruction of kinematic excitation, that for the A class road kinematic excitation resulted in IRI difference of 0.11 m/km and fit of 0.111% of standard deviation.

In the future research the authors plan to examine, how accurate the proposed method is when using real-life measurements. Non-linear or more complicated vehicle models will also be tested to determine if the proposed method yields similarly good results for those cases.

References

1. Z. Klockiewicz, G. Ślaski, *The method of estimating kinematic road excitation with use of real suspension responses and model*.
2. ISO, *INTERNATIONAL STANDARD ISO profiles — Reporting of measured data*, vol. 8608, 1997.
3. P. Můčka, *Road waviness and the dynamic tyre force*, *Int. J. Veh. Des.*, **36**(2/3) (2005) p. 216.
4. P. Můčka, *Current approaches to quantify the longitudinal road roughness*, *Int. J. Pavement Eng.*, **17**(8) (2016) 659 – 679.
5. M. W. Sayers, T. D. Gillespie, W. D. O. Paterson, *Guidelines for Conducting and Calibrating Road Roughness Measurements*, **46** (1986).
6. P. Můčka, *International Roughness Index specifications around the world*, *Road Mater. Pavement Des.*, **18**(4) (2017) 929 – 965.
7. M. Sayers, S. Karamihas, *The little book of profiling Basic Information about Measuring and Interpreting Road Profiles*, Univ. Michigan, September, (1998) p. 100.

Elements of the Statistical System for Vibration Tests of Machine

Bogdan ŻÓŁTOWSKI
UTH Warszawa,
bogdan.zoltowski@uth.edu.pl

Abstract

Presented considerations of this work includes selected issues in the area of statistical procedures use in vibration measures study and modal analysis methods to assess the machines state. The indicated statistical procedures are particularly important in vibration and modal research, where the multidimensionality of diagnostic signals requires a wide application of various statistical procedures at the stage of processing and decision-making. This paper presents the MATLAB program for determination of the Symptoms matrix, software tools for reading and exporting files to the unv format, the OPTIMUM computer algorithm, the Singular Values Decomposition (SVD) computer algorithm and the state matrix analysis program using the MAC theory.

Keywords: statistical methods, exploitation, diagnostics, redundancy, product life cycle

1. Introduction

The achievements presented in this work are a result from the implementation of many studies related to the description and statistical verification of the vibrational energy distribution usefulness in the state degradation assessment. Both the developed field of vibration diagnostics and applied modal analysis methods are based on the vibration process and use in the research as basic - different vibration estimators. The physical aspects of the vibration process are described in terms of time, frequency and amplitudes, giving in practice a large number of measures (often in excess) of the energy distribution containing a lot of information about the processes studied (objects). This forces the need for widespread use of statistical methods when developing research results for making rational decisions.

Diagnostic experiments should enable quantitative assessment and in-depth analysis of destructive processes occurring in constructions and machines, mainly at the stage of use and maintenance. An in-depth analysis of the results of the experiment, which is the basis for the operational decisions to be taken, should each time contain answers to users' questions [5, 8]:

- how to successfully recognize the technical condition of a structure, in general?
- how long and under what load can the system operate for the next technical support?
- how to change or shape the system load for maintaining task ability?
- what are the most advantageous ways and means of renewing the system?
- how to protect the system against the destructive effects of external factors?

Only a comprehensive application of diagnostics and effective diagnostic procedures for the state, distinguished in dedicated diagnostic experiments, guarantee the reliable operation of technical systems in the adopted structures of exploitation [1, 9].

Modern technical diagnostics very widely uses the possibilities offered by such a universal tool as virtual engineering. For a more effective use of these possibilities, there is a need to constantly search for new, more effective tools supporting the diagnostic process, as well as modeling phenomena whose characteristic parameters allow monitoring the increasing number of available symptoms [10].

The technical systems state analysis is compound for a set of mathematical procedures that they can be related to each other to develop analysis of superior order and to find relationships between procedures and states in different systems. There are many relationships that can be possible with the procedures, in this work is proposed only a few relations, it is possible to formulate other relations of procedures to do another kind of methodologies or analysis.

Authors of many studies assessing the correctness of diagnostic procedures most often use single-criterion indicators, which do not consider in detail the impact of operating conditions of technical means (the changing model of destruction) on the quality of formulated decisions (diagnoses and forecasts) [2, 3]. This is due to fact that the status recognition procedures are very sensitive to the complexity of the system structure and the randomly variable wear process. There is, therefore, a need to conduct sensitivity tests of these procedures depending on factors characteristic of the actual conditions of existence in service [6, 7].

In modern technical systems, considering technological advances as well as developed and available possibilities for signal acquisition and processing, it is possible to obtain a large amount of information from signals registered in various system states. This information must be processed and interpreted by the available procedures for the statistical processing of results, which is often used by technical staff to determine the status [4, 8]. Recognition of the degradation status of a complex system is based on a multidimensional analysis, for which it is possible to assess the relations between variables whose values have changed as a result of the developing damage [2, 11].

More and more often, dynamic state identification tests used to assess changes in the state of degradation, damage development and location of causes of the condition were the basis for the development of a specialized statistical software system. It enables acquisition and processing of measurement data, creation of many measures of diagnostic signals, testing their diagnostic sensitivity, statistical analysis of results and diagnostic inference [2, 9].

The subject of this work includes selected fragments of important research issues in the following areas:

- statistical procedures in the measurement of vibration energy flow measurements (acquisition, ordering, redundancy, modeling and presentation of results from tests and measurements);
- estimators of vibration diagnostics in studies of degradation of the condition of structures and construction machines (identification of needs and formulating requirements for measures, processes, products and constructions);

- rules for the use of modal analysis methods in the examination of structures and construction machines (rules and procedures for practical applications);
- maintaining the fitness of structures and technical facilities (shaping technical readiness and safety in the operation of facilities, introduction of new technologies and technical solutions, design, construction and rational use).

Studies of energy distribution measures (in vibration diagnostics and modal analysis methods) are used in many fields as a result of displacement, velocity or deformation measurements. Indirectly they serve to quantify the characteristics of material properties, e.g. functional properties, the state of destruction of the structure or the load-bearing capacity of old buildings in the field of cultural heritage. They can also be used in structural quality tests to detect damage affecting the fatigue properties of a structure. Vibration assessments of engineering structures degradation also enable assessment of the degradation status of materials, elements and structures, assessment, or delamination of composite panels used in industry.

Measurements of energy distribution used in the studies use various estimators of vibration diagnostics and modal analysis, the usefulness of which in indicated areas should be assessed by dedicated and specialized statistical procedures.

2. Statistical research space

All studied mass phenomena are characterized by certain regularities, which are difficult to study and not all are detected and investigated. Statistical assessments used for this characterize the quantitative side of the studied phenomena in an inseparable connection with their qualitative side. It should be remembered that in nature there are no numbers used by statistics, but only things and processes [2, 11].

Statistical methods using a numerical description make it possible to make the necessary generalizations of a large amount of detailed information. By using generalized statistical methods to make the necessary generalizations in the statistical description, order is introduced in the apparent chaos of random events. This allows detection of regularity in the form of cause and effect relationships occurring in the studied phenomena [2, 11].

The massiveness of the data requires the use of computer-aided research in the field of methods and means of modeling, acquisition, processing, inference, visualization, dissemination and storage of information. The current development of science requires from engineers the use of modern computer applications, thanks to which it becomes possible to make complex calculations and to analyze the obtained results in a short time [5].

In general, the proposed methodology for studying the consumption state includes detailed procedures for the development of a data acquisition system and their processing and statistical inference - repetitive in many different issues of testing many measures of signals.

The control tools of the considerations are the proposed statistical procedures that make up the measurement system of vibration energy propagation (acquisition, ordering, redundancy, modeling and presentation of results from tests and measurements) [1, 3, 6].

The obtained research data (uncertain, incomplete, random) are subjected to analysis and assessment of regularity in the field of mass phenomena. For the purpose of highlighting the main components of the observation matrix, the obtained results are combined into control charts, which are subjected to painstaking research in the scope of:

- a) data presentation:
 - statistical series: detailed, distributive, temporary;
 - statistical plots: linear, bar, point;
 - statistical tables: working - raw statistical material subjected to further processing.
- b) use statistical tools to describe the structure of the community:
 - arithmetic mean - average value,
 - geometric mean - used to examine relative changes a given feature,
 - dominant - the value of which is the most probable,
 - range - difference between the maximum value and the minimum value of a given feature,
 - standard deviation - of the value of a given feature from its arithmetic mean,
 - variance - the arithmetic means of the square deviations the feature from its arithmetic mean,
 - coefficient of variation - determines the degree of diversification of a given feature in the whole population,
 - asymmetry coefficient - determines the direction and strength of asymmetry,
 - concentration factor (kurtosis).

These analyzes determine the initial and justified selection of qualitative measures, further processed to highlight the components to the main model. Statistical analysis of the acquired data is also the basis for many interesting description and trends of the events studied. Basic statistical surveys use many methods for qualitative and quantitative analysis of the data obtained. These include analysis of variance, correlation analysis, regression analysis, factor analysis, discriminant analysis, time series analysis, canonical analysis, others, generally available in various informational statistical procedures [11].

The MATLAB program is used for basic engineering applications used in the analysis of results. This program is used for computer calculations, combining data logging and processing, specialized calculations, visualization and an easy-to-use programming environment [1, 7]. The program contains the following applications:

- mathematical algorithms and their calculation,
- the creating own calculation algorithms,
- modeling and simulation algorithms,
- data analysis and visualization,
- engineering graphics applications,
- application for creating own programs, creating their interface and graphical data analysis.

Depending on the application, the program includes specialized packages of calculation procedures from any areas of knowledge called toolboxes, for example: SIMULINK, Signal Processing Toolbox, STATGRAF, STATISTICA and others. Such packages make it possible to obtain basic knowledge a given scope and apply this knowledge to solve problems [2, 10]. Statistical procedures in studies of vibration energy propagation measures supports the conducted experiments and have been verified in many publications describing vibration tests, modal analyzes and ex-test systems.

To accomplish the objectives of the above tasks, an engineering application was developed: State Examination Procedures (PBS) - enabling the generation of dedicated sets of variables of independent symptoms of the degradation status of the tested structures and machines.

3. Main elements of the developed PBS system

Identification tests of structures and machines used to assess changes in the condition, damage development and location of causes of the existing condition constitute the basis for creating a specialized software system for statistical procedures. Modules of the developed system enable acquisition and processing of measurement data, creation of many signal measures, testing their sensitivity, statistical elaboration and inference.

The program modules correspond to the subsequent stages of the statistical survey of technical objects [2-4].

The processing of vibration processes to obtain the values of the vibration signal (estimators) allows you to generate own and mutual measures of the vibration signal that are used in various applications.

3.1. The ideal point method - OPTIMUM

Measured signals represent the space of observation, and indirectly the development of damages in the structure or construction machine. Using optimization, you can characterize the sensitivity of measured symptoms to state changes based on distance measurements from the ideal point [9, 10]. The algorithm presented below enables statistical evaluation of individually elaborated symptoms, resulting in the final qualitative ranking list of their sensitivity and usefulness. The next steps of this procedure and its result are shown in Fig. 1.

Having statistically significant good symptoms, it is possible to build cause and effect models on the state conclusion stage. However, the quality of the model depends on the number of measures taken, which can be indirectly estimated in the simplest regression models with the R^2 coefficient [2, 9].

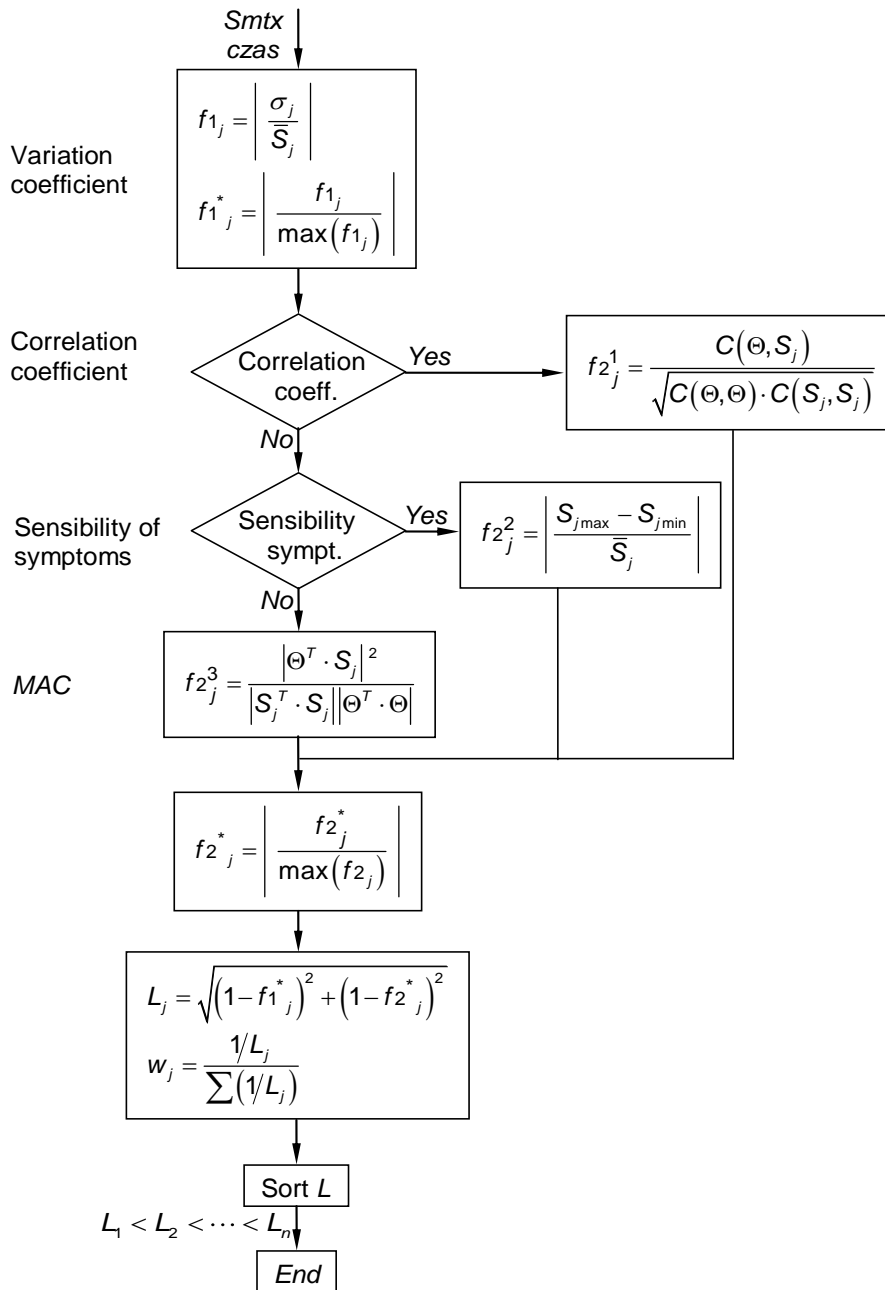


Figure 1. OPTIMUM procedure algorithm and an example of its result [2, 11]

3.2. Multidimensional system observation - SVD

SVD (Singular Value Decomposition) is a numerical procedure for multivariate tracking of changes in an object's degradation state.

The procedure uses all measured signals to assess changes in the state of the technical system under study, without losing any information possible to obtain. The algorithm of the method and an exemplary result of the applied procedure are presented in Fig. 2.

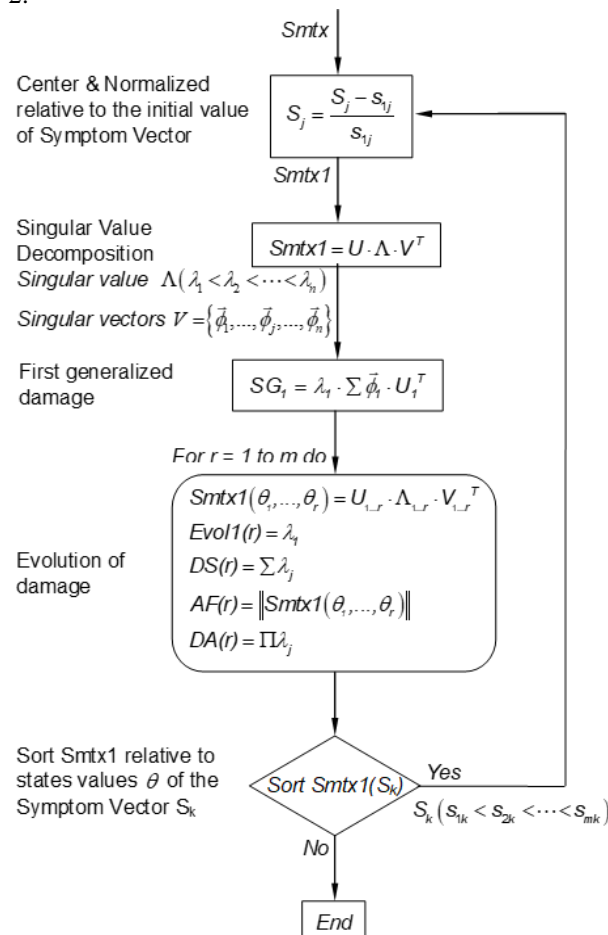


Figure 2. The algorithm of the SVD procedure and an exemplary result of its operation [2, 10]

The SVD procedure in the newer software implementations is modular (base) and allows further development of the algorithm, automatically searching for unnecessary measurement symptoms for a given research topic.

3.3. Information system for degradation studies

The degradation status identification tests of various technical facilities are increasingly the basis for the creation of a specialized software system. This program includes software for the needs of vibration acquisition, processing, statistical inference and visualization. It enables the acquisition and processing of measurement data, the creation of many measures of diagnostic signals, their testing of sensitivity, statistical elaboration and diagnostic inference.

The presented procedures of statistical surveys are the sum of experience from theoretical and experimental research of the field of vibration and modal testing, supported by statistical procedures [1, 2, 9].

The program structure is a modular structure composed of the following modules:

- A. Read unv module that allows processing from UNV format to XLS format.
- B. Symptoms module that allows defining, determining and creating a matrix of many measures of vibration processes.

Modules **A** and **B** form part of the software responsible for acquiring and processing vibration processes in order to obtain a matrix of observations of vibration estimates.

- C. The Optimum module uses the ideal point method for individual assessment of the qualitative sensitivity of the measured symptoms of vibration processes.
- D. SVD module (multidimensional description of the state of the tested object) used to quantify the generalized damage measures and to assess the damage development.
- E. Input / Output module used to analyze the similarity of vibration processes and to determine various operational measures of the tested object.
- F. Optimization module used to develop models and data in genesis (methods of approximation and interpolation), diagnosing and forecasting states.
- G. Network module using neural networks to classify states based on the obtained results in the form of time series.
- H. The MAC module is a procedure allowing the comparison of different vectors treated as a measure on the entry and exit of a system.

Modules **C**, **D**, **E**, **F**, **G** are elements of statistical inference and evaluation of cause-and-effect relations, and also serve to visualize the results obtained.

The exemplification of the developed solutions was carried out in the operational tests of selected objects (railway transport system, construction elements and constructions, internal combustion engines, gears, bearings) in which verification of modeling procedures and degradation status was carried out the basis of actual signal measurements.

4. Summary

More and more frequently conducted technical systems identification tests, also used to assess changes in this condition, damage development and location of the existing condition, constitute the basis for the creation of a specialized statistical survey system.

It enables the acquisition and processing of measurement data, the creation of many measures of diagnostic signals, their testing of diagnostic sensitivity, statistical elaboration and diagnostic inference.

The content of this study is the sum of experience from theoretical and experimental research in the field of vibration and modal research of various objects, supported by statistical procedures.

The implementation of the above assumptions required the use of the most modern specialized measuring equipment and programs enabling the execution of defined tasks at the required level, characterized by optimal technological, price and quality efficiency.

The proposed procedures have been verified in many studies (compact studies and publications), indicating their original capabilities useful in many applications [2, 4, 10, 11].

References

1. L. F. Castaneda, *Multicriterial system for evaluating the safety and comfort in railway vehicles*, Ph. D. thesis, UTP, Bydgoszcz 2007.
2. C. Cempel, *Evolutionary Symptom Models in Machine Diagnostics* (in Polish), Materials of the I Congress of Technical Diagnostics, Gdańsk 1996.
3. D. J. Ewins, *Modal Testing: Theory, Practice and Application*, Hertfordshire: Research Studies Press, 2000.
4. D. J. Inman, C. J. Farrar, V. Lopes, S. Valder, *Damage prognosis for aerospace, civil and mechanical systems*, John Wiley & Sons, Ltd, New York 2005.
5. J. Korbicz, J. M. Kościelny, Z. Kowalczyk, W. Cholewa, *Diagnostics of Processes* (in Polish), WNT (Scientific Technical Publishers), Warszawa 2002.
6. B. Peeters, C. Ventura, *Comparative study of modal analysis techniques for bridge dynamic characteristics*, Mechanical Systems and Signal Processing, 2011.
7. W. J. Staszewski, C. Boller, G. R. Tomlinson, *Health Monitoring of Aerospace Structures*, John Wiley & Sons, Ltd. Munich, Germany 2004.
8. T. Uhl, *Computer-aided identification of mechanical structure models* (in Polish), WNT (Scientific Technical Publishers), Warszawa 1997.
9. B. Żółtowski, M. Żółtowski, *Vibration signals in mechanical engineering and construction*, ISBN 978-83-7789-350-0, ITE-PIB, Radom, 2015.
10. B. Zoltowski, M. Zoltowski, *Vibrations in the Assessment of Construction State*, DYN-WIND, Applied Mechanics and Materials, **617** (2014) 136 – 141, Donovaly, SLOVAKIA.
11. B. Żółtowski, C. Cempel, *Engineering of diagnostics machines*, PTDT, ITE – PIB, Radom, ISBN 83-7204-414-7, 2004.

Designing of Quasi One-Dimensional Acoustic Filters Using Genetic Algorithm

Sebastian GARUS

*Institute of Mechanics and Fundamentals of Machinery Design,
Czestochowa University of Technology, ul. Dąbrowskiego 73,
42-201 Czestochowa, Poland, gari.sg@gmail.com*

Wojciech SOCHACKI

*Institute of Mechanics and Fundamentals of Machinery Design,
Czestochowa University of Technology, ul. Dąbrowskiego 73,
42-201 Czestochowa, Poland, w.sochacki@imipkm.pcz.pl*

Abstract

In phononic quasi one-dimensional structures, there is a phenomenon of a phononic bandgap (PhBG), which means that waves of a given frequency do not propagate in the structure. The location and size of PhBG depend on the thickness of the layers, the type of materials used and their distribution in space. The theoretical study examined the transmission properties of quasi one-dimensional structures designed using a genetic algorithm (GA). The objective function minimized the transmission integral and integral of the absolute value of the transmission functions derivative (to eliminate high transmission peaks with a small half width) in a given frequency range. The paper shows the minimization of transmission in various frequency bands for a 40-layer structure. The distribution of multilayer structure transmission was obtained through the Transfer Matrix Method (TMM) algorithm. Structures surrounded by water were analyzed and built of layers of glass and epoxy resin.

Keywords: acoustic filters, genetic algorithm, transfer matrix

1. Introduction

The beginnings of research on multilayer structures date back to the eighties of the last century [1, 2]. So far, the properties of multilayer structures for mechanical and electromagnetic waves have been analyzed [3-7]. The incident mechanical wave on the multilayer system propagates in it, but on each boundary of the layers there is a partial reflection. Due to multiple reflections and interference, the wave coming out of the system has different characteristics than the incident wave. For the assumed structure, waves of certain frequencies do not propagate through superlattice. This phenomenon is called phononic bandgap (PnBG). The location and size of the forbidden gap depends, among others, on the materials used, the thickness of individual layers, their distribution in space and the surrounding material [8-12]. Due to the structure, phononic (PnC) crystals with batch, quasiperiodic and aperiodic distribution are studied [6, 11, 12]. Phononic crystals can be one-, two- and three-dimensional. Various computational techniques are used to study the transmission properties of photonic crystals, such as Transfer Matrix Method (TMM) [13, 14], Finite Difference Time Domain algorithm (FDTD) [15-17] with Discrete Fourier Transform (DFT) [14],

Green’s functions [4, 5] and other. The special properties of multi-layer structures allow their use to noise control devices, acoustic and elastic filters, sensors, selective acoustic filters [18-24].

In the work, TMM algorithm was used to determine the transmission of multilayer structures. The propagation of the mechanical wave in layer i is determined by the equation

$$\frac{1}{v_i^2} \frac{\partial^2 p}{\partial t^2} - \nabla^2 p = 0 \tag{1}$$

where p is the pressure of an acoustic wave, t is a time and v_i is a phase velocity. In the case of a quasi one-dimensional structure, the solution to the above equation takes the form

$$p_i = \left(A_i e^{ik_i x} + B_i e^{-ik_i x} \right) e^{-i\omega t} = P_i(x) e^{-i\omega t} \tag{2}$$

Coefficients A_i and B_i describe respectively the wave propagating in accordance with the direction of propagation of the incident wave and the wave propagating in the opposite direction in a given layer i . The wave vector k_i of a given layer depends directly on the frequency f through

$$k_i = \frac{2\pi f}{v_i} \tag{3}$$

The transmission T for a given frequency can be determined directly from the characteristic matrix M of the structure as

$$T = \left| \frac{1}{M_{1,1}} \right|^2 \tag{4}$$

Mechanical wave propagation is described by the matrix equation (5) in which P_{in}^+ is incident wave, P_{in}^- reflected and P_{out}^+ transmitted.

$$\begin{bmatrix} P_{in}^+ \\ P_{in}^- \end{bmatrix} = M \begin{bmatrix} P_{out}^+ \\ 0 \end{bmatrix} \tag{5}$$

The characteristic matrix is defined as

$$M = \Phi_{in,1} \left[\prod_{i=2}^n \Phi_{i-1,i} \Gamma_i \right] \Phi_{n,out} \tag{6}$$

and consists of a matrix Γ_i describing propagation in a single layer i for a given thickness d_i as

$$\Gamma_i = \begin{bmatrix} e^{ik_i d_i} & 0 \\ 0 & e^{-ik_i d_i} \end{bmatrix} \tag{7}$$

and $\Phi_{i,i+1}$ transmission matrix on the border of i and $i+1$ layers, where ρ is the mass density of the appropriate layer, defined by

$$\Phi_{i,i+1} = \frac{1}{2} \begin{bmatrix} \frac{v_{i+1}\rho_{i+1} + v_i\rho_i}{v_{i+1}\rho_{i+1}} & \frac{v_{i+1}\rho_{i+1} - v_i\rho_i}{v_{i+1}\rho_{i+1}} \\ \frac{v_{i+1}\rho_{i+1} - v_i\rho_i}{v_{i+1}\rho_{i+1}} & \frac{v_{i+1}\rho_{i+1} + v_i\rho_i}{v_{i+1}\rho_{i+1}} \end{bmatrix} \tag{8}$$

The transmission properties of the structure largely depend on the distribution of individual material layers. The genetic algorithm (GA) is used to optimize the distribution of the phononic crystals structure [25, 26]. In this work, GA will be used to optimize the distribution of layers, and the scheme of its operation is shown in Fig. 1.

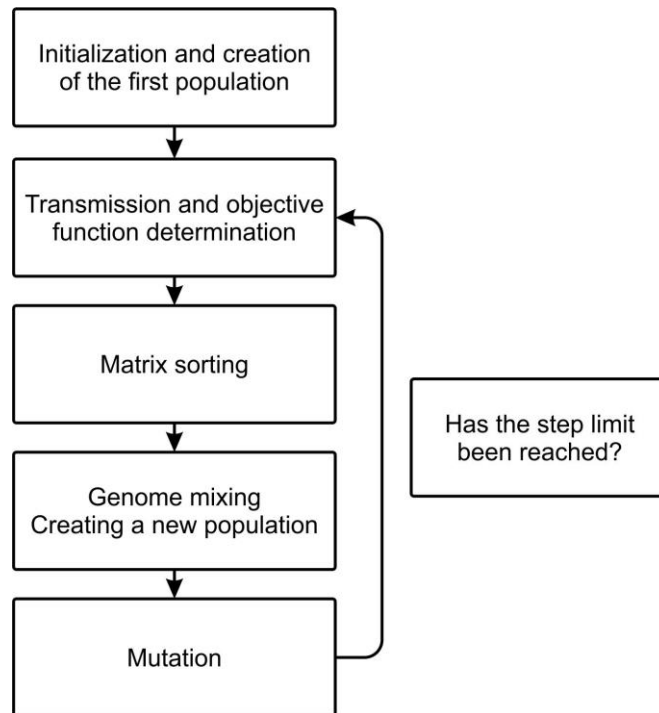


Figure 1. A flowchart of genetic algorithm

Initially, the algorithm's work environment is initialized and a preliminary population is created. Then the transmission of each structure is determined using the TMM algorithm and the value of the objective function is determined based on the formula

$$F_C = \left\| \int_{f_{\min}}^{f_{\max}} T(f) df \right\| \cdot \left\| \int_{f_{\min}}^{f_{\max}} \left| \frac{\partial T(f)}{\partial f} \right| df \right\| \quad (9)$$

The first normalized term is responsible for minimizing the value of the transmission function in a given frequency range, and the second minimizes the possibility of high transmission peaks with a small half width. Equation (9) was used to compare structures in a given population, while function (10) should be used to compare structures between populations.

$$F'_C = \int_{f_{\min}}^{f_{\max}} T(f) df \cdot \int_{f_{\min}}^{f_{\max}} \left| \frac{\partial T(f)}{\partial f} \right| df \quad (10)$$

Then a new population is built based on the sorted structures array by objective function and mixed (the two best structures remain unchanged), after which it undergoes a mutation process with a 1% chance of changing genes. Then the value of the objective function of the new population is determined again and the cycle is repeated. After a certain number of steps, the algorithm stops.

$$F_T = \frac{100\%}{T_{\max} f_{\max}} \int_{f_{\min}}^{f_{\max}} T(f) df \quad (11)$$

The ratio of the transmission area filling F_T is described by equation (10).

2. Research

The theoretical study analyzed multilayers made of glass (layer A, $v_A = 4000$ [m/s], $\rho_A = 3880$ [kg · m⁻³]) and epoxy resin (material B, $v_B = 2535$ [m/s], $\rho_B = 1180$ [kg · m⁻³]) surrounded by water ($v_w = 1480$ [m/s], $\rho_w = 1000$ [kg · m⁻³]) [7, 27]. The objective function was minimized for four frequency bands [kHz] in the ranges 0-5, 5-10, 10-15 and 15-20. The 40-layers structure were considered with a single layer thickness of 1 cm. Each population consisted of 20 structures.

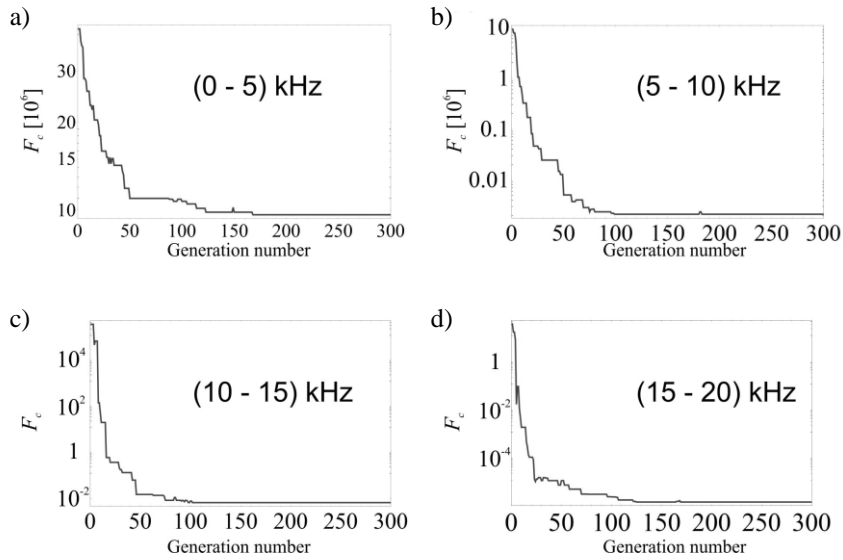


Figure 2. The objective function values of the best individuals (without normalisation) for each generation for subsequent analyzed bands

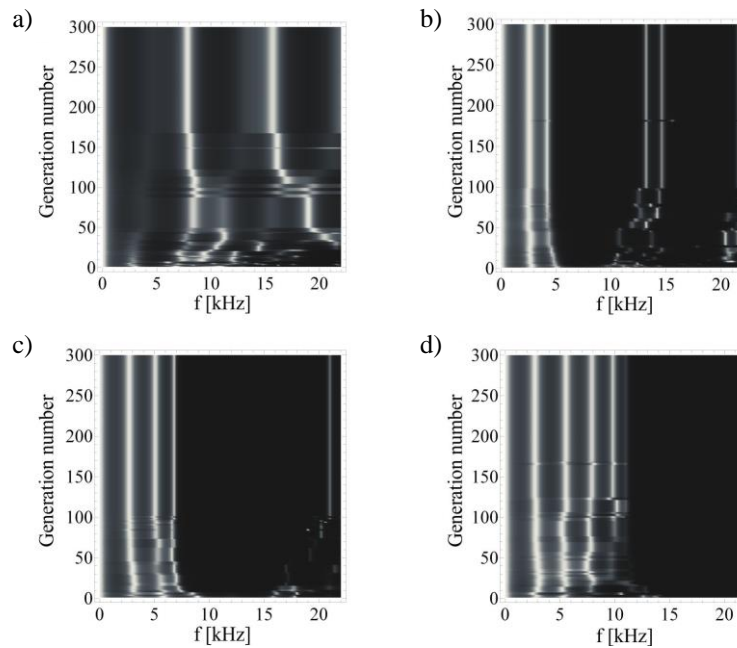


Figure 3. The density plots with transmission for the best individuals for each generation in searches for subsequent analyzed bands a) 0 kHz – 5 kHz, b) 5 kHz – 10 kHz, c) 10 kHz – 15 kHz, a) 15 kHz – 20 kHz

Fig. 2 shows how the function determined by equation (10) changed for the best structures of each generation. The value of the objective function on the graphs is presented on a logarithmic scale. Below 200 algorithm steps, the value of the objective function stabilized and the program reached the local minimum of solutions space. Small peaks after stabilization of the objective function were caused by the effect of the mutation on the entire population. Fig. 3 shows the transmission of structures with the lowest objective function from a given population. White means full transmission, and black means no transmission for a given frequency. The drawings show the evolutionary process and stabilization of the transmission structure after reaching the minimum of the objective function.

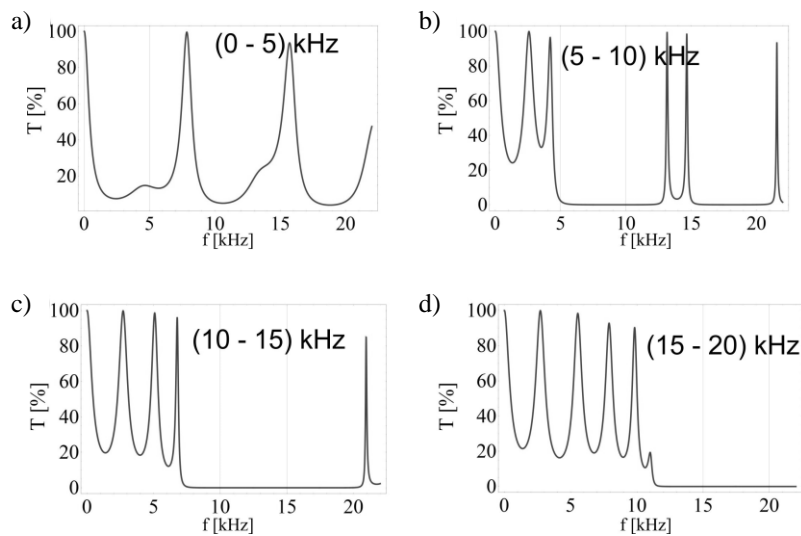


Figure 4. Transmission for the best found structures for each band a) 0 kHz – 5 kHz, b) 5 kHz – 10 kHz, c) 10 kHz – 15 kHz, a) 15 kHz – 20 kHz

Table 1. Best found structures for each band and the transmission integral for this band

Frequency range [kHz]	Transmission integral	Best found structure	Number of layers
0 – 5	$1.89 \cdot 10^{-1}$	$A_{26}B_{14}$	2
5 – 10	$1.78 \cdot 10^{-3}$	$A_7B_9A_9B_9A_6$	5
10 – 15	$5.81 \cdot 10^{-6}$	$A_6B_5A_6B_5A_7B_5A_6$	7
15 – 20	$7.30 \cdot 10^{-8}$	$A_3B_3A_4B_3A_4B_4A_4B_4A_4B_3A_4$	11

Fig. 4 presents transmission charts for structures with the minimum objective function value determined using a genetic algorithm. All graphs had high transmission peaks, but except for Fig. 4a, they had a low half width value. Table 1 shows the simplified notation of the structures found for the given bands (the value of subscript is the number of the layer repeats). It should be noted that the transmission integral

in subsequent bands significantly decreases when the number of layers in the structure increases. The total structure thickness was constant for all cases.

3. Conclusions

The paper shows that it is possible to use a genetic algorithm to search for multilayer structures with given transmission properties. The algorithm allowed to find multilayer structures built of glass and epoxy resin for four frequency bands where the objective function was to reduce transmission and eliminate high transmission peaks with a small half width. Such structures can be used as mechanical wave filters and noise control devices.

In the work, finding the optimal assumed structure took less than 200 iterations of the algorithm. The higher the band the smaller the transmission integral in the analyzed frequency range. The high value of the transmission integral for a band below 5 kHz results from the fact that the structure is thin compared to the wavelength of the propagating mechanical waves in this frequency range. For higher frequency bands, the number of layers of the found structure increased.

It is planned to verify the obtained data by using 4 microphones impedance tube.

References

1. L. M. Brekhovskikh, *Waves in Layered Media*, 2nd ed., Academic Press, New York, 1980.
2. P. Yeh, *Optical Waves in Layered Media*, John Wiley & Sons, New York, 1988.
3. J. Sapriel, B. Djafari-Rouhani, *Vibrations in superlattices*, Surf. Sci. Rep., **10** (1989) 189 – 275.
4. E. H. El Boudouti, B. Djafari-Rouhani, A. Akjouj, L. Dobrzynski, *Acoustic waves in solid and fluid layered materials*, Surf. Sci. Rep., **64** (2009) 471 – 594.
5. L. Dobrzynski et al., *Phononics*, Elsevier, 2017.
6. S. Garus, M. Szota, *Occurrence of Characteristic Peaks in Phononic Multilayer Structures*, Revista de Chimie, **69**(3) (2018) 735 – 738.
7. S. Garus, W. Sochacki, M. Bold, *Comparison Of Phononic Structures With Piezoelectric $0.62\text{Pb}(\text{Mg}_{1/3}\text{Nb}_{1/3})\text{O}_3$ - 0.38PbTiO_3 Defect Layers*, Engineering Mechanics 2018 (red.) Fischer Cyril, Naprstek Jiri, Institute of Theoretical and Applied Mechanics of the Czech Academy of Sciences, Prague, (2018) 229 – 232.
8. A. M. Badreddine, J. H. Sun, F. S. Lin, J. C. Hsu, *Hybrid phononic crystal plates for lowering and widening acoustic band*, Ultrasonics, **54**(8) 2159 – 64.
9. S. Garus, M. Szota, *Band GAP Frequency Response in Regular Phononic Crystals*, Revista de Chimie, **69**(12) (2018) 3372 – 3375.
10. L. Han, Y. Zhang et al., *A modified transfer matrix method for the study of the bending vibration band structure in phononic crystal Euler beams*, Physica B: Condensed Matter, **407** (2012) 4579 – 4583.
11. S. Garus, M. Bold, W. Sochacki, *Transmission in the Phononic Octagonal Lattice Made of an Amorphous $\text{Zr}_{55}\text{Cu}_{30}\text{Ni}_5\text{Al}_{10}$ Alloy*, Acta Phys. Pol. A, **135**(2) (2019) 139 – 142.

12. S. Garus, W. Sochacki, M. Bold, *Transmission Properties of Two-Dimensional Chirped Phononic Crystal*, Acta Phys. Pol. A, **135**(2) (2019) 153 – 156.
13. M. N. Armenise, C. E. Campanella, C. Ciminelli, F. Dell’Olio, V. M. N. Passaro, *Phononic and photonic band gap structures: modelling and applications*, Physics Procedia, **3**(1) (2010) 357 – 364.
14. S. Garus, W. Sochacki, *One Dimensional Phononic FDTD Algorithm and Transfer Matrix Method Implementation for Severin Aperiodic Multilayer*, Journal of Applied Mathematics and Computational Mechanics, **16**(4) (2017) 17 – 27.
15. T. Miyashita, *Sonic crystals and sonic wave-guides*, Meas. Sci. Technol., (2005) 16, R47.
16. S. Alagoz, O. A. Kaya, B. B. Alagoz, *Frequency controlled wave focusing by a sonic crystal lens*, Applied Acoustics, **70** (2009) 1400 – 1405.
17. M. M. Sigalas, E. N. Economou, *Elastic and acoustic wave band structure*, Journal of Sound and Vibration, **158** (1992) 377 – 382.
18. C. Y. Qiu, Z. Y. Liu, Z. M. Jun, J. Shi, *Mode-selecting acoustic filter by using resonant tunneling of two-dimensional double phononic crystals*, Appl. Phys. Lett. **87** (2005) 104101.
19. A. Cicek, O. A. Kaya, M. Yilmaz, B. Ulug, *Slow sound propagation in a sonic crystal linear waveguide*, J. Appl. Phys., **111** (2012) 013522.
20. M. D. Zhang, W. Zhong, X. D. Zhang, *Defect-free localized modes and coupled-resonator acoustic waveguides constructed in two-dimensional phononic quasicrystals*, J. Appl. Phys., **111** (2012) 104314.
21. J. Sánchez-Dehesa, V. M. Garcia-Chocano, D. Torrent, F. Cervera, S. Cabrera, *Noise control by sonic crystal barriers made of recycled materials*, J. Acoust. Soc. Am., **129** (2011) 1173.
22. T. T. Wu, L. C. Wu, Z. G. Huang., *Frequency band-gap measurement of two-dimensional air/silicon phononic crystals using layered slanted finger interdigital transducers*, J. Appl. Phys., **97** (2005) 094916.
23. I. Kriegel, F. Scotognella, *Three material and four material one-dimensional phononic crystals*, Physica E **85** (2017) 34 – 37.
24. S. Villa-Arango, R. Torres, P. A. Kyriacou, R. Lucklum, *Fully-disposable multilayered phononic crystal liquid sensor with symmetry reduction and a resonant cavity*, Measurement, **102** (2017) 20 – 25.
25. G. A. Gazonas, D. S. Weile, R. Wildman, A. Mohan, *Genetic algorithm optimization of phononic band gap structures*, Int. J. Solids Struct., **43**(18) (2006) 5851 – 5866.
26. H. W. Dong, X. X. Su, Y. S. Wang, C. Zhang, *Topological optimization of two-dimensional phononic crystals based on the finite element method and genetic algorithm*, Struct. Multidiscip. Optim., **50**(4) (2014) 593 – 604.
27. S. Garus, W. Sochacki, *High-performance quasi one-dimensional mirrors of mechanical waves built of periodic and aperiodic structures*, J. App. Math. Comp. Mech., **17**(4) (2018) 19 – 24.

Free Vibrations of the Column Taking Into Account Compressive and Thermal Load

Sebastian UZNY, Łukasz KUTROWSKI, Tomasz SKRZYPCZAK
*Częstochowa University of Technology, Institute of Mechanics
and Machine Design Fundamentals, Dąbrowskiego 73, 42-201 Częstochowa,
uzny@imipkm.pcz.pl, kutrowski@imipkm.pcz.pl, t.skrzypczak@imipkm.pcz.pl*

Abstract

Free vibrations of slender systems are the subject of many scientific and research works. In this work, the boundary problem of free vibrations of a compressed column, which is additionally heat loaded, is considered. The issue of heat flow in the column is solved using the Finite Element Method. Averaged distribution of material properties is obtained in individual segments of the column in subsequent heating times. The mathematical model of free vibrations takes into account the thermal expansion of the material and the effect of changing the Young's modulus resulting from the effect of heat load. The boundary problem of the free vibrations of the considered system is limited to the linear range (the linear component of natural frequency is considered). The influence of the heat source exposure time on the course of characteristic curves (on the plane: load – natural frequency) is determined. The results are presented for various column diameters.

Keywords: free vibrations, Euler's load, heat source, column

1. Introduction

In the case where mechanical constructions may be exposed to vibrations, an important element is to conduct vibration analysis to determine the natural frequencies. Knowing the values of the eigenfrequencies, it is possible to protect the systems against the occurrence of a dangerous resonance phenomenon. For this reason, there are many publications in the scientific literature concerning the problems of natural vibrations of mechanical systems [1-8].

The mathematical model of non-uniform beam vibration has been presented in [1]. The calculations assume variable mass, material damping and bending stiffness along the system length. The system vibration characteristics have been determined. Publication [2] presents a discrete model of non-linear vibrations of a damaged beam, additionally resting on a Winkler elastic foundation. The effect of location and crack size on the value of natural vibration frequency is investigated. The results obtained on the basis of this formulation are compared with the results for a continuous system. Work [3] covers the problem of forced vibration of a cantilever beam. Boundary problem is formulated on the basis of which frequencies and forms of vibrations are determined. The frame vibration analysis is undertaken in [3]. The wave propagation method is used and compared to the FEM. The procedure is extended for interconnecting members at an arbitrary angle. The effects of crack depth and crack location on the in-plane free vibration of cracked frame structures have been investigated numerically by using the Finite Element Method in work [4]. The effects of crack depth

and location on the natural frequency of multi-bay and multi-store frame structures are presented in 3D graphs. The results are compared with the results from ANSYS software. Publication [5] relates to non-linear vibrations of imperfect columns. The study shows that the frequency of a loaded system close to the critical value is infinitesimal value. Numerical tests have been confirmed by an experiment. The formulation of the boundary problem of column vibration using Timoshenko's theory with various mounting types is contained in [6]. The characteristic curves are presented and compared with the results obtained on the basis of Bernoulli-Euler theory. Thermal buckling and natural vibration of the beam with a specific boundary condition is analysed in the work [7]. Structure is subject to a uniformly distributed heating and has a frictional sliding end within a clearance. The impact of temperature on the material properties are assumed for high temperatures. The analytical solutions are derived for the buckling temperature and vibration frequency and different parameters of the system are under consideration. In the work [8] the primary resonance of heated beam under specific boundary conditions is analysed. Results from the analytical and numerical approach are compared, taking into account different parameters of the system. Thermal post-buckling and large amplitude vibration analysis of Timoshenko beams are presented in paper [9]. Solution is shown in the form of simple closed-form solutions by making use of the Rayleigh–Ritz method. Proposed approach is compared to the available results in the literature. Thermal buckling and elastic vibrations of functionally graded beams are under consideration in the work [10]. The Ritz method is adopted to solve the eigenvalue problems that are associated with thermal buckling and vibration in various types of immovable boundary conditions.

This paper presents the formulation of the boundary problem of column vibration, which is additionally exposed to a local heat source. This issue is limited to a linear range. As a result of thermal load, the material properties (e.g. Young's modulus) of the system under consideration change. By solving the boundary - initial heat flow problem, distributions of average values of Young's modulus are obtained in the next heating times. Using these results, the characteristic curves of the system depending on its diameter are determined for different times of exposure to the heat source.

2. The Initial-boundary problem of the heat flow

Transient heat transport in the column (Fig. 1a) is described by the following partial differential equation

$$\frac{\partial}{\partial x} \left(\lambda \frac{\partial T}{\partial x} \right) + \frac{\partial}{\partial y} \left(\lambda \frac{\partial T}{\partial y} \right) + \frac{\partial}{\partial z} \left(\lambda \frac{\partial T}{\partial z} \right) = c\rho \frac{\partial T}{\partial t}, \quad (1)$$

where: λ is the thermal conduction coefficient [W/mK], c represents the specific heat [J/kgK], ρ denotes the density [kg/m³], T represents the temperature [K], x , y , z are the Cartesian coordinates [m] and t denotes time [s].

Equation (1) is supplemented by the appropriate boundary and initial conditions:

$$q_b = -\lambda \frac{\partial T}{\partial \mathbf{v}_n}, T(x, y, z, t = 0) = T_0, \tag{2-3}$$

where: q_b represents the value of boundary heat flux [W/m²], \mathbf{v}_n is the direction of the vector perpendicular to the surface and T_0 represents the initial temperature [K].

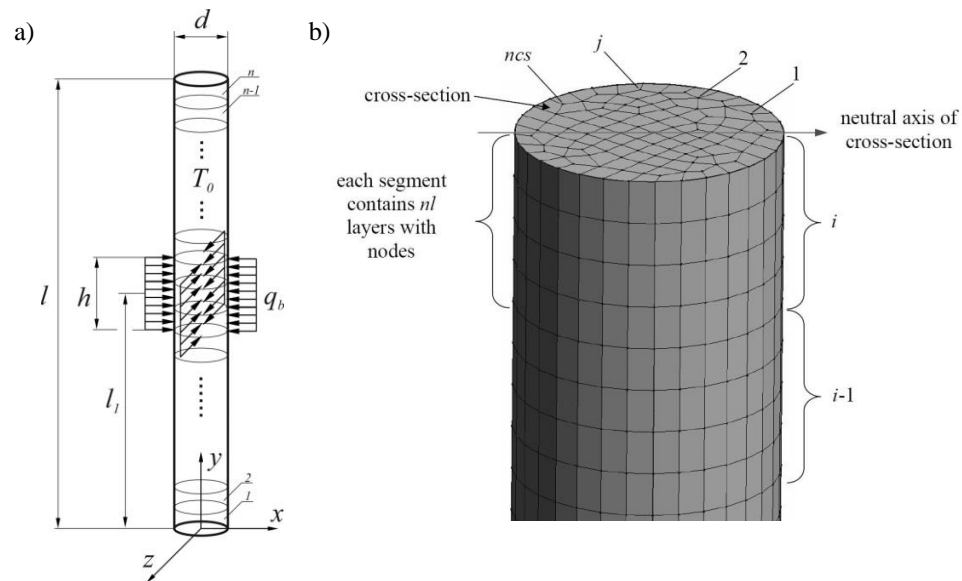


Figure 1. a) Scheme of the column with the thermal load b) fragment of the mesh

Equation (1) complemented by the conditions (2, 3) is solved by the means of FEM. Using the standard Galerkin formulation for the spatial discretization and then the procedure of aggregation of the finite elements and the Euler backward scheme of the integration with respect to time the final FEM equation is obtained:

$$\left(\mathbf{K} + \frac{1}{\Delta t} \mathbf{M} \right) \mathbf{T}^{f+1} = \mathbf{B} + \frac{1}{\Delta t} \mathbf{M} \mathbf{T}^f, \tag{4}$$

where: \mathbf{K} is the matrix of thermal conductivity, \mathbf{M} is the matrix of thermal capacity, \mathbf{B} is the vector containing boundary conditions, Δt represents the time step [s], f is the time level.

Scheme (4) is used to compute the temperature distribution in the column in the each time step. The investigation of stability of the column is preceded by the division of the column into n segments (Fig. 1a). The Young's modulus is the function of temperature calculated according to [11-12]:

$$\frac{E(T_C)}{E(20)} = 1 + \frac{T_C}{2000 \ln\left(\frac{T_C}{1100}\right)} \quad \text{for } 20^\circ\text{C} \leq T_C \leq 600^\circ\text{C},$$

$$\frac{E(T_C)}{E(20)} = \frac{690 - 0.69T_C}{T_C - 53.5} \quad \text{for } 600^\circ\text{C} \leq T_C \leq 1000^\circ\text{C},$$
(5)

where: T_C is the temperature expressed in degrees Celsius, $E(20)$ is the value of Young modulus for 20[°C].

The mesh is composed of the horizontal layers with the same distribution of nodes (Fig. 1b). Each segment of the column contains n_l of nodal layers. Computation of the stiffness to expansion-compression $(EA)_{cs}$, bending stiffness $(EI)_{cs}$ and temperature T_{cs} in every cross section of the column is performed in the following way:

$$(EA)_{cs} = \sum_{j=1}^{n_{cs}} (EA)_j, (EI)_{cs} = \sum_{j=1}^{n_{cs}} (EI)_j, T_{cs} = \frac{\sum_{j=1}^{n_{cs}} A_j T_j}{A_{cs}},$$
(6-8)

where: T_j is the temperature in the j -th node, E_j represents Young's modulus, A_j is the fragment of the cross-sectional area assigned to the j -th node, $I_j = A_j r_j^2$ is the moment of inertia, A_j, r_j – the distance between the neutral axis of the cross section and the j -th node, n_{cs} – the total number of nodes in the cross-sectional area, A_{cs} – the cross-sectional area of the column.

Averaged value of the parameters in the i -th segment are obtained as follows:

$$(EA)_i = \frac{\sum_{cs=1}^{n_l} (EA)_{cs}}{n_l}, (EI)_i = \frac{\sum_{cs=1}^{n_l} (EI)_{cs}}{n_l}, (T)_i = \frac{\sum_{cs=1}^{n_l} T_{cs}}{n_l}.$$
(9-11)

Above parameters are averaged for the segment which is composed of n_l horizontal layers of nodes. These nodes are vertices of quadrilateral finite elements which also form n_l cross sections in every segment of the column (Fig. 1b). EA, EI and T are initially calculated for every cross section (6-8) and then averaged for the segment (9-11). Such averaging is necessary for the boundary problem of free vibrations. Parameters (9-11) are finally saved in the text files for the next part of solution.

3. The boundary problem of free vibrations

The boundary problem of vibrations is formulated for the system presented in Figure 2. The column is considered to be articulated on both sides with a length of l , which has been divided into n equal segments. Such a division is made to obtain a distribution of the mean values of the Young's modulus along the length of the column. The system is loaded with force P , whose direction of action is constant and does not change with the

column displacement. In addition, the system is subjected to thermal load q_b on a defined column surface with a height h and at a distance of l_q from the bottom mounting.

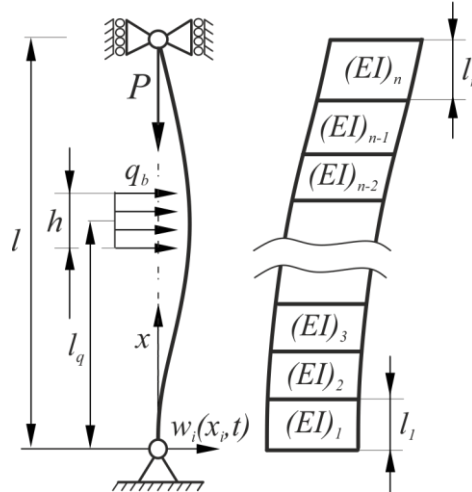


Figure 2. Scheme of the analysed system

The problem is formulated using the Hamilton principle (12). The potential energy V and kinetic energy T of the system can be written in the following form:

$$\delta \int_{t_1}^{t_2} (T - V) dt = 0, \tag{12}$$

$$V = \frac{1}{2} \sum_{i=1}^n (EI)_i \int_0^{l_i} \left(\frac{d^2 w(x)}{dx^2} \right)^2 dx - \frac{1}{2} P \int_0^l \left(\frac{dw(x)}{dx} \right)^2 dx, \tag{13}$$

$$T = \frac{1}{2} \rho A \int_0^l \left(\frac{\partial w(x, t)}{\partial t} \right)^2 dx. \tag{14}$$

The geometric boundary conditions and geometric continuity conditions are as follows:

$$w_1(0, t) = 0, w_n(l_n, t) = 0, w_i(l_i, t) = w_{i+1}(0, t), \tag{15-17}$$

$$\left. \frac{\partial w_i(x_i, t)}{\partial x_i} \right|_{x_i=l_i} = \left. \frac{\partial w_{i+1}(x_i, t)}{\partial x_i} \right|_{x_i=0}. \tag{18}$$

After applying the Hamilton principle and after performing appropriate mathematical transformations, differential equations of motion (19) and natural boundary conditions for individual system segments (20-23) are obtained:

$$(EI)_i \frac{\partial^4 w_i(x_i, t)}{\partial x_i^4} + P \frac{\partial^2 w_i(x_i, t)}{\partial x_i^2} + \rho A \frac{\partial^2 w_i(x_i, t)}{\partial t^2} = 0, \tag{19}$$

$$\left. \frac{\partial^2 w_1(x_1, t)}{\partial x_1^2} \right|_{x_1=0} = 0, \left. \frac{\partial^2 w_n(x_n, t)}{\partial x_n^2} \right|_{x_n=l_n} = 0, \tag{20-21}$$

$$(EI)_i \left. \frac{\partial^2 w_i(x_i, t)}{\partial x_i^2} \right|_{x_i=l_i} = (EI)_{i+1} \left. \frac{\partial^2 w_{i+1}(x_i, t)}{\partial x_i^2} \right|_{x_i=0}, \tag{22}$$

$$(EI)_i \left. \frac{\partial^3 w_i(x_i, t)}{\partial x_i^3} \right|_{x_i=l_i} = (EI)_{i+1} \left. \frac{\partial^3 w_{i+1}(x_i, t)}{\partial x_i^3} \right|_{x_i=0}. \tag{23}$$

In equations (15-23), the operation of separating variables is carried out, assuming:

$$w_i(x_i, t) = Y_i(x_i) \cos \omega t, \tag{24}$$

The solution of the equation of motion is assumed in the form of:

$$Y_i(x_i) = A_i \cosh(\alpha_i x_i) + B_i \sinh(\alpha_i x_i) + C_i \cos(\beta_i x_i) + D_i \sin(\beta_i x_i), \tag{25}$$

where:

$$\alpha_i = \sqrt{-\frac{k_i^2}{2} + \sqrt{\frac{k_i^4}{4} + \Omega_i^2}}, \beta_i = \sqrt{\frac{k_i^2}{2} + \sqrt{\frac{k_i^4}{4} + \Omega_i^2}}, \tag{26-27}$$

$$k_i^2 = \frac{P}{(EI)_i}, \Omega_i^2 = \frac{\rho A \omega^2}{(EI)_i}. \tag{28-29}$$

Substituting the solution (25) to the boundary conditions (15-18 and 20-23), a system of equations is obtained whose determinant of the matrix of coefficients compared to zero is a transcendental equation, used to determine the natural frequency of the system.

4. Results of numerical simulations

The results of numerical calculations are presented in the form of characteristic curves. The following dimensionless parameters were used to relate the results to a heat-free system:

$$\lambda = \frac{Pl^2}{(EI)_0}, \Omega^* = \frac{\rho A \omega^2 l^4}{(EI)_0}, \tag{30-31}$$

where $(EI)_0$ is the product of moment of inertia and Young modulus in temperature equal to 20[°C].

Calculations are carried out for a column with a length $l = 1$ [m], loaded with a heat flux $q_b = 200\,000$ [W/m²]. The column is thermally loaded in half its height ($l_q = 0.5$ [m]). The height of the heat source h is $= 0.2$ [m].

Fig. 3 presents characteristic curves for four variants of column diameters ($d = 0.01$; 0.015 ; 0.02 ; 0.025 [m]). In each case, calculations are made for subsequent exposure times to the heat source (with a time interval of 15 [s]). The characteristics are linear. Due to the adopted dimensionless parameters, the curves in the charts marked with the number 1 have the same form - they refer to a system that is not thermally loaded. Based on the calculations, it is found that as the heat load time increases, the characteristic curves move towards lower values. This results in a decrease in both the critical load of the system (in the case of the divergent system, the critical load corresponds to the case of $\Omega^* = 0$) and the natural frequency. The effect of heat load on column vibration is non-linear. Due to the assumed constant value of the heat load, along with the increase in the diameter of the system, the time after which the influence of the heat load has a significant effect on the system's vibration increases. For this reason, on the following charts for systems with higher diameters, the exposure time is greater.

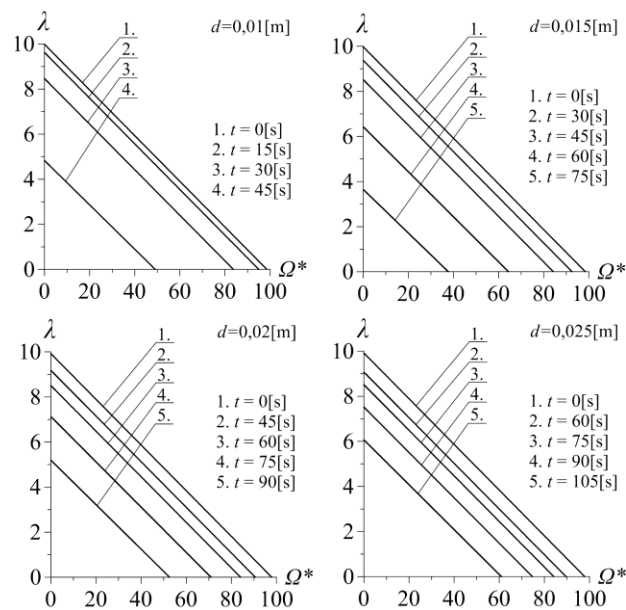


Figure 3. Impact of the heating time on the characteristic curves for different diameters of the analysed system

5. Conclusions

In this work, formulation of the boundary problem of column vibration exposed to Euler load and heat load was carried out. The issue of heat flow in the column was solved using FEM. Based on the Young's modulus distributions in the column for subsequent heating times, numerical simulations were performed regarding linear vibrations of the

system. The effect of column heating time on characteristic curves was determined, which in the case of slender support systems subjected to compression are of great importance in the process of designing support structures. The results are presented for various system diameters and different heating times. This problem will be developed in the future, in particular to include the stiffness of the supported system (the column can be treated as a slender support system) and to extend the formulation to the issue of non-linear vibrations.

Acknowledgments

This study was carried out within the statutory funds of the Czestochowa University of Technology (BS/PB 1-100/3010/2019/P and BS/MN 1-100-301/2019/P).

References

1. M. H. Taha, S. Abohadima, *Mathematical Model for vibrations of non-uniform flexural beams*, Engineering Mechanics, **15** (2008) 3 – 11.
2. A. Khnajar, R. Benamar, *A discrete model for nonlinear vibrations of a simply supported cracked beams resting on elastic foundations*, Diagnostyka, **18** (2017) 39 – 46.
3. P. Priyadarshan, A. Sarkar, *Vibration Control of Frame structure*, Procedia Engineering, **144** (2016) 414 – 424.
4. A. M. Ibrahim, H. Ozturk, M. Sabuncu, *Vibration analysis of cracked frame structures*, Structural Engineering and Mechanics, **45** (2013) 33 – 52.
5. M. Nagyová, J. Ravinger, *Stability and Vibration of Imperfect Column*, Procedia Engineering, **40** (2012) 286 – 291.
6. S. Uzny, K. Sokół, *The Bernoulli-Euler and Timoshenko Theories in the Context of Research on the Characteristic Curves of Column with Different Boundary Conditions*, AIP Conference Proceedings, **1648** 850036 (2015).
7. D. F. Cui, H. Y. Hu, *Thermal buckling and natural vibration of the beam with an axial stick-slip-stop boundary*, Journal of Sound and Vibration, **333** (2014) 2271 – 2282.
8. D. F. Cui, H. Y. Hu, *Primary resonance of lateral vibration of a heated beam with an axial stick-slip-stop boundary*, Journal of Sound and Vibration, **339** (2015) 230 – 246.
9. J. B. Gunda, *Thermal post-buckling & large amplitude free vibration analysis of Timoshenko beams: Simple closed-form solutions*, Applied Mathematical Modelling, **38** (2014) 4548 – 4558.
10. N. Wattanasakulpong, B. G. Prusty, D. W. Kelly, *Thermal buckling and elastic vibration of third-order shear deformable functionally graded beams*, International Journal of Mechanical Sciences, **53** (2011) 734 – 743.
11. CEN (European Committee for Standardization), *Design of steel structures - Part 1-2: General rules – Structural fire design*, Eurocode 3, (1993) Brussels.
12. A. Ancas, D. Gorbanescu, *Theoretical models in the study of temperature effect on steel mechanical properties*, The Bulletin of the Polytechnic Institute of Jassy, Construction. Architecture Section, **52** (2006) 49 – 54.

Fatigue Crack Detection Using Diffused Lamb Wave Field – Damage Index vs. Crack Length Estimation

Wiesław Jerzy STASZEWSKI

*Department of Robotics and Mechatronics, AGH University of Science and Technology,
Al. Mickiewicza 30, 30-059 Kraków, w.j.staszewski@agh.edu.pl*

Abstract

Fatigue crack detection is one of the major problems in maintenance of engineering structures. Ultrasonic guided waves are used for fatigue crack detection in metallic plate components. The application involves Lamb wave propagation and the analysis of the diffused wave field. The cross-correlation function is used to obtain a damage index that reveals the initiation of fatigue crack. The major focus of the paper is on crack length estimation. The results demonstrate that crack length estimation based on Lamb wave propagation is challenging but not impossible.

Keywords: Fatigue crack detection, Lamb waves, crack length estimation

1. Introduction

Many engineering structures rely on the damage-tolerant design concept. This concept assumes that structural damage is inevitable and therefore reliable damage detection and monitoring methods are required to guarantee safe operation. Various fatigue crack detection methods have been developed for the last decades. Maintenance of critical structures has benefited a lot from these developments. Non-Destructive Testing and Evaluation (NDT/E) techniques – such as visual inspection eddy current, acoustic emission, ultrasonic testing - are well established and widely used for crack detection in aerospace structures [1]. More recently a number of Structural Health Monitoring (SHM) approaches have been developed. These methods are less time consuming, less costly and offer real-time crack detection thanks to network of sensors that are permanently attached to monitored structures, as discussed in [1-5]. Ultrasonic techniques based on Lamb wave propagation belong to SHM methods that can be used for crack detection and monitoring. Despite many research efforts and literature reports engineering applications of Lamb waves are still limited. This is mainly due to the physical complexity of wave propagation that requires good monitoring strategies and experience with respect to data interpretation, as discussed in [1-8]. The vast majority of reported research developments in this field involve the application of low-profile, surface-bonded piezoceramic transducers and rely on the analysis of Lamb wave responses [6-8].

The application of Lamb wave techniques usually does not require complex data processing. Simple damage indices based on amplitude and/or phase of ultrasonic responses can provide some indication about crack initiation and growth. It is well known that the amplitude of the incident wave passing through the crack decreases and the amplitude of the wave reflected from the crack increases with the crack length.

However, for complex structures propagating wave components overlap, making the entire analysis difficult for the interpretation. Some effort has been undertaken to analyse the so-called diffused Lamb wave field - i.e. the wave field generated by multiple scattering and reflection of Lamb wave components – as demonstrated in [9]. This approach can lead to data signatures and even images can be used to detect and monitor the severity of damage. Nevertheless the estimation of real crack length still remains a difficult problem. Previous research work in this field indicates data processing of Lamb waves can be combined with fatigue and fracture analysis to estimate the crack length, as shown in [10]. The former involves the phase analysis of Lamb wave responses whereas the latter utilises the crack growth equation. This pioneering work has been recently extended to the probabilistic framework in [11] to provide damage prognosis, i.e. to predict the crack growth rate and possible failure.

The paper recalls the work presented in [10] and addresses the important problem of crack length estimation based on Lamb waves. In contrast to the previous research in this field – based on simple plate components – the current work focuses on the experimental work that involves a lap joint, multi-riveted aerospace component. The structure of the paper is as follows. The application of Lamb wave propagation for damage detection is briefly discussed in Section 2 for the sake of completeness. Section 3 demonstrates the component used in the damage detection investigation and the experimental procedure undertaken for crack detection. The experimental results are given in Section 4. Finally, the paper is concluded in Section 5. Although, the paper does not offer a unique solution to the challenging crack length estimation problem, the results indicate that Lamb wave responses can be used to achieve this goal. when Further research work needs to be focused on more experimental investigations.

2. Lamb Waves for Structural Damage Detection

It is well known that various types of ultrasonic waves can propagate in solids. Waves travelling in an unbounded bulk of elastic material are often called bulk waves. From the basic wave theory transverse (shear or S) waves exhibit particle movement in the direction perpendicular to the wave propagation. In contrast, longitudinal (or P) waves are wave in which particles of the medium move in the direction parallel to the wave propagation. Waves propagating in bounded media are known as guided waves. Lamb waves are guided ultrasonic waves that propagate in traction-free plates and are bounded by the upper and lower plate boundaries known as the waveguide. Lamb waves have a very complex mechanism of wave propagation. These waves are formed by the combined, bouncing P and SV (Shear Vertical) waves and are multimodal in nature. The thickness of the plate and the excitation frequency determine the wave propagation velocity of infinite number of symmetric and anti-symmetric modes. It is well known that these waves are also dispersive, i.e. the velocity of each mode varies with respect to its frequency. Lamb wave properties can be obtained from the classical elastodynamic wave equation given as

$$\rho \frac{\partial^2 u}{\partial t^2} - \nabla \cdot \tau = f \quad (1)$$

where u is the displacement, τ is the stress tensor, ρ is the density of the material, t is the time variable and f is the excitation. The relevant strain tensor can be defined as

$$\varepsilon_{ij} = \frac{1}{2} \left(\frac{\partial u_i}{\partial x_j} + \frac{\partial u_j}{\partial x_i} \right) \quad (2)$$

and is coupled to τ by the Hook's law. When the traction-free boundary condition are applied for the plate (i.e. the relevant components of stress at the top and bottom of the plate are zero) Equation (1) can be solved using the displacement potential and the partial wave technique, as demonstrated in [12]. The solution leads to the characteristic equation that is well known as the Rayleigh-Lamb frequency relations given as [12]

$$\frac{\tanh(0.5\beta d)}{\tanh(0.5\alpha d)} = \frac{4\alpha \beta k^2}{(k^2 + \beta^2)^2} \quad (3)$$

for symmetric modes and

$$\frac{\tanh(0.5\beta d)}{\tanh(0.5\alpha d)} = \frac{(k^2 + \beta^2)^2}{4\alpha \beta k^2} \quad (4)$$

for asymmetric modes, where

$$\alpha^2 = k^2 - \frac{\omega^2}{c_L^2} \quad \text{and} \quad \beta^2 = k^2 - \frac{\omega^2}{c_T^2} \quad (5)$$

and d is the plate thickness, ω is the angular frequency, k is the wave number c_L and c_T are the longitudinal and shear wave velocities respectively. Equations (4-5) can be solved numerically to obtain the dispersion curves that relate phase/group wave velocities to the fd product for various frequencies and thicknesses of plates. However, in practice these characteristics are not easy – or often impossible - to obtain and to analyse for complex materials and complex geometries. The so-called diffused Lamb wave field is than used. Lamb wave responses exhibit a number of different modes and wave components (i.e. incident, reflected and scattered waves) that are often overlapped. The diffused Lamb wave field can be also used for structural damage detection, as demonstrated in [9].

3. Fatigue Testing – Experimental Work

A complex metallic specimen – shown in Figure 1 – was used in the fatigue experiment. Two symmetrical aluminium-alloy multi-riveted plates (750 x 300 x 2 mm) were connected through a strap joint. The joint was fastened to either side by three rows of

rivets adding up to a total of 6 rows with 84 rivets. The 1.8 mm long notches on either side of the central rivets were introduced in the centre of the specimen by means of spark erosion. The central rivets were also slightly larger and stiffer to ensure crack propagation. Four piezoceramic SMART Layer® sensors from *Acellent Technologies, Inc.* were surface-bonded to the specimen for Lamb wave generation and sensing.

The *Schenck* servo-hydraulic test machine was used for fatigue testing. The specimen was loaded statically with a tensile load of 22 kN. Then a sinusoidal dynamic loading of ± 18 kN at a frequency of 6 Hz was applied to initiate and propagate the crack. The crack lengths were determined using a microscope.

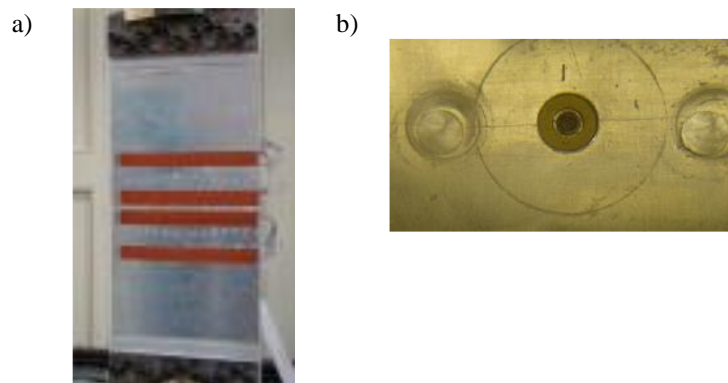


Figure 1. Aluminium lap joint used for crack detection investigations: (a) general view; (b) fatigue crack close-up in the centre of the specimen

4. Crack Length Estimation Based on Lamb Wave Responses

The fatigued specimen was monitored using the Lamb wave propagation approach. The *TTI TGA 130 30 MHz* arbitrary waveform generator was used for the excitation. Five cycles of the sine wave of 75 kHz frequency and 5 V amplitude were used as the excitation signal. Lamb wave responses were acquired using the *LeCroy 9303AM QUAD 200 MHz* oscilloscope. The sampling rate was equal to 25 MHz. Each recorded vector consisted of 5000 samples. Altogether 10 data vectors were recorded to produce averaged Lamb wave responses for different fatigue crack lengths. The results exhibited a number of overlapped wave packages, as expected. These wave responses were used for crack detection. The cross-correlation function for the Lamb wave responses representing the undamaged (intact) specimen and the damaged (cracked) specimen was calculated for various crack length to produce the so-called damage index *DI* defined as

$$DI = 1 - \rho_{xy} = 1 - \frac{C_{xy}}{\sigma_x \sigma_y} \quad (6)$$

where ρ_{xy} is the cross-correlation coefficient, C_{xy} the cross-correlation – that is used to assess the similarity between two Lamb wave responses - i.e. x (representing intact or undamaged condition) and y (representing the cracked condition) – and σ_x , σ_y are the

relevant standard deviations that assure the normalization. Since the correlation coefficient is normalized between -1 and 1, the defined damage index DI increases with the severity of damage (i.e. the crack length). However, the unsolved problem in these damage detection investigations is how to estimate the crack length from the analysed damage index. In other words, the major question is whether Lamb wave responses can be used to reliably estimate the fatigue crack length. An interesting observation can be made when the damage index DI and the crack propagation curve (i.e. crack length vs. fatigue cycles) are plotted together in logarithmic scales in Figure 2. Interestingly both characteristics are approximately parallel. The Crack Growth Rate (CGR) can be estimated from the well-known Paris-Erdogan equation given as

$$\frac{da}{dN} = C(\Delta K)^m \quad (7)$$

where a is the crack length, N is the number of fatigue cycles, ΔK is the range of the stress intensity and C , m are material constants that also depend on stress ratio, specimen size and environmental conditions. The stress intensity factor K estimates the load around the crack tip. The range of the stress intensity $\Delta K = K_{max} - K_{min}$ represents the difference between the maximum and minimum stress intensity K in a fatigue cycle. These results indicate that once material constants are known - for the case investigated - the estimation of crack length is possible from the damage index DI obtained from Lamb wave responses.

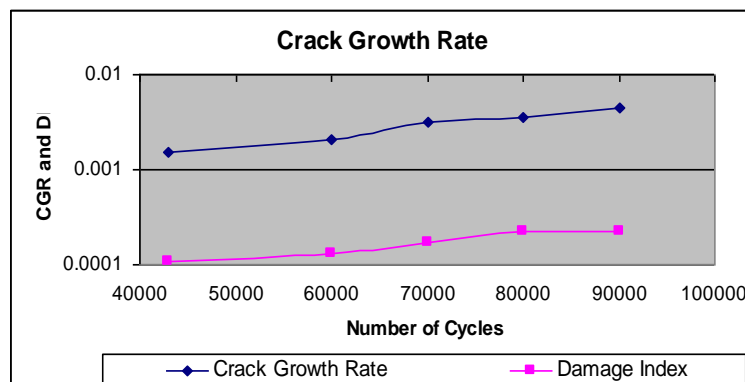


Figure 2. Crack Growth Rate (from fatigue analysis) and Damage Index (from Lamb wave propagation) characteristics for the tested aluminium lap joint

3. Conclusions

Lamb wave propagation was used in the riveted lap joint for fatigue crack detection. The cross-correlation between diffused field Lamb wave response – representing undamaged and damaged conditions – where used to obtain the damage index that can be used for crack detection. The results demonstrate that this index increases with the crack length. More interestingly, the results also demonstrate that the calculated damage

index can be directly related to the Paris-Erdogan fatigue equation through the crack propagation curve, making the estimation of crack length possible directly from the analysed crack length. The work presented does not offer a unique solution for different materials, components and damage scenarios but at least indicates that the estimation of crack length from Lamb wave responses is possible. It is clear that further theoretical and experimental research studies are required to confirm these findings.

Acknowledgments

The data analysis presented in this article has been performed using the Departmental Research funds. The specimen tested in these investigations has been manufactured within the EU Framework IV MONITOR project. The author is also grateful to Dr Graeme Manson from Sheffield University for the technical assistance with the fatigue test.

References

1. W. J. Staszewski, C. Boller, G. R. Tomlinson, Eds., *Health monitoring of aerospace structure*, Wiley, Chichester, 2004.
2. D. Adams, *Health monitoring of structural materials and components: methods and applications*, Wiley, Chichester, 2007.
3. C. Boller, F. K. Chang, Y. Fujino, Eds., *Encyclopedia of structural health monitoring*, Wiley, 2009.
4. Z. Su, L. Ye, *Identification of damage using Lamb waves: from fundamentals to applications*, Springer, Berlin, 2009.
5. T. Stepinski, T. Uhl, W. J. Staszewski, Eds., *Advanced structural damage detection: from theory to engineering applications*, Wiley, Chichester, 2013.
6. W. J. Staszewski, *Structural health monitoring using guided ultrasonic waves*. In: J. Holnicki-Szulc, C. A. Mota Soares, Eds., *Advances in Smart Technologies in Structural Engineering*, Springer, Berlin, (2004) 117 – 162.
7. A. J. Croxford, P. D. Wilcox, B. W. Drinkwater, G. Konstantinidis, *Strategies for guided-wave structural health monitoring*. *Proc. of the R. Society*, **463** (2007) 2961 – 2981.
8. A. Raghavan, C. Cesnik, *Review of guided-wave structural health monitoring*, *Shock & Vib. Digest*, **39** (2007) 91 – 114.
9. J. E. Michaels, T. E. Michaels, *Detection of structural damage from the local temporal coherence of diffuse ultrasonic signals*. *IEEE Trans. on Ultrasonics, Fer. and Freq. Control*, **52** (2005) 1769 – 1782.
10. W. J. Staszewski, *Structural health monitoring*, World Intellectual Property Organization, Int. Publication, No WO2003052400A2 (2003).
11. J. L. Rose, *Ultrasonic waves*, Cambridge University Press, Cambridge, 1999.
12. S. Yuan, J. Chen, W. Yang, L. Qiu, *On-line crack prognosis in attachment lug using Lamb wave-deterministic resampling particle filter based method*, *Smart Mater. Struct.*, **26** (2017) 085016.

Diagnostics of Rotary Vane Vacuum Pumps Using Signal Analysis and Processing Methods

Paweł ŁÓJ

*Institute of Fundamentals of Machinery Design, Faculty of Mechanical Engineering,
Silesian University of Technology, ul. Konarskiego 18A, 44-100 Gliwice,
pawel.loj@polsl.pl*

Wojciech CHOLEWA

*Institute of Fundamentals of Machinery Design, Faculty of Mechanical Engineering,
Silesian University of Technology, ul. Konarskiego 18A, 44-100 Gliwice,
wojciechl.cholewa@polsl.pl*

Abstract

Rotary vane vacuum pumps are devices widely used in various types of industries. A three-phase electric motor, which is a usual drive source in this group of devices, propels rotor, which is eccentric placed in the cylinder. The combination of this arrangement, between cylinder and rotor, with centrifugal force, forces the vanes to move out and into its slots milled in the rotor. As a result, the increase and decrease of the inter-vane volume occur, causing the air to be sucked into the pump. Due to improper exploitation, there is a possibility of a mechanical damage to the vane, and in some cases the vane can fall out of its groove, what leads to catastrophic failure. The article presents a new method for diagnostics of vanes, based on the observation and analysis of a pressure signal, generated by a rotary vane vacuum pump.

Keywords: vacuum pump, signal analysis, technical diagnostics

1. Introduction

Vacuum in industrial plants is produced using special designed vacuum pumps. There are a lot of different types of them, but rotary vane vacuum pumps are the most commonly used to produce, low vacuum (up to 1 mbar) and medium vacuum (up to 0.001 mbar). They can be found in various industries like pharmaceutical, food, chemical or even plastic processing. They are also used in pneumatic transport and in all kind of holding and moving operations of components during its production [1-3].

The group of rotary vane vacuum pumps can be divided to two separated categories – dry-running and oil-lubricated. Dry-running, also so-called “dry”, rotary vane vacuum pumps, use self-lubricated graphite vanes and they can operate with the capacity reaching up to 560 m³/h and 100 mbar of maximum pressure. However oil-lubricated, so called “wet”, rotary vane vacuum pumps can operate with the higher capacity reaching even 1600 m³/h and lower maximum pressure up to 0.1 mbar [2-4]. Technical data of selected pump models are presented in table 1.

Table 1. Technical data of selected oil-lubricated rotary vacuum pumps manufactured by BUSCH company [2]

Model	Nominal pumping speed [m ³ /h]	Ultimate pressure [mbar]	Nominal motor speed [min ⁻¹]	Weight [kg]
R5 RA0100 F	100	0.1	1500	73
R5 RA0302 D	300	0.1	1500	74
R5 RA0750 A	750	0.1	1200	670
R5 RA1000 B	1000	0.3	1000	1000
R5 RA1600 B	1600	0.3	1000	1330

These types of pumps, are usually built in the same way: electric motor permanently coupled with by the pump unit, which is flange-fitted to the oil-mist separator unit. A critical element of this kind of devices, is the pumps unit consisting of a cylinder, vanes, rotor, side covers with bearing supports, vanes and also inlet and outlet valves. The principle of operation of rotary vane vacuum pumps is illustrated in figure 1A.

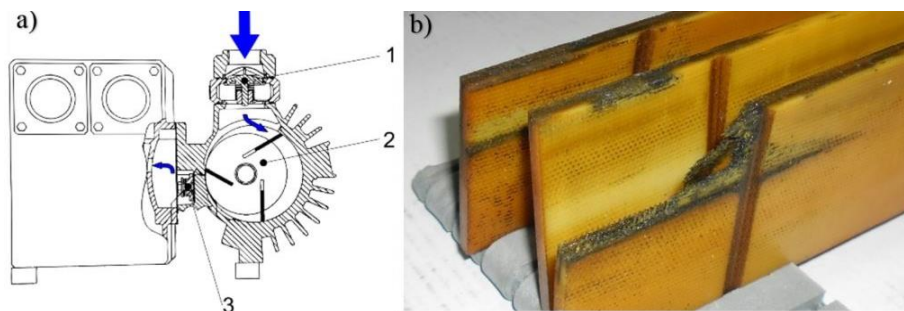


Figure 1. Principle of operation of oil-lubricated rotary vane vacuum pumps (a), and the view of a damaged vane (b) [1]

Electric motor, supplied by three phase current, generates torque, which is transmitted through the claw coupling to the rotor, (with milled slots for the vanes), setting it into the rotation movement [2-4].

The eccentric arrangement of the rotor in the cylinder, in combination with the centrifugal force, forces the vanes to move out and into the slots, what causes regular increase and decrease of the volume between the vanes, leading to suction, compression end exhausting the air into the oil-mist separator unit. Experience shows that properly operated and serviced rotary vane vacuum pumps can work for many years without showing significant wear symptoms [5, 6]. However even during normal exploitation, as a result of different random events, there may occur damages of the vanes, showed in the figure 1B, and sometimes even, as a result of its damage, uncontrolled displacement of the vanes, like falling out of its slot. Such situations leads to serious damage, which cost

of repair is similar to the price of a new device. The examples of such damages are showed in the figure 2.



Figure 2. Examples of damaged pumps due to vane malfunction [1]

2. Rotary vane vacuum pumps diagnostics

At this moment, there are two methods of operational maintenance, of rotary vane vacuum pumps. The first one assumes regular inspections and repairs, which frequency is defined by the manufacturer – what often results in excessive costs and pauses in production. The second method, assumes only regular replacements of oil and oil-mist separators, and exploitation of device until a noticeable decrease in the quality of the generated vacuum. This apprenticeship is intuitively and practically much more risky and dangerous, in case of the pump malfunction, but sometimes, in some specific cases, it allows to reduce downtimes. In each of the described scenarios, it is necessary to turn off the pump, disconnect it from the vacuum system and transport it to an external service company. To date, no diagnostic methods are known to identify progressive damages without shutting down the device.

The new diagnostic method, is based on the registration and analysis of the pressure signal, generated by the rotary vane vacuum pump. The specificity of this sort of pumps, imposes restriction on the construction of the measurement system. The first major limitation is its cost. The capacity of the most common oil-lubricated rotary vane vacuum pumps is $100\text{m}^3/\text{h}$, and a price for such device is around 3500 EUR. For this reason, it was assumed that the cost of components, used to build the measurement system, cannot exceed 5% of the value of a new device of this type device. The second major limitation is the location of the pressure sensor. This sensor should be located as close as possible to the cylinder, behind the inlet filter, to eliminate the influence of inertia and leakage in vacuum system, and to protect it from damage by sucked gases, liquids and solid particles from the technological process. The third and last important limitation is the requirement of the signal recorder mobility, due to the required scope of application and user convenience.

The pressure value is measured at the pump inlet, directly in the suction port, by the analog pressure sensor, connected to the pump, by the short vacuum hose. Then the signal is filtered using a low-pass filter, and together with the signal describing the angular position of the rotor, it is sent to Raspberry Pi microcomputer with an analog-digital converter.

3. Research and results

Experimental studies were carried out on a test device, with a capacity of 100 m³/h, with low wear rate. The measurement of pressure was carried out with a sampling frequency of 2048 Hz, while the rotor rotational frequency was ~25 Hz. During the tests, there was recorded the course of the pressure generated by the device, equipped with one damaged vane with low degree of its defect (a), with one damaged vane with high degree of its defect (b), with two damaged vanes with various degree its of defects (c), and equipped with undamaged vanes in conditions of lack of lubrication (d). Also the reference test, on the intact device, was performed (e).

The analysis of pressure signal, was carried out in time and in the frequency domain. In the time domain, the synchronous averaging and signal autocorrelation methods were used, while in frequency domain it was limited to spectrum analysis.

As a result of the synchronous averaging method, synchronized by the marked position of the rotor, an average time course of pressure was generated, for every individual state of the device. The coloured lines, which are shown in the figure 3a-e, present the pressure course during single rotations of rotor.

With an increase in the degree of damage of the vane, the chart shows increasing disorder. In the case of a heavily damaged vane, two inflection points are clearly visible, and in the case of a slightly damaged vane, there are visible three inflection points, and the shape of the graph is similar to the shape of an undamaged device. This phenomenon is directly related to the leakage through the edge of the vane. In the case of insufficient lubrication, much more pressure peaks are visible, what is related to the discontinuity of the oil film between the cooperating elements.

While analysing the graph of the normalized autocorrelation function, showed in the figure 4a-e it is possible to conclude about the condition of the vanes working in a vacuum pump. In the case of even small damage, a strong correlation can be seen only once per revolution, which in this measurement conditions is ~82 samples long. With the growing degree of damage to a single vane, the strength of this correlation decreases. In the case of efficient pumping, strong autocorrelation is visible 3 times per revolution, which is associated with the same operating conditions for all three vanes. In a situation where there is a lack of lubrication in the pump unit, a strong correlation occurs also 3 times per revolution, however, the shape of the autocorrelogram envelope is chaotic.

From the analysis of the amplitude spectra of the pressure signals generated by the rotary vane vacuum pump, shown in the figure 5a-e, it is also possible to detect damages of the vanes working in it. In the spectrum of the pressure, generated by an efficient pump, the frequency band of ~75 Hz dominates, which is related to the rotational frequency (25 Hz) of the rotor and the number of 3 rotating vanes. As the vane damage increases, the frequency band of ~25 Hz increase, which corresponds to the frequency at which the damaged vane passes by the suction port. In case of the insufficient lubrication, the pressure signal spectrum shows a significant increase in share of high-frequency components (over ~150 Hz), associated with the operation of moving elements (such as inlet and outlet valves), which are not directly related to the rotational frequency of the rotor.

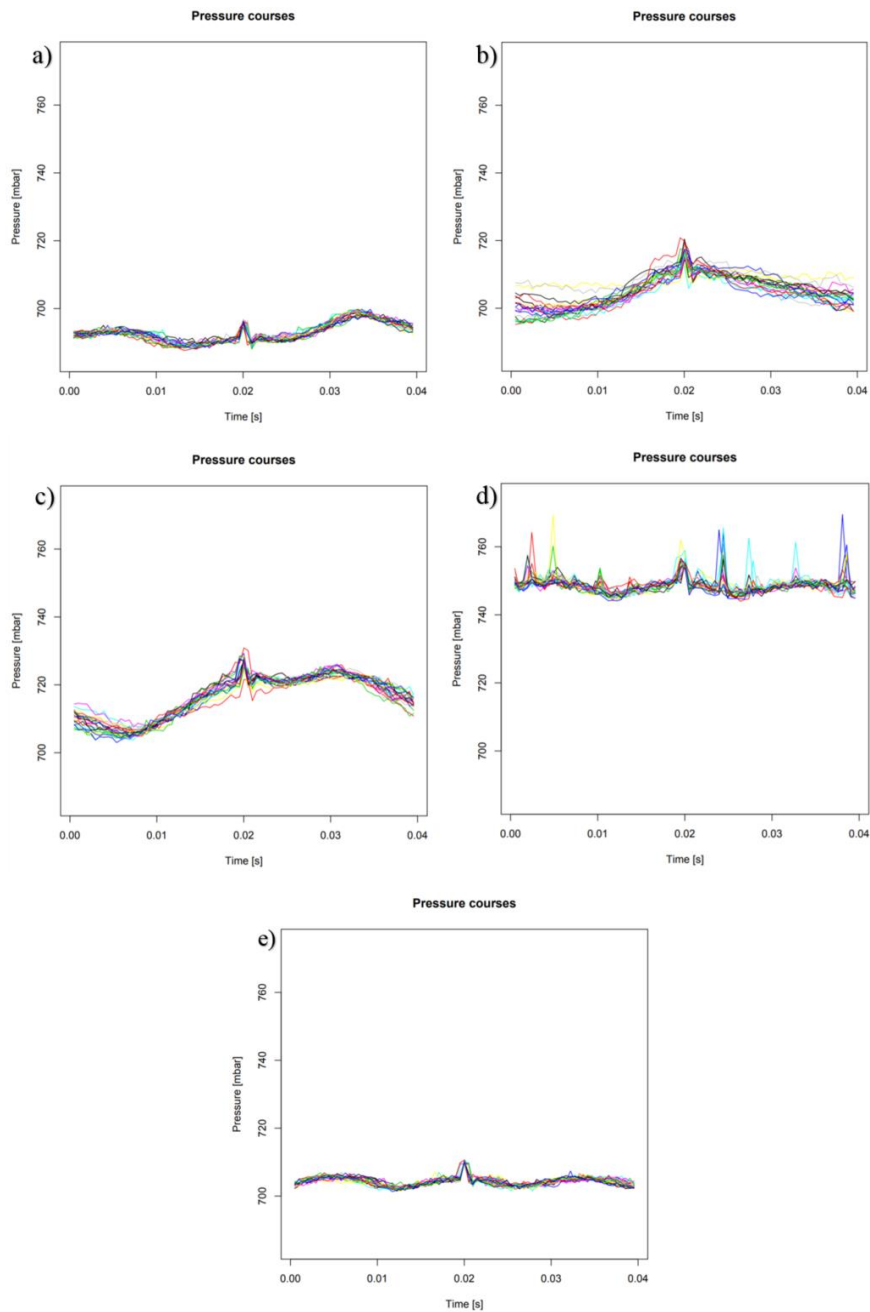


Figure 3. Time courses of the generated pressure signals (see section 3)

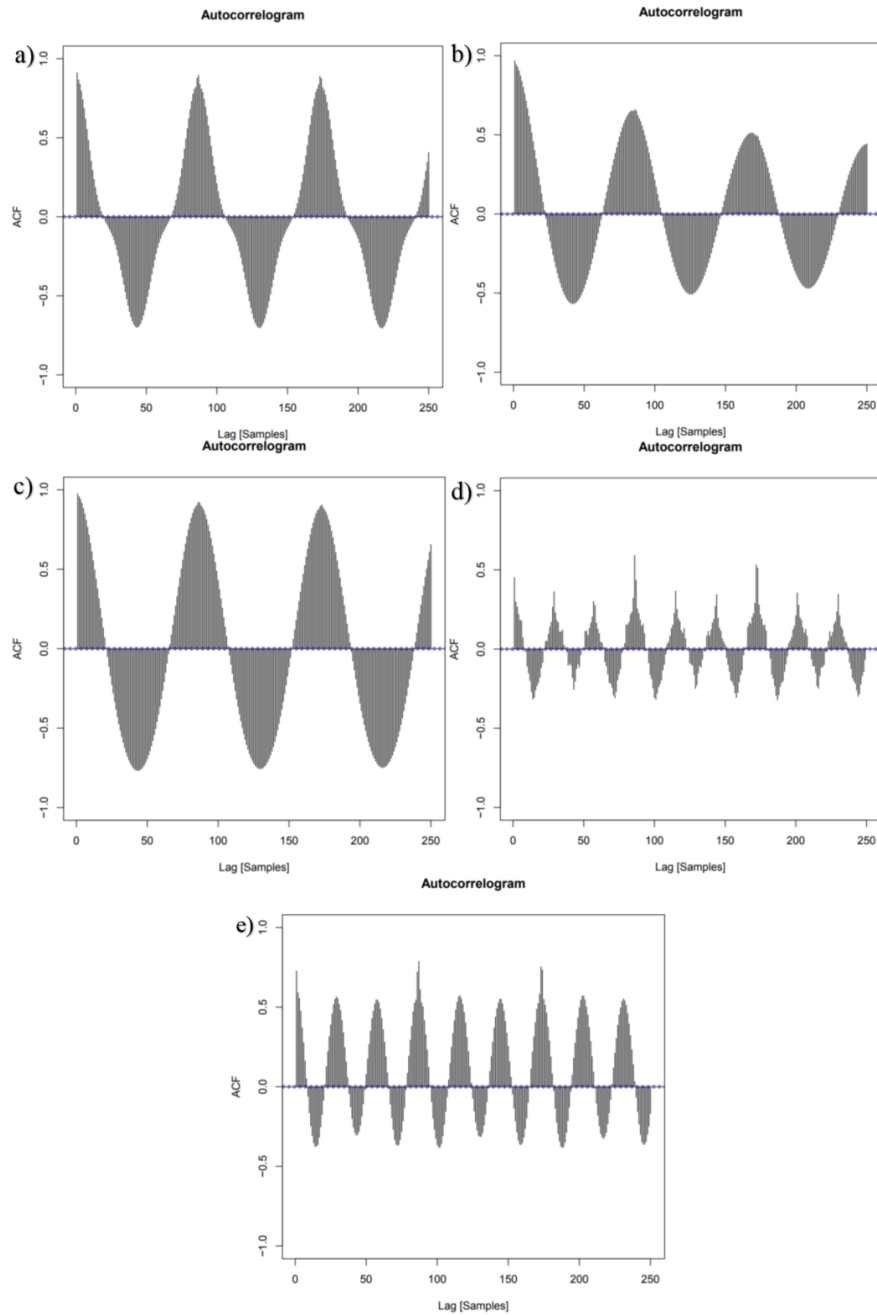


Figure 4. Graphs of the normalized autocorrelation function of the pressure signals (see section 3)

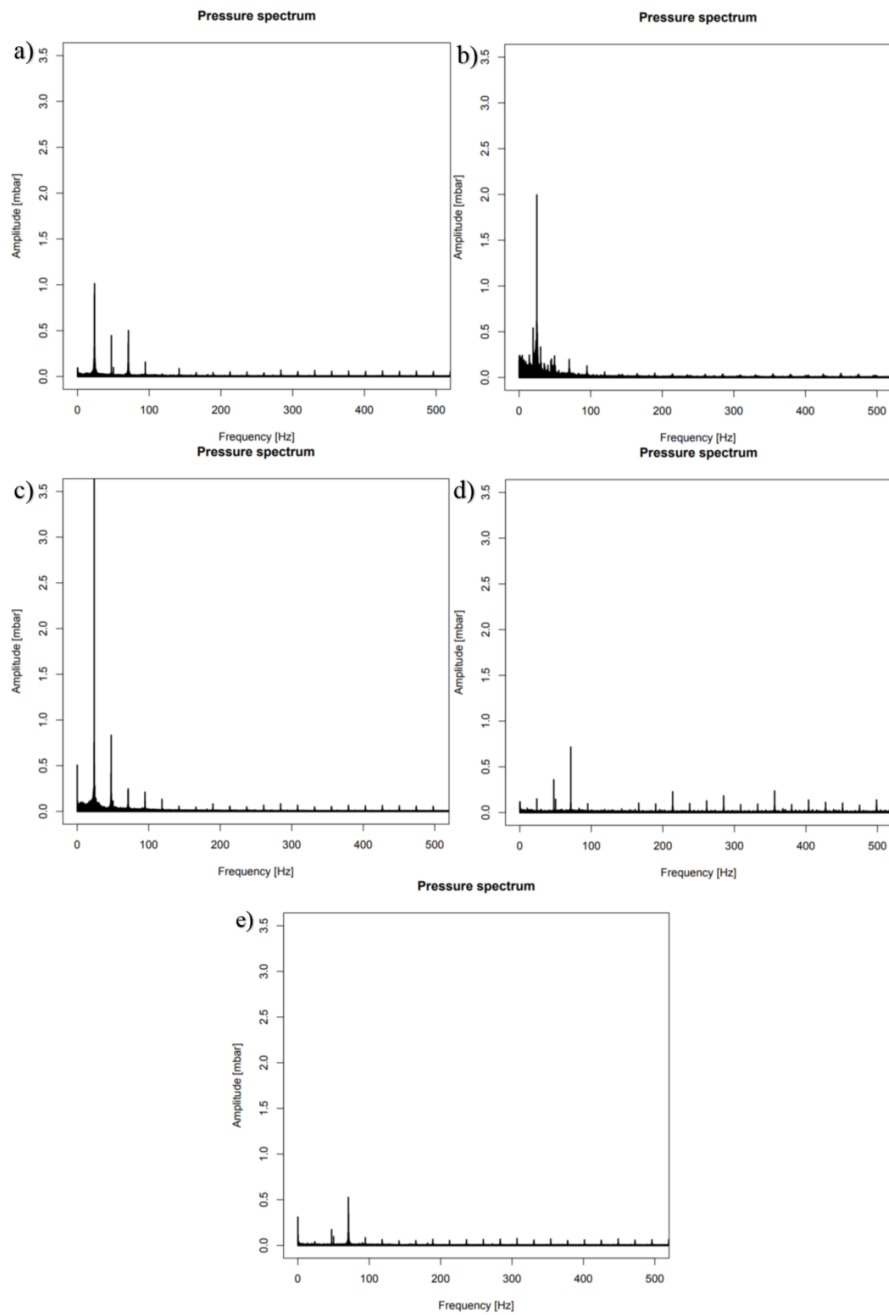


Figure 5. Amplitude spectra of the generated pressure signals (see section 3)

4. Conclusions

Synchronous averaging of pressure signals, allows to detect damages and identify the degree of its advancement, what combined with information about the angular position of the rotor, allows to identify the damaged vanes.

Normalized autocorrelation function of pressure signals, allows detection and identification of the degree of vanes damages, as well as problems occurring in the lubrication system.

The use of spectral analysis allows the detection of both vane damage and problems with the lubrication system.

The presented method enables early detection of damages, leading to catastrophic consequences. It also allows to improve planning and managing maintenance of rotary vane vacuum pumps in the production company, by providing information about the current state of the working device.

All discussed diagnostics methods, are based on a comparison of the pressure signal, generated by the tested device, with the reference pattern obtain during the operation of the intact device. In the further work, an automatic reasoning system for the diagnostic process of the rotary vane vacuum pumps based on presented methods, will be developed.

References

1. P. Łój, *Exploitation of rotary vane vacuum pumps*, Modelowanie Inżynierskie, Vol. 38, No. 69 (2018) 56 – 59.
2. BUSCH, <https://www.buschvacuum.com/pl/pl> (access 19.09.2019).
3. BECKER, <https://becker-polska.com> (access 19.09.2019).
4. Pfeifer Vacuum GmBH, *The vacuum technology book*, Pfeifer Vacuum GmBH, Aßlar 2013.
5. A. Hałas, *Vacuum Technique* (in Polish), Publishing House of Wrocław University of Technology, Wrocław 2017.
6. N. Yoshimura, *Vacuum Technology*, Springer-Verlag Berlin Heidelberg, Berlin 2008.

The Method of Estimating Kinematic Road Excitation with Use of Real Suspension Responses and Model

Zbyszko KLOCKIEWICZ
Poznan University of Technology,
zbyszko.j.klockiewicz@doctorate.put.poznan.pl

Grzegorz ŚLASKI
Poznan University of Technology,
grzegorz.slaski@put.poznan.pl

Abstract

The paper deals with the problem of vertical kinematic excitations in road vehicle dynamics simulation, with the main focus on reconstruction of random excitations using measured dynamic responses of a car suspension. The possibility of causing excitations adequately in terms of chosen conditions of exploitation and in reliable way is crucial to properly assess ride comfort, ride safety as well as rattle space and fatigue strength of suspension elements. The paper presents a method of generating equivalent kinematic excitation allowing for reconstruction of suspension dynamic responses in simulation. The method uses unsprung mass accelerations acquired during test rides and a model of vertical suspension dynamics. The method uses estimated displacements of unsprung mass as a preliminary approximation of kinematic excitation and tracking control system with a PID controller, which causes corrections of kinematic excitations transforming it to the form that allows for faithful reconstruction of unsprung mass accelerations and, in turn, kinematic excitations. The paper presents the basic structure of kinematic excitations' reconstruction system as well as a method of tuning PID controller's coefficients so that the error in estimation is minimized. Research and verification of results were done using a sine chirp signal and constant frequency sine waves. The similarity of estimated road profiles is high with error no larger than 8% of the original signal's amplitude.

Keywords: suspension, kinematic excitation, remote parameter control, simulation, PID controller

1. Introduction

A moving vehicle is subject to two types of excitations – dynamic and kinematic ones. The most common dynamic excitations are the forces connected with acceleration and deceleration of a vehicle. These however happen much more infrequently in comparison to the ones caused by road unevenness which are called kinematic excitations. These excitations are consequence of road irregularities' heights and velocity of their changes which are proportional to vehicle speed. It is impossible to create a perfectly smooth surface, on which the vehicles would travel. Every road has a profile of irregularities' heights – a geometric structure of the pavement [1]. In mathematical terms it can be described as a function in which the height of the profile is dependent on longitudinal and lateral coordinates along a plane that represents ideal road surface. In simulation the profile is often simplified to just a single longitudinal line directly under vehicle tyre – as this is the direction the vehicle is traveling and the lateral profile is often assumed to be the same on the whole width of road-tyre contact path or even the whole road. The effects such profile has on a vehicle depends however also on other factors, mainly the vehicle's

speed and tyre's filtering properties. Resulting function of the heights of the profile is time-dependent, not distance-dependent, as the road profile is. It is also subject to the tyre filtration, which acts as a low-pass filter. It smoothens sharp edges, which is known as tyre enveloping [2]. The knowledge of kinematic excitations is necessary if the goal of the simulation analysis is to evaluate ride comfort, safety or a durability.

The problems in estimation of these excitations comes from the fact that they are random in nature and there is no simple way to define all the factors and their influence on vehicle responses on a certain road. Given the long time for which the researchers have studied this topic (dating as far back as 1910s [3], for more information see [4]), there are many proposed methods of estimating kinematic excitations. Typical road surfaces such as different kinds of paved roads have been investigated thoroughly many times and the excitations' results acquired on them were used to create statistical databases. This in turn allows researchers to estimate expected levels of kinematic excitations on those types of surfaces. This lead to the creation of International Roughness Index (IRI in 1986 [5]), classifying roads based on total suspension deflection over distance travelled, and later of ISO 8608 standard (in 1995 [6]), which classifies roads based on power spectral density (PSD) of the road irregularities' heights encountered on them. Both of those have their limitations, though. IRI, being a 1-dimensional index, can describe vastly different roads as the same, based purely on the cumulative suspension deflection, as described in [7]. The PSD classification also does not work in every situation, as most real roads do not belong to one class only, but several at once in different frequency ranges (Figure 1) - [8], [9]. It should be noted, that normally PSD of road irregularities' heights is a function of spatial frequency, but can be easily recalculated to temporal frequency if a constant speed assumption is made. If that is the case, then the temporal frequency ω is equal to spatial frequency Ω times velocity v [10].

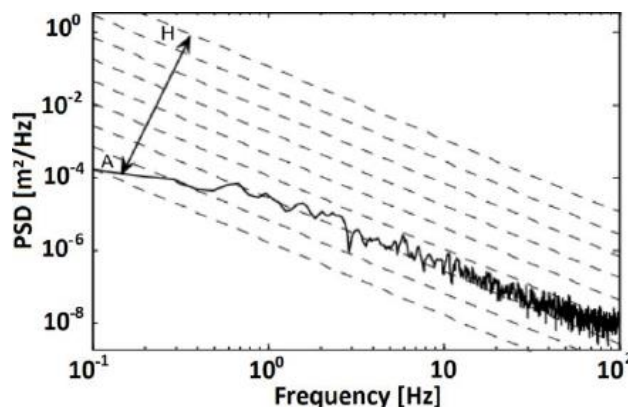


Figure 1. An example of a single road's PSD in multiple classes.

Dashed lines indicate borders between road classes from ISO 8608 standard [9]

The fact that roads of similar statistical characteristics can vary so much means that simulations need to be made on a case-by-case basis. The methods that can be used to

obtain kinematic excitations on a specific road vary, but can be generally divided into 2 categories:

- I. Profile measurements, which includes different forms of geodetic measurements that give the heights of irregularities very precisely. To derive kinematic excitations from these measurements one needs to know the transfer functions between profile and kinematic excitation. This can be done assuming that the road-tyre pair is a linear time-invariant system. This means the correlation between the system input and output can be written as in formula (1)

$$H(s) = \frac{Y(s)}{X(s)} \quad (1)$$

where $H(s)$ is a tyre transfer function, $Y(s)$ is a Laplace transform of kinematic excitation and $X(s)$ is a Laplace transform of the road profile. This assumption however does not apply to every situation and as such has limited use.

- II. Kinematic excitation estimation, which can be further divided into [2]:
 - a. direct measurement, which produces road profile data for further processing. It is slow to conduct and expensive and relies heavily on the parameters of a profilometer. The name “direct” comes from the fact, that the sensors used record the profile directly, with no need for further processing,
 - b. response-based methods, which register vehicle responses, which then need to be processed to kinematic excitations. These are the least costly and the fastest, but they their accuracy heavily depends on the accuracy of the model used as well as the sensors,
 - c. non-contact measurements that produce road profile. They are fast, easy to conduct and quite accurate, but expensive and prone to errors due to environmental factors. They combine the aspects from both previous groups – requiring vehicle models to work and correct errors stemming from vehicle movement, but measuring the displacements directly in reference to the road surface.

The response-based methods are not new – the first tries date as back as 1950’s when response-type road roughness measuring systems, RTRRMS for short, started gaining popularity. They consisted of a vehicle and a towed trailer with measuring equipment, that registered the responses of a trailer, such as accelerations. To use this data to reconstruct road profile, a vehicle model needed to be put together. Based on the test that were conducted in the 60’s and 70’s, quarter-car model was chosen as sufficient for kinematic-excitation estimation and “*the Golden Car*” model was created – which was aimed to simulate a typical passenger car using American roads at the time [11]. It was later used for example for defining IRI. The response-based method, while not very accurate for road-profile estimation, is actually quite well suited for kinematic excitation estimation, as the hardest part to simulate in a vehicle model are tire dynamics. These are responsible for changing the road profile signal into kinematic excitation via the tire filtration properties. The suspension on the other hand acts in a much more predictable way, especially if we do not exceed the range of its linear work. This approximation is permissible if simulation is set to recreate most asphalt roads of modest quality – [12].

One way to use the measured responses to replicate kinematic excitations is a method called Remote Parameter Control, or RPC. The basic concept is as follows: firstly, the real vehicle is driving on a chosen road and unsprung mass accelerations are being measured. Then, the same vehicle is placed in the lab on four hydraulic actuators and the accelerations from the tests are turned into displacements by a computer, which then activates the actuators. The accelerations in the test are measured and compared with the original ones – if there are differences spotted, the computer lowers or strengthens the kinematic excitation signal for that wheel accordingly. After a few iterations acceleration signals from the lab become very similar to those gathered in real life tests, forming the so-called “equivalent road”, equal to kinematic excitation [13].

The models used in all those methods however are far from perfect, so new methods of estimating kinematic excitations are being constantly developed, one of which will be presented in this paper. The innovations come in the form of possibility to easily switch between the linear and non-linear models for kinematic excitation estimation, as the whole vehicle model is treated like a black box, which needs only to have kinematic excitation as an input and unsprung mass acceleration as an output. Secondly, the method uses the PID controller, which makes it more flexible, as one can tune its coefficient to make the method work for different types of vehicles.

2. Proposed “Virtual RPC” method

The proposed algorithm (shown in Figure 2) works as follows: first, one needs to obtain an unsprung mass acceleration $\ddot{z}_{m_T}(t)$ signal from real life test (hence “T” in the underscore), which will act as a base signal, that the algorithm will try to reproduce. However to run a simulation, the kinematic excitation $h(t)$ signal is needed. By using double integration on unsprung mass acceleration $\ddot{z}_{m_T}(t)$, one will calculate the wheel displacement $z_{m_{T,E}}(t)$, which is assumed in this paper to be roughly the same as the kinematic excitation $h(t)$. This of course is not correct - that is the first estimation (hence the “E” in the underscore to mark that), however this estimation will serve as an input to the simulation, which will be corrected in the next steps. The reasons for which $z_{m_{T,E}}(t)$ and $h(t)$ are different are two-fold – first, they come from the faulty assumption that kinematic excitation $h(t)$ translates directly to the wheel displacements $z_{m_T}(t)$, secondly they come from the imperfections of recorded acceleration signal $\ddot{z}_{m_T}(t)$ which is used to calculate the estimated wheel deflection. Those imperfections include noise, trends appearing in the signal or inclusion of results of forces other than those caused by road unevenness. All this contributes to the fact that if a simulation was to be run with the input being double-integrated unsprung mass accelerations, the resulting responses would not match those registered in the tests. To calculate kinematic excitation from the measured accelerations that yields results closer to the responses from the test rides, the authors of this article proposed an algorithm that deals with these problems. It is noteworthy, that the first group of problems connected with the inherent difference between $h(t)$ and $z_{m_{T,E}}(t)$ is more pronounced, so the signal imperfection errors will be not be analyzed further, as they will be removed alongside the bigger error coming from the former source.

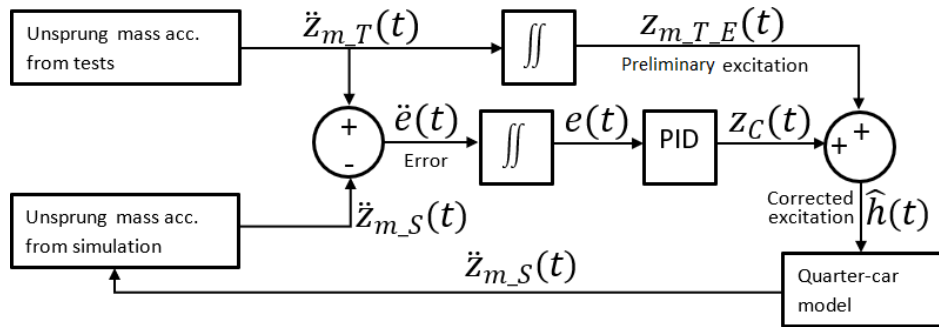


Figure 2. Diagram showing the principle of kinematic excitation estimation using “Virtual RPC” method

The algorithm works as follows: first, the unsprung mass acceleration $\ddot{z}_{m_T}(t)$ measured in the test is integrated twice and that signal ($z_{m_{T_E}}(t)$) is used as an input to the quarter-car model.

Table 1. Parameters of quarter-car model. “M” refers to sprung mass/suspension parameters, while “m” refers to unsprung mass/tire parameters.

	m [kg]	M [kg]	k_m [N/m]	k_M [N/m]	c_m [Ns/m]	c_M [Ns/m]
Value	50	400	138200	19300	220	2500

The springs and dampers in the quarter-car model were linear and were described using coefficients k_m , c_m , k_M and c_M . Based on that, the responses of the model are calculated, including a new unsprung mass acceleration from the simulation $-\ddot{z}_{m_S}(t)$. That acceleration $\ddot{z}_{m_S}(t)$ is then compared with the one from the tests $\ddot{z}_{m_T}(t)$ and the resulting error $\ddot{e}(t)$ is then also integrated twice, ran through a PID controller and that correction of wheel displacement $z_C(t)$ is added to the wheel displacement (preliminary excitation) $z_{m_{T_E}}(t)$ signal calculated from the acceleration $\ddot{z}_{m_T}(t)$. The correction is added, because the error is defined as the difference between acceleration from tests $\ddot{z}_{m_T}(t)$ and from the simulation $\ddot{z}_{m_S}(t)$. This means that if a simulation signal is smaller than the reference one, the error is positive and it will be added to the corrected signal and vice versa. That corrected signal $\hat{h}(t)$ then enters the quarter-car model as a new excitation $\hat{h}(t)$ and is used for the next iteration. As one can tell, the correction occurs an iteration after the original error was calculated, so it is obvious that the value of reference acceleration might be different in the next step, so it might seem redundant to apply an error correction that comes from the iteration before. This however is dealt with by using a simulation with a small time-step, so that the values of acceleration do not change too quickly for the correction to follow. The exact value for the time-step was chosen empirically to be 0.00001 s, keeping in mind that the changes to which the suspension is able to react do not exceed the frequency of 30 Hz, which translates to a period of 0.03 s repeating, which gives 3333 calculation points every period in the worst case scenario.

The tasks that the authors of the article were met with were as follows:

- to build a mathematical model and its Simulink implementation of presented estimation method,
- to choose PID controller's coefficient so that the error in excitation prediction is minimized,
- to create an array of test signals, which will be used to verify the degree of similarity of estimated profile.

3. Model and its parameters

The vehicle model was implemented in MATLAB/Simulink. The quarter car model was chosen being the simplest, which decreased the number of variables researchers had to take into account analysing the results with its parameters akin to the typical passenger car from C segment [12].

The PID controller's parameters were at first all set to 0, reflecting the situation with no correction. Then, a number of tests was conducted, in which consecutively k_p , k_i and k_d gain values were changed and the extent of allowed values (those that did not cause the simulation to crash) was established, creating three intervals – 1 to 91 for k_p , 0 to 100 for k_i and 0 to 0.2 for k_d . Having done that, the researchers picked 10 evenly distributed numbers within those intervals, with the lowest values being 0 and the highest being the borders of each consecutive interval. The authors ran then the simulation, listing the cumulative error that occurred when the algorithm was trying to reproduce a random signal of 0.01 m amplitude. The k_i coefficient had the biggest influence on the error, increasing it with when its value grew, that is why it was set to 0. The other two displayed similar levels of influence, with k_d having much bigger impact on the stability of the system – that is why the highest value that could be tested was 0.2. The results were then saved in 3-D errors matrix and the lowest value of that matrix was found. The coefficients' values for that lowest error are presented in Table 2.

Table 2. Empirically found optimal values for PID controller's coefficients

	k_p	k_i	k_d
Value	25	0	0.194

4. Verification of reconstruction procedure of kinematic excitation

After the model and its parameters were set, the verification process could begin. Firstly, there was a need to determine exactly what excitations should the authors try to estimate. The authors chose to focus on the determined excitations (sine wave – to be exact) as the results are easy to interpret, both when it comes to amplitudes as well as phase shifts. The important factors in the case of sine waves were their amplitudes and frequencies. The amplitude chosen was 0.003 m as this is also the amplitude of base displacements during EUSAMA test [14]. The frequencies on the other hand were chosen so that they covered the full range of meaningful excitations. Very low frequencies (below 0.5 Hz) do not affect responses of the vehicle in a significant way, as those excitations do not cause big enough accelerations. At the same time, they can be detrimental for this

estimation method, as they can cause the appearance of constant values, which lead to the creation of linear trends in estimated excitation signal. On the other side of the spectrum, high frequencies of over 25 Hz also do not contribute to the excitations, as they are filtered out in real life by pneumatic tyre. At the same time, in the simulation environment with tracking control their inclusion leads to destabilization of the estimation. That is why the chosen frequencies for the sine waves were discrete values 1 Hz, 5 Hz, 12 Hz and 25 Hz and also the linear chirp signal that changes frequency from 0.1 Hz to 30 Hz.

The verification method was as follows – firstly, the quarter car model was subjected to a chosen excitation and its unsprung mass acceleration signal was registered. Then, in another Simulink model, the unsprung mass acceleration signal was loaded as an input and based on it the algorithm proposed by the authors reconstructed the kinematic excitation, which caused that acceleration. That estimated kinematic excitation was then compared with the original signal, that the first Simulink model used as an input.

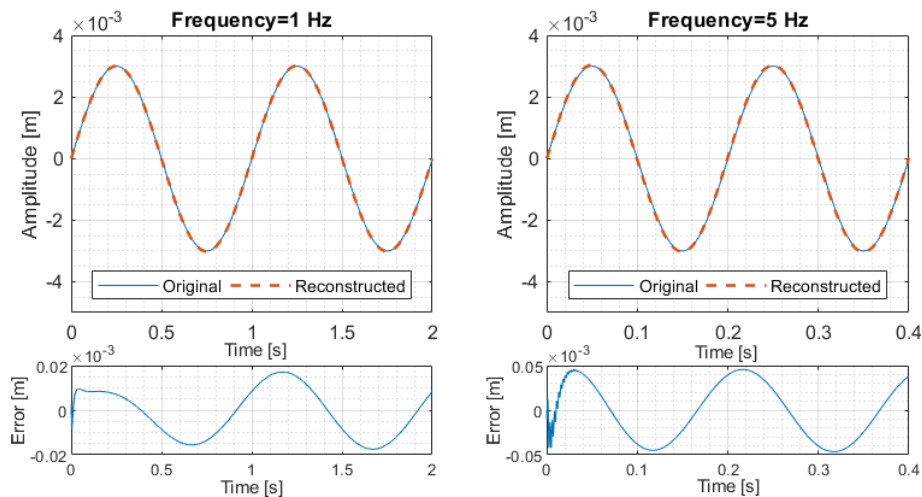


Figure 3. Original and reconstructed signals and errors for sine waves of constant frequencies 1 Hz and 5 Hz

The results for constant frequency sine waves are presented in Figure 3 and Figure 4. As was expected, the method is really effective for slow changing signal, with the maximum error between the original and reconstructed signal being $2 \cdot 10^{-5}$ m, which is 0.7% of the original signal. The error gets bigger with increasing frequency, until it reaches its maximum value for the 25 Hz sine wave – $2.3 \cdot 10^{-4}$ m, which translates to 7.7% of the original signal. The increase in error is almost linear between cases studied.

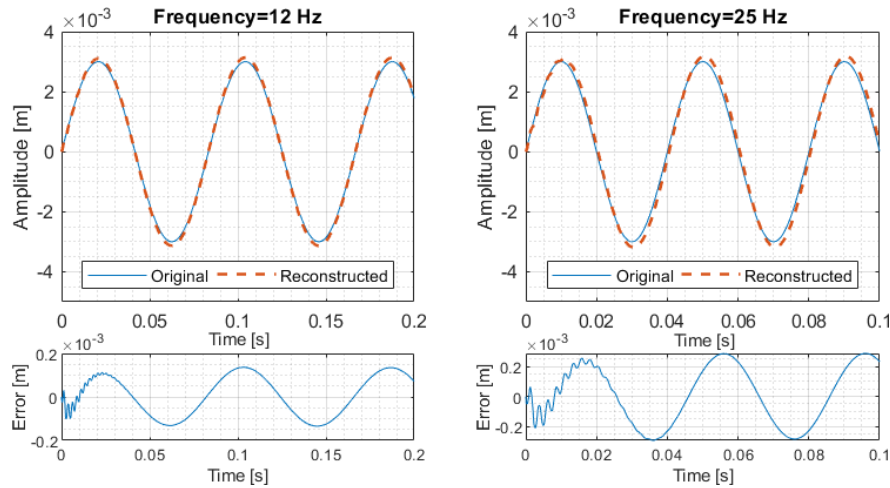


Figure 4. Original and reconstructed signals and errors for sine waves of constant frequencies 12 Hz and 25 Hz

The linear chirp signal is a sine wave that changes its frequency linearly over time. The amplitude was 3 mm, and the interval of frequencies was 0.1 Hz to 30 Hz changing over the span of 30 seconds. As one can see, these go beyond the limits described in the previous paragraph, to test whether or not the method would deal with more extreme cases than those anticipated.

The trend in the whole frequency range is depicted in Figure 5. The frequency changes from 0.1 Hz to 30 Hz in the span of 30 s, so the time is roughly equivalent to the frequency at that time. The relative error and phase shift were calculated by estimating transfer function between estimated and original kinematic excitation signals. The top chart shows the relative error that is slightly lower than the one calculated for constant frequency sine waves. This is because for constant sine waves, the error was calculated as the difference between time signals – and because there is a phase shift, the original signal was decreasing in value before the estimated signal could reach its peak, so that the momentary difference between the two was greater than the difference between peak values, as is the case here. The maximum error was calculated to be 6.1% for 21.5 Hz. The phase shift is very minimal for low frequencies up to about 15 Hz, where it starts to increase in absolute value linearly, reaching almost 6° for 30 Hz.

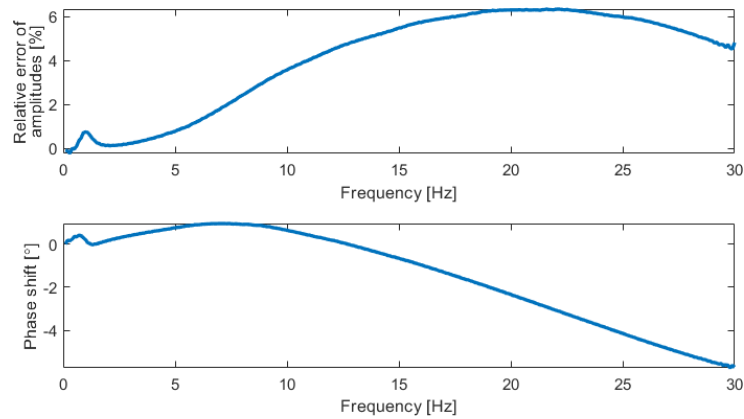


Figure 5. Relative error of estimated signal to the original one and the phase shift between them

5. Conclusions and further studies

The authors of the article set out to describe a new method of estimating kinematic excitations in the simulation based on the unsprung mass accelerations. In the process, they came to several conclusions concerning topics related to the stated goal.

First off, the proposed method can generate results containing quite big errors for frequencies outside of the described scope. This however does not diminish its usefulness, as in the real exploitation only a specific range of frequencies has significant influence on the vehicle's responses. The range of frequencies chosen as significant was between 0.5 Hz and 25 Hz. Taking this into consideration as well as the length of the tyre-pavement contact patch those temporal frequency values translate to the unevenness lengths of 20 cm and 120 m respectively (this is considering that maximum velocity a vehicle can achieve on a very few roads like German Autobahns is 60 m/s).

Considering those limitations, the method proves to be working very well in estimating the determined kinematic excitations that were tested. For low frequencies the error is very minor – not even 1%. It grows to 7.7% for 25 Hz or even 11.3% for 30 Hz, these however are high frequencies on the border or even outside of the scope of frequencies that are important in comfort, safety and fatigue analysis. For the 12 Hz sine wave, which corresponds roughly to the natural frequency of most passenger vehicles' unsprung masses, the error is 5.7%, which is satisfactory.

The fact that the results are satisfactory does not mean no further work is planned to improve the method. The method will be tested by estimating kinematic excitation signals that correspond to roads of classes defined in ISO 8608 standard to check if the results for sine waves and chirp signal correspond to random signals and more complicated tire models and what magnitude the errors would be. The influence of the noise in the signal will be examined and possible solutions to arising problems will be drawn.

References

1. F. Hu, *Road profile recovery using vertical acceleration data*, Electronic Theses and Dissertations, University of Windsor, <https://scholar.uwindsor.ca/etd/5299/>, 2015.
2. X. T. Yechen Qin, Hong Wang, Yanjun Huang, *Real-Time Road Profile Identification and Monitoring. Theory and Application Synthesis*, Morgan & Claypool, 2019.
3. J. H. Woodstrom, *Measurements, Specifications, and Achievement of Smoothness for Pavement Construction*, Publisher: Transportation Research Board, ISSN: 0547-5570, 1990.
4. M. G. Lay, *Ways of the World: A History of the World's Roads and of the Vehicles that Used Them.*, Rutgers University Press, 1992.
5. M. W. Sayers, T. D. Gillespie, C. V. Queiroz, *The International Road Roughness Experiment - Establishing Correlation and a Calibration Standard for Measurements*, Transportation Research Record 1084, Transportation Research Board, National Research Council, Washington, D.C., **45** (1986) 76 – 85.
6. G. Loprencipe, P. Zoccali, *Use of generated artificial road profiles in road roughness evaluation*, J. Mod. Transp., **25**(1) (2017) 24 – 33.
7. O. Kropáč, P. Můčka, *Be careful when using the International Roughness Index as an indicator of road unevenness*, J. Sound Vib., **287**(4–5) (2005) 989 – 1003.
8. P. Můčka, *Simulated Road Profiles According to ISO 8608 in Vibration Analysis*, J. Test. Eval., **46**(1) (2017), p. 20160265.
9. R. Zhang, X. Wang, S. John, *A comprehensive review of the techniques on regenerative shock absorber systems*, Energies, **11**(5) (2018).
10. R. V. Dukkipati, J. Pang, M. S. Qatu, G. Sheng, Z. Shuguang, *Road Vehicle Dynamics*, SAE International, 2008.
11. M. Sayers, *Two Quarter-Car Models for Defining Road Roughness: IRI and HRI*, Transp. Res. Rec., **6** (1995) 165 – 172.
12. Z. Klockiewicz, G. Ślaski, M. Spadło, *The influence of the conditions of use and the type of model used on the vertical dynamic responses of a car suspension*, **85**(3) (2019) 57 – 82.
13. J. Osiecki, T. Gromadowski, B. Stępiński, *Testing of automotive vehicles and their components on simulation test stands* (in Polish), Radom: WITE (Publishing House of the Institute for Sustainable Technologies), 2006.
14. P. Zdanowicz, *Assessment problems during the shock-absorbers condition tests on EUSAMA stand* (in Polish), Logistyka (Logistics), **4** (2010).

Acoustic Signal as a Carrier of Information on Breathing Sleep Disorders

Dorota GÓRNICKA

*Institute of Machine Design Fundamentals, Warsaw University of Technology,
ul. Narbutta 84, 02-524 Warsaw, Poland,
dorota.gornicka@pw.edu.pl*

Grzegorz KLEKOT

*Institute of Machine Design Fundamentals, Warsaw University of Technology,
ul. Narbutta 84, 02-524 Warsaw, Poland,
grzegorz.klekot@pw.edu.pl*

Michał MICHALIK

*Faculty of Sleep Apnea and Snoring, MML Medical Center,
ul. Bagno 2, 00-112 Warszawa, Poland,
m.michalik@mml.com.pl*

Abstract

The statement that an acoustic signal can be a good tool for assessing breathing during sleep is not revealing and certainly raises no doubts. Based on the experience of technical diagnostics, one can formulate the hypothesis about the suitability of sounds accompanying breathing to infer any specific disorders. The verification of this hypothesis was supported by a research experiment combining the experience of doctors and engineers. The obtained results was used to create the simple application for the initial diagnosis of respiratory problems while sleeping at home. Assuming the minimization of the use of an advanced mathematical apparatus, features that are the symptoms of basic respiratory disorders have been extracted from the signal. Thanks to this approach, the developed tool not only informs about the disorder, but also signals the potential cause of the problem. Thus, the inference procedure that is the basis of a useful application can also support doctors at the stage of preclinical diagnosis.

Keywords: acoustic signal, diagnosis of sleep breathing disorders

1. Introduction

Despite the increasing awareness, the problem of snoring is still largely treated as an “aesthetic” problem. In many cases this is indeed the case, however, snoring may be the result of serious breathing disorders [1, 2]. A good source of information about breathing problems occurring during sleep is an acoustic signal [3-6]. On the market there are many applications which record snoring. Most of them focus only on informing the user that the one “snore” and in some cases awake his/her in order to reduce the occurrence of annoying acoustic effects. Few applications indicate a potential disease aspect. The authors attempted to create an inference procedure for application which diagnoses sleep breathing disorders. The application is intended to inform the user about a medical problem and indicate the type of disorder.

2. Research experiment

The presentation of the procedure underlying the diagnostic application required the acquisition of representative samples of snoring associated with the patient's airway condition. To this end, a broad research experiment was carried out to build a database of signals representative of various disease stages. During the experiment, acoustic signals of patients referred for surgery were recorded. Acoustic recordings were carried out in the operating room, and patients were pharmacologically dormant. The measuring microphone was placed directly above the patient. Acoustic recordings of over 100 patients were obtained through the experiment. An example of registration is shown in Figure 1.

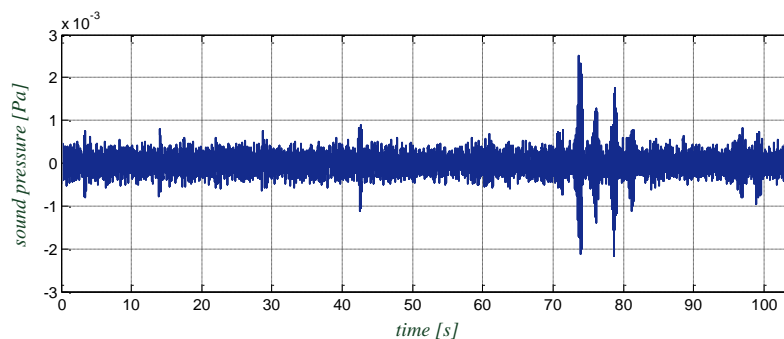


Figure 1. An example of changes in sound pressure during sleep breathing disorders

Recorded time courses contain a number of sounds and information not related to breathing. The fact that the recording of acoustic signals was carried out in pre-operative conditions meant that in addition, signals generated by operating medical equipment or conversations of medical staff were recorded.

3. Separation of useful information

For the purposes of analyzing the collected research material, information related to the analyzed disorders had to be separated from the general information. The frequency range in which information about breathing disorders is visible has been determined by analysis. Filtering frequencies out of range does not affect the correct conclusion of breathing disorders. The result of the filtration is shown in Figure 2. The development of a filtration procedure using a well-defined band containing information on breathing disorders allows to minimize the impact of external disturbances, not only generated by medical equipment. This conclusion was also confirmed on the basis of signals recorded at home.

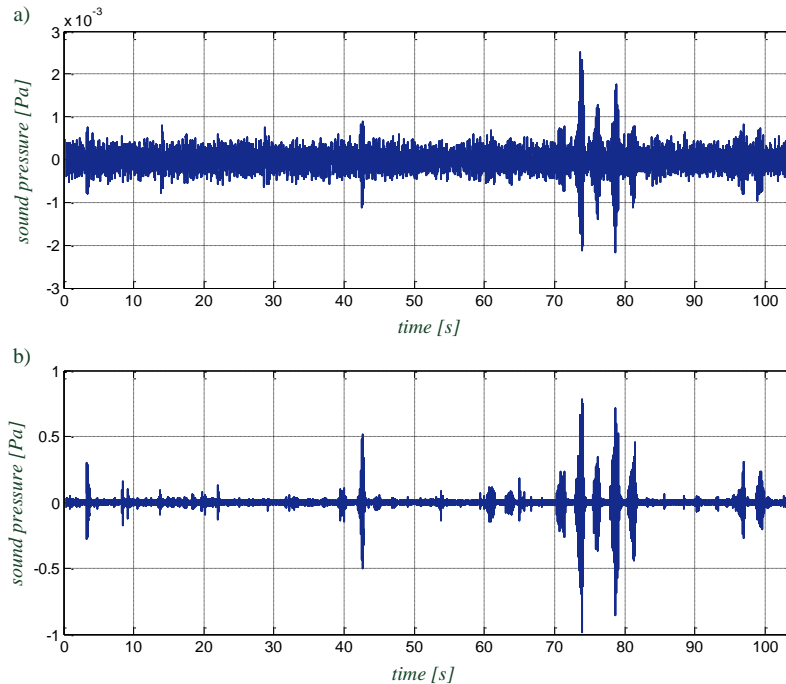


Figure 2. Recorded sound pressure waveforms:
a) original signal, b) signal after applying bandpass filtering

The signals prepared in this way could be further processed. The basic assumption was to create an inference procedure for an uncomplicated and universal application that allows for making a preclinical diagnosis at home using classic mobile devices. This forced minimizing the collected data. While collecting data from several hours of registration is not a problem, analyzing this data can be difficult, if at all possible. In this situation, it was decided to minimize the input data already at the registration stage. It was assumed that only data that contains as much information about breathing disorders as possible will be saved. It was therefore necessary to precisely determine the beginnings of subsequent registrations. For this purpose, simple indicators were calculated that would allow determining the threshold for triggering data recording. Finally, the effective value calculated in time intervals from $\frac{1}{4}$ second was selected. Figure 3 shows the rms value over a specific time period for the original signal (Fig. 3a) and the signal after applying bandpass filtration (Fig. 3b).

It seems that generally small, in terms of energy, external interference should not significantly affect the inference. Even if in total they constituted a significant part of the signal energy, it would be possible to apply appropriate procedures eliminating their adverse effect on the basic diagnostic information. Unfortunately, this makes it very difficult to determine the explicit starting point for registration (Fig. 3a).

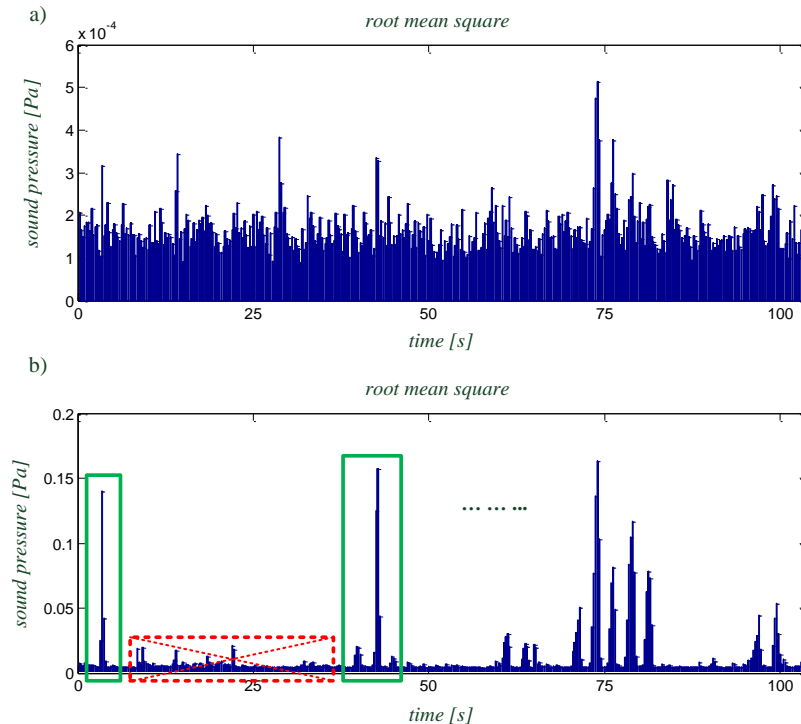


Figure 3. RMS waveforms calculated in $\frac{1}{4}$ second time intervals:
 a) original signal, b) signal after applying bandpass filtration

The use of bandpass filtration has allowed not only to precisely determine the start of registration, thereby limiting the input data, but also to select data relevant for inference. Finally, it was determined that a further 3-fold background exceeding by 20% by the effective value integrated in $\frac{1}{4}$ second intervals would initiate the recording of a 60-second fragment.

4. Proposal of a diagnostic indicators

In [7] has been shown that detailed analysis of the spectral images of structures allows precise and unambiguous identification of respiratory disorders of sleep phase. The assumption of using the inference procedure at home, using universal mobile devices, forced the minimization of the mathematical apparatus used. Unfortunately, in this case classical Fourier analysis is not enough. Based on FFT, it is possible to indicate the dominant problem, but without detailed inference. Therefore, it was finally decided to simultaneously analyze in the field of time and frequency. An example of the result is shown in Figure 4.

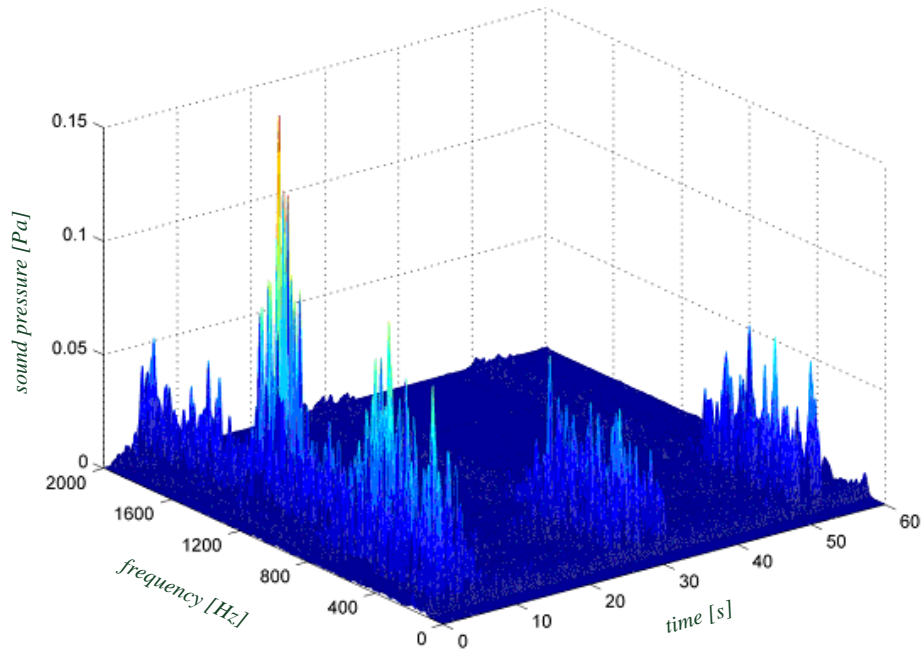


Figure 4. Instantaneous spectrum of the sample registration

Comparing the instantaneous spectra of different patients, similarities in structure were noted for patients who were medically diagnosed with similar respiratory problems; significant differences in spectrum structures were also found for various diseases. On this basis, the hypothesis was formulated that it is possible to build a database of measures allowing not only to determine whether a person requires the intervention of a doctor, but also to pre-select the disease. Simultaneous analysis in the time and frequency domains allowed for a broader structure assessment and specific indication of the problem. Ultimately, it should also be able to estimate the duration of the disorder, thereby determining the intensity of a particular breathing abnormality. Focusing on isolating the symptoms of basic respiratory disorders during sleep, a measure in the form of effective value of instantaneous spectra calculated in 500 Hz bands was proposed (Fig. 5).

Patients whose acoustic registrations were analyzed were previously comprehensively diagnosed in clinical settings. Detailed information about the diseases will confront the causes of the occurring disorders with the diagnostic measures obtained and will enable the assignment of measurements to a specific breathing disorder.

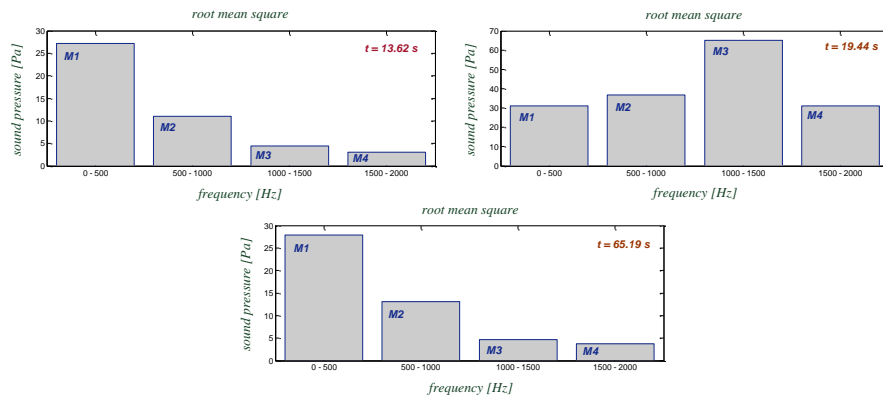


Figure 5. Examples of measures extracted from the instantaneous spectra

5. Conclusions

The results achieved during the work on the subject allowed to proceed to the development of an application for preclinical assessment of sleep breathing disorders based on an acoustic signal. Implementation of the application on mobile devices will allow patients to get a preliminary diagnosis about the potential health hazards and guidance of the possible desirability of detailed clinical diagnostics.

The experience to date creates premises for the possibility of using the developed methodology in the direction of the development of tools supporting ENT doctors in the process of diagnosing sleep breathing disorders, and even in choosing the appropriate, the most effective treatment.

References

1. M. Michalik, M. Wiśniewski, *Sleep apnea*, [in Polish:] *Bezdech senny*, Medical Tribune Stomatologia, **11** (2009).
2. M. Michalik, M. Wiśniewski, *Treatment of Obstructive Sleep Apnea Syndrome*, [in Polish:] *Leczenie OSAS*, Medical Tribune Stomatologia, **12** (2009).
3. A. Levartovsky, E. Eliran Dafna, Y. Zigel, A. Tarasiuk, *Breathing and snoring sound characteristics during sleep in adults*, Journal of Clinical Sleep Medicine, **12/3** (2016) 375 – 384.
4. C. Janott, B. Schuller, C. Heiser, *Acoustic information from snoring sounds*, HNO, **2** (2017) 107 – 116.
5. D. Pevernagie, R. M. Aarts, M. De Meyer, *The acoustics of snoring*, Sleep Medicine Reviews, **14/2** (2010) 131 – 144.
6. W. Wszolek, M. Kłaczyński, *Comparative study of the selected methods of laryngeal tone determination*, Archives of Acoustics, **31/4** (2006) 219 – 226.
7. D. Górnicka, G. Klekot, M. Michalik, *Examinations of acoustic signals of patients having snoring problem*, Journal of Vibroengineering, **19/7** (2017) 5553 – 5559.

Vibration Signal as a Support for the Processes Production Management in Enterprises of the Furniture Industry

Dorota GÓRNICKA

*Institute of Machine Design Fundamentals, Warsaw University of Technology,
ul. Narbutta 84, 02-524 Warszawa, Poland,
dorota.gornicka@pw.edu.pl*

Katarzyna SZWEDZKA

*Faculty of Engineering Management, Poznan University of Technology,
ul. Strzelecka 11, 60-965 Poznań, Poland,
katarzyna.szwedzka@put.poznan.pl*

Abstract

Activities of maintenance services cover not only the performance of ongoing repairs, but, above all, the prevention of failures and downtime. Adopting preventive measures to maintain machinery and equipment in manufacturing enterprises has a significant impact on the timely execution of orders, which is why monitoring the state of the machine park is becoming common in robotic manufacturing enterprises. Currently, the most frequently observed diagnostic parameters relate to machine vibrations. Information on exceeding the permissible thresholds allows for appropriate reaction of maintenance services aimed at minimizing unplanned downtime. The diagnostic aspect is beyond dispute here. However, there is a question whether the vibration signal can additionally be a carrier of information about the production process - information that can be used at the stage of technological process assessment, or even at the stage of process control?

Searching for the answer to this question, one of machining centres for mass production of glued panels in the furniture industry was analyzed. Information obtained from maintenance services was confronted with information from standard vibration measurements. The article is an attempt to answer the question of how to properly use at the management stage knowledge of vibration signals generated by motors mounted on the production line.

Keywords: machine vibration, management, machining centre, furniture industry

1. Introduction

The technological process in enterprises serially producing furniture requires the use of specialized machinery and equipment adapted to specific features of the products. These facilities are machining centres in which working functions are simultaneously performed, which are the result of coupled working and auxiliary processes carried out in various interconnected machines and devices operated by specialist personnel [1]. The task of machining centres is to use the processed material to obtain an object of the desired shape, dimensions, accuracy and surface roughness [2, 3]. In addition to high technological and production efficiency, a high level of reliability of the machine parks is expected to be realized by eliminating the occurrence of defects that stop the flow of materials during the production process.

The article focuses on one of the elements of the machining centre, which is the milling tenoning machine. In the analyzed enterprise, the machines belong to the class of roll-through machine tools designed for processing wooden elements. The work of sawing machines consists in formatting boards to the net dimension and making tenon joints. The tenoning machine enables the machining of tenons and bridle joints, especially in the case of frame components or other square timber, as well as making the desired profile or chamfer. The machine tool equipment includes sawing, formatting and grinding aggregates. Machining of elements on milling tenoning machines is carried out by means of feed motion at high speeds [4, 5].

Daily operation of electrically powered milling tenoning machines carries the risk of wear or damage to motors driving, among others, sawing, formatting and grinding spindles. In the case in question, despite the periodic inspection of vibration measurement, it happens that motor damage occurs prematurely and it is impossible to clearly determine the time of trouble-free operation. The durability of motors given by manufacturers is only an estimated period and the actual working time until damage occurs depends on many internal and external factors. The influence of internal factors includes quality of workmanship, assembly precision, proper lubrication and working temperature. External factors affecting the technical condition of motors include the direct impact of the material being processed and the degree of load on the machining centre caused by the execution of the production plan. In order to determine the current state of machinery and forecast the time of trouble-free operation of motors, the company regularly checks vibroacoustic measurements. In principle, such an action should prevent the occurrence of failures and assist maintenance services in planning necessary preventive measures as well as prevent premature replacement of a functioning bearing [6]. The use of diagnostics is particularly important in the described example because machining centres are a critical element of the technological process [7]. Damage to motors causes costly repairs and several hours of production downtime (the specificity of the material being processed causes a layer of dust and resin to form on the surface of the motor, which is extremely difficult to remove). Of course, early detection of damage to the motor element can prevent failures of its subsequent elements, which in turn can lead to the destruction of the entire motor. This, however, is associated with unplanned high financial outlays. Despite the possibility of generating losses, the company often decides to maximize the use of motors until they are completely damaged [8].

The polemic of the diagnostic technician and specialist in the field of maintenance of the production line undertaken in the study will, in effect, answer the question whether strictly diagnostic vibration information will allow the assessment of the technological process. The use of such information at the stage of optimization of the technological process would allow, while not increasing costs, to increase the reliability of long-term operation of machines, and thus the efficiency of production.

2. Information from the vibration signal

The company conducts diagnostics of production lines based on the DIN ISO 10816 standard “Mechanical vibrations – Assessment of machine vibrations based on

measurements of non-rotating parts.” This standard was developed to ensure the reliable and long-term operation of machinery. It sets general conditions and procedures for measuring and assessing the vibration of non-rotating machine parts whose general assessment criteria relate to both operational and acceptance tests.

The analyzed company conducts vibration measurements for all electric motors in the line along with their assessment in accordance with the assumptions of the standard. The recorded vibration parameter is the speed amplitude [9, 10]. The measuring points are located on bearing supports, both on the drive and anti-drive side. Vibration speed registration is carried out during the operation of the machine. The measurement includes not only two points for each motor, but also three measurement directions for each measuring point. For this class of machines, the standard provides for threshold limits (assessment zones):

- A – vibrations of newly introduced machines,
- B – machines that are usually considered fit for unrestricted long-term operation,
- C – machines that are usually considered unfit for continuous long-term operation,
- D – vibration values in this zone are usually considered to be intense enough to cause damage to the machine.

The presented analyses cover the work of the facility in the period from August 2014 to February 2017, with measurements carried out at three-month intervals.

Figure 1 shows an example of the course of instantaneous vibration speeds for the motor driving the S6L spindle. Machine vibrations reach a very high level with one of control measurements on the drive side. Besides this one measurement, the vibration of the machine is at the vibration level of newly introduced machines. The results of vibration registration on the drive side indicate that in the entire period considered the machine was working properly. The high level of vibration coincides with the slowdown of the production line speed. During this period the line speed was reduced from 45 m/min to 30 m/min. This situation was observed on several other motors of the machining centre, but it was not a general reaction of the system. Could the change in line speed be a direct cause of such a large increase in vibration, thereby significantly exceeding the D threshold? The fact that a significant excess of the “permissible” level of vibration occurs on several line motors at the same time rather leads to the conclusion that it is caused by the performance of the production process and not by sudden failure of several machines at the same time. It was necessary to check the response of maintenance services to the situation and answer the question whether any actions were taken and, if so, which ones.

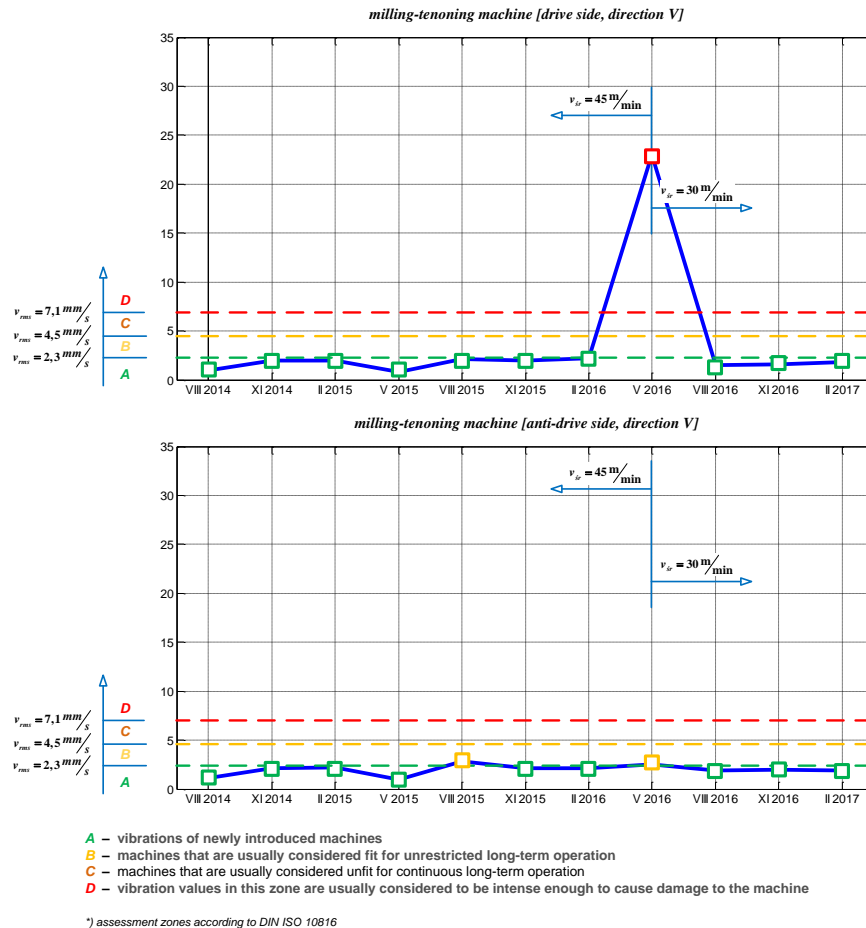


Figure 1. The course of momentary vibration speeds of the motor driving the S6L spindle

Figure 2 shows the course of momentary vibration speeds of the motor driving the S12L spindle. In this case, we also observe an increase in vibration, which coincides with the time of reducing the speed of the production line, with the difference that this increase occurs simultaneously on the drive and anti-drive side. In addition, it is worrying that after recording the first significant instance of exceeding the D threshold (vibration values in this zone are usually considered intense enough to cause damage to the machine) with the next measurement vibration speeds are even higher. Looking at the measurement results of the anti-drive side, we see that the motor mainly worked in zones where machines are considered unfit for long-term operation. Was corrective action taken in this situation? The results of vibration measurement allow us to state that such actions were not taken.

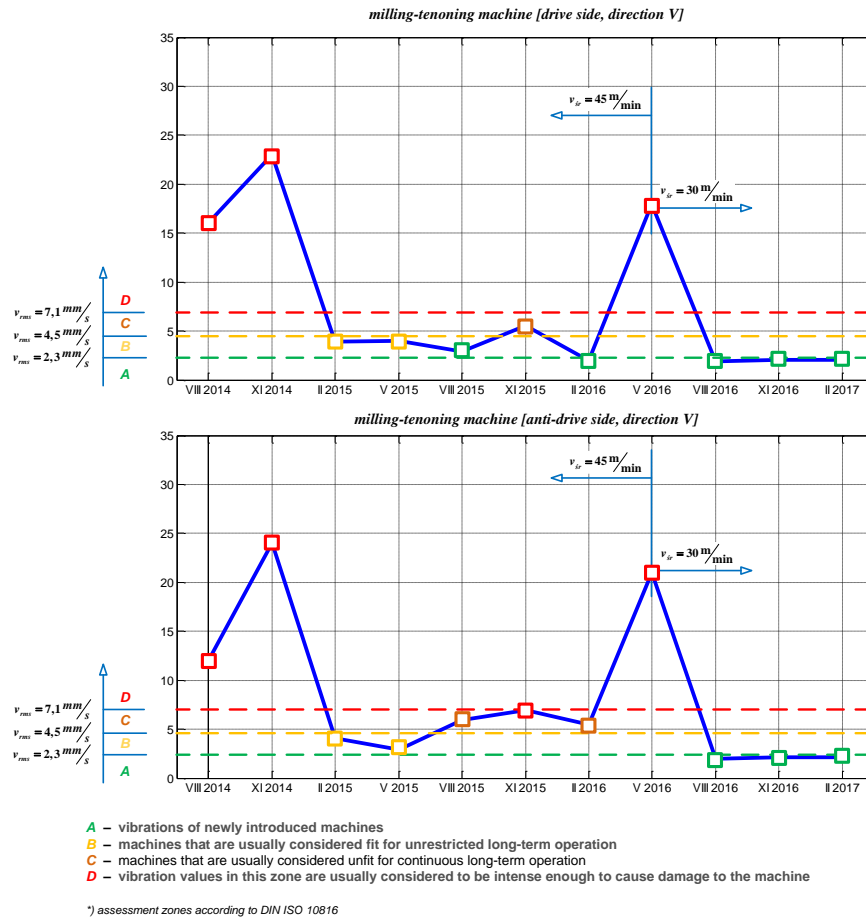


Figure 2. The course of momentary vibration speeds of the motor driving the S12L spindle

In the case of the motor driving the S13P spindle (Fig. 3), no increase in vibration was observed when the production line speed was reduced. Measurement on the anti-drive side indicates that the “safe” level of vibration is only slightly exceeded. In the next measurement, however, we observe, like in the case of the S12L motor, the long-term operation of the machine in a zone that should exclude the machine from operation.

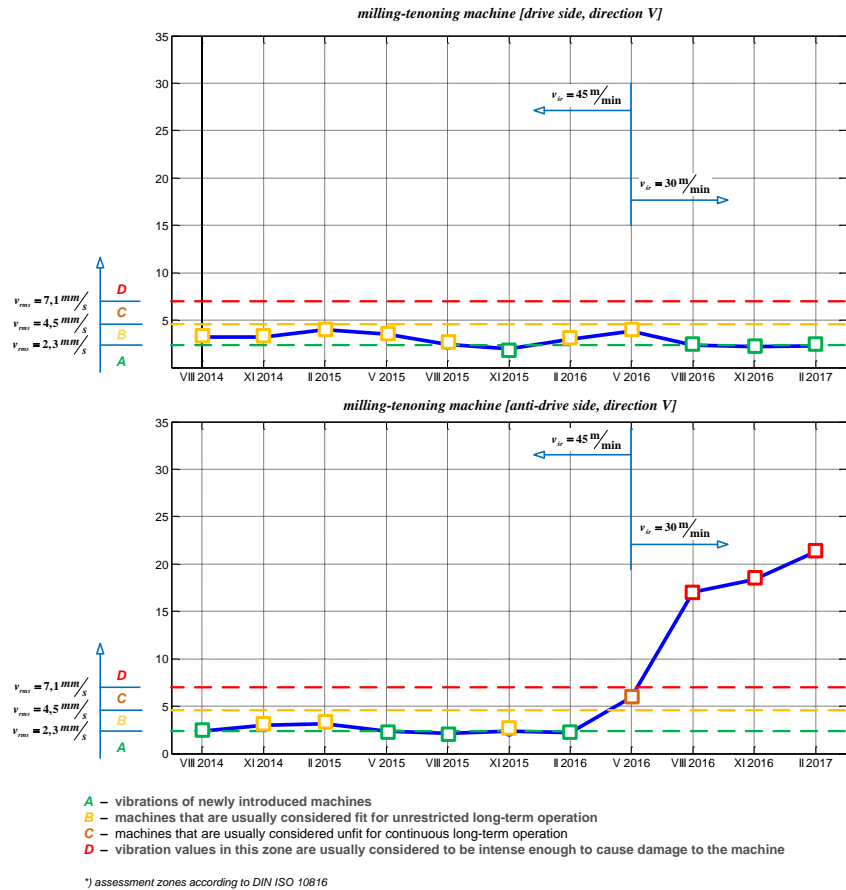


Figure 3. The course of momentary vibration speeds of the motor driving the S13P spindle

The conclusions drawn from the observation of standard vibration measurements enable us to state that the vibration signal can allow to infer about the correctness of the technological process carried out at the analyzed machining centre. However, final inference requires that information obtained from vibration measurements is confronted with information on actions taken by maintenance services.

3. Information from maintenance services

The machining centre described in the article is mainly intended for the production of large-dimension elements (theoretically it was designed in such a way). High working speeds with high demand of aggregates for power meant that motor components were subject to excessive wear, which ultimately led to frequent failures as a result of machining large profiles. The decision to reduce the conveyor speed significantly

extended the time of trouble-free operation of the technical system. Let us return to the comments presented in the previous chapter. The results of vibration measurements showed the work of motors in the zone in which the dynamic state of the milling tenoning machine was classified as “unacceptable”. The results of standard vibration measurements were compared with information collected by maintenance services. The information obtained from the company stated that exceeding the “permissible” levels of vibration resulted mainly from poor technical condition of bearings and improper balance of the tool. The diagnostic technician's recommendations included the necessity to carry out repairs involving the replacement of bearings as well as cleaning and balancing the tools. The decision of maintenance services was to increase the time the element went through the machining process (the speed of the milling aggregate did not change). From the perspective of the technical systems, the decision, mainly based on the knowledge possessed by maintenance services and servicing employees, was right. However, it is necessary to consider the efficiency of operating such a centre [11]. The decision slowed down the process of motor degradation only to some extent, because as a result of subsequent diagnostic measurements the dynamic condition of the milling tenoning machine was classified in zone C – “temporarily permissible”. The company consciously slowed down the technological process without exploring the essence of the problem. Activities undertaken were short-term. A direct consequence of the decision will be a short downtime caused by a failure (a random event occurring during the performance of a task). However, at this point it is worth considering whether losses associated with the inefficient use of the production line will not be higher. The analysis of the total availability of the facility proved that it was effectively operated at 45%. The remaining time is stoppages when theoretically the facility remains fit to be used. Practice shows that extensive knowledge of the facility is not fully utilized in activities undertaken by maintenance services and by persons responsible for controlling the course of the production of elements. As a result, financial losses are directly related to the major overhaul of the motor. Costs caused by the inefficient operation of the machining centre are not calculated. In a situation where it is possible to perform 100% of the order, the operator enters the “slow speed” code into the system and performs about 70-80% of the order [12, 13]. From his perspective, this is the right thing to do, because otherwise he would be forced to enter the “electrical failure” code, where the technical system would remain in a state of inactivity for 4 to 6 hours.

4. Conclusions

To summarize, one gets the impression that the company has knowledge of the technical condition of motors. However, this information is not fully consulted with persons responsible for the performance of the production plan, or it is not used constructively. The presented results of standard vibration measurements show that with the appropriate combination of information from maintenance services and information obtained through technical diagnostics, one can properly control the production, management and repair processes, thereby increasing production efficiency and reducing maintenance costs. Including in the inference additional information about the mass of manufactured elements would allow to perform a comprehensive assessment of the state of

the machine park and the course of the machining process. Information about the mass of manufactured elements and knowledge about their impact on the occurrence of failures can help in better planning of renovation and management tasks. Appropriate management of decision-making, preventive and corrective actions will reduce the occurrence of failures, which will result in a higher probability of timely execution of the process and reduce the costs related to failures.

References

1. J. Dietrich, *System i konstrukcja*, Wydawnictwo WNT, Warszawa, 1985.
2. T. Karpiński, *Inżynieria produkcji*, Wydawnictwo WNT, Warszawa 2013.
3. K. Szwedzka, M. Jasiulewicz-Kaczmarek, *Determining maintenance services using production performance indicators*, Research in Logistics & Production, **6**(4) (2016) 361 – 374.
4. T. Gawroński, *Technological process optimization for the pretreatment of solid wood furniture elements*, Forest Products Journal, **59** (2009) 63 – 68.
5. T. Gawroński, *Optimization of CNC routing operations of wooden furniture parts*, The International Journal of Advanced Manufacturing Technology, **67**(9) (2009) 2259 – 2267.
6. M. Jasiulewicz-Kaczmarek, P. Drożyner, *Maintenance Management Initiatives towards Achieving Sustainable Development*, In: P. Golinska et al. (eds.): Information Technologies in Environmental Engineering Environmental Science and Engineering, Springer - Verlag Berlin Heidelberg, (2011) 707 – 721.
7. K. Szwedzka, P. Szafer, R. Wyczółkowski, *Efficiency of complex technical systems – case study*, Topics in Intelligent Computing and Industry Design, **1**(1) 148 – 154.
8. L. Drelichowski, W. Bojar, M. Żółtowski, *Elementy zarządzania eksploatacją maszyn*, Wydawnictwo Uczelniane Uniwersytetu Technologiczno-Przyrodniczego, Bydgoszcz, 2012.
9. C. Cempel, *Mechanical Vibrations – Introduction* (in Polish), Poznań: Wydawnictwo Politechnika Poznańska (The Publishing House of Poznan University of Technology), 1982.
10. C. Cempel, F. Tomaszewski, *Diagnostics of machines* (in Polish), Radom: MCNEMT, 1992.
11. M. Jasiulewicz-Kaczmarek, *Integrating Lean and Green Paradigms in Maintenance Management*, In: E. Boje, X. Xia, (eds.), Proceedings of the 19th IFAC World Congress Cape Town, South Africa., 4471 – 4476.
12. M. Jasiulewicz-Kaczmarek, K. Szwedzka, *Were our leaders ready to implement the changes? – a case study*, in: X.-G. Yue, N. J. R. Duarte (eds.), Proceedings of the 2016 International Conference on Economics and Management Innovations, part of Advances in Computer Science Research, **57**, 267 – 271.
13. M. Jasiulewicz-Kaczmarek, T. Bartkowiak, *Improving the performance of a filling line based on simulation*, ModTech International Conference - Modern Technologies in Industrial Engineering IV, IOP Conf. Series: Materials Science and Engineering **145**, Iasi, Romania, June 15-18, 2016.

Nonlinear Vibrations of the Partially Tensioned System Taking into Account the Asymmetry of the Stiffness of Supports

Sebastian UZNY

*Częstochowa University of Technology,
Institute of Mechanics and Machine Design Foundations,
ul. Dąbrowskiego 73, 42-200 Częstochowa, uzny@imipkm.pcz.pl*

Michał OSADNIK

*Częstochowa University of Technology,
Institute of Mechanics and Machine Design Foundations,
ul. Dąbrowskiego 73, 42-200 Częstochowa, mosadnik@imipkm.pcz.pl*

Abstract

The nonlinear vibrations of the partially tensioned slender column are presented in this paper. The considered system is subjected to Euler's load, which direction of action is consistent with the non-deformed axis of the column. The magnitude of the external load is variable and its application point is located at different heights between the upper and lower supports. In addition, the longitudinal displacement and rotation of both of the system ends are limited by the discrete elements in the form of translational and rotational springs. This nonlinear system is based on the screw drive used in the vertical lift platform for disabled people or cargo lift equipped with an engine room located in the lower part of the frame. The boundary problem of free vibrations of the mentioned system has been formulated on the basis of Bernoulli – Euler theory and due to nonlinear expressions the solution of the problem was conducted with small parameter method. The results of numerical simulations are concern on linear and nonlinear component of vibrations in relation to the location of external load application and influence of asymmetric value of supports stiffness on the free vibration frequency.

Keywords: slender nonlinear systems, free vibrations, Euler's load

1. Introduction

Columns and beams are widely used as load-bearing or driving elements in mechanical engineering. Slender elements are increasingly used in construction to reduce production costs or perform specific functions. Therefore, the issue of free vibrations and stability is very important for scientific considerations. Particular attention should be paid to geometrically nonlinear systems in which the nonlinear theory and the theory of Bernoulli–Euler are used to formulate the boundary problem [1, 2]. Slender columns loaded with compressive forces usually form responsible support structures that can be exposed to dangerous resonance vibrations causing damage to the system. External loads can be classified into non-conservative [3] and conservative loads, which include Euler's force [4]. The load direction is consistent with the non-deformed axis of the system when tilting the system from the static equilibrium position. Interesting results of numerical simulations showing the impact of changes in cross-section and structure geometry on free vibrations of a non-prismatic column subjected to the active and passive follower force directed towards the positive pole are presented in [5]. In addition

to geometrical parameters and the type of system load, the use of discrete elements at supporting points has a significant impact on the system's behaviour during vibrations [4, 6, 8, 9] and critical force [7]. Partially tensioned columns including rotational and translational springs [8, 9] model the screw drive used in vertical platform lifts equipped with a machine room located in the lower part of the frame. Studies on slender partial tension systems have shown a significant effect of amplitude and susceptible elements to natural vibration frequency that can be controlled. This work concerns the numerical research on the mentioned systems regarding free vibration (linear and nonlinear component) at different locations of external load application, taking into account the asymmetry of the value of support stiffness.

2. Boundary value problem concerning free vibrations

The considered system is shown in Fig. 1. It is a column resiliently mounted at both ends (longitudinal (K_0, K_1) and rotational (C_0, C_1) elasticity limiting the rotation of the column ends were taken into account) and loaded with a force whose direction coincides with the non-deformed axis of the system. The system loading force occurs between the ends of the column. The position of the loading force was determined by the parameter ζ ($\zeta = l_1/l$). The part of the column situated above the load application point is tensioned while the part below this point is compressed. To develop the mathematical model, the column was divided into two parts.

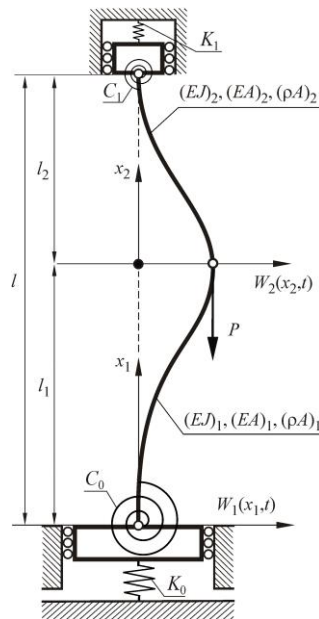


Figure 1. Physical model of considered column

The division point coincides with the point determining the position of the loading force. The lower (compressed) part is marked by index 1. The upper (tensioned) part is

marked by index 2. Bending and longitudinal stiffness and mass per unit length of rods marked with indexes 1 and 2 are the same $((EJ)_1 = (EJ)_2 = (EJ), (EA)_1 = (EA)_2 = (EA), (\rho A)_1 = (\rho A)_2 = (\rho A)$ (where: E_i – Young’s modulus of column material, ρ_i – density of column material, A_i – cross-section area, J_i – geometrical axial moment of inertia of the cross-section of i -th element of the structure).

The paper does not present in detail the boundary problem, which was formulated on the basis of the Hamilton principle and due to the occurrence of nonlinearity the small parameter method was taken into account (comp. [10]). Differential equations of motion in the transverse and longitudinal directions are as follows:

$$\frac{\partial^4 w_i(\xi_i, \tau)}{\partial \xi_i^4} + k_i^2(\tau) \frac{\partial^2 w_i(\xi_i, \tau)}{\partial \xi_i^2} + \Omega_i^2 \frac{\partial^2 w_i(\xi_i, \tau)}{\partial \tau^2} = 0 \tag{1}$$

$$u_i(\xi_i, \tau) - u_i(0, \tau) = -\frac{k_i^2(\tau)}{\Theta_i} \xi_i - \frac{1}{2} \int_0^{\xi_i} \left(\frac{\partial w_i(\xi_i, \tau)}{\partial \xi_i} \right)^2 d\xi_i \tag{2}$$

All nonlinear quantities describing the behavior of the system during vibrations were expanded into power series of a small parameter of amplitude. The dynamic properties of the column under consideration depend on the vibration amplitude. The following extensions of nonlinear components of equations into power series of the small parameter of vibration amplitude ε were used:

$$w_i(\xi, \tau) = \sum_{j=1}^N \varepsilon^{2j-1} w_{i2j-1}(\xi, \tau) + O(\varepsilon^{2(N+1)}) \tag{3}$$

$$u_i(\xi, \tau) = u_{i0}(\xi) + \sum_{j=1}^N \varepsilon^{2j} u_{i2j}(\xi, \tau) + O(\varepsilon^{2(N+1)}) \tag{4}$$

$$k_i^2(\tau) = k_{i0}^2 + \sum_{j=1}^N \varepsilon^{2j} k_{i2j}^2(\tau) + O(\varepsilon^{2(N+1)}) \tag{5}$$

$$\Omega_i^2 = \Omega_{i0}^2 + \sum_{j=1}^N \varepsilon^{2j} \Omega_{i2j}^2 + O(\varepsilon^{2(N+1)}) \tag{6}$$

$$\omega^2 = \omega_0^2 + \sum_{j=1}^N \varepsilon^{2j} \omega_{2j}^2 + O(\varepsilon^{2(N+1)}) \tag{7}$$

where:

$$w_{i1}(\xi, \tau) = w_{i1}^{(1)}(\xi) \cos \tau ; w_{i3}(\xi, \tau) = w_{i3}^{(1)}(\xi) \cos \tau + w_{i3}^{(3)}(\xi) \cos 3\tau ; \dots \tag{8, 9}$$

$$u_{i2}(\xi, \tau) = u_{i2}^{(0)}(\xi) + u_{i2}^{(2)}(\xi) \cos 2\tau ; \dots \tag{10}$$

$$k_{i2}^2(\tau) = k_{i2}^{(0)} + k_{i2}^{(2)} \cos 2\tau; \dots \tag{11}$$

In the expansions of formulas (3-7) $w_i(\xi_i, \tau)$, $u_i(\xi_i, \tau)$, $k_i(\tau)$ and Ω_i are dimensionless quantities, referred to the stiffness and length of each bars, related to transversal and longitudinal displacement, internal force and natural vibration frequency. All dependencies presented in the work were written using the following dimensionless quantities:

$$\xi_i = \frac{x_i}{l}; \zeta_i = \frac{l_i}{l}; w_i(\xi_i, \tau) = \frac{W_i(x_i, t)}{l}; u_i(\xi_i, \tau) = \frac{U_i(x_i, t)}{l}; \tag{12-15}$$

$$k_i^2(\tau) = \frac{S_i(\tau)l^2}{(EJ)_i}; \Omega_i^2 = \frac{(\rho A)_i \omega^2 l^4}{(EJ)_i}; \tau = \omega t; \Theta_i = \frac{Al^2}{J_i}; i = 1, 2 \tag{16-19}$$

Where: $W_i(x_i, t)$, $U_i(x_i, t)$ and $S_i(t)$ – dimensional quantities respectively transversal and longitudinal displacements and internal force.

The next components of nonlinear quantities are marked with the indices 0, 1, 2, For example, ω_0 – linear component of natural vibration frequency, ω_2 – nonlinear component of natural vibration frequency. The natural frequency, which is calculated using both linear ω_0 and nonlinear ω_2 components is calculated on the basis of the presented expansion into power series of small parameter (7) from the formula:

$$\omega = \sqrt{\omega_0^2 + \varepsilon^2 \omega_2^2} \tag{20}$$

The method of calculating the individual components of the quantities that are necessary to determine the natural frequency ω is as follows (see [10]):

– the distribution of external force into the bars of the column (linear component of internal forces):

$$k_{10}^2 = \frac{P \left(\frac{l^2}{(EJ)} \zeta_2 \frac{1}{\Theta_2} + \frac{1}{lK_1} \right)}{\frac{(EJ)}{l^3} \left(\frac{1}{K_1} + \frac{1}{K_0} \right) + \frac{\zeta_1}{\Theta_1} + \frac{\zeta_2}{\Theta_2}}; k_{20}^2 = k_{10}^2 - P \frac{l^2}{(EJ)} \tag{21, 22}$$

– the linear component of the natural vibration frequency ω_0 is determined from the transcendental equation obtained after taking into account the solutions of differential equations associated with ω_0 in appropriate boundary conditions.

– nonlinear components of internal forces:

$$k_{22}^{(0)} = - \frac{\frac{1}{4} \sum_i \int_0^{\zeta_i} \left(w_{i1}^{(1)}(\xi_i) \right)^2 d\xi_i}{\frac{(EJ)_2}{l^3 K_1} + \frac{(EJ)_2}{l^3 K_0} + \frac{1}{\Theta_1} \frac{(EJ)_2 \zeta_1}{(EJ)_1} + \frac{\zeta_2}{\Theta_2}}; k_{12}^{(0)} = k_{22}^{(0)} \frac{(EJ)_2}{(EJ)_1} \tag{23, 24}$$

$$k_{i2}^{(2)} = k_{i2}^{(0)} \tag{25}$$

– nonlinear components of free vibration frequency:

$$\omega_2^2 = \frac{\sum_i \left[\int_0^{\zeta_i} \frac{3(EJ)_i}{2l} k_{i2}^{(2)} w_{i1}^{(1)}(\xi_i) w_{i1}^{(1)}(\xi_i) d\xi_i + \frac{3(EJ)_1}{2l} k_{i2}^{(0)} w_{11}^{(1)}(0) w_{11}^{(1)}(0) - \frac{3(EJ)_2}{2l} k_{22}^{(0)} w_{21}^{(1)}(\zeta_2) w_{21}^{(1)}(0) \right]}{\sum_i \left[\int_0^{\zeta_i} (\rho A)_i l^3 \left(w_{i1}^{(1)}(\xi_i) \right)^2 d\xi_i \right]} \tag{26}$$

All quantities presented in this chapter (linear and nonlinear components defined by formulas (20-26)) are taken into account for presenting the results of numerical calculations.

3. Results of numerical simulations

Results of numerical simulations of free vibrations frequency of the considered partially tensioned slender system were presented in non-dimensional form, defined as:

$$\lambda = \frac{Pl^2}{(EJ)}; c_j = \frac{C_j l}{(EJ)}; k_j = \frac{K_j l^3}{(EJ)}; \zeta = \frac{l_1}{l}; \Omega^2 = \frac{\omega^2 (\rho A) l^4}{(EJ)}; j = 0, 1 \tag{27-31}$$

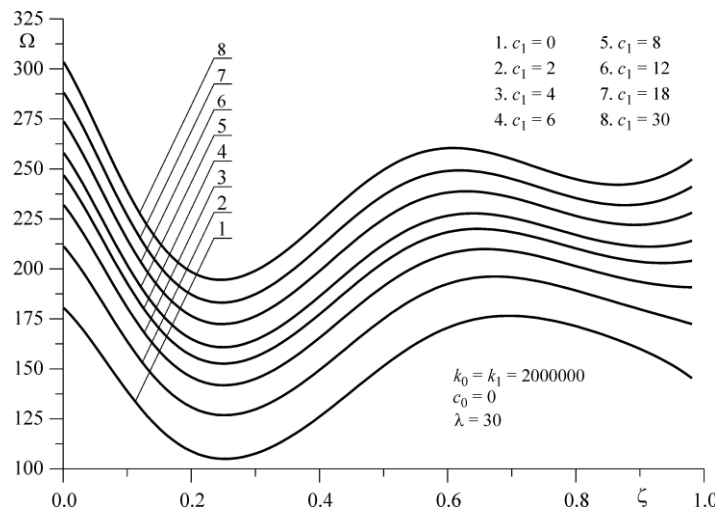


Figure 2. The relationship between natural vibration frequency Ω and the rotational springs stiffness c_0 and c_1 , at different points of external load application ζ taking into account the parameters: $k_0 = k_1 = k$; $c_0 = 0$; $\lambda = 30$

The amplitude of vibrations in numerical calculations is assumed as a double radius of gyration. Figures 2, 3, 4 show the relationship between the parameter of the first natural vibration frequency Ω and the point of external load application for different values of rotational spring stiffness limiting the rotation of the column ends. The assumed values of rotational spring stiffness are for the lower fastening $c_0 = 0, 15, 30$ and the upper $c_1 = 0, 2, 4, 6, 8, 12, 18, 30$. The value of the load parameter is constant $\lambda = 30$, while the point of its application moves along the length of the system $\zeta \in (0,1)$. The same stiffness of the translation springs at both attachment points ($k_0 = k_1 = 2 \cdot 10^6$) was assumed. Based on the numerical simulations performed, it has been observed that as the stiffness of both the lower and upper fastening increases, the natural vibration frequency increases (frequency containing both linear and nonlinear components – formula (20)).

The natural vibration frequency is strongly dependent on the position of the loading force. The difference between the highest and the lowest value of the natural vibration frequency from the factor ζ variation range depends on the stiffness of the rotational springs. With the rotational rigidity of the lower fastening $c_0 = 0$ (Figure 2) at $c_1 = 30$, the difference between the largest value and the smallest is about 35% of the value of the highest frequency from the considered factor ζ .

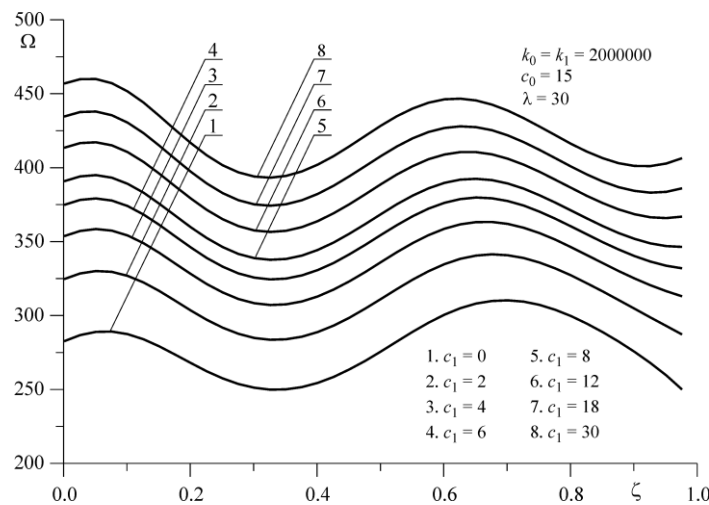


Figure 3. The relationship between natural vibration frequency Ω and the rotational springs stiffness c_0 and c_1 , at different points of external load application ζ taking into account the parameters: $k_0 = k_1 = k$; $c_0 = 15$; $\lambda = 30$

When the rotational rigidity of the lower attachment increases $c_0 = 30$, the difference considered is only about 15%. It was also observed that the highest value of the natural frequency (for bigger value of parameter c_1) occurs when the force loading the column is near the lower fastening. Depending on the rotational stiffness values, two or one local minimum and maximum of the considered curves are obtained.

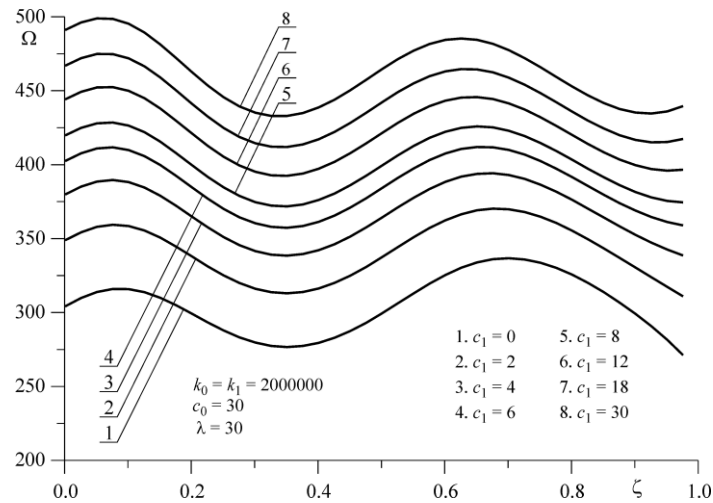


Figure 4. The relationship between natural vibration frequency Ω and the rotational springs stiffness c_0 and c_1 , at different points of external load application ζ taking into account the parameters: $k_0 = k_1 = k$; $c_0 = 30$; $\lambda = 30$

4. Conclusions

In this paper, the boundary problem of free vibrations of partially tensioned columns subjected to Euler's load was considered. The discussion includes both the linear component of the first vibration frequency and its nonlinear component, whose impact on the frequency depends on the vibration amplitude. The effect of asymmetry of the system mounting rigidity on its dynamic properties was analyzed. The considerations took into account the asymmetry in rotational stiffness limiting the rotation of both ends of the column. Based on the numerical tests carried out, it was shown that the considered natural vibration frequency is strongly dependent on the parameters of rotational stiffness. In addition, the frequency of free vibrations depends on other parameters such as location of external force, load magnitude, translational springs stiffness and physical and geometrical properties of the system. In the future, it is planned to study the effect of circular-shaped heads on free vibrations to prevent resonance in screw-driven platform lifts.

Acknowledgments

This study was carried out within the statutory funds of the Czestochowa University of Technology (BS/PB 1-100/3010/2019/P and BS/MN 1-100-301/2019/P).

References

1. L. Tomski, S. Kukla, B. Posiadała, J. Przybylski, W. Sochacki, *Divergence and Flutter Instability of the Column Supported by a Nonlinear Spring and Loaded by*

- a Partially Follower Force*, Akademiai Kiado, Publishing House of Hungarian Academy of Science, Budapest, (1990) 1227 – 1234.
2. J. Awrejcewicz, O. A. Saltykova, Yu. B. Chebotyrevskiy, V. A. Krysko, *Nonlinear vibrations of the Euler-Bernoulli beam subjected to transversal load and impact actions*, *Nonlinear Studies*, **18**(3) (2011) 329 – 364.
 3. M. A. Langthjem, Y. Sugiyama, *Dynamic stability of columns subjected to follower loads: a survey*, *Journal of Sound and Vibration*, **238**(6) (2000) 809 – 851.
 4. L. Tomski, S. Uzny, *A hydraulic cylinder subjected to Euler's load in aspect of the stability and free vibrations taking into account discrete elastic elements*, *Archives of Civil and Mechanical Engineering*, **11**(3) (2011) 769 – 785.
 5. J. Szmidla, A. Jurczyńska, *Free vibrations of the slender nonprismatic column under the passive and active follower force directed towards the positive pole*. *Engineering Mechanics*, **24** (2018) 845 – 848.
 6. E. Nowak, K. Nowak, P. Obara, *Influence of elastic support on the eigenvalues of stepped columns* (in Polish), *Metal Structures*, (2014).
 7. S. Uzny, M. Osadnik, *Influence of longitudinal elastic support on stability of a partially tensioned column*, *Engineering Mechanics*, (2017) 1006 – 1009.
 8. S. Uzny, M. Osadnik, *Influence of the longitudinal spring element on free vibrations of the partially tensioned column*, *Procedia Engineering*, **17** (2017) 135 – 140.
 9. S. Uzny, M. Osadnik, *Influence of rotational stiffness of support of a partially tensioned column on its free vibrations*, *Engineering Mechanics*, (2018) 889 – 992.
 10. S. Uzny, M. Osadnik, *Nonlinear component of free vibration frequency of a partially tensioned system with consideration of rotational stiffness of support*, *Journal of Applied Mathematics and Computational Mechanics*, **18**(3) (2019) 89 – 96.

The Opinion of Impact of Energy Dissipation in a Vehicle Suspension on Mechanical Energy Transfer

Jan WARCZEK

*Silesian University of Technology, Faculty of Transport,
Krasieńskiego street 8, 40-019 Katowice, jan.warczek@polsl.pl*

Abstract

Effective shock absorption of the body in the presence of excitations of a random nature results in the necessity of using vibration dampers. The classic solution is the viscous damper, which works by dissipating mechanical energy in the form of heat generated to the external environment. The characteristics of the flexible components in car suspensions (elastic and damping) affect the transfer of mechanical energy. The purpose of the research was to develop a method for assessing the impact of damping in a suspension system on the transfer of mechanical energy from unsprung masses to the body. The assumed research goal was carried out on a vehicle model with two degrees of freedom, whose parameters corresponded to the real object. The developed method uses energy relationships occurring between selected variables of the vibrating motion of inertial elements of a motor vehicle. The results obtained during simulation tests were empirically verified on a real object. The proposed method allows to assess how the damping in the suspension system affects the energy relationships occurring in the vehicle suspension vibrating motion.

Keywords: energy of mechanical vibrations, vehicle suspension, damping

1. Introduction

Vibration forces acting on the vehicle lead to vibrations in all its structural elements. To ensure comfort and safety of travel, the most measurable are the final effects of energy conversion of vibration excitations on the body (comfort) and on the wheels (safety). The negative impact of vibrations on persons and loads transported by road means of necessity of their minimization. To this end, solutions leading to vibration damping are commonly used in the construction solutions of vehicle suspension. The issue of vibration damping in the most general case boils down to the use of flexible (elastic) elements that act as time buffers in the transfer of mechanical energy [2, 3, 5, 8, 13, 14]. The use of a damping element with high compliance in the suspension leads to a favourable reduction of resonance vibration amplitudes at the expense of worsening of the depreciation in non-resonant areas. The characteristics of the flexible components in car suspensions (elastic and damping) affect the transfer of mechanical energy.

Depending on the adopted scale (size) of the object, vibration analysis can be carried out in relation to selected elements or entire objects. In special cases, vibration analysis can be carried out for individual material points. In motor vehicles, depending on the purpose adopted, the purpose of testing vibration properties is carried out in terms of full vehicle load or within the scope of selected subsystems or structural elements. The vibration properties of construction elements are also optimized, e.g. by using the finite or edge element method [1, 10, 11, 16, 18, 23].

2. The aim of research

Research on real objects is time consuming and very expensive. An alternative, which is simulation research, allows obtaining knowledge about physical phenomena using a computer and appropriate software. In the analysis of energy transformations occurring in a vibrating object, a very popular mathematical modelling tool is to describe such a system using second-order Lagrange equations. In modelling the work of a vehicle suspension, the system often used is to describe this system in the form of a two-mass model with two degrees of freedom [4, 6, 7, 9, 12, 15, 17, 19]. The purpose of the research was to develop a method for assessing the impact of damping in a suspension system on the transfer of mechanical energy from unsprung masses to the body. The assumed research goal was carried out on a vehicle model with two degrees of freedom, whose parameters corresponded to the real object. In the developed method, relationships between selected RMS of variables of vibrating motion of inertial elements of a motor vehicle were used. The results of simulation tests were verified by tests on a real object.

3. The simulation research

The physical model of the suspension has the following on figure 1.

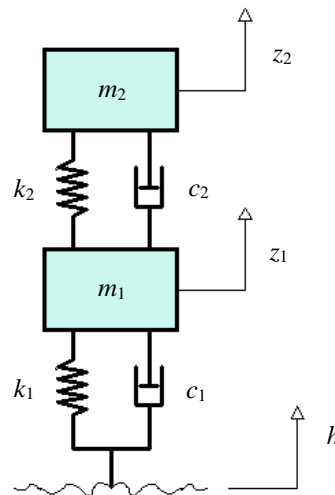


Figure 1. Model of vehicle suspension, m_2 – mass of the sprung part, m_1 – mass of the unsprung part, k_2 – suspension stiffness coefficient, k_1 – wheel stiffness coefficient, c_2 – suspension damping coefficient, c_1 – wheel damping coefficient, h – excitations from road roughness, z_2 – vertical displacements of the sprung mass, z_1 – vertical displacements of the wheel (unsprung masses)

The quarter suspension model can be treated as a good representation of the system dynamics provided that the following assumptions are taken into account:

- the vehicle has a symmetrical structure,
- the vehicle parts (sprung and unsprung parts) are rigid bodies whose masses are concentrated at their centres of gravity,
- mechanical ratios resulting from the design of the suspension linkage system will be taken into account. So the damping characteristics and stiffness of the respective elements are multiplied by these coefficients.

The assumed physical suspension model was introduced in the form of a system of differential equations to the Matlab / Simulink program.

Motor vehicles are operated on roads with different surfaces. The road profile can theoretically take a variety of deterministic and stochastic forms, but in practice only for special road test sections can it be assumed that the surface can be described by strict mathematical functions. In real conditions, road surfaces on which motor vehicles travel are best characterized by the road profile defined by the power spectral density of inequalities [6, 20, 21, 22]. In accordance with applicable standards, the road profile is described by means of unevenness of the road surface measured along the trace of cooperation of the vehicle wheel with the road surface. Measurements of the height of unevenness of the road surface are recorded with a constant distance of the road length. The irregularity profile registered in this way is the basis for calculating the parameters of longitudinal unevenness. Based on the uneven profile, a set of longitudinal road unevenness parameters is calculated, of which the most important is the IRI (International Roughness Index).

In the conducted simulation tests deterministic extortion was used. The use of explicitly defined enforcement allows a convenient qualitative and quantitative interpretation of the obtained results. Knowing the nature of the functioning of the tested system, it is possible to extend the scope of analyzes to include random excitations that correspond to the actual operating conditions of the vehicle suspension system.

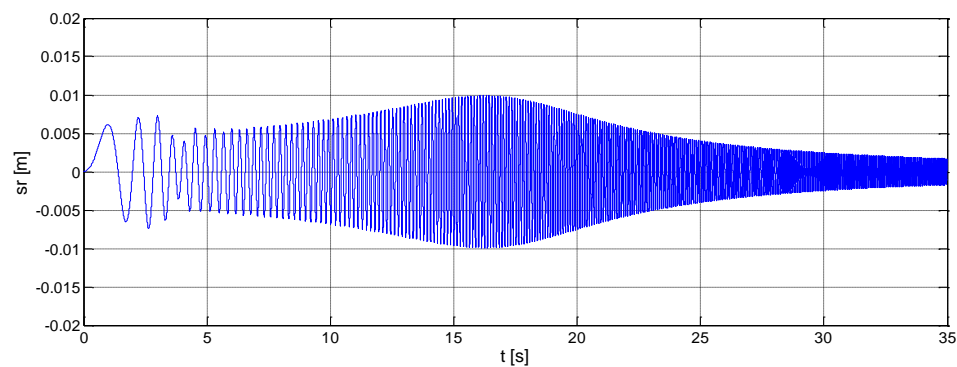


Figure 2. Relative masses displacements (m_2 and m_1) for chirp type excitation (amplitude 6 mm, frequency range 0-20 Hz)

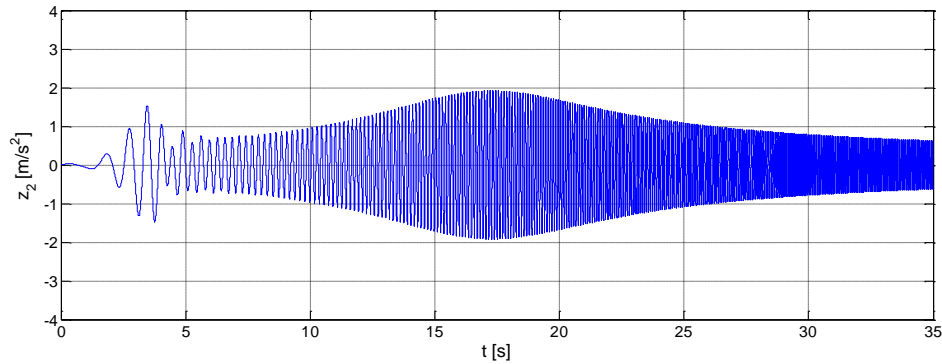


Figure 3. Acceleration of mass m_2 for chirp type excitation (amplitude 6 mm, frequency range 0-20 Hz)

Figures 2 and 3 show the vibration signals obtained during the simulation tests of body accelerations and suspension deflections under sinusoidal excitation with a linearly increasing frequency (chirp), whose amplitude was 6 mm.

The measures of vibration energy used to analyze the vibration energy transfer were the effective values of selected physical quantities describing the object's vibration. The kinetic energy of the vehicle body mass oscillation is dependent on the square of velocity. The effective values of vibration acceleration are an energy measure that describes the energy of the system. Potential energy in oscillating motion depends on the square of the suspension spring deflection. The effective spring deflection value is related to the potential energy transferred by the spring to the body. These are not simply energy values, but rather measures describing the energy relationships occurring during the motion of a vibrating suspension. For certain conditions of excitation of vibrations, the amount of dissipated energy is constant and the suspension system is in a specific dynamic state. Changing the damping in the system with constant excitation leads to changes in the energy transmitted to the vehicle body. To assess the transmission of vibration energy on the body, the relationship between the effective values was used: acceleration of body vibration and relative wheel displacement relative to the body defined as:

$$sr_{\text{RMS}} = \sqrt{\frac{1}{T} \int_0^T sr(t)^2 dt} \quad (1)$$

$$\ddot{z}_{2\text{RMS}} = \sqrt{\frac{1}{T} \int_0^T \ddot{z}_2(t)^2 dt} \quad (2)$$

where: $sr(t)$ – suspension deflection,

$\ddot{z}_2(t)$ – acceleration of the sprung mass.

The recorded signals were divided into time fragments with a length of 1 second and effective values were determined for each window in accordance with formulas 1 and 2. Then the determined values were marked on a common plane of energy relationships between the analyzed vibration signals. Figure 4 presents the impact of the damping change on the determined relationships.

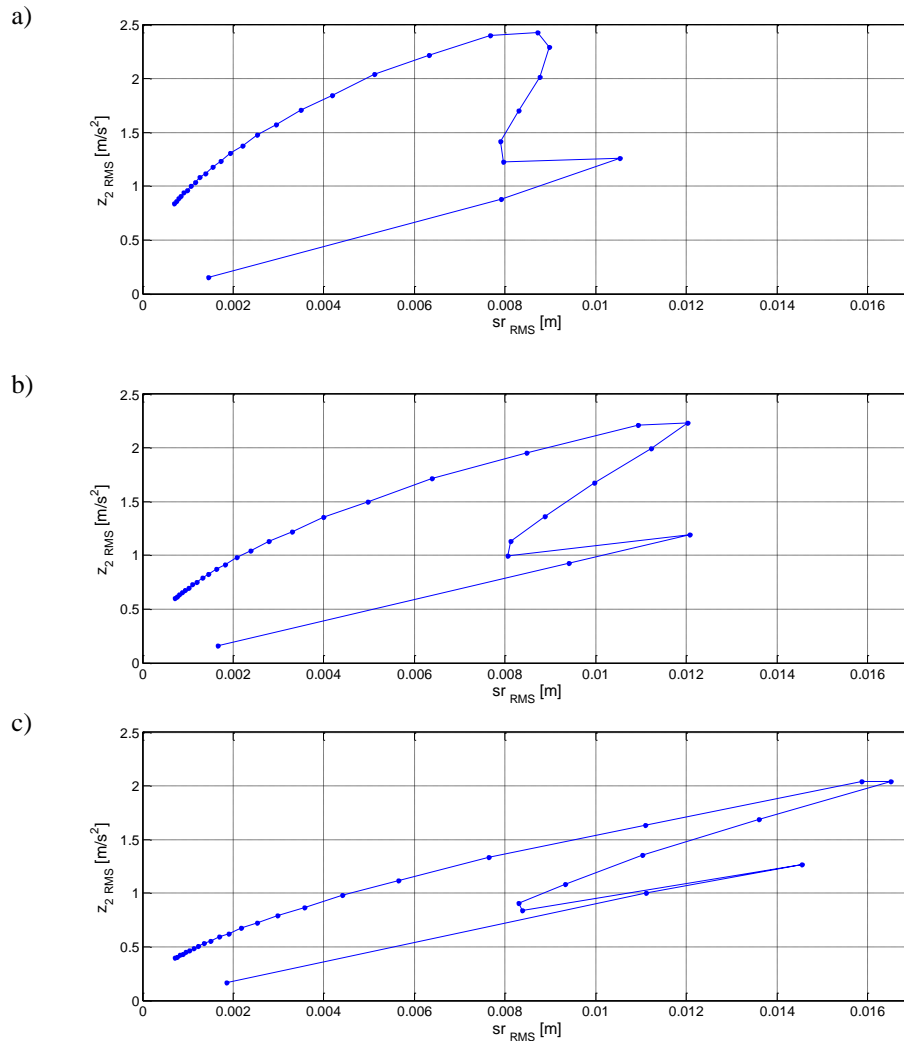


Figure 4. The relations of RMS of body of car accelerations (m_2) and suspensions deflections (sr) for excitations with an amplitude of 6 mm in the frequency range from 0 to 30 Hz for damping of: a) 100% nominal, b) 70% nominal, c) 40% nominal

The determined curves show similarity to the attractors used in the analysis of chaotic vibrations. Along with the progressing wear of the shock absorber and thus the damping in the suspension, which decreases in this way, the designated curve gradually turns in the direction of the abscissa with a clear narrowing (Fig. 4c).

4. Research on a real object

Experimental confirmation of the correctness of the proposed method was carried out during the bench tests of the hydropneumatic suspension of a passenger car, the basic element of which is a hydropneumatic column. The damping characteristics of the hydropneumatic column were determined during the tests at the indicator stand. In this way, work charts for different sinusoidal excitation frequencies were obtained. On the basis of the intersection points of the work charts with the abscissa, where the maximum damping force occurs for the highest relative speed of the piston movement, points describing the damping characteristics have been determined (Fig. 5). The choice of the hydropneumatic column as the research object resulted from the fact that the length of the excitation stroke was negligible on the result obtained in the form of damping characteristics.

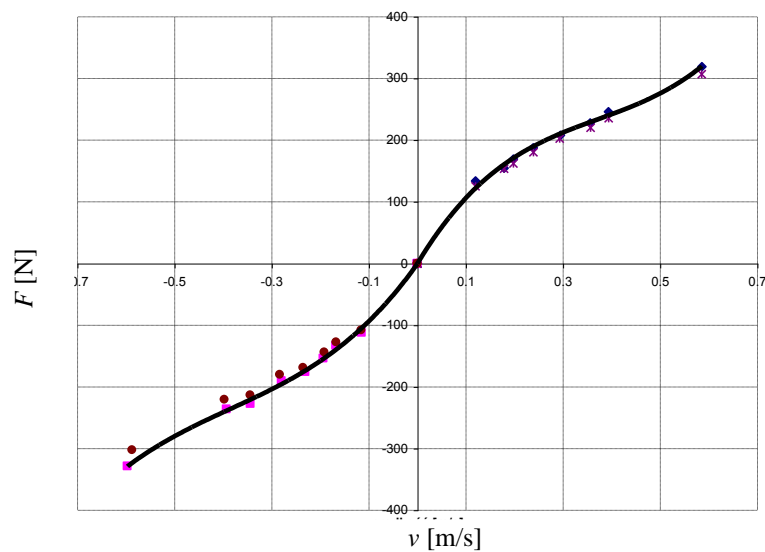


Figure 5. The damping characteristics of hydropneumatic column determined for a sphere of nominal pressure $p_0 = 5.5$ MPa

The column of identified technical condition was built into the suspension, which was then excited by vibration using a high power exciter analogous to the solutions used in suspension testing stands at PTI (Periodical Technical Inspection) station. The amplitude of the exciter plate vibration displacements was constant and amounted to 6 mm, while the use of a frequency converter in the control system enabled the

adjustment of the length of forcing cycles. During the tests, the following signals were recorded: acceleration of body vibrations at the point of upper attachment of the suspension column and relative displacements of the wheel and the body. Examples of real time object acceleration vibration accelerations and suspension deflections recorded during real object tests are shown in Figures 6 and 7.

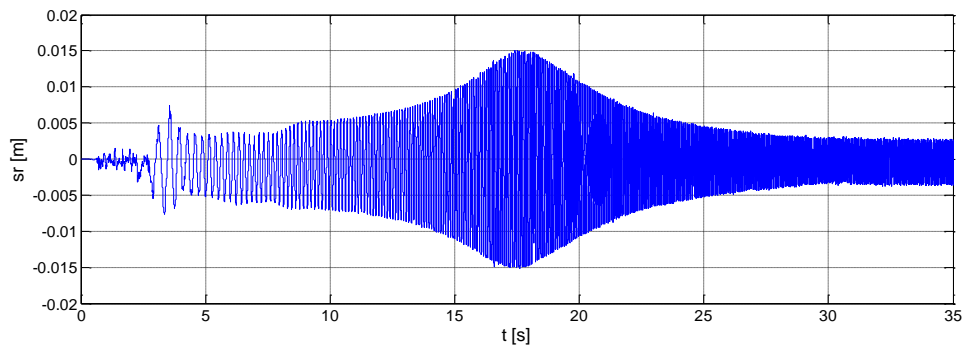


Figure 6. Recorded signal of wheel displacements relative to body of car (suspension deflections) in the vertical direction

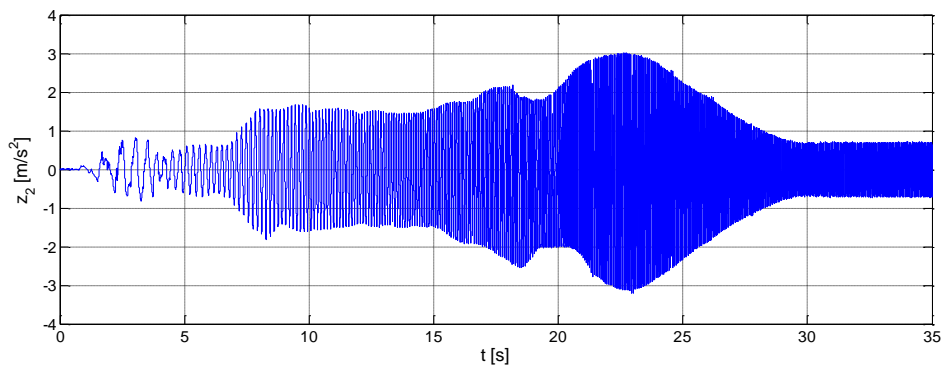


Figure 7. Recorded signal of acceleration of body vibration in the vertical direction

The results obtained were analyzed and the energy relationships between the analyzed signals were determined, as shown in Figure 8.

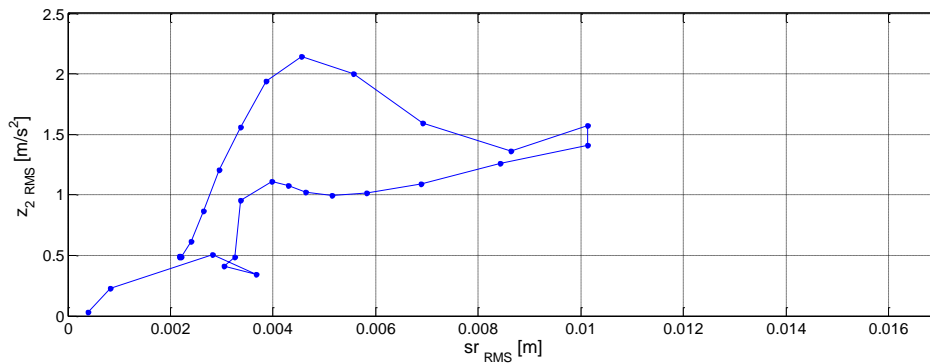


Figure 8. The relations between of accelerations of the body (RMS) and relative displacements of the wheel and the body (RMS) determined for the real object

The analysis was carried out for 1 second time windows that can be treated as signal fragments recorded at a quasi constant frequency of excitation. Using the point markers, the determined energy relations between the studied motion parameters were marked on the graph.

The relationship between the analyzed signals is clearly visible, which results from the operating parameters of the tested suspension system. The obtained results confirm the calculated energy relations between the analyzed signals.

5. Conclusions

The effective value of body vibration acceleration is a measure of vibration energy. The effective values of vibration accelerations are used to assess the criteria for daily vibration exposure, which are regulated by law. The test results show that the same RMS acceleration of body of car vibrations occurs for different frequencies of excitations. The monitored suspension deflection is related to the mechanical energy in spring converted vehicle suspension. Only the combined presentation of body accelerations and suspension deflections in the form of RMS gives the opportunity to assess the impact of energy dissipation in the shock absorber on the vibroactivity of the entire system. The obtained results in the form of occurring between the analyzed parameters of the vibrating motion are presented in the form of graphs containing characteristic curves describing the studied phenomenon. The results obtained during simulation tests were empirically verified on a real object. Depending on the damping properties of the suspension, the vibrations of the sprung mass analyzed on the energy dependence plane of selected parameters of the vibrating motion are specific and allow the assessment of the way of mechanical energy transfer in the system. The proposed method allows to assess how the damping in the suspension system affects the energy relationships occurring in the vehicle suspension vibrating motion.

References

1. Cheng Liu, Guowei Cai, Deyou Yang, *Design nonlinear robust damping controller for static synchronous series compensator based on objective holographic feedback–HN*, *Advances in Mechanical Engineering*, **8**(6) (2016) 1 – 11.
2. F. C. Crawford, *Waves*, PWN, Warszawa 1972.
3. Z. Dąbrowski, J. Pankiewicz, *Diagnosing a Vehicle’s Suspension System on the Basis of the Non-linear Effects of the Dynamic Response*, *Machine Dynamic Problems*, **26**(2/3) (2002).
4. J. C. Dixon, *The Shock Absorber Handbook*. Society of Automotive Engineers, Warrendale, PA, 1999.
5. U. Ferdek, J. Łuczko, *Vibration analysis of a half-car model with semi-active damping*, *Journal of Theoretical And Applied Mechanics*, **54**(2) 321 – 332.
6. T. D. Gillespie, *Fundamentals of Vehicle Dynamics*, Society of Automotive Engineers, Warrendale, PA, 1992.
7. N. Giorgetti, A. Bemporad, H. E. Tseng, D. Hrovat, *Hybrid model predictive control application towards optimal semi-active suspension*, *Int. J. Control*, **79**(5) (2006) 521 – 533.
8. E. Guglielmino, A. Edge Kevin, *A controlled friction damper for vehicle applications*, *Control Engineering Practice*, **12** (2004) 431 – 443.
9. Hailong Zhang, Enrong Wang, Fuhong Min, Ning Zhang, Chunyi Su, Subhash Rakheja, *Nonlinear Dynamics Analysis of the Semiactive Suspension System with Magneto-Rheological Damper*. *Shock and Vibration*, Volume 2015.
10. I. M. Ibrahim, D. A. Crolla, D. C. Barton, *Effect of frame flexibility on the ride vibration of trucks*, *Computers and Structures*, **58**(4) (1996) 709 – 113.
11. S. Rakheja, S. Sankar, *Vibration and shock isolation performance of a semi-active “on-off” damper*, *J. Vib. Acoust. Stress Reliab. Des.*, **107** (1985) 398 – 403.
12. M. Ieluzzi, P. Turco, M. Montiglio, *Development of a heavy truck semi-active suspension control*, *Control Engineering Practice*, **14** (2006) 305 – 312.
13. D. C. Karnopp, M. J. Crosby, R. A. Harwood, *Vibration control using semi-active force generators*, *Trans ASME: J Eng Ind*, (1974) 619 – 26.
14. Ł. Konieczny, R. Burdzik, J. Warczek, *Research on dynamics of car suspension system in MSC. Adams software*. *Dynamical systems. Control and stability*. Łódź: Wydaw. Politechniki Łódzkiej, (2015) 317 – 326.
15. G. Litak, M. Borowiec, M. I. Friswell, K. Szabelski, *Chaotic vibration of a quarter-car model excited by the road surface profile*, *Communications in Nonlinear Science and Numerical Simulation*, **13** (2008) 1373 – 1383.
16. L. I. Nkomo, A. Dove, M. T. Ngwako, O. T. Nyandoro, *Control for ride comfort and actuation energy optimisation in half-car suspension systems*, *IFAC Papers On Line* 50-2 (2017) 259 – 264.
17. G. Rill, *Vehicle dynamics*. University of Applied Sciences, 2006.
18. I. M. Ryabova, K. V. Chernyshova, A. V. Pozdeeva, *Energy Analysis of Vehicle Suspension Oscillation Cycle*, *Procedia Engineering*, **150** (2016) 384 – 392.

19. M. Siewe Siewe, *Resonance, stability and period-doubling bifurcation of a quarter-car model excited by the road surface profile*, Physics Letters A, **374** (2010) 1469 – 1476.
20. J. Warczek, R. Burdzik, Ł. Konieczny, *Analysis of the forces generated in the shock absorber for conditions similar to the excitation caused by road roughness*, Dynamical systems: theoretical and experimental analysis, Łódź, Poland, December 7-10, 2015. Ed. Jan Awrejcewicz. Berlin : Springer International Publishing, (2016) 373 – 383.
21. J. Warczek, R. Burdzik, Ł. Konieczny, *The concept of autonomous damper in vehicle suspension*, Dynamical Systems in Applications. DSTA 2017, Łódź, Poland December 11-14, 2017. Ed.: Jan Awrejcewicz. Cham : Springer, 2018, (Springer Proceedings in Mathematics & Statistics ; vol. 249 2194-1009) pp. 401 – 410.
22. J. Warczek, *Research of damping influence for the transmission of energy in multi-masses systems*, Vibroengineering Procedia, **19** (2018) 32 – 35.
23. Y. Xiong, A. Tuononen, *Rolling deformation of truck tires: Measurement and analysis using a tire sensing approach* ,Journal of Terramechanics, **61** (2015) 33 – 42.

The Use of Computer Simulations in the Analysis of Physical Phenomena Models

Jacek DZIURDŹ
*Institute of Machine Design Fundamentals,
Warsaw University of Technology,
84 Narbutta str., 02-524 Warsaw*

Abstract

Tests of the technical condition of machines sometimes involve the analysis of dynamic phenomena associated with their work. The simplest methods are based on basic measurements, e.g. effective velocities and body vibration accelerations as well as sound pressure levels recorded in close vicinity of the tested object. For analysis, more advanced techniques use signals recorded in a certain period of time representing the studied phenomena. The development of computer techniques has enabled a relatively convenient modelling of technical objects. A well-identified model allows to extend research on real objects to include comprehensive computer analyses, thanks to which we can reduce time-consuming measurements or perform analyses for excitations which are difficult to perform at a test stand. Another application of a model is to generate signals, on the basis of which we can choose parameters of analysis methods to increase the effectiveness of diagnosis or test new analysis and inference algorithms. Several presented examples were implemented in the Matlab Simulink environment. Because the presented methods are universal, they can be used to analyze any physical phenomena described with more or less complicated models.

Keywords: dynamic models, simulation, signal analysis

1. Introduction

Processes related to designing and physical system tests should be supported by computer calculations. In addition to designing and manufacturing support methods, all types of simulation methods, including those related to dynamic phenomena, are becoming more and more popular. They complement dynamic properties tests carried out during active experiments. In many cases, it is impossible to conduct an experiment, e.g. due to technological reasons or because of the cost of carrying it out. An important factor is also the duration of the test which can be very long (lasting up to several years).

Regardless of the field of technology, the computer simulation process should be preceded by modelling of a real system. This is most often done on the basis of the physical description of the examined object. It should take into account basic characteristics of the system and the medium (cooperating systems) with which the examined system interacts (cooperates). Based on the physical model, we create a mathematical model, which is an abstract description that can be used in computer modelling. Its degree of simplification should not introduce significant errors in the reproduction of basic physical phenomena.

If the created model is to support diagnostics of the technical condition of tested machines, it should be correctly identified and verified [1]. Signal processing and analysis

methods are often used for this purpose. Models underlying simulation can also be used to test and examine the effectiveness of applied or new inference algorithms.

2. Application of signal analysis to simulation studies

The combination of computer simulation with the interpretation of obtained results, based on the methods of signal analysis, may create some technical problems. Algorithms for iterative solving of ordinary differential equations are usually based on various modifications of the Runge-Kutta method. In these methods, step sizes of calculations are important [2]. The step size will vary depending on the dynamics of the model. With rapid changes in the state of the model, the step size is reduced in order to maintain the accuracy of calculations. When the states of the model change slowly, the step size increases.

Calculations performed using digital signal analysis methods require the adoption of a constant step Δt between individual points of time series [3]. This is due to the lack of explicit representation of t time in computer calculations, which is replaced by the numbers of consecutive n points (time $t_n = (n-1) \cdot \Delta t$). With a variable step, in extreme cases, there can be a significant difference in the reproduction of the function. As a result, there will be analysis errors obtained from the simulation of signals. An example of the influence of step variability on signal reproduction is shown in Figure 1.

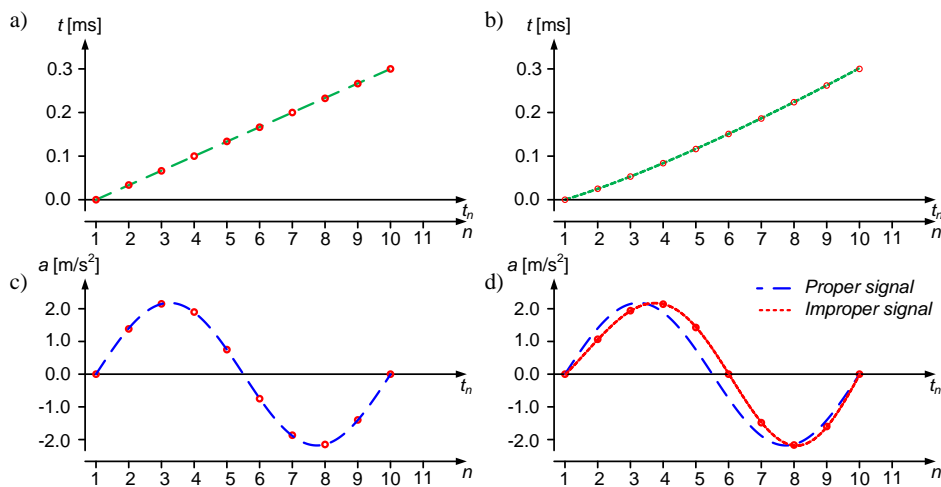


Figure 1. Example of the influence of the variable time resolution Δt :

- a) constant value Δt , b) variable value Δt , c) properly sampled signal ($\Delta t = \text{const}$),
d) comparison of proper and improper signals

However, the use of constant-step simulation methods suffers from several disadvantages, the most important of which is a decrease in accuracy and increase in calculation time. However, a variable step is recommended for models in which states

change rapidly or which contain discontinuities. In these cases, the variable step simulation method requires fewer time steps than the constant-step method to achieve a comparable level of accuracy. This can significantly reduce simulation time.

The right way seems to be to use simulation with a variable step, but with a limited maximum value to the value of constant time resolution Δt , required in digital signal analysis, equal to the inverse of sampling frequency f_s . Figure 2 presents a modification of the parameters of solution methods in Matlab Simulink.

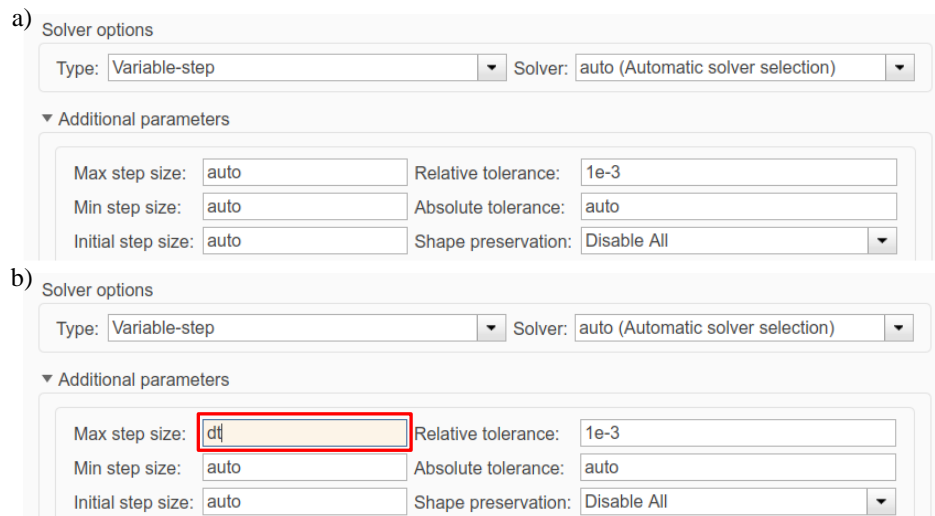


Figure 2. Limitation of the maximum integration step of methods for solving differential equations: a) parameters automatically selected, b) to obtain results for the adopted step Δt

The analyses of complicated systems with many degrees of freedom confirm the effectiveness of this approach. However, one should remember to supplement the simulation and analysis of the results with checking the variability of solution steps. Figure 3 shows examples of the course of changes in the integration step with the maximum step set as *auto* and equal to Δt . A simple system was analyzed, where a rectangular pulse with the minimum possible duration was introduced at the input at $t = 0.2$ s. With automatic step determination, the simulation only takes place after the system is activated and quickly stabilizes with a large, little variable step of the order of $\Delta t_n = 25\text{-}30$ ms. When setting the maximum step to the expected value, the calculations will unfortunately take longer, but in addition to cases where Δt_n is not equal to Δt , we get relatively long sections for which signals resulting from the simulation were generated with the required constant step.

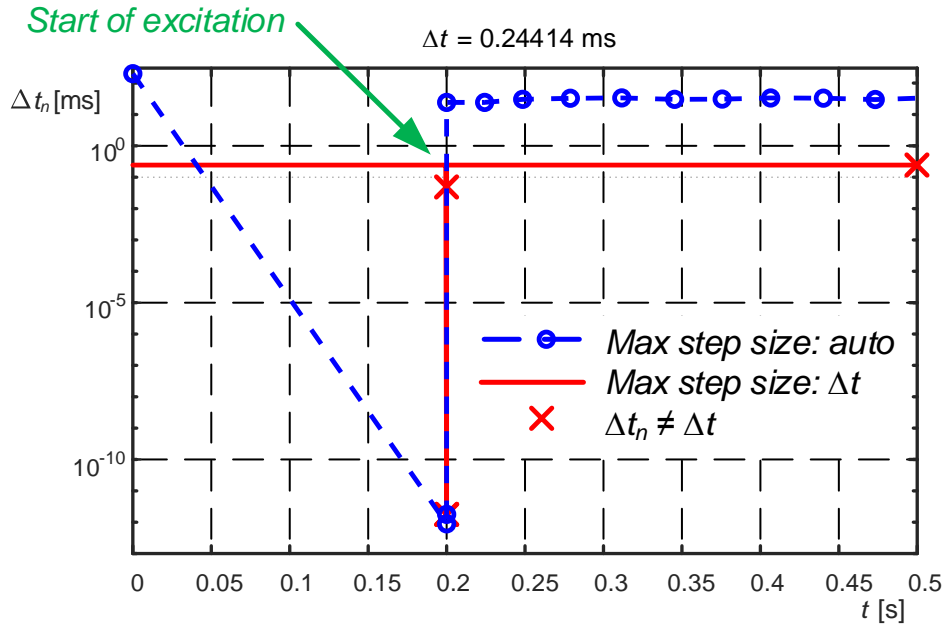


Figure 3. Comparison of integration step changes for different *Max step size* settings

3. Different ways to describe the models

It often happens that the dynamic properties of the same system can be modelled with a differential equation (system of equations), transfer function or spectral transmittance. In this case, an interesting issue may be the analysis of connections of several, theoretically independent, fields of knowledge such as automatic control, vibration theory or signal analysis.

Let us consider, for example, a linear oscillating system with one degree of freedom with damping and excitation with force varying in time $F(t)$:

$$m\ddot{x} + c\dot{x} + kx = F(t) \tag{1}$$

where: m – body weight, c – system damping, k – system stiffness.

The same system can be presented using the concept of a transfer function using the Laplace transform:

$$mX(s)s^2 + cX(s)s + kX(s) = F(s) \tag{2}$$

where: $X(s)$ – Laplace transform of the output signal $x(t)$ (system response), and $F(s)$ is the Laplace transform of the excitation force $F(t)$.

These two quantities are associated with a transfer function, which characterizes dynamic properties of the system in the s domain:

$$G(s) = \frac{X(s)}{F(s)} \quad (3)$$

In the case of a simple system, dynamic properties can be determined by solving equations (1) or (2). Of course, this description will be used in other areas.

In the case under consideration, the solution to equation (1) is, among others, a formula for the vibration amplitude of the system at a given frequency ω of a force harmonically variable in time:

$$A(\omega) = \frac{F(\omega)}{m} \frac{1}{\sqrt{(\omega_0^2 - \omega^2)^2 + 4h^2\omega^2}} \quad (4)$$

where: ω_0 – natural frequency of the undamped system, $h = \frac{c}{2m}$.

The problem appears when we analyze systems with a greater degree of complexity for which it is difficult to obtain a solution analogous to the one described by equations (1) and (4). Searching for a solution consisting in determining system parameters for different excitation frequencies may be reduced in simulation tests to repeated repetition of calculations. Such an approach significantly extends the solution time. An alternative solution is to use links with spectral transmittance $H(f)$ [4]:

$$X(f) = H(f) \cdot F(f) \quad (5)$$

$$H(f) = |H(f)|e^{-i\varphi(f)} \quad (6)$$

where: $X(f)$ – spectrum of the signal at output $x(t)$, $F(f)$ – spectrum of the signal at output $F(t)$, $|H(f)|$ – gain factor, $\varphi(f)$ – phase factor.

In the example shown, for a system with one degree of freedom, a relationship is observed:

$$|H(\omega)| = \frac{A(\omega)}{F(\omega)} = \frac{1}{m} \frac{1}{\sqrt{(\omega_0^2 - \omega^2)^2 + 4h^2\omega^2}} \quad (7)$$

where: $\omega = 2\pi f$.

Instead of repeating calculations for harmonic excitations many times, in accordance with the definition of spectral transmittance, it is necessary to stimulate the system with impulse excitation and determine characteristics defined as a function of the frequency response. The calculation time will only depend on the processing speed and the adopted frequency resolution of spectral analysis. Figure 4 shows a comparison of simulation results for a system with one degree of freedom with the values obtained from formula (7).

In the models of examined physical phenomena, e.g. those being the basis for simulation in Matlab Simulink, different description methods can be used interchangeably, and elements of the system described by means of a transfer function (e.g. PID controller) can be combined with the system described by differential equations. The relationship between these systems will be time functions.

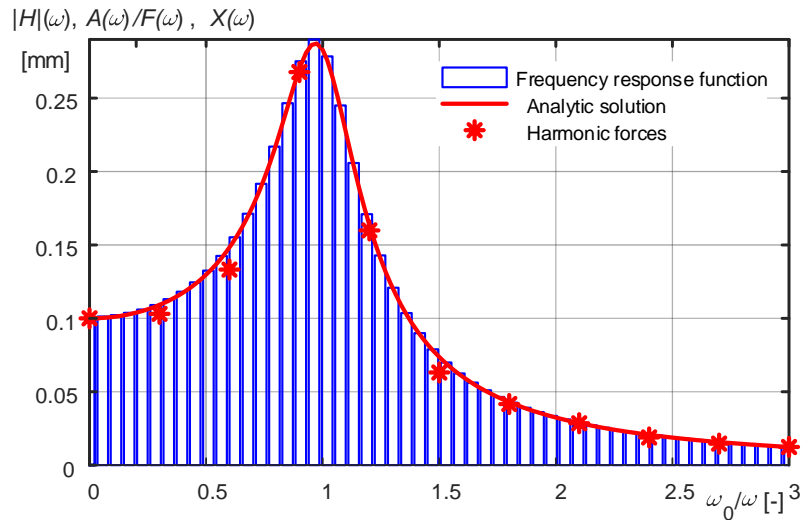


Figure 4. Comparison of different methods for determining the system characteristics

4. Analysis of system dynamics in the time-frequency domain

In many cases of dynamic system modelling, the type of excitation is an important issue. Response characteristics depend on it. This is especially important in systems with more degrees of freedom than one and in nonlinear systems.

Let us consider, for example, a linear vibration system with one degree of freedom without damping, with force varying over time, for which an undamped dynamic vibration eliminator was used. When excited by harmonic force, the system will vibrate at a frequency equal to the excitation frequency. In theoretical considerations amplitude and phase frequency characteristics can be determined. This system has two resonant frequencies, and for the frequency to which the damper has been tuned, the vibration amplitude is zero.

In the case of analysis with excitation by force with frequency of amplitude changes increasing over time, system dynamics should be considered over time and not just in the frequency domain. In a system where vibrating elements are not damped, subsequent forms of vibrations are generated after exceeding resonance frequencies by excitation frequency. Figure 5 shows a change in the response of the vibrating system with a damper when excited by a force with increasing frequency of amplitude changes over time, and Figure 6 shows a change in the response of the system with inertia excitation.

Simultaneous analysis in the time and frequency domain is even more indispensable for a system with dampening. This method of testing can be used to analyze the effects of eliminator tuning and the impact of damping on system vibrations and in technical diagnostics it can be used to determine the impact of changes in the parameters of the vibration eliminator (damper) associated with its degradation. Figure 7 shows vibrations of the system with a dampened eliminator at inertia excitation with the frequency of amplitude changes increasing over time.

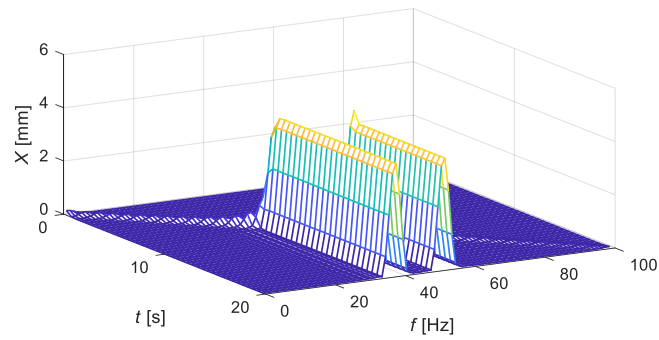


Figure 5. Vibrations of the system with an eliminator when excited by force with increasing frequency of amplitude changes over time

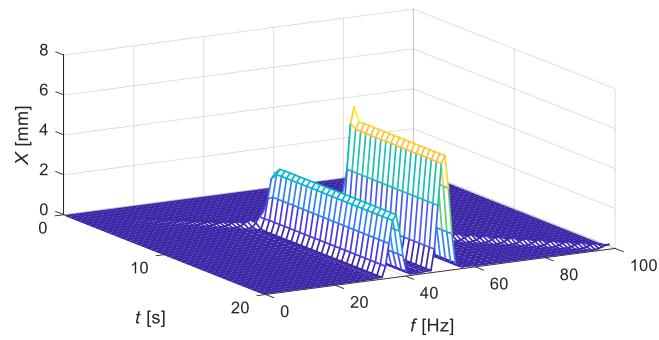


Figure 6. Vibrations of the system with an eliminator at inertia excitation with the frequency of amplitude changes increasing over time

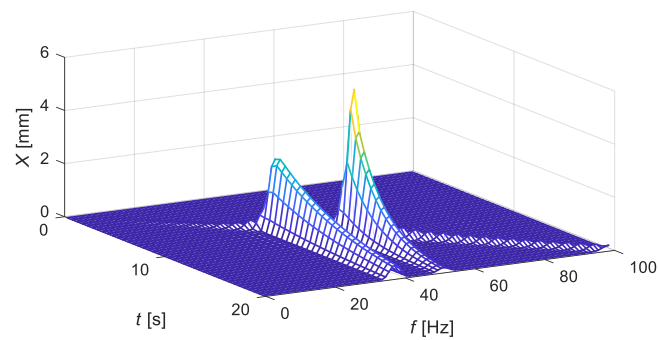


Figure 7. Vibrations of the system with a dampened eliminator at inertia excitation with the frequency of amplitude changes increasing over time

5. Conclusions

The history of simulation research is very long. Antoni Gaudi is the best known person who introduced physical models into structural analysis [5]. For this purpose, he studied laws of structural mechanics, using, among others, catenary curve properties. This method, however, does not take into account dynamic interactions. The development of electrical engineering enabled the creation of analog computers [6] that use electrical-mechanical analogies [4] to create simulation models. These methods already took into account the dynamics of systems operation. The development of digital methods and computational systems meant that the principles used in analog technology can, in effect, be applied in their entirety in discrete technology. The best example would be the development of MathWorks's Matlab Simulink program. Over 25 years, many libraries (including specialized libraries) have been created to support simulations in many fields of physics. Other simulation programs have also been created, e.g. Scilab Xcos, operating similarly to Simulink or MSC Softwares' Adams program.

The use of advanced simulations allows, among others, to analyze changes in system dynamics for various physical parameters [7] (characteristics of elements, e.g. non-linear [8]) without the need for labour- and material-intensive research. In technical diagnostics, simulations can be used to determine the impact of the degradation of mechanical system components on their dynamics and create effective methods of assessing technical condition based on the analysis of obtained signals.

References

1. A. Rauh, L. Senkel, H. Aschemann, *Verified Parameter Identification for Dynamic Systems with Non-Smooth Right-Hand Sides*, M. Nehmeier, J. Wolff von Gudenberg, W. Tucker (eds), Scientific Computing, Computer Arithmetic, and Validated Numerics, SCAN 2015, Lecture Notes in Computer Science, Springer, Cham, **9553** (2016) 236 – 246.
2. A. Marciniak, B. Szyszka, *Interval Runge-Kutta Methods with Variable Step Sizes*, Computational Methods in Science and Technology, **25** (2019) 17 – 30.
3. R. B. Randall, *Frequency Analysis*, Brüel&Kjær 1987.
4. J. S. Bendat, A. G. Piersol, *Random data: Analysis and measurement procedures*, John Wiley, New York 2010.
5. R. Makert, G. Alves, *Between Designer and Design: Parametric Design and Prototyping Considerations on Gaudi's Sagrada Familia*, Periodica Polytechnica Architecture, **47**(2) (2016) 89 – 93.
6. B. Chatterji, *Analog Computer Simulation*, IETE Journal of Education, **34** (2015) 27 – 38.
7. J. Dziurdź, R. Pakowski, *Analysis of Action Viscous Torsional Vibration Damper of the Crankshaft Based on Transverse Vibration the Engine Block*, Solid State Phenomena, **236** (2015) 145 – 152.
8. Z. Dąbrowski, P. Deuzkiewicz, J. Dziurdź, *Modelling of Composite Elements of Power Transmission Systems Considering Nonlinear Material Characteristics*, Journal of Machine Construction and Maintenance, **3** (2018) 87 – 94.

Modelling of a Rotor with Gyroscopic Coupling in a Rotating Reference Frame Using Ansys and Matlab

Mateusz KOZIOŁ

AGH University of Science and Technology, Faculty of Mechanical Engineering and Robotics, al. Mickiewicza 30, 30-059 Kraków, makoziol@agh.edu.pl

Abstract

The work presents a method that expands Ansys capabilities and allows for studying the dynamics of rotors with significant gyroscopic coupling in reference to rotating coordinates. The analyses of rotors in the rotating reference frame are less common, and in FEM software some limitations in such cases can be observed. There are specialised rotors for which the use of a non-inertial reference frame is inevitable. The current work proposes a solution. In the presented method, Ansys is used to generate and export systems matrices so that the manual creation of an FE model is unnecessary. The rest of the operations are realised in Matlab. A simple numerical example is presented to clarify all the steps and a more complex example concludes the paper.

Keywords: rotor dynamics, FEM, Ansys, Matlab, gyroscopic coupling, rotating reference frame

1. Introduction

The dynamics of rotating machines incorporates a wide range of knowledge with many phenomena that often have a non-intuitive nature. There are many programs that support engineers in the design of such machines. Besides the general-purpose FEM software (Ansys, Nastran), one can find many specialised programs that are designed to cope only with rotor problems (XLRotor, DynRot, MESWIR). In general, in numerical models of rotors, the approach that the system motion is analysed with reference to the inertial frame is dominant. Such results are consistent with real-life observations. However, there are less common cases where the analysis in a rotating reference frame is inevitable.

The current work is motivated by an attempt to analyse the structure that has rotor-mounted sensors and actuators. For such a structure, the use of the rotating reference frame is necessary and in Ansys (as available option), when one performs such an analysis, the gyroscopic coupling is neglected (a short summary of all capabilities can be found in the Ansys manual [1] or in ref. [2]). In the following work, the author proposes a method that completes the FE model so that the analysis can be correctly performed. A similar approach can be found in the author's earlier works [3, 4], however the effect of gyroscopic coupling was not considered.

In general, the presented models use a linear approximation of dynamics of gyroscopic systems and are valid for small deflections.

2. The studied geometry and analytical considerations

The work analyses the dynamics of a Stodola-Green rotor, as shown in Fig. 1. The structure consists of an elastic shaft, which at its end has a symmetric and rigid disc.

The bearing is idealised. The rotor rotates with the constant rotational speed Ω . In particular, the work considers a shaft with a square cross-section, which can be treated as of circular type [5]. Two sets of coordinates are introduced. The xyz axes represent an inertial or stationary reference frame (SRF). The $\xi\eta\zeta$ axes rotate with the shaft and will be referred to as a rotating reference frame (RRF). The equations of motion of the structure with respect to stationary reference frame (SRF) are as follows [5]:

$$\begin{bmatrix} m & 0 & 0 & 0 \\ 0 & m & 0 & 0 \\ 0 & 0 & J_t & 0 \\ 0 & 0 & 0 & J_p \end{bmatrix} \begin{Bmatrix} \ddot{x}_c \\ \ddot{y}_c \\ \ddot{\varphi}_x \\ \ddot{\varphi}_y \end{Bmatrix} + \Omega \begin{bmatrix} 0 & 0 & 0 & 0 \\ 0 & 0 & 0 & 0 \\ 0 & 0 & 0 & J_p \\ 0 & 0 & -J_p & 0 \end{bmatrix} \begin{Bmatrix} \dot{x}_c \\ \dot{y}_c \\ \dot{\varphi}_x \\ \dot{\varphi}_y \end{Bmatrix} + \begin{bmatrix} K_{11} & 0 & 0 & -K_{12} \\ 0 & K_{11} & K_{12} & 0 \\ 0 & K_{21} & K_{22} & 0 \\ -K_{21} & 0 & 0 & K_{22} \end{bmatrix} \begin{Bmatrix} x_c \\ y_c \\ \varphi_x \\ \varphi_y \end{Bmatrix} = \begin{Bmatrix} F_x \\ F_y \\ M_x \\ M_y \end{Bmatrix} \quad (1)$$

$$\mathbf{Mu} + \mathbf{Gu} + \mathbf{Ku} = \mathbf{w} \quad (2)$$

where: x_c, y_c are displacements and φ_x, φ_y are rotations of the disc in SRF, m – reduced mass, J_t – transverse mass moment of inertia, J_p – polar mass moment of inertia, K_{ij} – the stiffness of a shaft with respect to transversal and rotational deflections [5].

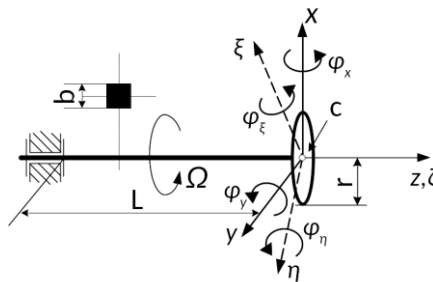


Figure 1. The Stodola-Green rotor with coordinate systems

In the literature one can find different forms of eq. (1), where the assumed direction of rotation about the x axis is the opposite [6] or where the equations are interlaced and the stiffness matrix has the opposite cross-coupling elements [7]. The opposite elements in the stiffness matrix are the result of a different coordinate system. The form of eq. 1 has been chosen because the directions of the rotations are adopted in the same way as in Ansys, using the right-hand screw rule (positive rotation φ_x will cause a right-hand screw to advance in x direction).

In a linear approximation of a motion of the disc (eqs. (1) and (2)), it is assumed that the inclination angles (φ_x, φ_y) are small. Using this assumption the rotations can be treated as a generalised coordinates, and therefore a transformation to the rotating coordinate system is possible. Between the variables from stationary and rotating reference frames there is the following relation:

$$\begin{Bmatrix} x_c \\ y_c \\ \varphi_x \\ \varphi_y \end{Bmatrix} = \begin{bmatrix} \cos(\Omega t) & -\sin(\Omega t) & 0 & 0 \\ \sin(\Omega t) & \cos(\Omega t) & 0 & 0 \\ 0 & 0 & \cos(\Omega t) & -\sin(\Omega t) \\ 0 & 0 & \sin(\Omega t) & \cos(\Omega t) \end{bmatrix} \begin{Bmatrix} \xi_c \\ \eta_c \\ \varphi_\xi \\ \varphi_\eta \end{Bmatrix} \quad (3)$$

where: ξ_c, η_c are displacements and $\varphi_\xi, \varphi_\eta$ are rotations in RRF.

The equations in a rotating frame of reference can be obtained by differentiating of the eq. (3) so as to get velocities and accelerations. The additional terms come from the fact that the time derivative with respect to the rotating coordinate system is calculated. The equations of motion in RRF are:

$$\begin{aligned} & \begin{bmatrix} m & 0 & 0 & 0 \\ 0 & m & 0 & 0 \\ 0 & 0 & J_t & 0 \\ 0 & 0 & 0 & J_p \end{bmatrix} \begin{Bmatrix} \ddot{\xi}_c \\ \ddot{\eta}_c \\ \ddot{\varphi}_\xi \\ \ddot{\varphi}_\eta \end{Bmatrix} + \left(\begin{bmatrix} 0 & 0 & 0 & 0 \\ 0 & 0 & 0 & 0 \\ 0 & 0 & 0 & J_p \\ 0 & 0 & -J_p & 0 \end{bmatrix} + 2\Omega \begin{bmatrix} 0 & -m & 0 & 0 \\ m & 0 & 0 & 0 \\ 0 & 0 & 0 & -J_t \\ 0 & 0 & J_t & 0 \end{bmatrix} \right) \begin{Bmatrix} \dot{\xi}_c \\ \dot{\eta}_c \\ \dot{\varphi}_\xi \\ \dot{\varphi}_\eta \end{Bmatrix} \\ & + \left(\begin{bmatrix} K_{11} & 0 & 0 & -K_{12} \\ 0 & K_{11} & K_{12} & 0 \\ 0 & K_{21} & K_{22} & 0 \\ -K_{21} & 0 & 0 & K_{22} \end{bmatrix} - \Omega^2 \begin{bmatrix} m & 0 & 0 & 0 \\ 0 & m & 0 & 0 \\ 0 & 0 & J_t & 0 \\ 0 & 0 & 0 & J_p \end{bmatrix} + \Omega^2 \begin{bmatrix} 0 & 0 & 0 & 0 \\ 0 & 0 & 0 & 0 \\ 0 & 0 & J_p & 0 \\ 0 & 0 & 0 & J_p \end{bmatrix} \right) \begin{Bmatrix} \xi_c \\ \eta_c \\ \varphi_\xi \\ \varphi_\eta \end{Bmatrix} = \begin{Bmatrix} F_\xi \\ F_\eta \\ M_\xi \\ M_\eta \end{Bmatrix} \end{aligned} \tag{4}$$

$$\mathbf{M}\ddot{\mathbf{v}} + (\mathbf{G} + 2\mathbf{MH})\dot{\mathbf{v}} + (\mathbf{K} - \Omega^2\mathbf{M} + \mathbf{GH})\mathbf{v} = \boldsymbol{\tau} \tag{5}$$

Comparing the eqs. (2) and (5) one can observe that only one additional matrix is needed to obtain equations in RRF. This is the so-called circulatory matrix \mathbf{H} , which is skew-symmetric and proportional to rotational speed (the same as the gyroscopic matrix \mathbf{G}). The presented method proposes to determine the matrix \mathbf{H} utilising the Coriolis effect matrix ($2\mathbf{MH}$). In Ansys, the Coriolis matrix is generated during analyses in RRF and its elements are added to the damping matrix.

In order to create a model in Ansys, it is assumed that shaft is made from aluminium, has a length of $L = 0.7$ m and side length $b = 15$ mm. The disc has a radius $r = 70$ mm and mass $m_d = 604.2$ g (which is equivalent to a steel disc with thickness equal to $t = 5$ mm). The proposed dimensions are considered to be used in future experiments. The assumed constant rotational speed Ω is 45 rad/s.

3. Ansys – modelling and exporting of system matrices

As a numerical example, the simplest possible FEM realisation of the proposed geometry is created. The shaft is modelled by one element of beam type and, as a disc, a point mass element with rotary inertia is used. When the free side of the shaft is fixed, the model has 6 DOFs. To obtain the same size of matrices as in the presented equations, two additional DOFs have been removed, i.e. displacement in z direction and rotation about z axis.

Before the exporting of system matrices in Ansys, all necessary steps that are typical for modal analysis should be performed (the assignment of elements, materials and constants, definition of boundary conditions). In order to export damping related matrices, the damped modal solver should be pre-set. As mentioned earlier, in Ansys the analysis of rotating systems can be done with respect to the stationary and rotating reference frames (*coriolis* command). A model of the gyroscopic system in the rotating reference frame can be created by making both analyses – the first one is realised to obtain mass, stiffness and gyroscopic matrices, and the second one focuses on a Coriolis

matrix. All needed matrices can be exported by using an assembled global matrix file (generated during solution) and *hbm* command. The generated files utilise the Harwell-Boeing format, which is efficient with sparse matrices. The Ansys manual [1] informs that in the case of a system with non-symmetric matrices (which includes all rotor dynamics problems), then the transpose of the matrices is written to files.

The physical meaning of the particular elements in the matrices can be found by using mapping files, which are optionally generated together with the matrix files. The mapping file links the row/column number with the node number and with one of the degrees of freedom that is available for a particular node. In other words, the mapping file shows for each DOF the corresponding row/column and node number.

In the analyses that prepare system matrices, it is advisable to avoid modelling of damping because it will add further elements to the gyroscopic or Coriolis matrices.

4. Matlab – model preparation and solution

By default, Matlab does not recognise the Harwell-Boeing format, however software tools can be found that import the model data [8, 9]. Next, the mapping file is utilised to read the order of DOFs: $[UX, UY, ROTX, ROTY]^T$ (the same as in eqs. (1), (3) and (4)). Six matrices are obtained because two types of analyses have been solved. The obtained matrices (after the transposition that restores its original shape) are presented below, where the first three are from SRF and the additional three from RRF (subscript R):

$$\mathbf{M} = \text{diag}[0.746, 0.746, 7.428e-4, 7.428e-4]$$

$$\mathbf{G} = \begin{bmatrix} 0 & 0 & 0 & 0 \\ 0 & 0 & 0 & 0 \\ 0 & 0 & 0 & 0.0669 \\ 0 & 0 & -0.0669 & 0 \end{bmatrix}, \quad \mathbf{K} = \begin{bmatrix} 5.35e4 & 0 & 0 & -1.87e4 \\ 0 & 5.35e4 & 1.87e4 & 0 \\ 0 & 1.87e4 & 6.976e3 & 0 \\ -1.87e4 & 0 & 0 & 6.976e3 \end{bmatrix}$$

$$\mathbf{M}_R = \mathbf{M}$$

$$\mathbf{Cor}_R = \begin{bmatrix} 0 & -67.14 & 0 & 0 \\ 67.14 & 0 & 0 & 0 \\ 0 & 0 & 0 & 0.0669 \\ 0 & 0 & -0.0669 & 0 \end{bmatrix}, \quad \mathbf{K}_R = \begin{bmatrix} 5.20e4 & 0 & 0 & -1.87e4 \\ 0 & 5.20e4 & 1.87e4 & 0 \\ 0 & 1.87e4 & 6.976e3 & 0 \\ -1.87e4 & 0 & 0 & 6.976e3 \end{bmatrix}$$

The mass of the node in the mass matrix \mathbf{M} (and \mathbf{M}_R) is bigger than the mass of the disc. The difference is due to the non-zero mass of the shaft, which to some extent adds to the mass of the disc. Comparing the matrix \mathbf{Cor}_R with the corresponding one in eq. (4), it can be observed that two elements have the opposite sign. The same effect was consequently observed for other models and always just the rotational degrees-of-freedom was involved. By transposing only the rows and columns that are linked with the rotational DOFs, the Coriolis matrix gets the same form as in eq. (4).

The circulatory matrix can be determined by using the following relation:

$$\mathbf{H} = \frac{1}{2} \mathbf{M}^{-1} \mathbf{Cor}_{RM} \quad (6)$$

where the \mathbf{Cor}_{RM} indicates that eventual partial transformation of \mathbf{Cor}_R was realised (as mentioned above). Substituting numeric values one can obtain:

$$\mathbf{H} = \begin{bmatrix} 0 & -45 & 0 & 0 \\ 45 & 0 & 0 & 0 \\ 0 & 0 & 0 & -45 \\ 0 & 0 & 45 & 0 \end{bmatrix}$$

which clearly shows its dependence on rotational speed.

Knowing all the necessary matrices, the rotor model can be recreated in Matlab using, for example, a space-state approach. The descriptor space-state model (*dss* command) can assume the following form:

$$\begin{bmatrix} \mathbf{1} & \mathbf{0} \\ \mathbf{G} + 2\mathbf{MH} & \mathbf{M} \end{bmatrix} \begin{Bmatrix} \chi_1 \\ \chi_2 \end{Bmatrix} = \begin{bmatrix} \mathbf{0} & \mathbf{1} \\ -(\mathbf{K} - \Omega^2\mathbf{M} + \mathbf{GH}) & \mathbf{0} \end{bmatrix} \begin{Bmatrix} \chi_1 \\ \chi_2 \end{Bmatrix} + \begin{bmatrix} \mathbf{0} \\ \mathbf{1} \end{bmatrix} \boldsymbol{\tau} \tag{7}$$

$$\mathbf{v} = \begin{bmatrix} \mathbf{1} & \mathbf{0} \end{bmatrix} \begin{Bmatrix} \chi_1 \\ \chi_2 \end{Bmatrix} + \mathbf{0}\boldsymbol{\tau}$$

where $\mathbf{1}$ and $\mathbf{0}$ are, respectively, the identity and zeros matrices.

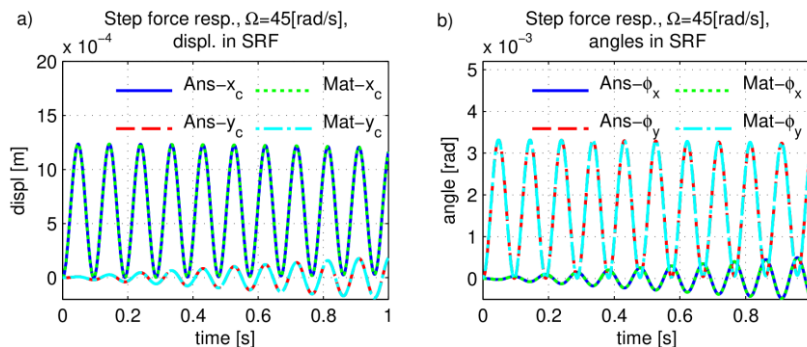


Figure 2. Comparison of results obtained in Ansys and in Matlab (w/o damping):
 a) displacements in SRF, b) angles in SRF

The method has been verified by comparing Matlab results with those obtained in Ansys. As excitation, a step force that acts in x direction (in SRF) was chosen. To excite the RRF referenced model in the same manner, the force has to be appropriately transformed. Two models have been simulated – the first one in Ansys in SRF (prefix Ans- in Fig. 2) and the second one in Matlab, with respect to RRF (prefix Mat- in Fig. 2). The results obtained in Matlab are transformed using eq. (3) to allow direct comparison. The results from both models are exact (Fig. 2). The gyroscopic coupling causes vibrations to arise in a y direction.

In the presented method damping can be also introduced. In rotating systems the overall damping is distinguished between internal and external damping, and both mechanisms should be included. In Ansys, the internal damping can be modelled as

proportional to stiffness. In the case of the external damping, Ansys (in SRF) offers more sophisticated models, e.g. damping related to anisotropic bearings.

To allow the comparison between models simulated in Ansys and Matlab, the Rayleigh damping has been utilised. The same damping conditions can be realized using the α part (proportional to a mass matrix) as a model of the external damping, and β part (proportional to the stiffness matrix) as a model of the internal one. The eq. (5) with such defined damping takes the form:

$$\mathbf{M}\ddot{\mathbf{v}} + (\mathbf{G} + 2\mathbf{MH} + \alpha\mathbf{M} + \beta\mathbf{K})\dot{\mathbf{v}} + (\mathbf{K} - \Omega^2\mathbf{M} + \mathbf{GH} + \alpha\mathbf{MH})\mathbf{v} = \boldsymbol{\tau} \quad (8)$$

where α and β are Rayleigh damping coefficients. The term $\alpha\mathbf{MH}$ results from a transformation of forces related to external damping into RRF. The details can be found in [7].

Two solutions have been obtained using the same Rayleigh damping coefficients (i.e. $\alpha = 0.5 \text{ s}^{-1}$, $\beta = 1 \cdot 10^{-4} \text{ s}$) and the same as before excitation. The first solution comes from the Ansys solver and the model referenced to the inertial frame (prefix Ans-). The second one comes from Matlab by solving the eq. (8), i.e. the model referenced to the rotating frame (prefix Mat-). The results (after transformation) are presented in Fig. 3. These results are the same, proving the correctness of the presented approach. Using this method other damping models can be also introduced, however it is beyond the scope of this article.

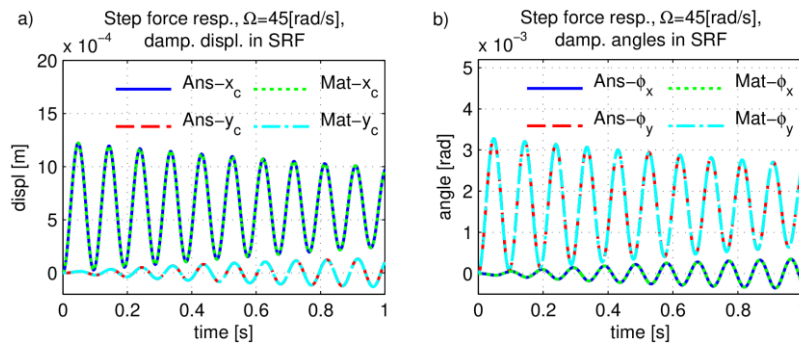


Figure 3. Comparison of results obtained in Ansys and Matlab (with damping): a) displacements in SRF, b) angles in SRF

It should be noted that both the gyroscopic and circulatory matrices depend not only on the value of rotational speed but also on the direction of rotation. In the analysed example, the system could rotate in the opposite direction and it would result in transposed matrices \mathbf{Corr} and \mathbf{G} . To avoid confusion, the system matrices should be exported using the same direction of rotation.

5. Application example

In the case of simple rotors, the usefulness of the described method is questionable. However, for more complex systems the proposed method can be unavoidable.

As a sample, an elastic rotor with piezoelectric patches on the surface of the shaft will be considered.

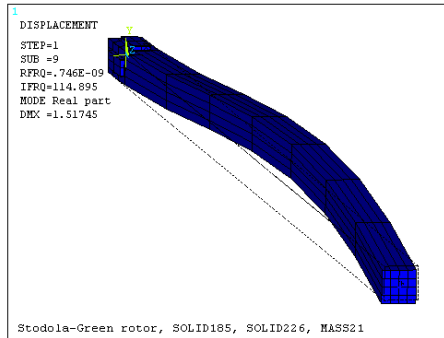


Figure 4. The second lateral mode of the analysed rotor

The deflected rotor is shown in Fig. 4. The model consists mainly of brick elements and, as a disc, a point mass element is used (the same as before, symbolised by an asterisk). Between the shaft and the disc the rigid connection is set. The four piezoelectric patches have pre-set polarisation and their electrodes are modelled by coupling electrical DOF of proper nodes. The dimensions of the rotor are the same as earlier, thus significant gyroscopic coupling exists. To obtain the voltages generated by the piezoelectric patches, the rotating reference frame has to be used, consequently this method is utilised. Figure 5 shows the final results obtained in Matlab. When the model contains the electrical DOFs, the imported mass matrix is rank deficient. To solve eq. (6), only the mechanical part of the system should be used. Further information can be found in refs. [3, 4].

When comparing Fig. 5a and Fig. 3a, one can notice that qualitatively the displacements are very similar. The quantitative differences result from other degrees of models complexity. Fig. 5b shows voltages generated by piezoelectric elements that are bonded to the shaft, thus they rotate with it. These elements can be also used as actuators, however it requires additional steps when the model is being prepared in Matlab. Some details can be found in refs. [3, 4].

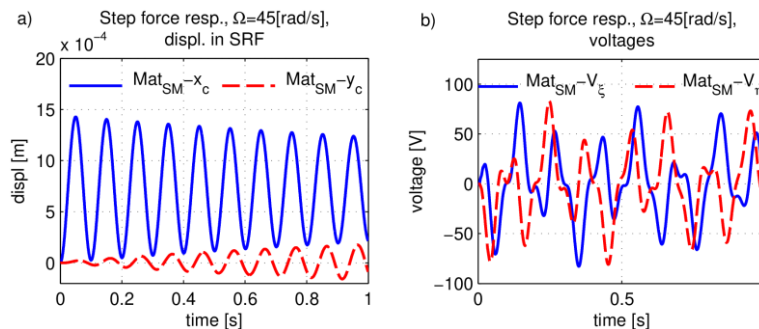


Figure 5. The results for an elastic rotor with piezoelectric patches: a) displacements transformed to SRF, b) voltages generated by piezoelectric patches

6. Conclusions

The article presents a combined method which expands Ansys capabilities. In particular, this method concerns the dynamics of rotors referenced to a rotating frame. Less popular analyses in RRF are limited because of lack of gyroscopic coupling in Ansys. The author proposes a solution whereby Ansys is used to create an FE model of a structure and then to move the system matrices into Matlab. In Matlab, by using imported system matrices, one can obtain a so-called circulatory matrix that allows for recreating a system's dynamics in RRF. A simple numerical example is provided to clarify all the needed steps. More complex systems such as smart rotors can be also analysed.

The described method has some limitations. The overall number of DOFs cannot be too large, otherwise it causes memory problems in Matlab. Another limiting factor is the characteristic of the bearings, which currently can be only isotropic.

References

1. ANSYS 17.2 Help // Mechanical APDL, SAS IP, INC., n.d.
2. M. S. Kumar, *Rotor Dynamic Analysis Using ANSYS*, in: K. Gupta (Ed.), IUTAM Symposium on Emerging Trends in Rotor Dynamics, Springer Netherlands, (2011) 153 – 162.
3. P. Cupiał, M. Koziół, *Dynamic and control analysis of a smart rotor by combining the ansys and matlab software*, Vibroengineering PROCEDIA, (2014), <https://www.jvejournal.com/article/15470> (accessed September 29, 2019).
4. M. Koziół, *Combined, Ansys and Matlab based approach to the analysis of smart rotor dynamics*, Mechanics and Control, (n.d.).
5. E. Krämer, *Dynamics of Rotors and Foundations*, Springer-Verlag, Berlin Heidelberg, 1993, <https://www.springer.com/gp/book/9783662028001> (accessed July 10, 2019).
6. A. Muszyńska, *Rotordynamics*, CRC Press, Boca Raton, 2005.
7. G. Genta, *Dynamics of Rotating Systems*, Springer-Verlag, New York, 2005, <https://www.springer.com/gp/book/9780387209364> (accessed July 15, 2019).
8. T. Davis, (2011), <https://github.com/rstebbing/SuiteSparse/tree/master/RBio>.
9. J. Burkardt, (2014). https://github.com/johannesgerer/jburkardt-m/tree/master/hb_to_msm.

Numerical Investigation of the Influence of Aerodynamic Forces and Wheel Dynamic Loads of a Vehicle Subjected to Kinematic Excitations

Michał MAKOWSKI

*Warsaw University of Technology, Institute of Vehicles,
ul. Narbutta 84, 02-524 Warszawa, michal.makowski1@pw.edu.pl*

Wiesław GRZESIKIEWICZ

*Warsaw University of Technology, Institute of Vehicles,
ul. Narbutta 84, 02-524 Warszawa, wgr@simr.pw.edu.pl*

Abstract

This paper presents the investigations of vibrations of a vehicle equipped with controlled magneto-rheological (MR) dampers and aerodynamic elements. A scaled sports vehicle model was developed to conduct this research. The tests were carried out with kinematic excitation resulting from road roughness and motion at a variable speed. During the airflow, the aerodynamic elements forces and moments on the test body. Vehicle vibrations are limited by the means of MR controlled dampers. The damping force is determined on the basis of an algorithm, where various strategies for determining forces in MR damper have been adopted. Two criteria were considered for assessing the effectiveness of the control algorithm - minimising vertical acceleration and changes in wheel normal reactions on road surface. This paper presents the results of those studies.

Keywords: magneto-rheological damper, vehicle, control algorithm, vibration

1. Introduction

This paper addresses vibrations of a vehicle moving at high speed during acceleration or deceleration. The system vibrations are determined with the application of a model as stipulated in the papers [2, 6] presenting a mathematical model of a vehicle being equipped with magneto-rheological (MR) [6, 10] or with other controlled dampers described in [3, 4, 9]. It causes an occurrence of the inertia force being a reason for a change of wheels normal reaction forces on a road surface leading towards the wheel slip. In order to avoid this problem, high-speed vehicles are equipped with special aerofoils to generate higher normal reactions on road [7, 11].

The main objective of the work is to propose the methodology to take into account the impact of vehicle longitudinal acceleration and aerodynamic forces and qualitative and quantitative assessment of this influence on the level of wheel dynamic loads. The authors investigated the vibrations caused by unevenness of the road surface, inertia forces acting on the vehicle's body when accelerating and decelerating, as well as aerodynamic forces. The paper presents simulated tests conducted using the model described in [5]. The discussed model has been upgraded with an influence of the aerodynamic forces on the vehicle's vibration.

2. Aerodynamic forces and moments

In [1, 5, 11] an extensive analysis is presented on the influence of air flow on the moving vehicle. The resultant influence of air pressure on the vehicle’s surface is determined by three forces and moments – presented in Figure 1 in the vehicle’s local coordinate system.

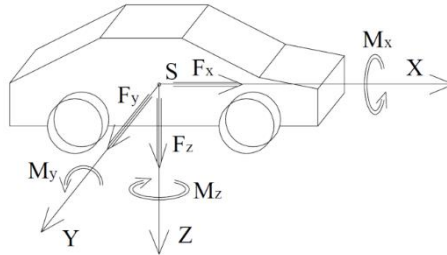


Figure 1. Problem schematic and its coordinate system

Due to the distribution complexity of the air pressure on the vehicle’s surface, the effect was assumed to act in a steady motion, utilising the resultant force and moment. The description of these forces and moments, following the convention from Figure 1, is usually presented in the following form:

$$\begin{aligned}
 F_x &= \frac{1}{2} \rho V^2 A c_x, & F_y &= \frac{1}{2} \rho V^2 A c_y, & F_z &= \frac{1}{2} \rho V^2 A c_z \\
 M_x &= \frac{1}{2} \rho V^2 A l c_{mx}, & M_y &= \frac{1}{2} \rho V^2 A l c_{my}, \\
 M_z &= \frac{1}{2} \rho V^2 A l c_{mz}
 \end{aligned}
 \tag{1}$$

where: ρ – air density, V – vehicle velocity, A – frontal area of the vehicle, l – vehicle wheelbase, c_x, c_y, c_z – dimensionless coefficients of aerodynamic forces: frontal, side, down force (or lift), c_{mx}, c_{my}, c_{mz} – dimensionless coefficients of aerodynamic moments of forces: tilting, inclining, deflecting.

The values of those aerodynamic coefficients are determined based on the measurement results obtained in wind tunnels [1, 7, 11].

As this consideration is limited to vertical vibrations in a rectilinear motion, only F_z force and M_y moment will be considered and the rest of the aerodynamic forces will be neglected. For convenience, some other equivalent dimensionless aerodynamic coefficients determining pressure on the front and rear axles will be considered.

$$c_1 := \frac{a_2}{l} c_z - c_{my}, \quad c_2 := \frac{a_1}{l} c_z - c_{my}
 \tag{2}$$

where: a_1, a_2 – dimensions marked in the Figure 2.

Aerodynamic forces pressing the axles down are computed as per the following formula:

$$N_1 = \frac{1}{2} \rho V^2 A c_1, \quad N_2 = \frac{1}{2} \rho V^2 A c_2
 \tag{3}$$

It should be noted that all of the aforementioned aerodynamic forces act on the vehicle's body. Moreover, one must realize that F_z force refers to the downforce pressing the vehicle's body to the road while in common practice the considerations are based on lift, conventionally facing in the opposite direction.

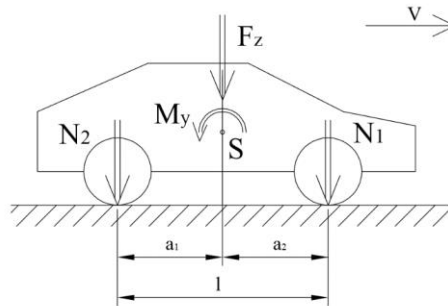


Figure 2. Scheme of vehicle's body aerodynamic forces, F_z – resultant downforce, M_y –inclining moment, N_1 – downforce of the front axle, N_2 – downforce of the rear axle

In some high-speed cars, one might find controllable aerodynamic wings being able to adjust its position to maximize the aerodynamic forces depending on conditions. Within this work an additional tilting moment ΔM_y resulting from the aerofoil geometry is included in the considerations.

$$\Delta M_y = \frac{1}{2} \rho V^2 A l \Delta c_{my} \tag{4}$$

Where in variable Δc_{my} is given by the formula:

$$\Delta c_{my} \in [-\Delta c_{my0}, +\Delta c_{my0}] \tag{5}$$

where Δc_{my0} indicates a limit value of coefficient Δc_{my} .

The value of Δc_{my} coefficient characterizes the aerodynamic configuration of the aerofoil. In this paper, it will be adjusted to the vehicle's longitudinal acceleration in order to decrease the axle load caused by the inertial force of the body.

The moment of force induced by the controlled aerofoil can also be expressed by a change of the normal reactions on road.

$$\Delta N_1 = -\frac{\Delta M_y}{l}, \quad \Delta N_2 = +\frac{\Delta M_y}{l} \tag{6}$$

3. Description of the vehicle's model

A detailed description of the vehicle's mathematical model is provided in [5] and [10]. The model was adopted in a form of a mechanical system, as presented in Figure 2 along with the coordinates describing the respective wheels degrees of freedom.

The model under consideration describes the vehicle equipped with magneto-rheological (MR) dampers, controlled in order to decrease the total level of vibration. Attenuating forces in MR dampers were assumed to act to minimize the square of norm of the body acceleration vector. Leading the following expression to reach the minimum at any time, where w_x, w_y [m²] – weighting coefficients.

$$\mathcal{K} := \ddot{z}^2 + w_x(\ddot{\Phi}_x)^2 + w_y(\ddot{\Phi}_y)^2 \left[\frac{\text{m}^2}{\text{s}^4} \right] \tag{7}$$

The vehicle’s parameters assumed for simulation purposes are presented below. It should be noted that vehicle model discussed within [5, 6] was upgraded with the aerodynamic forces $F_z, M_y, \Delta M_y$ according to the relations given above in formulas (1), (4), (5) and (6).

The following parameters defining the vehicle were adopted: $m = 1250$ kg – mass of the vehicle’s body; $m_0 = 25$ kg – reduced mass of the wheel and components of suspension; $J_x = m\rho_x, \rho_x = 0.6$ m – moment of inertia of the body relative to the longitudinal axis; $J_y = m\rho_y, \rho_y = 1.15$ m – moment of inertia of the body relative to the transverse axis; $a_1 = 1.4$ m, $a_2 = 1.45$ m, $b_1 = b_2 = 0.725$ m – dimensions determining the position of the centre of the body’s mass relative to the wheels, where b_1, b_2 - represent the track width of the front and rear axles of the vehicle.; $k_1 = k_2 = 14.5$ kN/m – stiffness of the front and rear wheels’ suspension; $k_0 = 200$ kN/m – stiffness of the wheel tire; $c_0 = 2.5 \cdot 10^5$ Ns/m – tire damping coefficient.

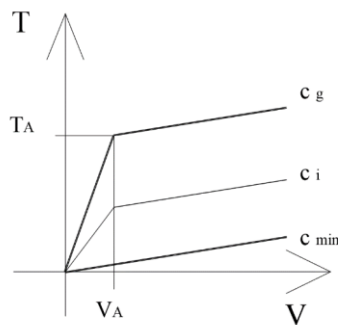


Figure 3. Assumed characteristics of MR damper

The characteristics of magneto-rheological dampers are depicted in Figure 3. The following parameters were assumed: $T_A = 400$ N, $V_A = 0.0075$ m/s, $c_{min} = 210$ Ns/m, $I_{max} = 2A$ (Fig. 3). All of the other parameters regarding the electric power supply system were adopted as per [8, 12].

Moreover, the authors assumed the vehicle to move on a road with an irregularity described by the following function: $\xi(s) = \xi_0 \sin 2\pi \frac{s}{L}$, where $\xi_0 = 5$ mm, $L = 12$ m, s – travelled distance, additionally, the surface profiles were assumed to be shifted in phase by $\Delta s = a_1$. The vehicle moves with a time-dependent speed as presented in Figure 4. The vehicle moves at variable speed to obtain different aerodynamic forces on the flaps. Initially, the vehicle accelerates is $\ddot{x} = 2.85$ m/s² and then drives at constant speed of

100 km/h . After 15 seconds the vehicle accelerations to 150 km/h and in the last distance it moves with constant speed 50 km/h.

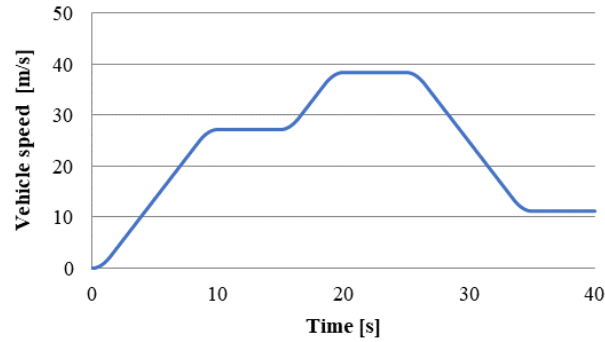


Figure 4. The vehicle speed versus time

Since the investigation conducted had only a comparative purpose, the reference vehicle was assumed to be equipped with the standard dampers characterized by two coefficient: $c_1 = 500$ Ns/m – when damper is compressed, $c_2 = 2.5 \cdot c_1$ – when damper is extended.

To compute the aerodynamic forces, the following data was adopted $\rho = 1.225$ kg/m³ – air density, $A = 1.74$ m² – cross-sectional area of the vehicle, $c_z = 0.2$, $c_{my} = 0.04$ – nominal values of aerodynamic drag coefficients. The Δc_{my0} coefficient is changed when the acceleration of the vehicle is greater than ± 1 m/s². When the vehicle accelerates, we take the value $\Delta c_{my0} = -0.1$, it causes the front axle to be overloaded. In case of braking, the value $\Delta c_{my0} = 0.1$, and this causes the rear axle to be overloaded.

4. Results of simulations

Simulations were performed with the speed given by the relationship depicted in Figure 4. Changing the acceleration of the vehicle causes the inertial forces that cause body roll. These forces can be reduced by external forces, which are formed on the aerodynamic elements. Additionally, the vibration of a vehicle were excited from the ground by the function in the form of $\xi(s)$. These vibrations can be reduced by using MR dampers.

In order to rate intensity of the vehicle body vibration two indicators were proposed. First one defined as a sum of squares of acceleration at points of the body located above the wheels of the vehicle.

$$W_p := \left(\int_0^{t_{\text{end}}} \sum_{i=1}^4 P_i^2(t) dt \right)^{1/2}, \quad t_{\text{end}} = 40 \text{ s} \quad (8)$$

where: P_i , $i = 1, \dots, 4$ – functions defining accelerations at the specified points of vehicle body.

The second indicator is based on variation of wheels normal reaction relative to the static normal force.

$$W_N := \left(\int_0^{t_{\text{end}}} \sum_{i=1}^4 F_i^2(t) dt \right)^{1/2}, \quad t_{\text{end}} = 40 \text{ s} \tag{9}$$

where: F_i , $i = 1, \dots, 4$ – functions describing deviation coefficient of normal reaction (1 – right wheel on front axle, 2 – right wheel on rear axle, 3 – left wheel on front axle, 4 – left wheel on rear axle), given by:

$$F_i = \frac{\Delta N_i}{Q_i} \tag{10}$$

where: ΔN_i – deviation of normal reaction during vehicle vibration, Q_i – wheel static load equals for the wheels.

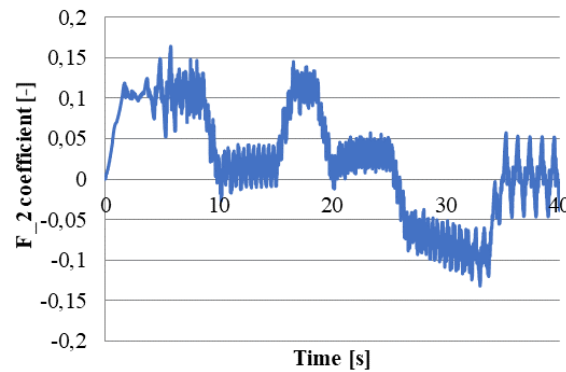


Figure 5. Influence of the aerodynamic forces on a deviation of normal reaction on the road surface – case I (MR damper) – rear axle

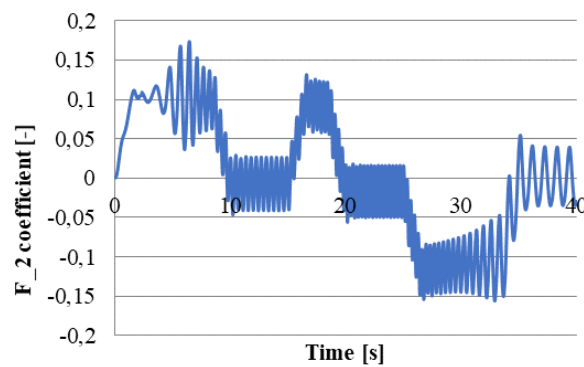


Figure 6. Influence of the aerodynamic forces on a deviation of normal reaction on the road surface – case II (classical damper) – rear axle

The influence of the aerodynamic forces on the deviation of normal reaction on the road surface was presented with the application of relative force plots. This might be defined as a ratio of a deviation and static value of normal reaction of the rear axle. The presented simulation results have only exemplary meaning. Figure 5 presents the results for case I (tab. 1) of the vehicle with MR dampers and Figure 6 presents the results for case II (tab. 1) of the vehicle with classical dampers.

Table 1. Values of coefficient c_z and type of damper for different cases

Case	Coefficient c_z	Damper
I	-0.2	MR
II	0.2	Classical

The comparative analysis of the influence of aerodynamic forces was carried out considering only negative values from the figures, determining the axle underload relative to the static load.

Table 2. Values of coefficients W_p and W_N

Case	W_p	W_N
I	3.095	0.448
II	4.958	0.494

Comparing the graphs (Fig. 5 and Fig. 6) for case I and II, it can be stated that the application of MR dampers results in a decrease of the axle load oscillation amplitude of the factor F_2 . This led to a decrease of the axle load instantaneous values during vehicle braking, observable in the range [27 s ÷ 34 s]. The average value was determined in this range on the basis of the trend line. This value was - 0.08 in the case of I (Fig. 5), and in the case of II (Fig. 6) it was - 0.11. This change is related to the action of aerodynamic forces. In the discussed section, there is also a visible decrease in the values of amplitudes, where in the case of I the value of the amplitude is about 0.03 and in the case of II it is about 0.05. The reduction of the changes of the amplitudes of the rear axle wheel normal reaction forces on the road surfaces ΔN_2 is associated with the control of the MR damper.

Table 2 presents the comparison of the accelerations factor and the dynamic load factor. In case I of using MR controlled dampers and control of the aerodynamic flap, the acceleration ratio was reduced (37.5%) and the dynamic load factor was kept constant compared to vehicle with classic suspension.

5. Summary

This paper considered the influence of aerodynamic forces on a vehicle's vibration during its rectilinear motion with a variable velocity. In order to assess this, two indicators determining the intensity of body vibration and also changes in wheels normal reactions on road on a road surface were chosen.

The values of the chosen indicators were determined based on the simulation results of vehicle vibration during a 40-second run with variable velocity.

Based on the comparative analysis of the test results depicted in table 1 and the graphs illustrating the axels normal reactions on road surface it might be stated that: the utilisation of MR dampers significantly reduced the vehicle's body accelerations and fluctuations in wheel normal reactions on road.

The results of the investigations showed that the use of controlled MR dampers and controlled flap reduced the acceleration factor as well as kept the dynamic load factor constant compared to the results of vehicle tests with classic dampers.

Acknowledgments

This project was funded by the Polish National Centre for Research and Development allocated on the basis of the decision number PBS3/B6/34/2015.

References

1. R. Bansal, R. B. Sharma, *Drag reduction of passenger car using add-on devices*, Journal of Aerodynamics, Volume 2014, Article ID 678518, 13 pages.
2. M. W. Dobry, *Energy Analysis of a Mechanical System with a Dynamic Vibration Absorber*, Vibrations in Physical Systems, **27** (2016) 10-1 – 10-8.
3. R. Faraj, C. Graczykowski, *Hybrid Prediction Control for self-adaptive fluid-based shock-absorbers*, Journal of Sound and Vibration, **449** (2019) 427 – 446, DOI: 10.1016/j.jsv.2019.02.022.
4. C. Graczykowski, R. Faraj, *Development of control systems for fluid-based adaptive impact absorbers*, Mechanical Systems and Signal Processing, ISSN: 0888-3270, DOI: 10.1016/j.ymsp.2018.12.006, **122** (2019) 622 – 641.
5. W. Grzesikiewicz, M. Makowski, *Optimisation of vehicle vibration damping in a semi-active system*, Modelowanie Inżynierskie, **68** (2018) 38 – 46.
6. D. C. Karnopp, *Active damping in road vehicle suspension system*, Vehicle System Dynamics, **12** (1983) 183 – 188.
7. K. Kurec, M. Remer, J. Broniszewski, M. Bibik, S. Tudruj, J. Piechna, *Research Article Advanced Modeling and Simulation of Vehicle Active Aerodynamic Safety*, Journal of Advanced Transportation, Volume 2019, doi.org/10.1155/2019/7308590, 2019.
8. M. Makowski, L. Knap, *Investigation of an off-road vehicle equipped with magnetorheological dampers*, Advances in Mechanical Engineering, **10**(5) (2018) 1 – 11, DOI: 10.1177/1687814018778222.
9. M. Michajłow, T. Szolc, Ł. Jankowski, R. Konowrocki, *Semi-Active Reduction of Vibrations of Periodically Oscillating System*, Solid State Phenomena, **248** (2016) 111 – 118, DOI 10.4028/www.scientific.net/SSP.248.111.
10. M. Rosół, B. Sapiński, *Ability Of Energy Harvesting Mr Damper To Act As A Velocity Sensor In Vibration Control Systems*, Acta_Mechanica Et Automatica, **13**(2) (2019) DOI 10.2478/ama-2019-0019.
11. T. Schütz, *Hucho-Aerodynamik des Automobils*, Springer Fachmedien Wiesbaden, 2013.
12. Thomas Lord Research Center, www.mrfluid.com, 2019.

Application of Machine Learning to Classify Wear Level of Multi-Piston Displacement Pump

Marek IWANIEC

*AGH University of Science and Technology, al. Mickiewicza 30, 30-059 Krakow Poland,
WIMiR, Department of Process Control, iwaniec@agh.edu.pl*

Jerzy STOJEK

*AGH University of Science and Technology, al. Mickiewicza 30, 30-059 Krakow Poland,
WIMiR, Department of Process Control, stojek@agh.edu.pl*

Abstract

This article specifies application of machine learning for the purpose of classifying wear level of multi-piston displacement pump. A diagnostic experiment that was carried out in order to acquire vibration signal matrices from selected locations within the pump body is described herein. Measured signals were subject to time and frequency analysis. Signal attributes related to time and frequency were grouped in a table in accordance with pump wear level. Subsequently, classification models for the pump wear level were developed through application of Matlab package. Assessment of their accuracy was carried out. A selected model was subject to confirmation. The article includes its summary.

Keywords: machine learning, diagnostics, signal analysis, multi-piston pump, vibrations

1. Introduction

Multi-piston pumps make a significant part of the high-power actuator-based hydraulic systems. More than once, proper operation of the entire hydraulic system is made conditional on proper action of the pumps. Wear of individual elements of the pump leads frequently to a drop of its operational pressure, increase of volumetric loss, and as a consequence to a reduction of delivery of pump, increase of vibrations, and increase of pump noisiness. The pump operational vibroacoustic diagnostics is focused on searching symptoms of damages within a vibration signal. In case of high-level noise and mechanical high-complexity (as in the pumps), obtained assessments of wear level of tested elements are burdened with significant uncertainty. The authors of this article specified potentials for application of machine learning for the purpose of classification hydraulic pump wear level on the basis of deliberated vibration signals within typical locations of its body.

2. Pump specification

Figure 1 shows a simplified drawing that includes an axial multi-piston disc-deflected displacement pump. In such a pump, its rotor (2), piston (3), and nose bearing (7) are installed coaxially on a driving shaft (1). Glide shoes (4) on the pistons mate with immovable swashplate (5) deflected at γ angle relative to the pump rotor axis. Pistons along with the rotor rotate and at the same time their shoes (4) that glide on the surface of the immovable swashplate enforce reciprocating motion within the rotor cylinders.

Additionally, the rotor glides on the immovable valve plate (6) which is equipped with suction and pressing openings.

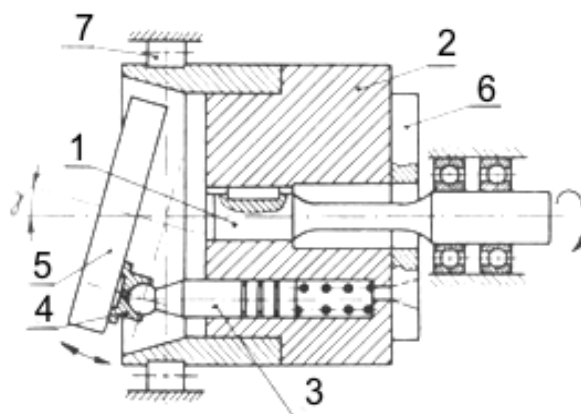


Figure 1. Simplified structural diagram of axial multi-piston disc-deflected pump:
 1– shaft, 2 – rotor, 3 – piston, 4– glide shoe, 5 – swashplate, 6 – valve plate,
 7 – bearing [5]

Wear of displacement pump elements is caused both by forces that arise during mating its individual parts which make kinematic pairs (e.g. piston-cylinder, valve plate-rotor, piston shoe-swashplate) and inadequate conditions related to pump operation such as exceeding nominal pressure, operation at too low viscosity of working medium, loss or insufficient filtration of working medium.

Abrasive wear is the most frequent type of wear to displacement pump elements. Excessive load on the rotor unit leads to a/o abrasive wear of its elements and increasing radial clearance within piston-cylinder kinematic pairs. It results in increasing volumetric loss and lowering pump general efficiency.

Wear of the deflected disc, which mates with surfaces of rotor piston shoes, leads to occurrence of elliptical notch (Figure 2) on its surface and as a consequence to total wear of this surface. It causes reduction of pump mechanical and hydraulic efficiency. Conversely, wear of the valve plate is caused by a/o decay of lubrication layer between the disc surface and a surface of the rotor face. It results in occurrence of flow micro-conduits (Figure 3) on the surface of the swashplate bridge. Such conduits cause flow of the working medium between suction and pressure zones within the pump; as a result, loss of tightness, reduction in operational pressure and volumetric efficiency of the pump occur.



Figure 2. Demonstration of deflected swashplate wear



Figure 3. View of flow micro-conduits on worn valve plate

3. Test run

Testing of multi-piston pump wear level was carried out in a special-design laboratory station. One of major purpose of testing was to obtain some wear on the pump elements in a natural way; for this reason, such multi-hour testing was carried out in real operational conditions. In the course of testing, diagnostic signals - such as working medium flow rate, static and dynamic pressure, as well as pump body vibration acceleration - derived from measuring transducers were recorded systematically. Measurements of the body vibration acceleration were carried out on three testing axes (X, Y, Z) upon earlier installation of transducers on the pump body in the vicinity of the valve plate and the swashplate. Frequency of signal sampling was 50 kHz. A simplified diagram of the pump body vibration measurement including vibration transducers is shown in Figure 4. Cumulative root mean square related to short-time Fourier transform from vibration signals recorded on three operational conditions of the pump is shown in Figure 5.

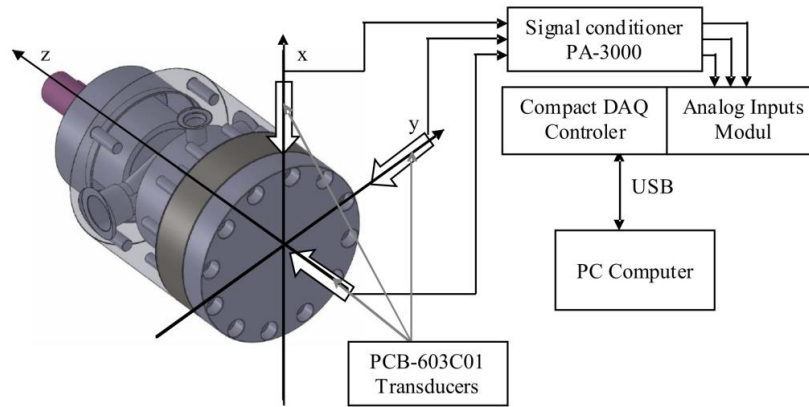


Figure 4. Simplified block diagram related to measurement chain for pump body vibration acceleration on laboratory station

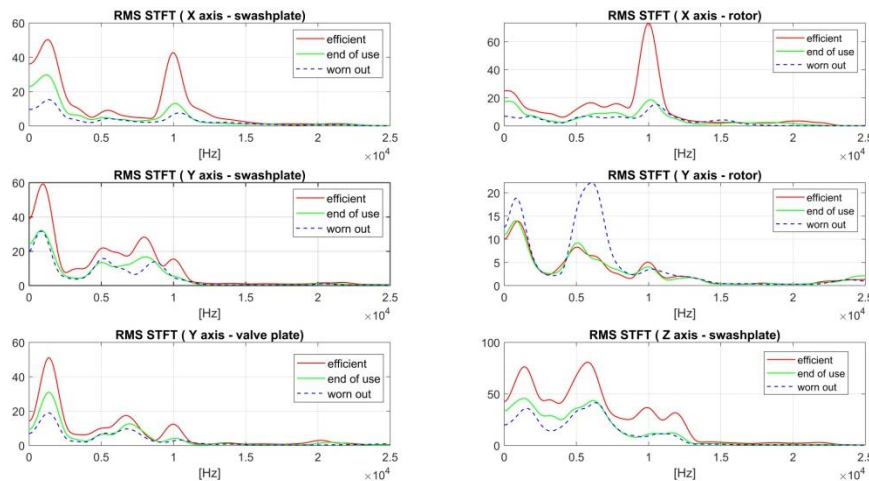


Figure 5. Cumulative root mean square related to short-time Fourier transform from vibration signals recorded on three operational conditions of the pump

Upon completion of laboratory testing, the pump was subject to assessment in relation to wear of its components. Basing on visual inspection, wear of the rotor unit and wear of the valve plate were confirmed. Neither the swashplate surface nor the piston foot surfaces were worn. Such kinematic pair was not obtained due to the pump static operational conditions as the effect of decay of lubricating surface between mating surfaces of the swashplate and the piston foot did not occur. Wear of the rotor unit consisted in (on average) approx. 10 μm enlargement of radial clearance in each piston-cylinder pair. Additionally, wear of the rotor end face mating with surface of the valve plate was

confirmed. Degradation of the rotor end face was measured with a profile measurement gauge [4] within three selected directions (Fig. 6). Upon comparison of profile courses, identical wear of the rotor end face was confirmed with its average depth approximately 50 μm .

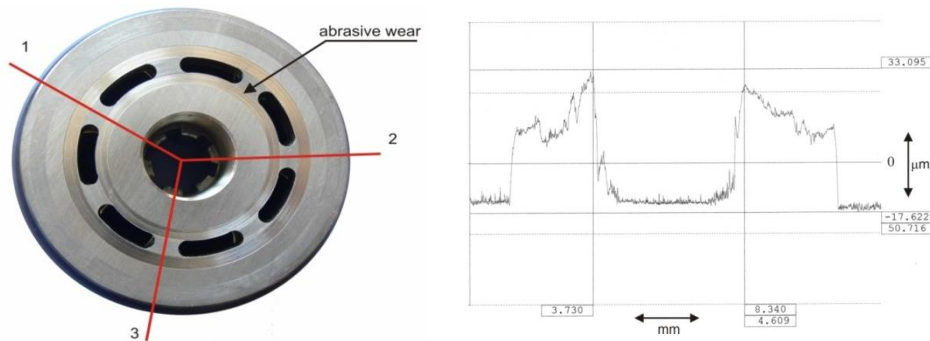


Figure 6. View of wear of rotor end face and a wear profile

Wear of surfaces on the valve plate caused occurrence of flow micro-conduits on the surfaces of the transition zones (so-called bridges) between suction and pressure conduits, Fig. 7. Upon measuring profiles on A transition zone (transition from suction side to pressure side) and B transition zone (transition from pressure side to suction side) uneven wear of the transition zones was confirmed (Fig. 7). However, surface of A transition zone (transition from suction to pressure side) was subject to increased degradation.

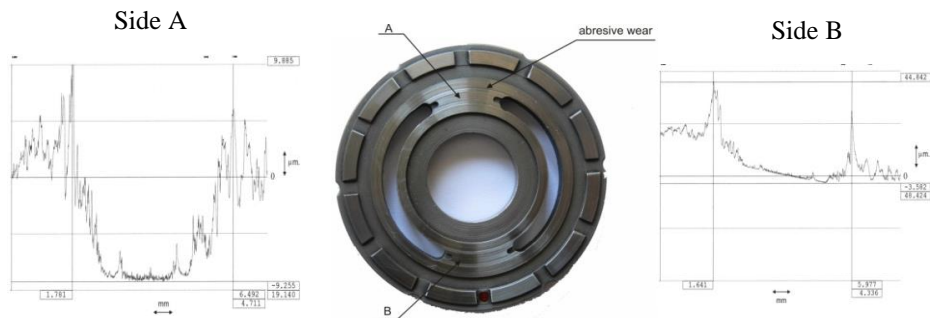


Figure 7. View of worn surface on the valve plate and wear profiles on transition zones

Obtained courses of the pump body vibration were grouped in accordance with the pump efficiency level and attributed with the following grades (labels): *efficient*, *end of use*, *worn*. The next stage of testing included creation of models related to classification of the pump efficiency on the basis of vibration courses that have been grouped.

4. Machine learning

Considering complexity of physical phenomena during the unit operation (usually intensely non-linear and intensely non-stationary), modelling of multi-piston pumps is a hard task in terms of mechanics. Current mathematical models usually constitute approximation of phenomena that occur within pumps during their operation [3]. As part of the operations engineering, machine learning systems have been applied more and more frequently; these form conditions for industrial process or its elements (e.g. machines) only on the basis of available measurement data ascribed to the process conditions (grade). Machine learning systems have been widely used in multiple industries. These are applied a/o in finance, power energy, machine vision, and (broadly defined) operations engineering for the purpose of anticipation of machine wear level and discovery of their damages. In particular, machine learning is applied in all locations where (considering complex conditions within the testing item) it is not possible to provide a full mathematical description of phenomena that occur inside the unit (as such a description does not exist or it could be inaccurate), and the signals recorded at the output (which are responses to input function) make the only available information to be provided.

Considering methods of learning, machine learning can be divided into supervised and non-supervised systems. Supervised learning includes creation of a process model (an issue) on the basis of input data only (collected earlier) and reference output data (labels, grades). This is widely applied to classification in order to use obtained model to classify input data (e.g. recognition of sounds, speech, illness in a patient) as well as regression for the purpose of continuous anticipation of changes to a certain output value induced by alteration of input value. Non-supervised learning, however, is based only on input data, collected earlier, and their grouping as well as interpreting. Such systems are applied for the purpose of data grouping and detecting hidden properties [1]. In case of classification of wear of displacement multi-piston pump, supervised learning algorithms are to be used.

4.1. Arrangement of data for machine learning system

Recorded measurement signals that have been obtained every day during the experiment related to operation of the multi-piston pump were subject to qualitative assessment in order to recover potential major error resulting from a/o unpredictable faults (interference) in the course of recording. Subsequently, constant component was removed from the signals and then subject to wall filtration at cut-off frequency $f = 20$ kHz. Bearing in mind that during signal measurement, a signal related to pump shaft rotation marker was also recorded, all recorded signals were divided as per such marker signal. Matrices related to a single-rotation length were obtained in that manner.

Considering hydraulic oil temperature growth during test, input data of the machine learning system constituted only courses obtained at temperature $T = 50^\circ$ [C] at which oil viscosity does not undergo alteration and may be accepted as a constant. 429 courses of the pump body vibration signals were recorded in total, whereby signals measured for an *efficient* pump constituted 144 of these and signals measured for a pump in transition condition (*end of use*) constituted 144 of these courses. Last 141 courses were obtained from operation of a *worn* pump. A consecutive stage related to arrangement of data for

machine learning system was its division into data applied in the process of learning classifier model and data for its later attestation. 25% of general data were used for testing of operation accuracy of the classifier model that has been obtained. Data received in such a manner were read in to the operational space of Matlab package [2], where further analysis was carried out in the following way:

- selection and calculation of signal properties,
- selection of classifier model,
- assessment of the applied classifier efficiency.

4.2. Selection of signal properties

Another important issue related to a structure of machine learning system is selection of signal features on which the learning system will be basing. Quantity of calculated features is theoretically countless, but practically it is aimed at obtaining a minimum number of properties to describe signal features. It favours obtaining a dense model including accurate mating. Signal property selection optimisation may be carried out with one of available methods [1], that is Correlation Matrix, Principal Component Analysis (PCA), and Sequential Feature Reduction.

For each of obtained matrices related to the pump body vibration signals, time and frequency-feature signals were determined. In case of time-feature signals, standard deviations, entropies, and root-mean-square values were calculated. In case of frequency-feature signals, signal spectrum entropy, maximum power spectral density, and frequency at which maximum power spectral density occurred were accepted. 56 features were obtained in total.

Calculated features of vibration signals were grouped in the table in which pump operational grades (labels) were specified in its last column i.e. *efficient*, *end of use*, *worn* pump. Basing on a cumulative curve including standard deviations related to 56 features (of each pump efficiency grade), their quantity was narrowed to 19 most separative towards individual grades (Figure 8).

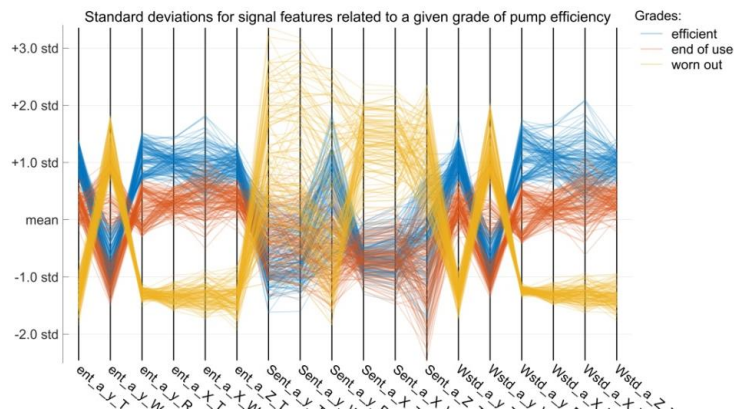


Figure 8. Distribution of standard deviations for signal features related to a given grade of pump efficiency

Vibration signal entropy and their standard deviations were selected as the most convenient. An example of distribution of vibration signal entropy measured in the vicinity of the pump swashplate (along Y and Z measurement directions) that properly separate grades related to pump efficiency are specified in Figure 9.

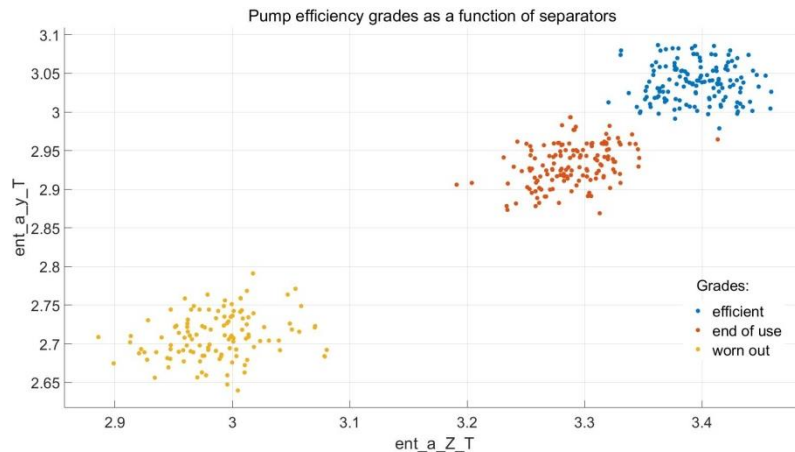


Figure 9. Example of separation of efficiency grades on the tested pump with application of entropy from swashplate vibration signals along Y and Z measurement directions

4.3. Selection of classification algorithm

Both in case of systems that use supervised and non-supervised learning, there is a large group of learning algorithms; selection of the most convenient algorithm is subject to multiple factors. First of all, in order to select an appropriate learning algorithm, it is necessary to determine properly a relevant task for a model (classification, regression, grouping). The next issue is related to the type and quantity of input data which has an impact on learning rate, load of computer memory (controller) as well as accuracy of output data prediction (model response). Selection of an appropriate type of algorithm is not explicit; only an experienced researcher is able to quickly determine an exact algorithm. Usually, selection of the most relevant algorithm of classification is carried out on the basis of multiple type tests as well as provision of assessment related to classifiers that have been obtained in terms of action swiftness, accuracy of classification, and memory load of a computing unit.

A group of algorithms that meet classification requirements related to wear of multi-piston pump include [1]:

- *Decision Trees*

Within this algorithm, in order to classify data, a decision tree is based on a starting point and branching which make a binary decision system; its end branches make a result of attributing data to a specific grade.

- *Discriminant Analysis*

It is based on analysis of signal Gaussian distribution received from observation (input) set. The classifier provides estimation of parameters of Gaussian distribution received from observation set; on such a basis the classifier will ascribe those to a relevant grade.

- *Support Vector Machines*

It classifies data through finding the most relevant hyperplane which separates data of a grade from another grade. The most convenient hyperplane to be considered is the one that separates data with the biggest possible margin.

- *Nearest Neighbour Classifiers*

It determines affiliation of a new data (received from an input set) to the specified grade on the basis of location of anticipated number (K Nearest Neighbour) related to nearest (neighbouring) input set data in relation to this data. However as a position measure, a measure of distance related to classified data from neighbouring data is accepted.

- *Naive Bayes Classifiers*

It makes a probable classifier in which mutual independency of input variables is assumed (naively). Following the Bayes' theorem, this classifier is used to calculate probability related to affiliation of input data to a specific grade.

In the course of classification of the pump wear level, it was decided to test two of previously mentioned algorithms, i.e. algorithm of decision trees and algorithm of K Nearest Neighbour.

4.4. Classification of pump wear level

With application of previously specified data, vibration signal features provide the best possible separation of efficiency grades; decision tree classifier was applied in the course of classification process.

Accuracy of the classifier was estimated through application of Confusion Matrix which is shown in Figure 10. From amongst 144 input signals received from vibrations of *efficient* pump body, the model was able to recognise 142 signals accurately and remaining 2 signals were incorrectly ascribed as *end of use*. Within *end of use* grade the model recognised 142 observations correctly and 2 observations were incorrectly classified as *efficient* pump. All signal observations as part of *end of use* grade were recognised properly. Obtained model is used to classify the pump wear level at 99.1% accuracy; relevant learning time was 0.95 s.

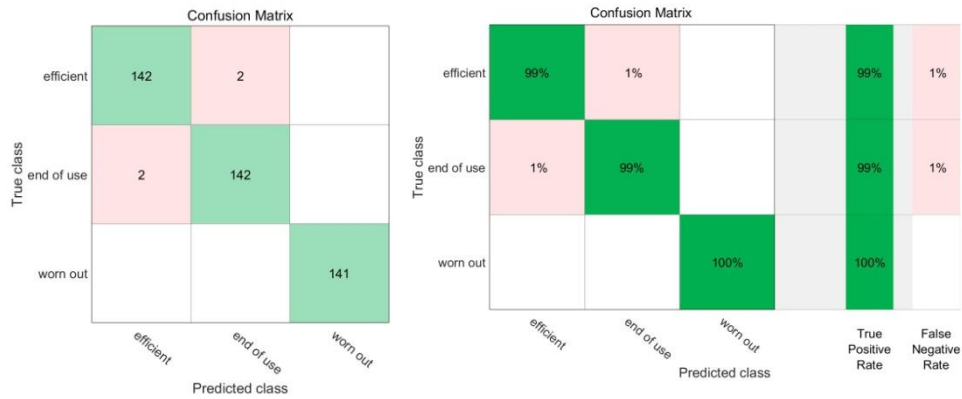


Figure 10. Confusion matrices for pump wear level with application of decision tree model

In order to reduce the dimension of the obtained model (which is to prevent against its overtraining and to ensure better physical implementation), Principal Component Analysis (PCA) was applied. From amongst 19 signal features that has been applied for the purpose of determination of initial classifier model, only those that totally circumscribe 95% of signal variance value within the optimised model were retained. Within examined model, the features that circumscribed 95.9% of signal variance were constituted by entropy of recorded vibrations at the pump swashplate along Y measurement direction and vibration entropy recorded at the pump rotor along Y measurement direction. Accuracy of the pump efficiency grades (as per optimised model) was estimated with confusion matrix; its shown in Figure 11.

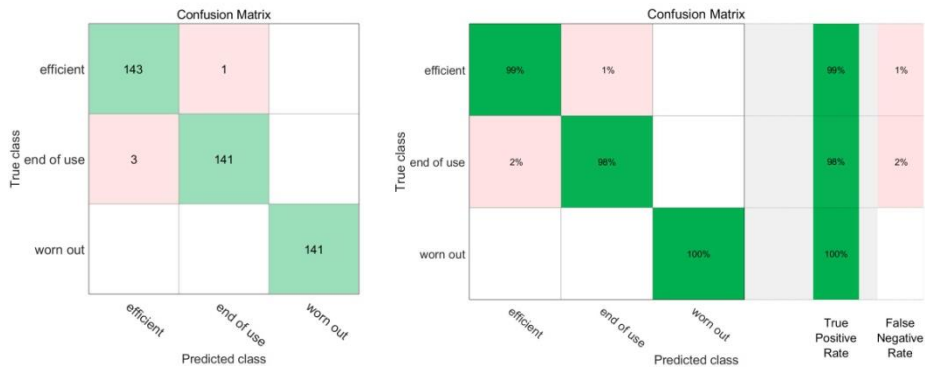


Figure 11. Confusion matrix for pump wear level with application of optimised decision tree model

The obtained model provides classification of the pump wear classification at 99.1% accuracy. From amongst 144 input signals that have been obtained from vibrations of efficient pump body 143 were properly recognised by the model and 1 was recognised

incorrectly as *end of use*. Within *end of use* grade, the model recognised 141 observations correctly, and 3 observations were qualified incorrectly as *efficient* pump. Similar to the basic model, all 141 observations (as part of *worn* pump grade) were recognised properly. A model prediction of the pump deflection gear vibration signal entropy (along Y and Z measurement directions) obtained through estimated model of decision tree is shown in Figure 12.

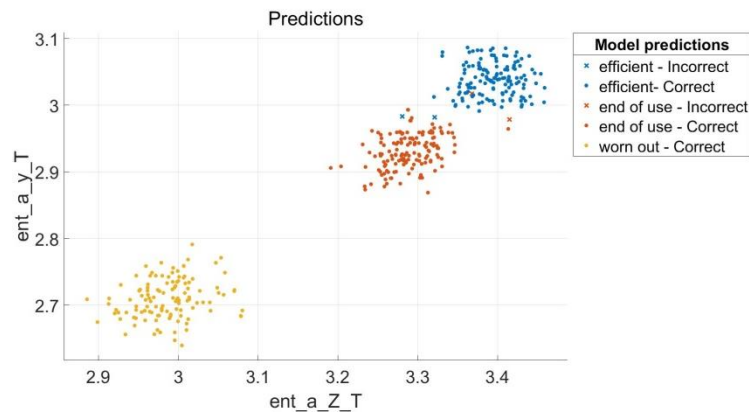


Figure 12. Example of prediction of the pump swashplate vibration signal entropy obtained through optimised model of decision tree

The subsequent algorithm used to classify efficiency of the tested pump was *K* Nearest Neighbour. As in case of the previous classifier, 19 vibration signal features were used; those were separating individual grades of pump efficiency in the best possible way. Correctness of the classifier operations were estimated through application of Confusion Matrix, which is shown in Figure 13. The obtained model classifies the pump wear level at 100% accuracy; learning time was 3.77 s.

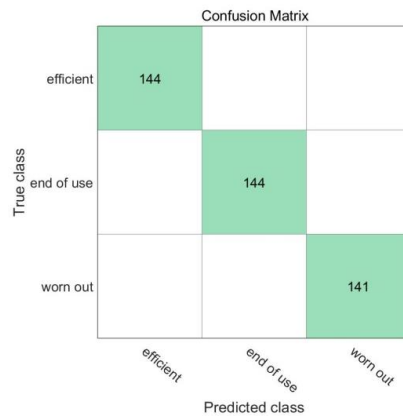


Figure 13. Confusion matrix for pump wear with application of *K* Nearest Neighbour

The optimisation of the obtained model with application of Principal Component Analysis caused reduction of its dimension. As part of the optimised model, features that describe totally 97.7% of signal variance are entropy of vibrations measured at the deflected gear along Y measurement direction and entropy of vibrations measured at the impeller along Y measurement direction. Results of estimations for parameters of optimised model were determined through application of Confusion Matrix; these are shown in Figure 14.

The obtained model classifies the pump wear level at 99.5% accuracy; the training time was 1.76 s. From amongst 144 input signals received from vibrations of *efficient* pump body, 143 were recognised correctly by the model and 1 was incorrectly recognised as *end of use*. As part of *end of use* grade, 143 observations were recognised correctly while 1 observation was incorrectly qualified as *efficient* pump. Similar to the basic model, all 141 signal observations as part of *worn* pump grade were recognised properly.

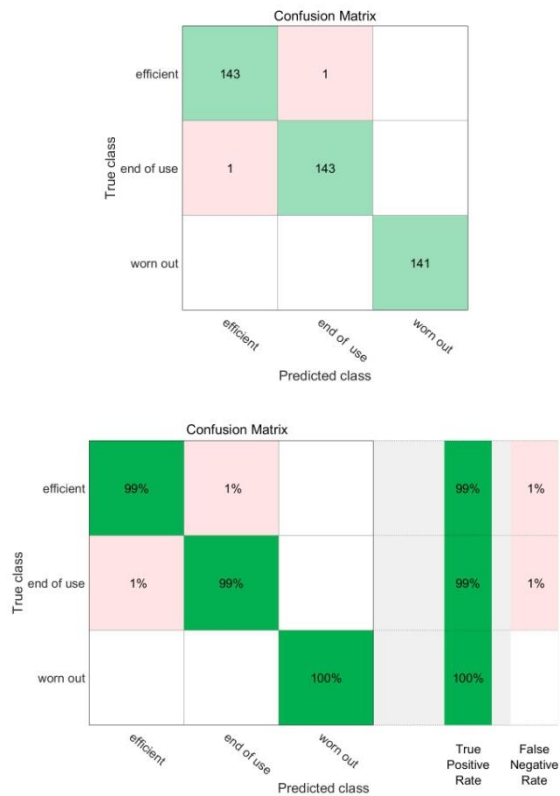


Figure 14. Confusion matrix for pump wear classification with application of K Nearest Neighbour

An example distribution of the pump deflected gear vibration signals (along Y and Z measurement directions) obtained through application of K Nearest Neighbour is shown in Figure 15.

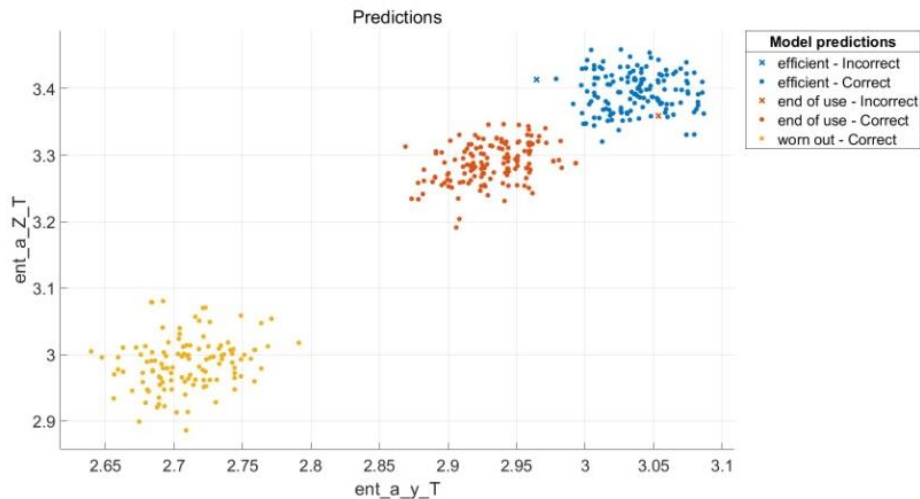


Figure 15. An example of deflected gear vibration signal entropy distribution with application of K Nearest Neighbour

On the basis of analysis of obtained results related to classification of the pump wear level with application of engineered model set it was confirmed that K Nearest Neighbour separates the pump efficiency grades at the highest possible accuracy. This model was subject to further verification that included check of accuracy of the classification related to new measured pump body vibration signals in three levels of efficiency. Basing on pre-calculated features of measured signals the classifier model (exported to Matlab) recognised the pump efficiency grades at 90% accuracy.

5. Summary

As part of issues related to classification of damages to machines and equipment which operations are determined by occurrence of complex mechanical and fluid phenomena (as in case of displacement pumps) the major factor is to carefully arrange input data for machine learning system. Relevant selection of signals and locations for the purpose of measurement provision makes reception of highly informative data possible. With reference to classification of displacement pumps, input data sets that contain measured signals should be as numerous as possible. Input data must include operation courses within entire range of operational pressure changes as well as operational medium viscosity that changes in accordance with temperature fluctuations. It has an impact on the training of obtained classifier model and obtained efficiency during classification of the pump wear level. The next important issue is a selection of such signal features which

separate efficiency grades or machine damages in the best possible way. In case of classification of multi-piston pump, features which separated its efficiency grade in the best way were entropies related to vibration signals. Minimum number of applied features during classification process has an impact on the classifier learning time and prevents against its overtraining. Selection of relevant machine learning algorithms is decisive in relation to obtained accuracy of classification. Basic and modified algorithms of decision tree and nearest neighbours confirmed their usefulness for the purpose of classification of the displacement multi-piston pump wear level at a satisfactory accuracy.

References

1. I. Goodfellow, Y. Bengio, A. Courville, *Deep learning: systemy uczące się*, Wydawnictwo Naukowe PWN SA, 2018.
2. J. Kiusalaas, *Numerical methods in engineering with MATLAB*, Cambridge University Press, 2005.
3. W. Łatas, J. Sojek, *Dynamic model of axial piston swash-plate pump for diagnostics of wear in elements*, The Archive of Mechanical Engineering, **2** (2011) 135 – 155.
4. A. Sadowski, E. Miernik, J. Sobol, *Length and angle metrology* (in Polish), Wydawnictwa Naukowo-Techniczne, Warszawa 1978.
5. S. Stryczek, *Hydrostatic drive* (in Polish), Wydaw. Nauk.-Techniczne, Warszawa 1990.

Localization of Noise Sources in Electric Cookers Based on Sound Pressure and Intensity Measurements

Bartosz JAKUBEK

*Poznan University of Technology, Faculty of Mechanical Engineering and Management,
3 Piotrowo St, 60-965 Poznan, bartosz.jakubek@put.poznan.pl*

Roman BARCZEWSKI

*Poznan University of Technology, Faculty of Mechanical Engineering and Management,
3 Piotrowo St, 60-965 Poznan, roman.barczewski@put.poznan.pl*

Maciej TABASZEWSKI

*Poznan University of Technology, Faculty of Mechanical Engineering and Management,
3 Piotrowo St, 60-965 Poznan, maciej.tabaszewski@put.poznan.pl*

Abstract

The main aim of the study was to compare the features of acoustic maps created on the basis of measurements of sound pressure and intensity in a near acoustic field. Data for comparisons were obtained within the framework of acoustic tests of electric cookers. The results of these studies may help in the selection of acoustic mapping and optimization methods according to individual needs and/or requirements concerning selectivity, measurement bandwidth, dynamics and the ability to locate sound-emitting areas. The paper also presents the results of the spectral analysis of the dominant sources of noise in the cooker, which was helpful in identifying and locating paths of noise propagation from the inside of the cooker.

Keywords: electric cooker, acoustic pressure, sound intensity, noise source localization

1. Introduction

From the point of view of consumers, the class of household appliances is demonstrated, among other things, by the noise it emits. This concerns both devices with significant vibroactivity, such as washing machines or kitchen robots [1], as well as devices with medium and low vibroactivity, such as dishwashers or fridges [2]. The latter group also includes electric cookers. The generation of sound in these devices may be of different nature, e. g. aerodynamic noise (hot air circulation, cooling system) [3], mechanical noise (drive and spit gear), magnetoelectric noise (motors and induction heating systems) [4, 5] and thermal noise (resulting from the formation of stresses and their relaxation). As a consequence, producers carry out vibroacoustic (VA) testing of these devices. Their aim is to obtain information enabling identification of noise sources in prototypes and its reduction. VA tests may also be a tool for post-production quality control of products. In this aspect, the article compares two methods of obtaining information about local sources of sound emitted by devices: measurement of acoustic pressure in a near acoustic field and measurement of sound intensity. A freestanding stove with an electric oven and an induction cooktop was tested. The test results allowed us to specify the advantages and limitations of both measurement methods and their suitability for the above purposes.

2. Object of research

The object of the study used to compare the efficiency of sound source locations was a free-standing cooker with an induction cooktop and an electric oven. This device has components that may be local sound sources. Figure 1 shows the tested stove, the measurement grid used for measurements in a near acoustic field and indicates the components - sound sources.



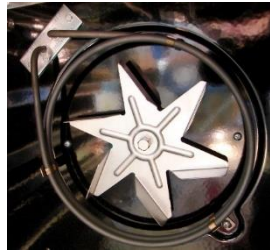
Figure 1. Tested object; view; rear wall with measuring grid and after removing the cover (1 – ventilation grilles, 2 – outlet duct from the oven, 3 – spit drive, 4 – motor for the hot air circulation fan)

Sound sources can be of a different nature. In the examined model of the cooker, the sources of mechanical noise are: fans, spit and electric motors partially driving these components. The motors also generate noise from magneto-electric phenomena. Noise of a similar nature is emitted by inductive heating fields.

There are 2 fans in the cooker. A centrifugal fan without a typical housing is used in the hot air circulation system. A second fan is located in the space between the oven and the cooktop and ensures air circulation. The fans are flow-through machines and therefore mainly emit aerodynamic noise. In the noise spectrum of fans, the components of the vane frequency and its superharmonics can be expected, as well as the broadband noise associated with the airflow. The noise from the inside of the oven propagates, among other things, through the outlet channel at the back of the stove (see Figure 1).

The views of the components in the tested stove and the octave spectra of the sound pressure levels recorded during their operation are shown in Figures 2 to 6. On the bar charts, gray color was used to distinguish the acoustic background level. The signals were recorded at a distance of approx. 100 mm from the working components. The comparison of spectra and A-weighted sound levels allowed to determine the dominant source of noise in the tested cooker.

The presented spectra largely facilitated the analysis of acoustic maps in terms of identification of noise sources and paths of noise propagation from the inside of the stove.



Hot air circulation fan without cover

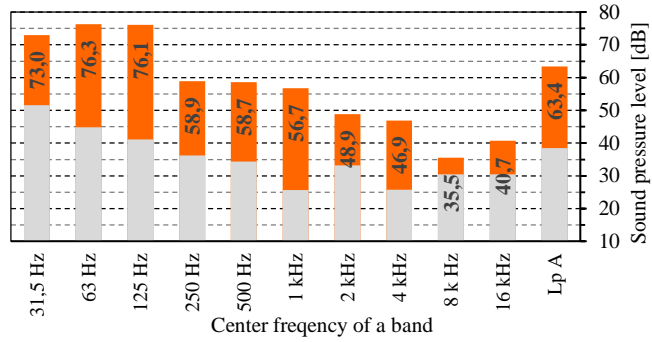


Figure 2. Octave spectrum of the noise of the hot air circulation fan



Spit drive

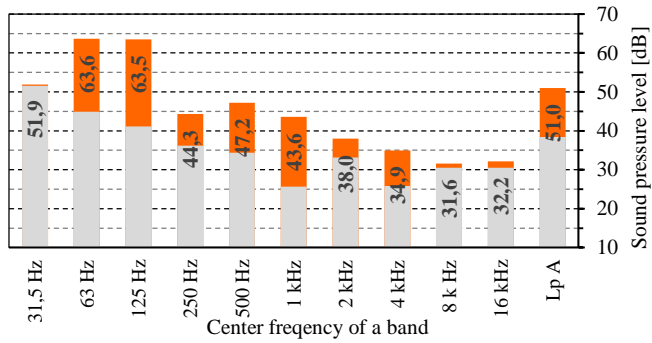


Figure 3. Octave spectrum of the noise of the spit drive



Centrifugal fan (above the oven)

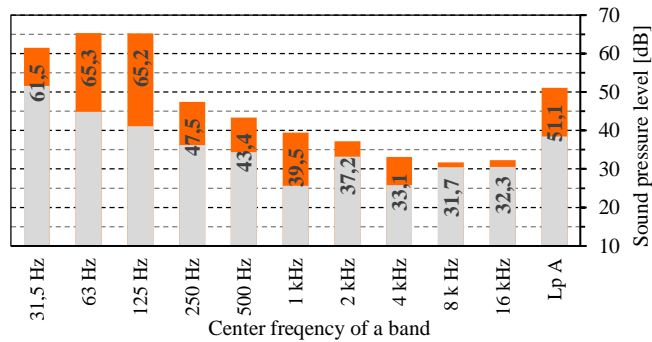


Figure 4. Octave spectrum of the noise of the centrifugal fan

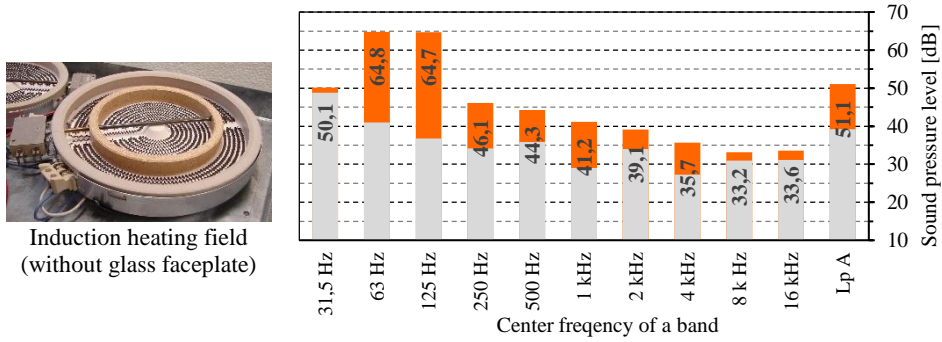


Figure 5. Octave spectrum of the noise of the induction heating field, continuous operation

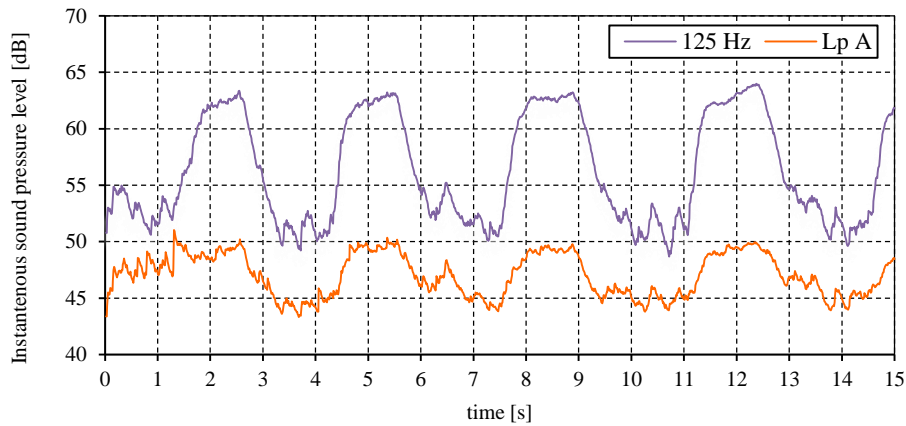


Figure 6. Changes in the sound pressure levels recorded during the cyclical switching on of the heating field (50% power)

When the oven is heated, crackling occurs due to the relaxation of stresses caused by the thermal expansion of the elements in the oven. This noise has an impulse character and is characterized by significant changes in instantaneous sound levels. Examples of changes of the sound pressure level recorded inside the oven in the initial phase of heating are shown in Figure 7a. The octave spectrum of noise in the heating phase (averaged over a 30-second signal sequence) is shown in Figure 7b.

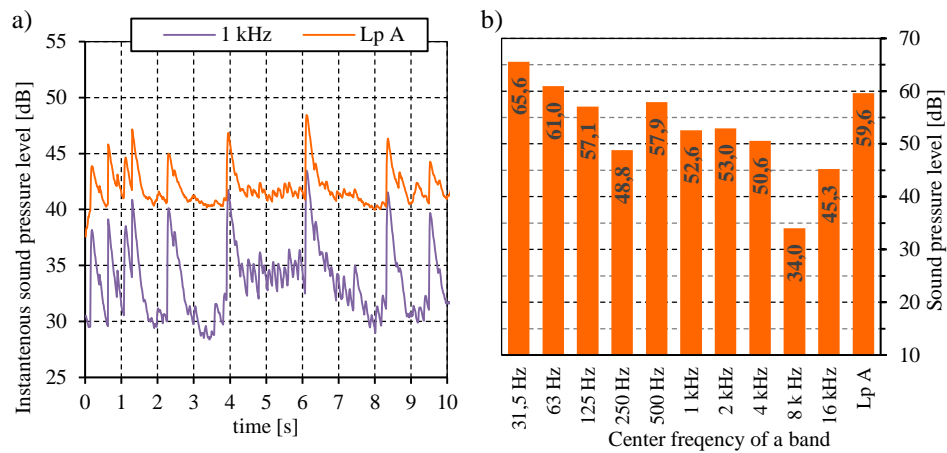


Figure 7. Changes in sound pressure levels and the octave spectrum of noise during the preheating phase of the oven

Impulse noise associated with oven heating in comparison with the noise emitted by the presented components has also important components in higher frequency bands (up to 4 kHz).

3. Methods for locating noise sources

The main purpose of the study was to compare the effectiveness of two methods used to identify and locate paths of noise propagation from inside of the oven. The noise mapping methods were compared in qualitative and quantitative terms based on:

- sound pressure measurements in a near acoustic field,
- measurements with an intensity probe.

3.1. Sound pressure measurements

Measurements of acoustic pressure in the near acoustic field of the cooker were performed with the use of a condenser microphone GRAS 40AN (polarizing voltage: 200V) with a SVAN 01A preamplifier cooperating with a SVAN 912AE analyzer. During the measurements, the following analyzer settings were used:

- FUNCTION 1/1 Oct (type of analysis),
- RMS_DET Slow (time characteristics),
- A.REPEAT Off (auto-repetition),
- AVERAG. Linear (type of averaging),
- AV.TIME 20s (time of averaging).

Scanning of the kitchen walls with a microphone was carried out at a distance of 100 ± 1 mm from the surface of the tested object. For the rear panel, which is not flat, the distance of 100 mm was determined from the heptagonal embossed plane (see Fig. 1). Octave analysis was performed in the full acoustic band, however, the subject of

comparisons were sound pressure levels in octave bands with mid-band frequencies from 63 Hz to 2000 Hz, which resulted from a limited band of intensity measurements. The assumed 20-second averaging time was sufficient due to the stationary nature of the emitted noise. The measuring grid was composed of 228 sub-areas with dimensions as close as possible to a square with a side $a = 100$ mm. The surface of the cooktop was divided into 30 fields (5 columns and 6 rows), side walls - 45 fields (5 columns and 9 rows), and the front and back of the stove - 54 fields (6 columns and 9 rows). The total measurement time was 76 minutes, this time did not include preparatory and finishing activities and time related to moving the microphone between subsequent measurement fields. In order to obtain reliable results with this method, it was necessary to guarantee a sufficiently low level of acoustic background (minimum 10 dB less than the level of noise emitted by the object).

An example of a map of sound pressure levels is presented in Figure 8. Due to the location of dominant sound sources in the back wall of the stove, the comparison of methods was based on acoustic maps of the back wall.

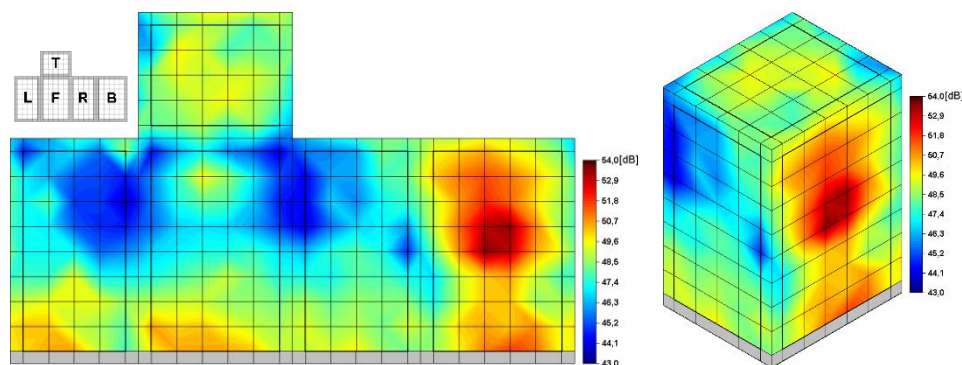


Figure 8. Map of sound pressure levels in an octave with a mid-band frequency of 250 Hz, in a developed view and in isometry

3.2. Sound intensity measurements

Sound emitting areas can also be located based on sound level maps. In this case, measurement at discrete points method was used [6]. It involves measuring sound intensity with a two-microphone probe (Fig. 9) at a short distance from the tested surface. For comparative purposes, an analogous measuring grid with uniform density was adopted. The normal component of the averaged sound intensity was measured, both its active part related to the energy radiated by the source and the reactive part related to the circulating energy (not radiated outside) [7].

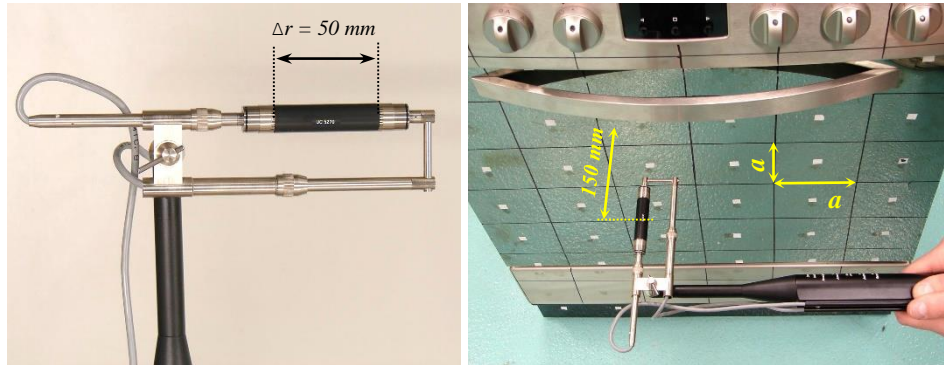


Figure 9. Two-microphone sound level probe with a separator of length Δr ; carrying out measurements

Sound intensity is a vector that expresses the flow of sound energy through a unit surface. It is defined as the time-averaged product of the sound pressure and the speed of the particle [7]:

$$\vec{I} = \overline{p(t)\vec{u}(t)}, \tag{1}$$

or the time-averaged product of the sound pressure and particle speed in the direction r :

$$I_r = \overline{p(t)u_r(t)}, \tag{2}$$

where: $p(t)$ – instantaneous sound pressure at the point, $\vec{u}(t)$ – particle velocity at the same point, and the bar indicates time averaging.

The active part of the intensity measured in the direction r may be expressed as [8]:

$$I_r = \frac{-p_{\text{RMS}}^2}{\rho ck} \cdot \frac{\partial \varphi}{\partial r}, \tag{3}$$

where: p_{RMS} – rms value of sound pressure, φ – phase between pressures measured by two microphones, ρ – density of the medium, c – speed of sound in the medium, k – wave number.

In measurement practice, when using a two-microphone intensity probe, the intensity is determined in the frequency domain from the formula [7]:

$$I_r = \frac{-1}{\rho \omega \Delta r} \text{Im}(G_{AB}), \tag{4}$$

where: ω – frequency, Δr – distance between microphones, $\text{Im}(G_{AB})$ – the imaginary part of the mutual spectrum of sound pressures measured in points A and B.

The reactive part of the intensity can be defined as [9]:

$$\vec{J} = \frac{1}{2} \text{Im}(p\vec{u}^*), \tag{5}$$

where u^* indicates the complex conjugate of u .

However, in the direction r the reactive part of the intensity can be determined as [8]:

$$J_r = \frac{-1}{2\rho ck} \cdot \frac{\partial p_{\text{RMS}}^2}{\partial r} \quad (6)$$

It is also worth mentioning another possibility of creating sound intensity maps. If the sense of the intensity vector (negative values of the intensities obtained in the measurements) is taken into account, the acoustic energy absorption areas may also be determined.

In order to compare the results of the intensity method with the method of acoustic pressure measurements, the intensity measurements at the points of the measurement grid were used. Only the normal component to the measurement area was taken into account, which required proper maintenance of the probe direction during the measurement. Wherever possible, measurements were taken using a tripod. A constant distance of 150 mm between the probe and the object surface was maintained during the measurement (see Figure 9). The averaging time at each of the measurement points was 60 seconds.

The measurements were performed with B&K 3548 sound intensity probe coupled with B&K 2144 real-time frequency analyzer. The frequency range of the spectral analysis was related to the linear response of the probe: 31.5 Hz to 1250 Hz. In this band the highest levels of noise emitted by components of the stove were present, shown in Figures 2, 3 and 4. This limitation also resulted from the use of a separator between microphones with a length of $\Delta r = 50$ mm. The use of separators with a length of 12 mm or 6 mm would allow to obtain results in higher frequency bands of 125 Hz to 5 kHz or 250 Hz to 10 kHz respectively [10, 11]. Measurement of sound intensity in the band from 31.5 Hz to 10 kHz would require the use of at least 2 separators with lengths of 6 and 50 mm.

4. Results (acoustic maps)

The acoustic maps of the back wall of the stove were analyzed in order to compare the described methods. Acoustic maps for bands from 125 Hz to 2 kHz are presented. These are the bands in which the noise emitted by the components shown in Figures 2, 3 and 4 was expected to be visible.

For intensity measurements with a 50 mm separator, the map in the 2 kHz band is for illustrative purposes only (this band is outside the linear range). The results may be affected by an error of up to approx. 3 dB [11].

The following conclusions can be drawn from the comparison of the acoustic maps:

- Both the pressure and intensity maps in the 125 and 250 Hz bands clearly show the sound emission area in the middle of the rear wall. This is very likely to be due to the noise emitted by the motor driving the hot air circulation fan (see Fig. 1).
- The 1000 Hz band shows the area of noise emission from the ventilation duct from the oven (see Fig. 1).
- In the upper part of the map of sound pressure levels in the 2000 Hz band, two local noise sources can be distinguished - ventilation grilles. On the other hand, the intensity level map does not distinguish between these two point sources of noise. It should be noted, however, that measurements in this band exceed the linear range of operation of the intensity probe (for a 50 mm separator).

- In the 500 Hz band, the local maxima occur in different areas, which results in a low correlation coefficient between the maps in this octave. It is also difficult to unambiguously link local maxima with a specific component.

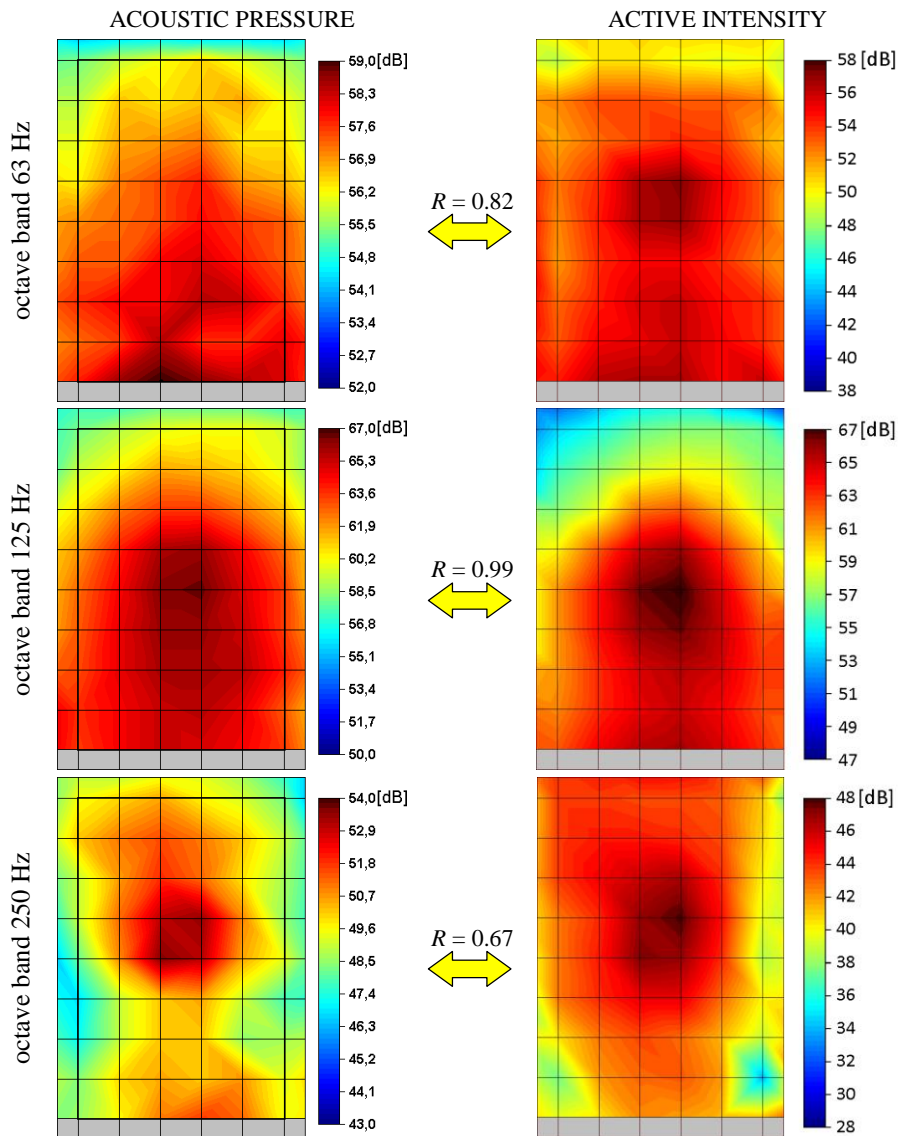


Figure 10. Comparison of acoustic maps based on the results of measurements of sound pressure and intensity in a near acoustic field; octaves 63 Hz, 125 Hz and 250 Hz (R – correlation coefficient between maps, the graphics were prepared in scilab-6.02 environment [12])

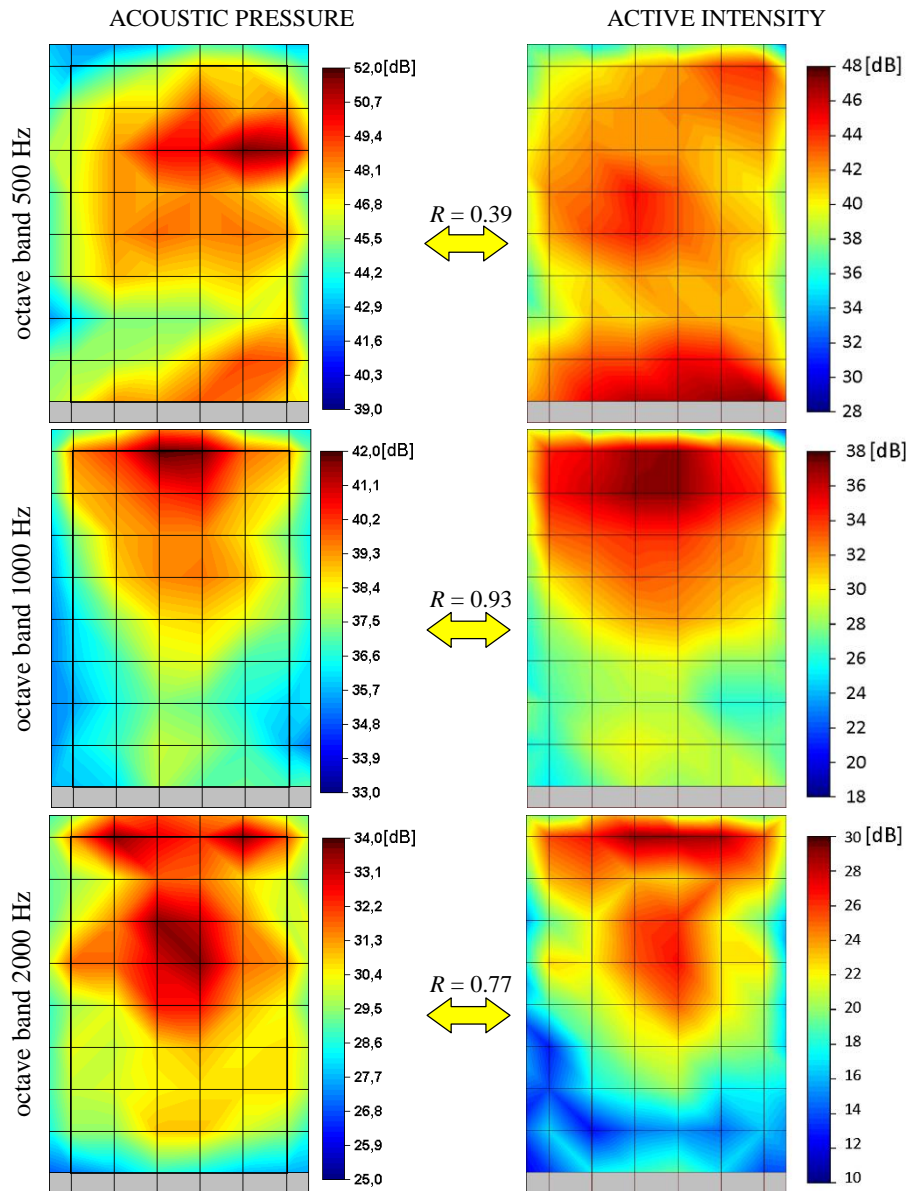


Figure 11. Comparison of acoustic maps based on the results of measurements of sound pressure and intensity in a near acoustic field; octaves 500 Hz, 1000 Hz and 2000 Hz (R – correlation coefficient between maps, the graphics were prepared in scilab-6.02 environment [12])

From the point of view of the assessment of the effectiveness of the location of areas emitting sound on maps obtained by the two methods, it was advisable to estimate the dynamics and selectivity of maps. To estimate the dynamics, the maps (bands: 125 Hz, 250 Hz and 1 kHz) for which the highest differentiation of levels was noted and where the areas emitting sound were clearly visible were taken into account. To compare the selectivity in terms of location capabilities, a map for an octave of 125 Hz was selected, characterized by a well visible local sound source. To estimate the selectivity, the criterion of a 3 decibel drop in the levels in the local maximum environment was adopted. The obtained result was related to the measuring grid size a . The results of the assessment of selectivity and dynamics of acoustic maps made by two methods are presented in Figure 12 in Table 1.

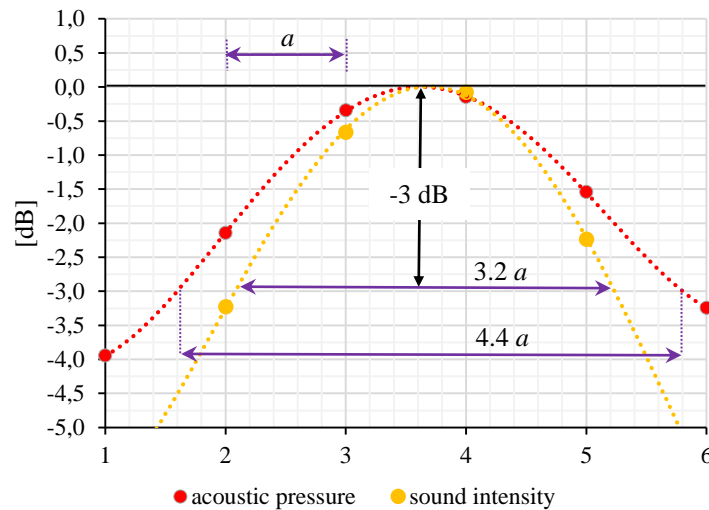


Figure 12. Example of comparison of selectivity of acoustic maps, octave 125 Hz, polynomial interpolation

Estimation of the selectivity of the source location was made, for example, for maps in the 125 Hz octave band, where the highest pressure and intensity levels were recorded, and in the central part one local noise source was clearly visible. The selectivity of sound source location based on acoustic maps is better for intensity measurements. It is related to the grid size and is $3.2 a$ (for pressure measurements the selectivity is $4.4 a$). These values are only estimates but this regularity applies to other maps in other octave bands.

Table 1. Maximum and minimum levels and map dynamics

octave	pressure level [dB]			intensity level [dB]		
	L_{max}	L_{min}	ΔL	L_{max}	L_{min}	ΔL
125 Hz	66.5	58.0	8.5	67.0	53.4	13.6
250 Hz	53.5	46.8	6.7	47.9	33.9	14.0
1000 Hz	41.9	35.5	6.4	37.3	24.5	12.8

From the data in Table 1 it can be concluded that the maps made using the intensity method are more dynamic than the maps made using pressure measurements. It can be estimated that the dynamics of the former is on average by approx. 6 dB higher.

The conducted research allowed to compare the properties, advantages and limitations of the presented two measurement methods being the basis for the creation of acoustic maps. Such a comparison of maps obtained during the tests of electric cooker is presented in Table 2.

Table 2. Comparison of the characteristics of the methods used to locate the sources of noise emitted by the stove

	Intensity method	Pressure measurement
Measuring band	Depends on the length of the separator, 31.5 Hz – 1250 Hz (Δr 50 mm); 125 Hz – 5 kHz (Δr 12 mm); 250 Hz – 10 kHz (Δr 6 mm)	20 Hz – 20 kHz; Wider bandwidth possible
Measuring time at one point	60 s	20 s, or shorter
Number of measuring points	216	216
Total time of measurement	216 min (1 separator, limited bandwidth) 432 min using 2 separators (e.g. Δr 50 mm and 6 mm, band from 31.5 Hz to 10 kHz)	72 min in full acoustic range
Possibility of use in industry	Can be used with most appliances [13], according to IEC 60704-2-10 [14] cannot be used for inspection of cookers	Limited, requires a separate measurement room, preferably with acoustic adaptation
Impact of the measurement environment	Insignificant impact of interferences	Significant influence of acoustic background and interferences and, to a lesser extent, of the sounds reflected in the test room
Experience of the measuring operator	Required extensive experience and knowledge of sound intensity measurement and analysis	Required basic knowledge and skills in the field of acoustic measurements and analysis
Automation of measurements	Possible with automatic probe positioning system (measuring frame, industrial manipulator)	Possible with automatic microphone positioning system (measuring frame, industrial manipulator)
Interpretation of results (shown in the form of a map)	Easy based on the active part of the intensity; not intuitive based on the reactive part of the intensity	Easy (intuitive)
Determination of the sound power level	Possible in a near acoustic field, in the presence of interfering sources and under any ambient acoustic conditions [15] e. g. based on ISO 9614 [16]	Possible after taking into account the influence of background noise and reflected sounds, required fulfillment of conditions concerning the measuring environment, e. g. based on ISO 3746 [17]
Equipment	Advanced, rather expensive	Commonly used, moderate cost
Dynamics	higher	lower
Selectivity	higher	lower

5. Conclusions

The results of the research may be helpful in the selection of the method of acoustic mapping and optimization of operations depending on individual needs and/or requirements concerning selectivity, measurement bandwidth, dynamics and ability to locate sound-emitting areas.

To sum up, it can be concluded that the intensity method allows to obtain maps with better selectivity and dynamics compared to the pressure level maps. However, obtaining results in the band from 20 Hz to 20 kHz is guaranteed by sound pressure measurements (the upper limit of the measuring band is only limited by the linear microphone bandwidth). The use of the intensity probe allows to create maps in a range up to approx. 10 kHz. In this case, it is necessary to use 2 separators $\Delta r = 50$ mm and $\Delta r = 6$ mm. The consequence of this is at least 2 times longer time of measurements (assuming the same measurement time - averaging time).

An alternative way of creating intensity maps enabling to avoid this inconvenience is to use a *Microflown* probe. It guarantees measurements up to approx. 11 kHz [15].

The results concerning dynamics and selectivity are for illustrative purposes only and are related to a specific object. For more accurate results, targeted research is required.

Acknowledgment

The work was financed by science grant 02/21/SBAD/3558 from the Ministry of Science and Higher Education.

References

1. M. Wojsznis, I. Mazurek, L. Róžański, R. Barczewski, *The influence of vibrations generated by handheld household appliances on temperature changes of user hands*, Journal of Vibrations in Physical Systems, **29** (2018) 24-1 – 24-8.
2. R. Barczewski, B. Jakubek, *Problems of in-situ vibroacoustic testing of low-vibroactive devices*, Journal of Vibration in Physical Systems, **25** (2012) 59 – 64.
3. T. Bose, *Aerodynamic noise an introduction for physicists and engineers*, Springer, New York 2013, 1 – 29.
4. A. F. Ohnacker, *Maintenance of electrical equipment in maintenance engineering handbook*, Ed. L.R. Higgins, New York 1988, 7-1-7-28.
5. C. Cempel, *Applied vibroacoustics*, PWN, Warszawa 1989, 91 – 92.
6. PN-EN ISO 9614-1:1999, *Acoustics. Determination of sound power levels of noise sources using sound intensity. Part 1: Measurement at discrete points*, IDT EN ISO 9614-1:1995.
7. S. Gade, *Sound Intensity (Theory)*, Bruel & Kjaer Technical Review, **3** (1982) 3 – 39.
8. K. B. Ginn, *Active and Reactive Intensity Measurements using the Dual Channel Real-Time Frequency Analyzer 2133*, Application Notes, Bruel & Kjaer.
9. F. Jakobsen, *Sound Intensity and its Measurement*, Fifth International Congress on Sound and Vibration, Dec. 15-18, 1997, Adelaide, Australia.
10. S. Gade, *Sound Intensity (Part II Instrumentation & Applications)*, Bruel & Kjaer Technical Review, **4** (1982) 3 – 32.

11. S. Gade, *Validity of Intensity Measurements in Partially Diffuse Sound Field*, *Bruel & Kjaer Technical Review*, **4** (1985) 3 – 31.
12. B. Jakubek, *Comparative analysis of vibroactivity maps of household appliances on the example of an electric oven*, Poznan University of Technology, Faculty of Mechanical Engineering and Management (master's thesis), Poznan 2013.
13. M. Meissner, *Acoustic energy density distribution and sound intensity vector field inside coupled spaces*, *Journal of the Acoustical Society of America*, **132**(1) (2012) 228 – 238.
14. IEC 60704-2-10:2011, *Household and similar electrical appliances - Test code for the determination of airborne acoustical noise - Part 2-10: Particular requirements for electric cooking ranges, ovens, grills, microwave ovens and combination of these*.
15. S. Weyna, *Rozpływ energii akustycznych źródeł rzeczywistych*, WNT, Warszawa 2005.
16. PN-EN ISO 9614-2:2000, *Acoustics. Determination of sound power levels of noise sources using sound intensity. Part 2: Measurement by scanning*, IDT EN ISO 9614-2: 1996.
17. ISO 3746:2010, *Acoustics — Determination of sound power levels and sound energy levels of noise sources using sound pressure — Survey method using an enveloping measurement surface over a reflecting plane*.

The Steam Pressure Impacts Reducing System for a Biomass Cogenerator Based on Monitoring of the Frequency Characteristics of the Steam Actuator

Krzysztof LALIK

AGH University of Science and Technology, Faculty of Mechanical Engineering and Robotics, Al. Mickiewicza 30, 30-059 Krakow, Poland, klalik@agh.edu.pl

Szymon PODLASEK

AGH University of Science and Technology, Faculty of Energy and Fuels, Al. Mickiewicza 30, 30-059 Krakow, Poland, podlasek@agh.edu.pl

Wojciech GORYL

AGH University of Science and Technology, Faculty of Energy and Fuels, Al. Mickiewicza 30, 30-059 Krakow, Poland, wgoryl@agh.edu.pl

Grzegorz GÓRA

AGH University of Science and Technology, Faculty of Mechanical Engineering and Robotics, Al. Mickiewicza 30, 30-059 Krakow, Poland, ggora@agh.edu.pl

Abstract

Introduced through policy instruments, as well as due to increase awareness of and demand for energy, alternative, renewable energy sources are becoming increasingly popular and necessary. The growing market and standards are forcing producers of renewable energy sources to constantly improve the quality of their products. Biomass trigenerators are one way of obtaining such energy, both in the form of electricity, heat and cold. These are elements generating steam by burning various solid, liquid or gaseous fuels of organic origin. Rotating machines in the form of turbines or steam engines are used to generate electricity. Unfortunately, they are particularly exposed to steam impacts associated with discontinuous work. This article presents the monitoring and prevention system for such impacts. It is based on the analysis of the frequency spectrum of vibrations of such generators and can be used to implement a trigenerator control system that will reduce the influence of such impacts. With proposed diagnostic system, the efficiency and life span of a Renewable Energy Source can increase significantly

Keywords: steam generator, fault diagnosis, vibration response, biomass, water hammer

1. Introduction

According to the new emission reduction requirements, conventional energy systems will be replaced by technologies that do not require fossil fuels. Solutions are sought that will allow heat, energy, chill to be generated irrespective of atmospheric conditions, diversify source of heat and develop a distributed energy system. The system that meets the above issues could be a partly solution of the European Union's Energy and Climate Policy. This program assumes a 20% reduction in greenhouse gas emissions compared to 1990 emissions, an increase in the share of energy consumption from renewable energy

sources to 20% and an increase in energy efficiency by 20% compared to forecasts for 2020 [1].

One idea is to use a cogeneration or trigeneration system on a micro, small and medium scale powered by biofuels. Systems can be divided into due of generating electric power as follows:

- Micro scale systems – up to 50 kWe,
- Small scale systems – from 50 kWe to 1 MWe,
- Medium scale systems – from 1 MWe to 50 MWe [2].

Depending on the fuel, these installations may use different executive elements. Most often these elements are Otto engines powered by biogas, fuel cells for hydrogen, an external heat source for the Stirling engine. However, these installations are expensive both during construction and operation or they are test installations.

2. Installation under examination

An alternative may be steam systems using steam machines adapted to a much smaller scale than in the case of commercial power engineering. This solution uses the Rankin cycle known from coal power plants but allows it to be supplied with different fuels depending on the selected heat source.

Heat generated during the combustion process allows to evaporate water, which is used as a working medium. Steam goes from boiler to the turbine and expands passing the blades disposed on the rotor (transfers to the rotor the part of its energy). Mechanical energy is converted to the power using a dedicated power generator. In the typical power plant, partially expanded medium goes next to the condenser what allows to utilize the heat of the condensation. An extension of classical Rankine Cycle (RC) is the Organic Rankine cycle (ORC). In ORC cycle the working medium (water) is replaced by low-boiling fluid, such as silicone oil, benzene, toluene etc. The use of organic working fluids results in the ORC cycle having several advantages over the steam cycle. Higher molecular weight than water increases the mass flow rate of the fluid for the same size of turbine. The result is a better power generation efficiency (about 10-20%). Most importantly, the boiling point of ORC fluids is much lower than that of water, so they can be applied in lower temperatures.

In the case of liquid or gaseous biofuels, the solution does not require change in RC, however for solid fuels it is beneficial to expand the system with an additional intermediate medium. The use of thermal oil cycle between heat source and evaporator will allow for increased thermal inertia, which will prevent from peak increases or decreases temperature in steam cycle. The proposed system based on the extended Rankine cycle is presented in Fig. 1.

The use of cogeneration systems equipped with the biomass-fired boilers is possible both in the case. It is really important especially in the cases, where the problems with access to the grid occur. In such facilities the oil-fired external combustion engines, which operation is really expensive are mostly used. Replacing such devices by biomass-fired CHP systems will allow reducing energy costs and obtaining full or partial energy independence [2, 3].

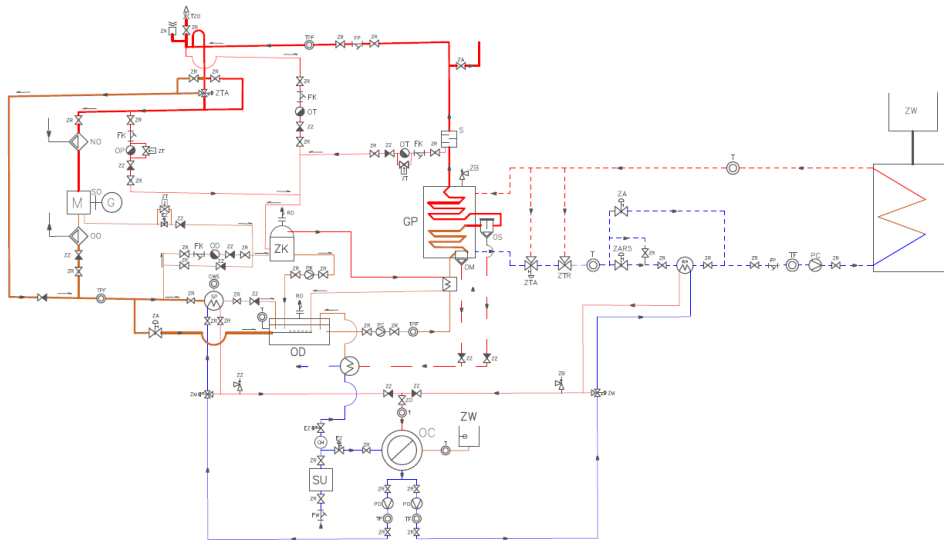


Figure 1. Diagram of a cogeneration system with a heat source in form of a straw boiler and an additional thermal oil circuit, where GP – steam generator (evaporator), M – steam machine (steam engine/steam turbine), SP – condenser, OD – degasser, OC – water tank, TPF – temperature, pressure and flow sensors, OT, OP, OD – various types of steam traps, PC, PK, PO – various types of pumps, ZR, ZZ, ZA, ZB, ZTA – various types of valves

However, the operation of this type of installation requires design experience and professional training of the operator. Occurring vibrations and hydraulic shocks can destroy individual components as well as the whole system. Steam engines and steam turbines are most exposed to vibrations, while hydraulic shocks are created by the so-called steam plugs and apply to places of condensation accumulation. The first threat results from the expansion of high pressures steam in engine cylinders or on turbine blades. They are particularly disadvantageous in the case of engines that operate cyclically. The second threat arising from the movement of the steam and condensate mixture at high speed occurs mainly on pipe sections and drainage elements themselves. Condensate pushing at high speed can also damage other system components. For safety reasons, it is important to minimize the risk of hydraulic shocks in each area of the instance, for economic and operational reasons, proper operation of the steam traps is particularly important. Detection of failure is particularly important because incorrect operation may result in condensate piling up, which results in limitation of its operation, and puncture of the steam trap may cause uncontrolled flow of fresh steam through the steam trap, which results in losses and risk of destroy condensate mains. The steam trap may also malfunction due to incorrect selection: oversizing or improper use [4]. Examples of devices exposed to vibrations and hydraulic shocks are shown in Fig. 2.

Detect of damage the steam traps and support devices can be done by:

1. Visual and auditory diagnostics

It consists of organoleptic observation of the work of individual sections of the installation with particular emphasis on steam traps. Observation of the condensate behind steam trap allows determining whether steam does not penetrate the trap, correctly drains the condensate or does not have leaks or punctures on the vent.

2. Ultrasound diagnostics

Another method is the use of ultrasound devices that give relatively clear signals of the steam trap. Ultrasounds issued during the operation of steam trap are compared with the scope of proper operation and information is sent if it is exceeded. This solution is troublesome due to the device being adapted only to selected dehydrator modes and requires each adjustment.

3. Temperature diagnostics

The third analysis option is to measure the temperature before and after steam trap. The most commonly used are pyrometers, termovision cameras or temperature sensors. At a much lower temperature behind steam trap, it can be assumed that the device does not drain the condensate properly. If the temperature difference is small, it is possible for steam to penetrate the trap.



Figure 2. Fragment of steam-condensate installation including steam turbine, steam engine and separation-drainage unit marked in red

Only a combination of all three methods, taking into account a number of operational factors, will make the assessment correct. Due to this, the method using the vibration diagnostics of the steam installation was tested [5]. Similar use for elastoacoustical materials were presented in [7, 8].

3. Results

The system is equipped with a piezoelectric sensor located on the steam turbine flange. The signal from the sensor goes to the conditioning system, and then is measured by the measuring card with a frequency of 50 kHz. A continuous spectrum analysis is carried out.

Steam impact was simulated by opening the compressed steam valve in the turbine steam supply system. This valve was located a long distance from the turbine so that the turbine received a steam blow after about 15 seconds. The steam, traversing the piping, hit the next bends of the pipeline. Figure 3 shows the next frequency characteristics for vibration measured on a steam turbine.

Analyzing the presented frequency characteristics, it can be seen that the closer the steam is to the turbine, the more visible are the frequency peaks for the range of 600-800 Hz. In the moment of steam impact to the turbine these frequencies have a higher amplitude than the vibrations associated with the normal operation of the steam installation.

The reduction of covering of the steam valve as described in [6], will reduce the vibrations on the turbine blades, and thus lengthen the lifespan.

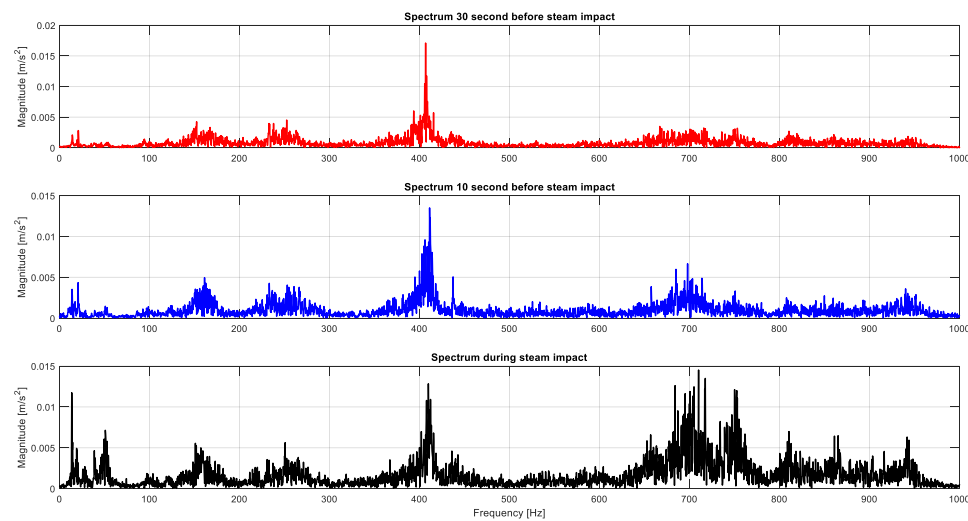


Figure 3. Diagnostic system vibration spectrum

The idea of this approach is to construct the envelope of the Fourier transform of the signal taken from the measurement. Figure 4 presents an example of the simulated envelope system. It can clearly show the principle of operation for the measurement of the signal with two simulated frequencies. In the proposed system, the model envelope is confirmed as a reference one and the system is monitored. A change in the characteristics associated with the propagation of steam impact will result in a shift or increase in the given mode. In this case, the measured signal is going beyond

the envelope boundaries. This, in turn, will entail the activation of the alarm and writing to the txt file the frequency and amplitude for which the envelope was broken.

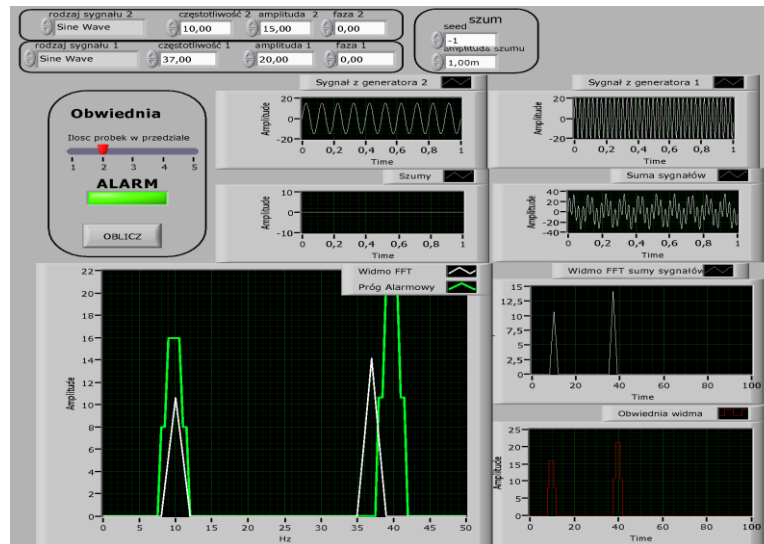


Figure 4. Interface of the envelope diagnostic error system

The feedback from the envelope building system allows the steam valve to be automatically adjusted by a distributed control system.

The algorithm of the envelope creator is to remove the DC bias from the input signal initially. Algorithm computes the envelope further by several steps. First is to remove the noise using the band-pass filters. First order (FIR) band-pass filters are specified by the parameter of cutoff frequencies at f_o and f_{end} . The signal is computed then using hilbert function. The Hilbert transform is useful in calculating instantaneous attributes of a time series, especially the amplitude and the frequency. The instantaneous amplitude is the amplitude of the complex Hilbert transform; the instantaneous frequency is the time rate of change of the instantaneous phase angle. For a pure sinusoid, the instantaneous amplitude and frequency are constant. The instantaneous phase, however, as is for example a sawtooth, reflecting how the local phase angle varies linearly over a single cycle. For mixtures of sinusoids, the attributes are short term, or local, averages spanning no more than two or three points. The Hilbert transform estimates the instantaneous frequency of a signal for monocomponent signals only. A monocomponent signal is described in the time-frequency plane by a single “ridge”.

The analytic signal $x = x_r + jx_i$ has a real part, x_r , which is the original data, and an imaginary part, x_i , which contains the Hilbert transform. The imaginary part is a version of the original real sequence with a 90° phase shift. Sines are therefore transformed to cosines, and conversely, cosines are transformed to sines. The Hilbert-transformed series has the same amplitude and frequency content as the original sequence. The transform includes phase information that depends on the phase of the original.

After this transformation the analytical signal is constructed. A steady state envelope is obtained by using this method.

4. Conclusions

All modern trigeneration devices require advanced diagnostic mechanisms for non-destructive testing of their condition. Such systems allow to increase their efficiency and significantly increase uptime.

This paper proposes a simple measurement system for analyzing vibrations of a steam installation. This system allows to create a frequency spectrum, which is analyzed by the envelope system. The analysis system works in a continuous mode. This arrangement allows to be included in the decision-making process by feedback for a distributed control system of the trigenerator. With this coupling it is possible to limit the impact of the steam impact by adjusting the steam supply valve. In this case, it has a positive effect on the steam turbine operation characteristics.

Acknowledgments

This paper was written under grant entitled “The Self-Excited Acoustic System (SAS) for Monitoring Safety Levels in Mine Workings.” Agreement No. TANGO2/340166/NCBR/2017 and under grant No. D-WPP/II2.0/7.

References

1. W. Goryl, A. Guła, *Analysis of energy potential of agricultural biomass – a case of a typical agricultural commune with perspective of creation a local biomass exchange* (in Polish), *Czasopismo Inżynierii Łądowej, Środowiska i Architektury* (Journal of Civil Engineering, Environment and Architecture), t. XXXI, z. 61 (3/II/14) 173 – 182.
2. S. Podlasek, K. Lalik, M. Filipowicz, *Mathematical modeling of control system for the experimental steam generator*, EPJ Web of Conferences 114, 02151 (2016).
3. D. Markuszewski, *Comparison of various types of damage symptoms in the task of diagnostics composite profiles*, *Diagnostyka*, **20**(3) (2019) 105 – 110, doi:10.29354/diag/111799.
4. D. Astolfi, F. Castellani, F. Natili, *Wind turbine generator slip ring damage detection through temperature data analysis*, *Diagnostyka*, **20**(3) (2019) 3 – 9, doi:10.29354/diag/109968.
5. Spirax Sarco, *The staeam and condensate loop*, Spirax Sacro Limited 2014.
6. P. Pawlik, *The diagnostic method of rolling bearing in planetary gearbox operating at variable load*, *Diagnostyka*, **20**(3) (2019) 69 – 77, doi:10.29354/diag/111567.
7. I. Dominik, J. Kwaśniewski, K. Lalik, K. Holewa, *Influence of acoustoelastic coefficient on wave time of flight in stress measurement in piezoelectric self-excited system*, *Mechanical Systems and Signal Processing*, doi:10.1016/j.ymssp.2016.02.035, 2016.
8. J. Kwaśniewski, I. Dominik, K. Lalik, *Application of self-oscillating system for stress measurement in metal*, *Journal of Vibroengineering*, ISSN 1392-8716, 2012.

